FIBRE METAL LAMINATES SUBJECTED TO PRELOAD AND LOW VELOCITY IMPACT

A thesis submitted in fulfilment of the requirements for the degree of Doctor of Philosophy

Minoo Rathnasabapathy

B. Eng (Aero) (RMIT University)

School of Engineering

College of Science, Engineering and Health

RMIT University

April 2018

DECLARATION

I certify that except where due acknowledgement has been made, the work is that of the author alone; the work has not been submitted previously, in whole or in part, to qualify for any other academic award; the content of the thesis is the result of work which has been carried out since the official commencement date of the approved research program; any editorial work, paid or unpaid, carried out by a third party is acknowledged; and, ethics procedures and guidelines have been followed.

I acknowledge the support I have received for my research through the provision of an Australian Government Research Training Program Scholarship.

Minoo Rathnasabapathy
April 2018

ACKNOWLEDGEMENT

I sincerely thank my Senior Supervisor Associate Professor Adrian Orifici for his excellent guidance and vital feedback. I am incredibly grateful for his tremendous support and encouragement over the duration of this PhD project. Additionally, I would like to thank my Associate Supervisor Professor Adrian Mouritz for his invaluable input and for taking the time to review this work.

I extend my thanks the RMIT technical staff, and in particular Peter Tkatchyk and Robert Ryan for sharing their technical expertise and their assistance in the manufacturing and experimental testing components of this PhD project. Special thanks to Mrs Lina Bubic who supported the administration of my PhD program, and who's help and guidance I am grateful for.

I want to thank my fellow researchers for their assistance at various points in my work. I am grateful for the feedback and insights from my colleagues at the RMIT Composites Team. In particular, special thanks to Andrew Litchfield, Anthony Zammit, Maajid Chishti, Minki Kim and Sawan Shah who started the postgraduate course with me, and who were there to share the highs and lows.

I would like to thank my family and friends for their infinite support throughout the duration of my PhD. I am beyond grateful to the Sullivans, Hills, Johnstons and Svobodas for making me part of their respective families when mine was so far away. Special thanks to Amar, Anna, Emma, Karsh, Susi, Jaime, Jess and Jan whose friendship and encouragement I am forever indebted to.

Last but not least, I would like to sincerely thank my mom, Dino, Karen, Daneel and Udhay for their unceasing love for me throughout every stage of my life.

Dedicated to my mother, Kasturi Padayachee

ABSTRACT

This PhD thesis presents an original research study into the dynamic response, damage and failure of Fibre Metal Laminates (FMLs) when subject to low velocity impact events. FMLs are currently used in a variety of aerospace structures, most notably fuselage sections to the Airbus 380 aircraft, which may experience point impact loading from bird strike, large hailstones or other localised damaging events. Therefore, understanding the impact behaviour of FMLs is essential for damage-tolerant design and structural integrity assessment.

This PhD project aims to develop a physics-based finite element model capable of accurately predicting the impact response of FMLs under unloaded and pre-loaded conditions (tension and compression) as well as the post-impact mechanical properties. The model is validated using data obtained from a comprehensive suite of low velocity impact tests performed on several types of FMLs representative of the materials used in aircraft structures. The model is shown capable of analysing all the critical damage modes of FMLs at the intra-ply and ply-based levels. This includes predicting the sequence of damage initiation and progression as well as the interactions between the various damage modes. Such a high fidelity model for analysing the impact response of FMLs has not been previously reported.

A comprehensive literature review into published research into the impact response of FMLs is presented in the PhD thesis. The review reveals that while numerous studies have assessed the low velocity impact response of FMLs, most studies have been experimental. However, experimental studies are usually limited to quantification of damage after the impact event, and lack the ability to detect in-real-time the interior damage to FMLs. Several numerical models have been developed to analyse the impact damage to FMLs, however due to the layered structure and different material properties of the individual metal and composite constituents, the existing FE models lack the capability to analyse all possible impact damage mechanisms.

A research study is presented in the PhD thesis into the FE analysis of FMLs subjected to impact while in a stress-free (unloaded) state. A full description of the FE model is presented, including its capability to predict the deformation and damage to the individual metal and composite layers and the interfacial regions between the layers. The FE modelling methodology takes into account three modelling parameters; namely the choice of element,

material and mechanical behaviour, and relevant failure criteria for each of the FML constituents as well as the interfaces. Appropriate geometric dimensions and boundary conditions were defined to represent the experimental impact test conditions used for validation. The numerical accuracy of the FE model is assessed using data obtained from low velocity impact tests performed on two types of FML configurations: (i) FML 1 2/1-0.4 and (ii) FML 2 3/2-0.4 consisting of thin layers of aluminium alloy and glass-epoxy composite. The FML configurations were chosen to replicate two commercially available GLARE materials. Impact tests were performed using an instrumented drop-test impact rig fitted with a spherical steel impactor. Different impact energies were achieved by adjusting the impactor drop height. Data obtained from the experimental tests include the dynamic response, damage profile and damage severity to the FMLs for a range of impact energy levels. The FE model is found capable of predicting such impact parameters as the impact force-time response, dent depth, deformation and cracking to the aluminium layers, intraply and interlaminar cracking to the composite layers, and interfacial cracking between the metal and composite layers. The FE model also predicted with good accuracy the increases to the different types of damage with increasing impact energy.

The literature review revealed that virtually all experimental and numerical studies into FMLs subject to low velocity impact have been conducted under stress-free conditions, which is not representative of real-world aircraft applications when loads are exerted on FML structures. The FE modelling methodology was therefore extended to predict the impact response of FMLs under tension and compression pre-load conditions. Experimental impact-under-load tests were performed on FMLs to validate the FE model.

The research revealed that tension preloading of FMLs has a significant influence on the impact response due to the increase in rigidity and overall flexural stiffness. The FE model revealed that the contact duration of the impact event was reduced, and this allows impact-induced stress waves to propagate faster through FMLs causing damage to initiate earlier than the stress-free condition. Simulations and analyses performed using the FE model also revealed that the initiation and severity of impact damage modes such as plastic deformation, fibre failure, adhesive failure and delamination increased with the tension preload level exerted on the FMLs. Under tensile preload, intralaminar and interlaminar damage to the composite layers propagated further, thereby extending the visible damage region.

The application of a compressive preload gave rise to a ‘softening effect’ that reduces the

flexural stiffness of the FMLs. The FE model predicted that interlaminar and intralaminar damage would develop in a more localised region directly under the impact site, and this was confirmed by experimental impact tests. The FE model provided new insights into the evolution of some damage modes after the impact event due to an 'additional buckling effect' as the FMLs exposed to compressive loads as the impactor rebounds.

This PhD project also involved a comprehensive experimental investigation into the compression-after-impact (CAI) properties and damage tolerance of FMLs subject to low velocity impact. The research revealed that the impact damaged FMLs experience significant delamination and debonding under axial compression loading, and this created multiple sub-laminates within the materials. As the buckling stress of any sub-laminate is lower compared to the intact material, the FMLs underwent sub-laminate buckling. The combination of local buckling and sub-laminate buckling during CAI testing reduced the residual compressive failure stress of the FMLs. Aluminium cracking and fibre failure were also identified as critical damage mechanisms that reduced the CAI strength of FMLs.

Significant research outcomes have been produced as a result of this PhD project. The development of a new FE analysis modelling methodology, extensively validated using experimental results, has provided novel insight into all critical damage modes, the sequence in which they occur, and their dynamic interactions under stress-free and stress-loaded conditions. Research into the damage tolerance of FMLs and assessment of the level of degradation due to impact-induced damage modes provides a full picture of the effect of critical damage modes that influence the CAI strength of FMLs.

TABLE OF CONTENTS

LIST OF FIGURES

LIST OF TABLES

CHAPTER 1 : INTRODUCTION

1.1 HISTORICAL BACKGROUND AND DEVELOPMENT OF FMLs

Over the past decades, there has been an increase in demand of high performance materials for aircraft primary and secondary structures. Design drivers such as high damage tolerance, durability and light-weight efficient designs are necessitated by airworthiness authorities to ensure improved safety that enable aircraft structures to function in the presence of significant damage. In addition, economic drivers such as weight savings, minimising maintenance and operation costs, as well as a reduction in production and assembly times are essential when considering the design of principal structures in the aerospace industry.

Aluminium alloys have been the dominant material choice for both commercial and military aircraft over the past seventy years. Due to their light weight, high strength and moderate cost, aluminium alloys are widely used in wing and fuselage structures. More recently, advanced manufacturing techniques, material combinations, and the need to reduce weight and fuel consumption have led to a gradual shift from aluminium to fibre-reinforced composite. Owing to their high specific strength and stiffness, corrosion resistance and excellent fatigue performance, the use of fibre-reinforced composite materials offers considerable advantages over conventional metal alloys. Despite the advantageous properties, composites are susceptible to damage during initial processing and in-service. Weak interlaminar strength and toughness, low ductility, and poor impact and residual strength associated with composites can compromise the safety and structural integrity of the overall aircraft structure.

In order to design a more efficient material for optimal performance, the concept of forming a hybrid structural material has been investigated. Stemming from research conducted in the late 1960s, Kaufman [1] demonstrated that adhesively bonded sheets of aluminium exhibited a higher fracture toughness compared to monolithic aluminium plate of the same thickness. Schijve et al. [2] showed a significant increase in resistance to fatigue crack propagation in aluminium laminates compared to monolithic aluminium.

The laminated components displayed superior fatigue resistance, with crack growth on average four times slower in laminated aluminium specimens compared to monolithic aluminium. The presence of thin adhesive layer between each of the aluminium layers in the laminated specimen acts as a crack divider, aiding to slow crack propagation through the panel. In addition, plane stress conditions exist in the thin aluminium layers of the laminated material. An increase in the plastic zone around the crack tip due to the plane stress conditions of the laminated aluminium cause an increase in fracture toughness [3]. The study demonstrated the potential of designing a damage tolerant structure using laminated materials; a precursor to the development of Fibre Metal Laminates (FMLs).

Stemming from research conducted by Schijve et al. [2], work into Fibre Metal Laminates (FMLs) was undertaken at the Technical University of Delft (TUDelft) to develop a hybrid structural material employing two key constituents - metal and fibre-reinforced. Comprising of alternating layers of thin metal sheets bonded to fibre-reinforced composite plies to form one laminate, FMLs provide a combination of the advantages of the mechanical properties of both materials. Figure 1.1 illustrates a typical FML 3-3/2 laminate. The fibre orientation denotes the direction of the composite plies with respect to the rolling direction of the aluminium. Following the conventional terminology scheme for FMLs, FML 3 3/2 denotes the name of the FML (FML 3) followed by the lay-up scheme, whereby 3/2 represents three layers of aluminium sheets and two composite laminate layers.

Early development of FMLs in the 1980s saw the introduction of aramid fibre-reinforced epoxy/aluminium laminates (ARALL). Later patented [4] and put into production by Alcoa Company, there exist four commercially available ARALL variants (Table 1) offering high strength, high impact resistance and excellent fatigue resistance under tensile and flexural loads [5]. However, several critical problems were found with ARALL variants including fibre failure under tension-compression fatigue loading, moisture adsorption, and low interface failure stress between the aramid fibre and matrix [6].

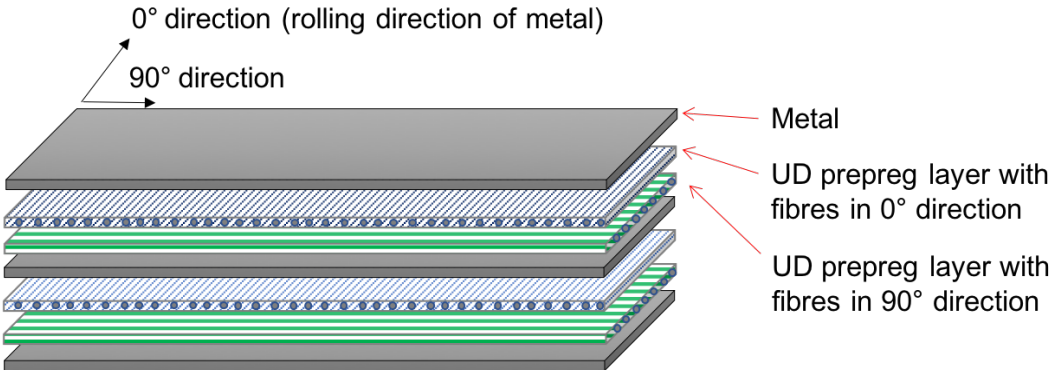

Figure 1.1 Typical Fibre Metal Laminate (FML) 3-3/2 configuration consisting of three layers of metal and two unidirectional (UD) composite prepreg layers.

This led researchers to investigate a stiffer FML material consisting of carbon fibre-reinforced epoxy/aluminium laminate (CARALL). CARALL offers some advantages over ARALL such as higher specific modulus and significantly low crack growth rates due to the presence of high stiffness carbon fibres for crack bridging. However, relatively low values of specific strength and failure strain of the carbon fibres as well as galvanic corrosion between the carbon fibres and aluminium alloy were problems with CARALL. Current research efforts are being made to re-investigate the use of carbon fibre hybrid materials by substituting the aluminium layers with stronger and more corrosion resistant titanium alloys [7-9].

The use of glass fibre as a replacement of aramid and carbon fibres in FMLs was investigated in 1990 at TUDelft. The use of alternating layers of unidirectional glass fibre-reinforced epoxy/aluminium laminates (GLARE) produced superior mechanical properties compared to its predecessors including higher tensile and compressive strengths, impact resistance and post-impact residual strength [10]. The glass fibres provide GLARE with excellent tensile fatigue resistance, and high specific stiffness and strength in the fibre direction. In particular, improved adhesion between glass fibres and matrix allowed for multi-directional laminates to be developed, which are necessary for biaxial and multi-axial stress applications [3]. Due to its low moisture adsorption and density combined with high damage tolerance, GLARE has been increasingly used in aircraft applications. Currently, there are six commercially available GLARE variants tailored to meet certain characteristics and structural requirements, as listed in Table 1.1. The table also lists the different types of ARALL.

	Fibre Type	Metal Type	Metal Thickness (mm)	Fibre Layer (mm)	Fibre Orientation (º)
ARALL 1	Aramid	7075-T6	0.3	0.22	0/0
ARALL 2	Aramid	2024-T3	0.3	0.22	0/0
ARALL 3	Aramid	7475-T76	0.3	0.22	0/0
ARALL 4	Aramid	2024-T8	0.3	0.22	0/0
GLARE 1	Glass	7475-T76	0.3-0.4	0.266	0/0
GLARE 2A	Glass	2024-T3	0.2-0.5	0.266	0/0
GLARE 2B	Glass	2024-T3	0.2-0.5	0.266	90/90
GLARE 3	Glass	2024-T3	0.2-0.5	0.266	0/90
GLARE 4A	Glass	2024-T3	0.2-0.5	0.266	0/90/0
GLARE 4B	Glass	2024-T3	0.2-0.5	0.266	90/0/90
GLARE 5	Glass	2024-T3	0.2-0.5	0.266	0/90/90/0
GLARE 6A	Glass	2024-T3	0.2-0.5	0.266	+45/-45
GLARE 6B	Glass	2024-T3	0.2-0.5	0.266	+45/-45

Table 1.1 Commercially available ARALL and GLARE laminates [11].

Although the majority of aerospace applications employ commercially available FML variants, the development of other FMLs to include metallic alloy alternatives such as titanium and magnesium are currently being studied [11, 12]. Researchers are also investigating the use of natural fibres such as bamboo and ramie, and thermoplastics in FMLs [12]. Optimisation of processing methods is also being investigated. These studies may lead to new hybrids that extend the current application of FMLs to possibly include the naval and automotive sectors.

1.2 PROPERTIES OF FMLs

The hybrid nature of FMLs combines the advantageous mechanical properties of metallic materials and fibre-reinforced epoxy composites. Experimental studies [13] have shown that the effective mechanical properties of GLARE vary linearly with the Metal Volume Fraction (MVF) using the following equation:

$$MVF = \frac{\sum_i^n h_i}{h_{tot}} \tag{1.1}$$

where $\sum_i^n h_i$ is defined by the ratio of total thickness of the metal layers, n is the number of metal layers and h_{tot} is the total thickness of the FML.

High bearing strength, impact resistance, and isotropic nature of metals combined with the high strength and stiffness, low density and excellent fatigue performance of the unidirectional fibre-

reinforced composite [14] allow FMLs to provide a high performance, light-weight replacement to conventional monolithic materials in aircraft structural applications.

A major advantage of monolithic metals over fibre-reinforced composite is their high resistance to impact damage. Due to the ductile nature and ability to absorb larger amounts of energy, impact damage is not often considered to be significant in metal structures. On the contrary, the brittle nature of composites makes them highly susceptible to damage often resulting in undetectable internal damage at relatively low impact energies, reducing the mechanical properties of the laminate. The presence of aluminium constituents in FMLs has been proven to be highly advantageous, improving the impact damage resistance.

A critical aspect of aircraft structural design must incorporate high fatigue resistance against skin cracks that can lead to catastrophic failure. In the event of a fatigue crack, the presence of fibres in FMLs reduces the fatigue crack growth between the aluminium layers by acting as a crack divider, as shown schematically in Figure 1.2. Fibres orientated in the loading direction bridge the crack, thereby reducing the stress intensity at the crack tip and restricting crack growth. The improved fatigue resistance and slower fatigue crack growth rates of FMLs have led to increased fracture toughness properties compared to monolithic aluminium alloys, with FMLs exhibiting crack growth rates that are 10 to 100 times slower [15]. Flame resistance properties of FMLs also compare favourably to monolithic aluminium alloys. The lower thermal conductivity of the composite layers provides a protective barrier for the rear aluminium layer of the FML. The improved fire resistance capabilities of FMLs therefore provide increased evacuation time for passengers exposed to a fire threat in an aircraft [10].

The presence of metal constituents in FMLs also offers numerous advantages. Impacted at higher energy levels, FMLs are shown to have similar types of damage and plastic deformation compared to that of monolithic aluminium alloys [15]. In particular, metal alloys increase the visibility and detection of impact damage in the exterior metal layers of FMLs, while minimising the internal damage to the composite layers. The metal layers of FMLs also act as an outer protective barrier against moisture adsorption, while the fibre-reinforced composite provides an inner moisture resistance barrier between the aluminium layers [16]. FMLs therefore have excellent moisture and corrosion resistance and lower material degradation compared to their individual metallic and composite constituents.

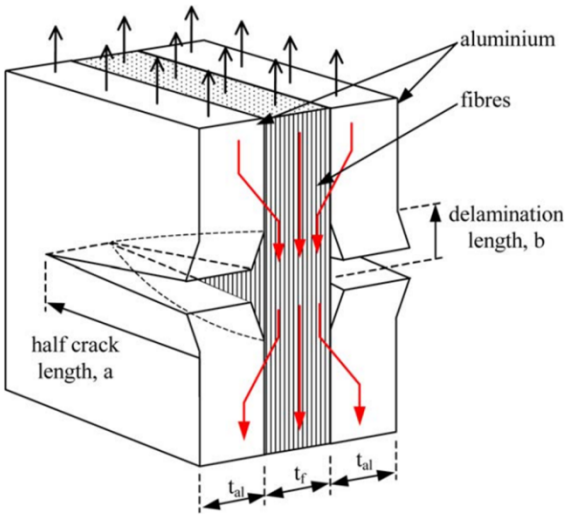

Figure 1.2 Crack fibre bridging in GLARE [17].

In addition to the increased safety aspects noted above, potential costs saving benefits provided by FMLs are critical in the development of new aerospace structural materials. Due to the low density of the fibre-reinforced epoxy composites and metal layers, FMLs provide significant weight savings for aerospace structural applications. Excellent fatigue and impact performance of FMLs allow for reductions in maintenance and repair costs. Various combinations and constituents of FMLs can be developed to optimise material characteristics depending on specific applications and requirements.

1.3 AEROSPACE APPLICATIONS

Implementation of FMLs in primary and secondary aerospace structures has been seen in recent years, offering an alternative to conventional aluminium alloys. Major aircraft manufacturers are evaluating and qualifying FMLs for applications ranging from cargo doors to upper fuselage skin panels.

The introduction of FMLs as aircraft structural materials was first implemented in the Fokker F-27 wing panel. The use of ARALL resulted in increased safety levels and a weight saving of 33% compared conventional aluminium. This led to the extension of ARALL in other aircraft structures [18]. Test applications of ARALL to impact prone, high fatigue areas of aircraft structures showed many structural benefits compared to other materials. Applications of ARALL are the aft cargo door of the Douglas/USAF C-17, and the fuselage and wing structures of the Lockheed C-130 and

Bombardier Aerospace DHC 8. ARALL can also be used as a ballistic armour material in military applications [3].

The development of GLARE has further widened the range of FMLs used in aerospace applications. The combination of high stiffness and impact resistance of GLARE has led to applications in cargo bulk floors, fuselage skins and leading edges. The most significant application of GLARE is the fuselage skin material to the Airbus A380. GLARE is also used for the leading edges of the vertical and horizontal tail plane, and forward and aft sections of the upper fuselage, making up 27 skin panels with a total surface area of 470 m^2 [19].

Due to the increased durability and weight savings, GLARE also offers excellent fire resistance and some explosion containment properties, and is therefore suited for floor panels and liner material to bulk cargo aircraft. In addition, due to the high blunt notch strength and fatigue resistance, some variants of GLARE are increasingly being used as a bond repair patch for cracked monolithic aluminium fuselage skins in order to extend the life of aircraft [15]. Although offering numerous advantages, FMLs have several disadvantages associated with the high cost and manufacturing issues. Long processing times required to cure matrix polymers in epoxy based FMLs lead to time consuming and costly manufacturing process, particularly for large scale aircraft components.

Although FMLs are primarily considered for advanced aerospace structural applications, new developments have expanded their use in a wide range of fields including the maritime and transport sectors. FMLs may provide a light-weight solution to develop energy efficient structures in the transport sector by allowing for decreased fuel consumption. Fire and corrosion resistant properties of FMLs are attractive for marine applications.

1.4 KEY RESEARCH AREAS

Impact damage is a critical issue for virtually all aircraft structures. Aircraft structures are exposed to different impact scenarios at varying energy levels including bird strike, runway debris, ice, engine debris, hail, maintenance damage, and tire rubber impact. Of particular interest in this thesis are low velocity impact events that cause significant internal damage to aircraft structures with minimal exterior visual detectability; so called ‘barely visible impact damage’. Research into understanding the impact response in order to characterise and predict damage formation and its effect on structural performance is therefore fundamental.

1.4.1 BIRD STRIKE AND FOREIGN BODY IMPACT OF FMLs

Bird strike and foreign body impact present a significant source of risk of damage that may compromise the safety and structural integrity of aircraft. A large number of birds in flight at low levels pose a risk of bird strike during the take-off, climb, approach and landing phases of an aircraft. These impact loads can lead to substantial structural damage, as shown for example in Figure 1.3.

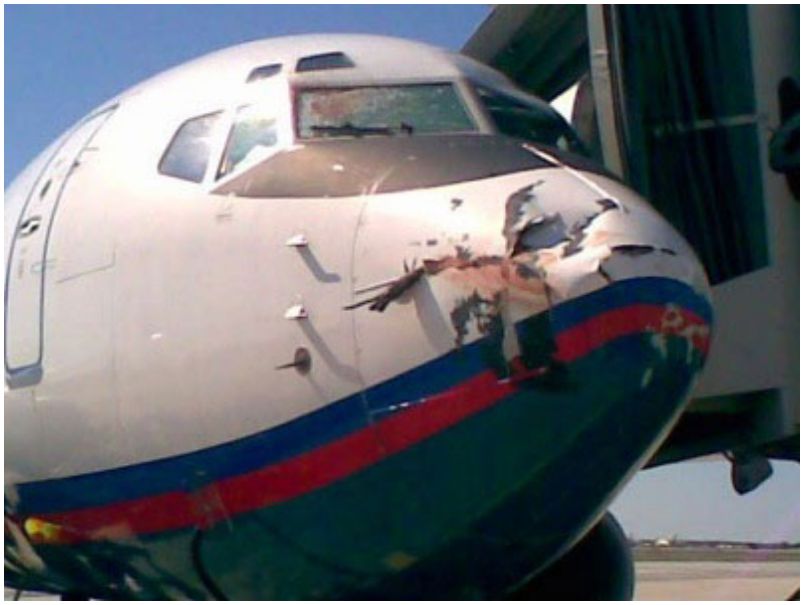

Figure 1.3 Damage to aircraft due to bird strike [20].

Of particular vulnerability are forward facing aircraft structures such as engine fan blades, windshield, window frame, forward fuselage skin, and the leading edge of wings and tailplane. A study conducted in 2009 on bird strikes to civil aircraft in the United States showed that approximately 90000 events were reported to the Federal Aviation Administration (FAA) between 1990 to 2008 [21]. Due to the large and sustained increase in commercial air traffic over recent years, experts within the FAA, U.S. Department of Agriculture (USDA), and U.S. Air Force predict an increase in the risk and frequency of bird strike [22]. As such, aviation authorities mandate aircraft structures fulfil airworthiness requirements ensuring they are designed to withstand bird strikes and other foreign body impacts, assuring continued safe flight and landing after impact. For example, criteria specified by FAA, Federal Aviation Regulations (FAR), European Joint Aviation Regulations (JAR) and the European Aviation Safety Agency (EASA) mandate that the leading edges of the wing and tailplane of a civil aircraft at operational speed are designed to withstand a 1.8 kg and 3.6 kg bird respectively. As specified by FAR/JAR/25.571,

25.631[23], these damage-prone areas must not suffer critical damage to the front spar elements or the wing box in the event of penetration due to impact of the leading edge skin.

Although 90% of all impact damage to aircraft is reportedly due to bird strike [24], other forms of foreign body impact damage (FOD) are also a problem. Hail or ice released from propeller blades, aircraft rubber tire fragments, and runway debris propelled during take-off and landing typically reach impact energies of 17 J to 194 J, each having a mass of 10 g to 15 g [25]. These impact events can be categorised into low velocity and high velocity impacts. This can pose a significant threat to aerospace structures and cause extensive damage such as denting, tearing, and puncturing of the aircraft skin [26].

1.4.2 PRELOAD OF FMLs

Aircraft fuselage and wing structures must withstand in-plane quasi-static loads up to the design limit load during in-flight impact events; typically reaching a pre-tension strain level of 4000-5000 microstrain for military aircraft [27]. In order to replicate realistic loading and damage types in aircraft structures, it is important to understand the behaviour of impact whilst under load. Foreign object impacts usually occur on preloaded structures which may influence the damage tolerance limit. Research on the impact behaviour of preloaded fibre-reinforced composite structures have shown that catastrophic failure can occur due to a significant reduction in residual strength compared to unloaded composite panels [28]. In addition, research has shown that tensile preload can change the failure behaviour and failure mode of fibre-reinforced composite panels [29]. It is therefore necessary to have an understanding of the influence of preload on the structural behaviour of materials, particularly in the case of FMLs whereby the failure behaviour of fibre-reinforced composites is different to that of metals.

FMLs used in aerospace structures may be subject to compressive, tensile or shear loads in an operational environment. Although numerous studies have been conducted on the impact behaviour of FMLs, nearly all of the studies have been performed with the impact taking place on unloaded structures. This does not truly represent events likely to be encountered in real life situations, such as impact by runway debris, hailstones and bird strikes. Due to the complex damage mechanisms of FMLs and its individual constituents, the effect of preload on FMLs is of particular significance. Currently, no studies have been undertaken on the identification and characterisation of critical failure modes of preloaded FMLs subject to impact. This PhD thesis therefore aims to provide a complete understanding of the failure processes of preloaded FMLs

subject to low velocity impact by experimentally and numerically investigating the damage initiation and progression of key failure mechanisms.

Experimental investigations by Vlot [30], Krishnakumar [31] and Esfandiar [32] into the effect of preload on ARALL and GLARE concluded that preloading FML structures leads to permanent deformation of the aluminium layers and longitudinal tensile stresses in the aramid/glass epoxy plies. Vlot [30] also noted a significant reduction to the residual strength of ARALL for impact damage obtained under a preload stress less than 200 MPa.

1.4.3 RESIDUAL STRENGTH OF FMLs

Damage to an aircraft structure may cause a reduction to the static strength. Residual strength is therefore defined as the amount of static strength available during the service period of an aircraft as damage grows as a function of service load and time. In order to satisfy safety requirements, residual strength must be considered during the aircraft design. As such, impact-induced failure processes and mechanisms that reduce the static strength must be well understood. This is possible only when the failure processes and the related mechanisms which cause the reduction to static strength are well understood and correctly addressed in terms of failure criteria.

Aircraft designers are currently considering several materials with respect to their structural response and energy absorbing abilities against impact such as runway debris and bird strike. In particular, modes of damage initiation and growth vary between materials. Given their superior impact resistance and fatigue performance, FMLs offer an excellent alternative to monolithic metals and composite materials for impact susceptible aerospace structures.

Various studies have been conducted on the impact performance of metal alloys, such as Al 2024-T3, used in aerospace structures. Impact to metal alloys results in plastic deformation and is often visible as a surface dent. In comparison, composites experience internal damage (eg. delaminations, matrix cracks) which are often undetectable by visual inspection [33]. Damage can extend to a large region around the impact location due to the poor through-thickness strength and low interlaminar fracture toughness of composite materials. Of particular interest are the internal defects produced by low velocity impacts that significantly affect the residual strength of the structure and hence decrease the overall performance of the material [29, 33, 34]

Researchers have recently begun investigating the response of FMLs subject to various impact scenarios. FMLs experience plastic deformation of the metal layers and delamination to the

composite plies under low velocity impact events. Upon impact, a visual dent similar to that of impacted monolithic aluminium is observed on FMLs. Research conducted by Vlot [35] concluded that FMLs exhibited increased impact resistance and energy adsorption characteristics in comparison to monolithic aluminium of the same areal density. In addition, FMLs are shown to have a significantly smaller impact damage zone compared to conventional fibre-polymer composites.

1.5 AIMS AND SCOPE OF PhD THESIS

Due to their excellent mechanical properties, including high impact resistance and damage tolerance, FMLs are increasingly being used in aircraft applications. Until recently, experimental analysis has been the most common method for determining damage initiation and progression in FMLs subject to impact. Although numerous experimental studies have been conducted on the impact response of FMLs, the detection of complex damage modes located within the FML is limited, and remains an important safety issue for the aerospace industry.

This PhD thesis therefore aims to develop a validated finite element (FE) analysis methodology to identify and characterise the critical damage mechanisms to FMLs subject to low velocity impact events. It is expected that the development of an FE modelling methodology to numerically analyse the structural performance of FMLs will compliment and extend on the capabilities of experimental analyses. Experimental analysis is included in this PhD research to validate and quantify the numerical accuracy of the FE modelling approach. Commercially available FE packages are widely used for aerospace applications, and are used for predicting the behaviour of composite materials. In addition, FE allows for reduction in time consuming and expensive experimental testing required for complex structures.

The FML analysed in this PhD research are representative of aircraft fuselage materials. Of particular relevance to this PhD project is the effect of loading conditions on the resulting impact damage types of FMLs. In addition, the research provides an accurate prediction of the post-impact behaviour of FMLs to determine the structural integrity of the damaged structure. The scope of this PhD project is the application of an FE analysis methodology for accurate impact damage modelling, allowing insight into the internal damage of the FML as well as to explore the possibility of developing an optimum damage tolerant design.

As such, the main scientific and technological objectives of the PhD project are defined as follows:

1. Develop and validate an FE analysis methodology to simulate the damage mechanisms in order to identify and characterise the critical failure modes of FMLs subject to low velocity impact.

2. Investigate the effect of tension and compression preloading conditions on the impact behaviour and damage of FMLs.

3. Investigate the influence of impact damage on the residual properties and damage tolerance of FMLs subject.

1.6 OUTLINE OF PhD THESIS

A comprehensive literature review is presented in Chapter 2, covering a range of topics relevant to the analysis of FMLs subject to impact. A critical review of published experimental and numerical studies is presented into the impact damage mechanisms of FMLs and their effect on the structural integrity and residual mechanical properties. Current limitations of experimental and numerical techniques to predict damage initiation and progression are identified for further study. In particular, the capabilities of current analysis tools to predict the impact damage modes of FMLs are critically evaluated. The findings of the literature review are used to develop an analysis methodology to identify critical damage modes of FMLs subject to impact.

Chapter 3 presents an FE methodology developed using the commercial FE software program Abaqus/Explicit to predict the damage initiation and progression in FMLs subject to low velocity impact. Parametric numerical studies into the model construction, mesh type, and impact contact behaviour are performed. Particular attention to the damage modelling approach is investigated to ensure that all damage modes in the FML constituents are accuracy captured. Plastic deformation of the aluminium layers as well as matrix cracking, fibre failure and delamination of the glass/epoxy composite layers are critical impact damage modes that are modelled using a ply-based damage modelling approach. The numerical analysis is validated using experimental results that are conducted on FML test coupons. Experimental tests at various impact energies were conducted to investigate the impact response and failure mechanisms of FMLs. Experimental analysis is important in establishing the benchmark behaviour of FMLs and is used to validate the applicability and accuracy of the FE methodology.

Chapters 4 and 5 extend the damage modelling technique to investigate the effects of tension and compression preload on the impact behaviour of FMLs, respectively. A numerical modelling and experimental investigation into the impact performance of FMLs is conducted to characterise the

complex damage responses resulting from combined impact and in-plane loading. The FE modelling approach is further developed to accurately analyse the damage modes observed from experimental tests on FMLs under particular impact and loading conditions.

Chapter 6 investigates the residual structural integrity of FMLs in the presence of damage caused by low velocity impacts. The damage tolerance of aerospace structures subject to induced impact is dependent on the type of damage modes initiated and their subsequent progression. Compression-After-Impact (CAI) experimental tests are conducted to analyse the residual strength and structural degradation of FMLs.

A summary of the key findings and conclusion to this work is presented in Chapter 7. In order to extend the application of FMLs, recommendations to further the research work are presented.

CHAPTER 2 : LITERATURE REVIEW

ABSTRACT

The chapter presents a comprehensive review of the published scientific literature into the low velocity hard body impact response of Fibre Metal Laminates (FMLs). The objective of this chapter is to identify research progress towards the experimental and numerical investigation of the impact damage mechanisms of FMLs. Current limitations of experimental and numerical techniques to predict damage initiation and progression are identified, and thus determine areas of new research work required to characterise the dynamic force response, deformation and failure modes that occur with FMLs subject to low velocity impact.

The literature review examines the impact process and subsequent damage mechanisms on the impact response of FMLs subject to low velocity impact loading. Scientific studies into the influence of key parameters such as lay-up configuration, strain rate sensitivity and preload are also assessed. Similarly, a review of published research on the Finite Element (FE) modelling strategies and numerically predicted damage mechanisms of FMLs are assessed. Limitations of the current FE models are thoroughly reviewed, and form the basis of the modelling methodology developed in the PhD project.

The final section of this chapter is dedicated to reviewing published research work performed on the post-impact mechanical properties of FMLs, primarily the compressive residual strength, and identifies key gaps in the current literature. An important outcome of this literature review is the identification of gaps and limitations in our understanding of the dynamic impact process of FMLs, and the subsequent damage initiation, progression and potential interactions between damage modes. The findings from the literature review is used for the basis for the research work performed in this PhD project.

2.1 EXPERIMENTAL STUDIES OF LOW VELOCITY IMPACT RESPONSE OF FMLs

2.1.1 INTRODUCTION

A major advantage of monolithic metals over fibre-reinforced composites is their higher resistance to impact damage. Due to the ductile nature and ability to absorb larger amounts of energy, low energy impact events are not often considered to be significant to the damage tolerance of metal structures. On the contrary, the brittle nature of composites makes them highly susceptible to impact damage, often resulting in undetectable internal cracking at relatively low impact energies, thus reducing the stiffness, strength and other mechanical properties. The presence of metal layers in FMLs has proven to be highly advantageous in improving the impact damage. While much of the earlier work focused on ARALL and CARALL [9, 30, 35-46] containing thin aluminium layers, and more recently alternative metals such as magnesium [11, 47-50] and titanium-based [51-54] FMLs, GLARE is still the primary FML considered for aerospace structures due to its superior impact properties and similar areal density to monolithic aluminium alloys [55]. The hybrid nature of FMLs such as GLARE consisting of multiple high-strength thin layers makes them capable of enduring large deformations resulting in increased energy absorption compared to a thick plate with high bending stiffness [56].

As such, the focus of this PhD thesis will concentrate on FMLs employing aluminium/Glass Fibre-Reinforced Plastic (GFRP) constituents. This section presents an overview of published research into the damage induced by low velocity foreign body impacts on FMLs and the factors affecting their impact resistance. In particular, experimental investigations into the identification, characterisation and sequence of failure modes within the impacted FML are reviewed. Following the conventional laminate designation for FMLs, the reader is reminded that GLARE X 2/1 denotes the laminate name (GLARE X) and 2/1 indicates the lay-up scheme, which in this example represents two layers of aluminium sheet and one GFRP layer.

A growing concern of FMLs in aerospace applications focuses on low velocity impacts (typically less than 11 m/s) that simulate impact events that may occur during maintenance and in-flight operations. Damage resulting from low velocity impacts may not be easily detected during routine visual inspection; however significant internal damage may be present. Extensive experimental investigations over recent years have assessed the damage tolerance of FMLs subject to low velocity impacts. Vlot [30, 35, 41, 42, 57] conducted multiple studies on the impact response of

FMLs, however these studies did not address the corresponding failure modes initiated during impact. Hagenbeek [58] and Laliberte et al. [59] evaluated the damage process, but failed to capture all the failure mechanisms that are present in each of the FML material constituents. Similarly, Caprino et al. [60] correlated the initiation of failure modes relative to the force-displacement curve, however accurate predictions of initial failure are not generally available.

In this literature review, experimental tests for evaluating the complex damage mechanisms arising from low velocity impacts on FMLs are reviewed. Particular focus is given to experimental techniques capable of capturing damage development during the impact event and impact damage detection. The identification of gaps in the literature to fully characterise damage initiation and evolution within the FML structure provides the basis for the research work performed in this PhD project. In-depth understanding of impact damage initiation and progression, as well as the key failure modes and the way in which they interact, are critical for the development of damage prediction models to design impact-resistant FML aerospace structures.

2.1.2 IMPACT PROCESS

Impact is defined as a dynamic and transient event whereby deformation and failure processes occurs to a structure during a collision with an impactor. During a low velocity impact event, the stress distribution between the impactor and target is three-dimensional in nature [61]. As the impactor makes contact with the target, a series of compressive, shear and surface waves are produced that rapidly propagate away from the impact region by travelling through the FML structure. The FML therefore deforms and bends, and damage is introduced under a dynamic bending moment.

The energy absorbing capability of the FML governs the resulting damage created by the impactor, and is determined by three factors, namely (i) the build-up of stresses in the target; (ii) how the stresses are redistributed as the fracture progresses; and (iii) the fracture energies compared to the energy available to drive the fracture process. Other factors are also important, including the target thickness, thickness of the metal and composite layers, and the lay-up pattern. This allows for the deformation mechanisms during an impact event to be divided into three components (i) membrane strain deformation due to in-plane normal stresses; (ii) flexural deformation; and (iii) transverse shear deformation [58].

2.1.3 IMPACT TESTS

An important factor that affects the response of the target being impacted is the initial kinetic energy of the impactor [61]. An impactor with a large mass and low impact velocity does not necessarily induce the same amount of damage as a higher impact velocity event. Test procedures to simulate low and high impact velocities are dependent on the type of impact scenario that is being investigated. Numerous impact tests have been suggested by researchers to simulate the low velocity impact of FMLs. While some researchers have used pendulum-type systems (Charpy tests) [52, 62-66], drop weight impact testing is often the primary choice of researchers in experimentally investigating the impact response of FMLs. Although details of the test apparatus differ between studies, the testing procedure is predominantly based on the ASTM-D7136 standard [67] for measuring the damage resistance of fibre-reinforced polymer matrix composites. Drop weight impact testing allows for different impact events to be simulated by varying the mass, height and shape of the impactor. However, this testing procedure is dependent upon several parameters such as geometry, thickness, stiffness, mass, and boundary conditions of the specimen that can affect the experimentally-derived damage resistance of the FML.

2.1.4 FAILURE MODES OF LOW VELOCITY IMPACT DAMAGE OF FMLs

Capturing the dynamic deformation of FMLs and the subsequent failure mechanisms under impact loading is of primary importance in order to assess the damage tolerance of the material when used in aerospace applications. In this section, the failure mechanisms relevant to FMLs subject to low velocity impact damage are described, with a focus on addressing the key damage mechanisms in each of the FML constituents. The hybrid nature of FMLs combines the excellent impact resistance properties of metals with the lightweight characteristics of GFRP. The combination of the metal and composite constituents in FMLs therefore offers higher impact resistance compared to its individual constituents. The critical failure modes occurring in FMLs subject to low velocity impacts, as illustrated in Figure 2.1 can be classified as (not in sequential order):

(i) plastic deformation of the metal layers (local deformation);

(ii) matrix cracking (perpendicular to fibres and splitting between fibres) and fibre failure ("intralaminar" damage);

(iii) delamination between composite plies ("interlaminar" damage); and

(iv) debonding of the metal and composite layers.

The complexity of each of the failure mechanisms makes the quantification of the damage resistance of FMLs rather difficult. Failure in GFRP laminates initiate at a local level in an individual ply or interface between plies, however ultimate failure may only occur when failure has propagated to several plies [27]. 'First ply failure' is often referred to when damage is initiated and 'ultimate failure' when the material can no longer absorb energy on impact. It should be noted however, that the load-carrying capacity of a structure does not cease when either failure or damage is first initiated [27]. Internal material failure occurs before changes to the macroscopic appearance of the structure are observed, allowing the impacted structure to remain effective in supporting loads before complete failure. Thus, in addition to capturing the failure mechanisms, the literature review highlights the need to focus on the sequence and interaction of the various damage and failure mechanisms that contribute to the degradation of FMLs under low velocity impact.

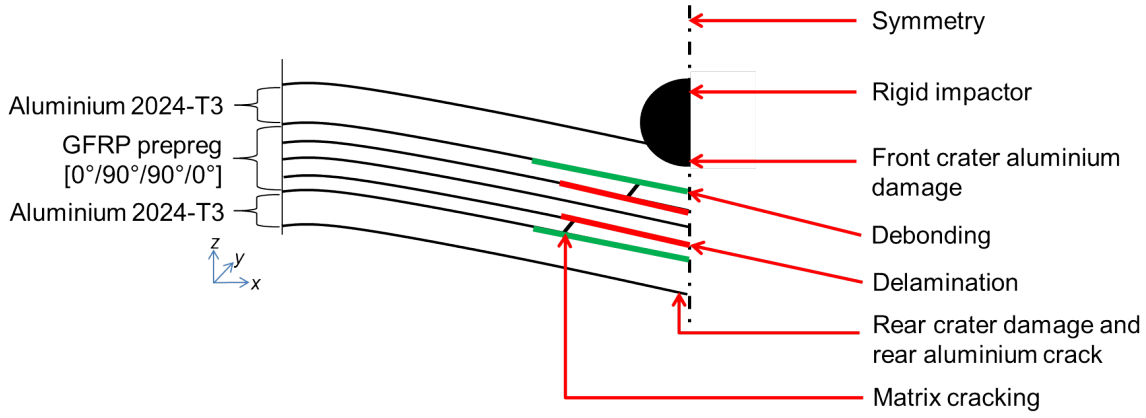

Figure 2.1 Potential failure modes of FML specimen subject to low velocity impact event.

2.1.4.1 PLASTIC DEFORMATION OF FMLs

The dynamic response of thin metallic plates subjected to impact has been studied extensively [42, 57, 59, 64-67] for a large range of impact loading cases. The low velocity impact response of FMLs is known to be similar to monolithic aluminium alloys [50]. The presence of metallic layers in FMLs provides increased ductility resulting in plastic deformation in the form of surface indentation and central plastic deformation during low velocity impact, and complete perforation at high velocities, as seen in Figure 2.2a and Figure 2.2b respectively. Experimental investigations [42, 48, 49, 59, 60, 68-72] have shown that plastic deformation of FMLs subject to low velocity impact typically results in a visible dent damage on the front surface of the metal layer (impacted side). This is due to a thinning process as membrane stretching and yielding of the surface metal layer occurs.

With an increase in impact energy, the size of the dent increases and a localised crack develops in the outer metal layers. This type of damage is referred to as the first crack. At low velocity impacts, the first crack forms on the rear metal surface (non-impacted side) of the FML, typically in the rolling direction of the metal surface, and can be easily detected by visual inspection. Vlot and Krull [57] observed that GLARE had an approximately equal or 15% increase in specific minimum cracking energy at low velocity impact compared to monolithic aluminium. At relatively low impact energies, Caprino et al. [60] reported that GLARE exhibited only small cracks on the non-impacted side of the FML, while ARALL suffered from considerable indentation. This is a result of the GFRP prepreg in GLARE being stronger and more ductile compared to the aramid/epoxy prepreg in ARALL. The initiation of a crack to the rear metal surface layer has been shown to activate intralaminar and interlaminar damage in the forms of debonding and delamination in GLARE [73, 74]. Experimental investigations by Vlot [30, 42] show that fibre cracking in the GFRP plies in GLARE do not occur without cracking of the aluminium layers. Further increase in impact energy leads to the perforation threshold of the FML being reached and full penetration occurs.

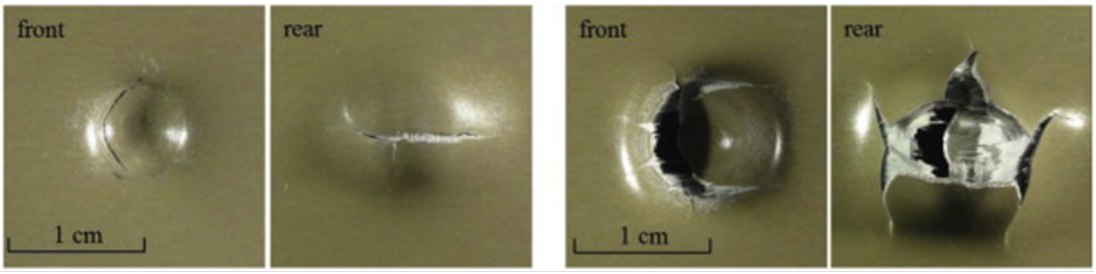

Figure 2.2 a) Perforated and b) penetrated GLARE 5 2/1-0.4 specimens subject to varying impact energies [75].

2.1.4.2 FIBRE FAILURE IN FMLs

As the primary load-bearing constituent in fibre-reinforced composites, fibres provide the principle resistance against applied loads. Fibre failure necessitates the redistribution of loads to adjacent regions in composites that further promotes failure due to a lack of alternate load paths [76]. Consequently, the onset of fibre failure may result in complete structural collapse and rupture of the impacted specimen.

A number of researchers investigating FMLs subject to low velocity impact have observed the presence of fibre failure [18, 30, 41, 60, 77, 78]. Vlot et al. [30, 35] demonstrated that in ARALL and GLARE specimens, fibre failure in the impact damage region was approximately limited to the zone of cracked fibres and was directly linked with cracking of the aluminium layers. Caprino et al. [60] observed that first fibre failure occurred at an impact energy slightly lower than that needed to induce visible aluminium cracking in GLARE specimens. Similarly, Lawcock et al. [79] and Seyed Yaghoubi et al. [78] linked the initiation of fibre failure to a drop in the force-time curve for CARALL and GLARE. The studies showed that fibre failure coincided with the development of a crack in the rear (non-impacted) aluminium surface layer, as shown in Figure 2.3. Moreover, Seyed Yaghoubi et al. [78] demonstrated the presence of fibre failure by conducting post-impact analyses on GLARE 5 3/2 specimens through C-scan ultrasonics and mechanical sectioning.

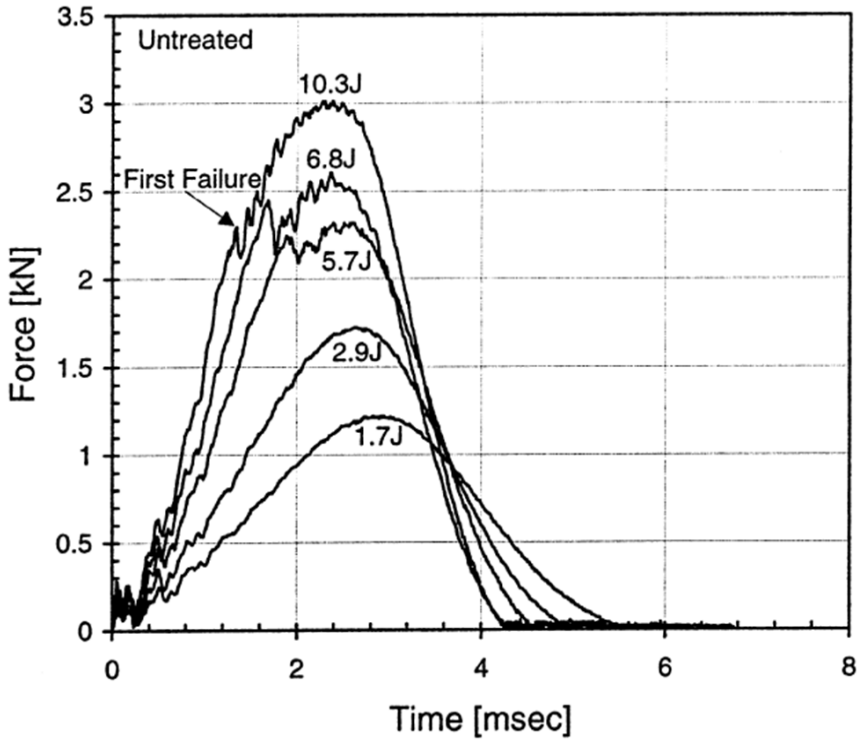

Figure 2.3 Impact force-time curve indicating fibre failure as reported by Lawcock et al. [79].

2.1.4.3 MATRIX CRACKING IN FMLs

Matrix cracking is a form of intralaminar damage within the composite laminate, and is often the first form of damage [48]. Matrix cracks are initiated at or near the fibre and matrix interface due to the localised stress concentration. Matrix cracks typically develop into a series of cracks that

traverse the thickness of the ply and run parallel to the fibres in the ply, stopping at the interface of an adjacent ply having a different fibre orientation. Although the initiation and growth of matrix cracks is crucial to damage progression in FMLs under impact loads, matrix cracks do not lead to a noticeable reduction in stiffness of the laminate [80]. However, it is still important to fully understand the development and, in particular, the coalescence of matrix cracks as they can initiate other forms of damage such as delamination and/or fibre failure. As the interlaminar delamination propagates, additional transverse matrix cracks can be initiated [49].

Vlot [30] investigated the impact damage to ARALL and discovered that until fibre failure, damage of the prepreg layers was mostly limited to matrix cracking. Wu et al. [71] observed extensive matrix cracking in GLARE 5 2/1 subject to an impact energy of 12.7 J. The studies showed that matrix cracks were orientated approximately 45° in the 90° GFRP plies. Wu et al. [71] concluded that this was due to the influence of transverse shear stresses, that in-turn initiated delamination between the 0° and 90° plies as the matrix cracks were unable to penetrate the 0° ply. Similarly, numerous experimental observations [50-52, 54, 63, 77] of FMLs subject to low velocity impact evidence matrix cracking as a critical failure mode that can lead to delamination in the material.

2.1.4.4 DELAMINATION IN FMLs

Delamination occur at the resin-rich interface between two composite plies, and can significantly decrease the global stiffness and residual strength of the overall structure [81]. Delamination failure is crucial to the study of low velocity impacts of FMLs as it can result in significant mechanical degradation of the overall structure. Delamination is induced when high through-thickness stresses produced during the impact event are greater than the interlaminar bond strength between adjacent plies. In-plane fibres of the laminate provide low through-thickness strength; hence the laminate relies on the relatively weak matrix to carry loads in the thickness direction. During impact, this failure is mostly initiated and propagated from manufacturing defects, cut-outs and existing transverse cracks [49]. Under impact loading, shear delamination mode is expected to be dominant [49, 53], propagating rapidly as the loading energy reaches a critical value [49]. Experimental studies on low velocity impacts have shown that delamination often occurs between plies of different orientations [82]. The delamination area may exhibit a ‘peanut shape’ that is inclined in the direction of fibres of the lower plies of the interface [82].

Over the past 20 years, significant process has been made to predict delamination failure modes in FMLs [60, 63, 69, 70, 78, 83-88]. These experimental observations have shown that delamination is a key failure mechanism in FMLs subject to impact loads. Typical post-impact analysis show that delamination is primarily induced in the deformed region directly under the point of impact, but varies in size and shape depending on the impact energy. This was confirmed by several researchers, including Tsartsaris et al. [70] using cross-sectional images. Researchers have employed several post-impact analysis techniques such as C-scan ultrasonics and Scanning Electron Microscopy (SEM) to assess delamination damage in FMLs subject to impact [60, 63, 71, 77-79]. While NDT methods have been widely used in fibre-reinforced composites, difficulties in using ultrasonics stem from large differences in the acoustic impedance values between the metal and composite layers causing ultrasonic wave scattering and reflections. Researchers have therefore employed chemical etching or mechanical removal of the metal layers to evaluate the location and extent of delamination damage of impacted FMLs. Although this necessitates destructive evaluation, numerous methods used in combination such as visual inspection, optical microscopy, ultrasonics as well as cross-sectioning damaged specimens often provide a more detailed evaluation.

The influence of interfacial adhesion strength between adjacent plies on delamination initiation and overall impact response of FMLs has also been highlighted in a number of investigations [79, 83, 85]. With the exception of plastic deformation of the metal layers, Liu and Liaw [63] and Starikov [69] have determined that impact energy is mainly dissipated through delamination. Although these studies have provided insights into the influence of interfacial adhesion strength between adjacent GFRP plies in FMLs subject to low velocity impact, further understanding into the delamination initiation and progression, and their role in energy absorption during impact events is crucial.

2.1.4.5 METAL-COMPOSITE DEBONDING IN FMLs

Among the damage mechanisms to FMLs under impact loads is debonding between the metal and composite layers. In most instances, delaminations occur between two adjacent plies with different fibre orientations, however due to the hybrid nature of FMLs, the interface between the metal and composite layers poses another potential site for delaminations to occur. The distinction between the terms ‘delamination’ and ‘debonding’ is therefore employed in this PhD thesis to assist the reader to differentiate between the failure modes.

Debonding failure at the metal and GFRP interface contributes to the energy absorption and impact perforation resistance of FMLs due to low bond strength between the layers [70, 89, 90]. Wu et al. [71] observed that debonding length in GLARE specimens increased with an increase in impact energy. The study by Wu and colleagues concluded that this damage was due to interfacial shear stresses at the metal/GRFP interface induced by bending [71]. Sadighi et al. [91] reported that debonding between the aluminium and GFRP laminates allows the released metal layers to dissipate more strain energy through membrane deformation during the impact event. The process of debonding is therefore significant, and allows FMLs to deform and fracture in a more efficient way, such that the laminate acts as a number of separate thin layers contributing to improved energy absorption, compared to monolithic materials [35, 57, 71].

2.1.5 DAMAGE QUANTIFICATION IN FMLs

A majority of researchers have used four specific impact damage criteria to quantify and describe the severity of impact damage. These are (i) maximum permanent deformation (maximum dent depth after impact); (ii) crater damage; (iii) minimum cracking energy; and (iv) energy restitution coefficient which is defined as the ratio of the kinetic energy of the impactor before and after impact. Maximum permanent deflection is dependent on the thickness of the FML specimen [58], and decreases with an increase in specimen thickness. Hagenbeek [58] studied the dent depth of GLARE subject to low velocity impact, and showed that increasing the FML thickness over a relatively narrow range (1.4 mm to 3.7 mm) greatly increases the indentation resistance. Additionally, crater damage on the front (impacted) and rear (non-impacted) sides of the FML can be easily measured by determining the damage width of the respective front and rear surface metal layers. Similarly, upon removal of the outer metal layers of the impacted FML specimen, delamination of the composite constituent can be observed [58].

Analysis of the energy restitution coefficient in low velocity impact tests allow for the quantification of absorbed energy of the FML specimens. At impact energies resulting in non-perforation of the FML panel, energy is stored elastically resulting in the impactor to rebound. However, even at a low impact energy range, the absorbed energy of the FML panels is typically greater than the residual energy. To calculate the energy absorbed by the FML specimen, the ratio of the kinetic energy of the impactor before and after impact can be measured, and is defined as the energy restitution coefficient (E):

$$E = \frac{E_{\text{rebound}}}{E_{\text{impact}}} \tag{2.1}$$

Where E_{rebound} is the kinetic energy of the impactor after impact and E_{impact} is the kinetic energy of the impactor before impact. For a fully elastic collision, whereby no damage to the FML was initiated, $E = 1$. As the value of E decreases, more inelastic energy is absorbed by the specimen, indicative of greater damage in the FML. Sadighi et al. [48] experimentally investigated the influence of increasing impact energy on the energy restitution coefficient for three FML configurations, namely (i) GL5-1 (Glare 5 3/2-0.4); (ii) GL5-2 (Glare 5 3/2-0.5); and (iii) Mg-GL5 (Glare 5 3/2-0.5-Mg). The latter configuration replaced the aluminium layers (Al 2024-T3) with magnesium sheets (Mg AZ31B-H24). Sadighi and colleagues showed that an increasing impact energy produced a decrease in the energy restitution coefficient value. At impact energies approaching an energy coefficient value of zero, specimens exhibited extensive damage including perforation. Additionally, at low impact energies (less than 30 J), Mg-GL5 absorbed less energy compared to aluminium-based FMLs (GL5-1 and GL5-2).

Finally, the minimum energy required to initiate a first crack or a through-crack in the FML allows researchers to measure the impact damage resistance. In FMLs, first crack is defined as the minimum impactor kinetic energy needed for visible fibre failure or through-crack formation (cracking of the impacted and non-impacted metal layers). Vlot and Gunnink [18] compared the minimum cracking energy of monolithic aluminium and GLARE specimens, and found that for low velocity impacts a majority of tested GLARE specimens outperformed the monolithic aluminium alloys.

2.1.6 PARAMETERS AFFECTING LOW VELOCITY IMPACT DAMAGE IN FMLs

Extensive experimental work [35, 37, 38, 41, 51, 57, 60, 63, 68, 92-96] has been conducted into the governing parameters that affect the initiation and growth of impact damage in FMLs. A comprehensive review of all experimental work published on the impact resistance of FMLs, detailing the influence of each of the governing parameters is presented in Chai and Manikandan [97] and Sadighi et al. [91]. Chai and Manikandan [97] propose that these can be classified into material-related parameters and geometry-related parameters, as summarised in Figure 2.4.

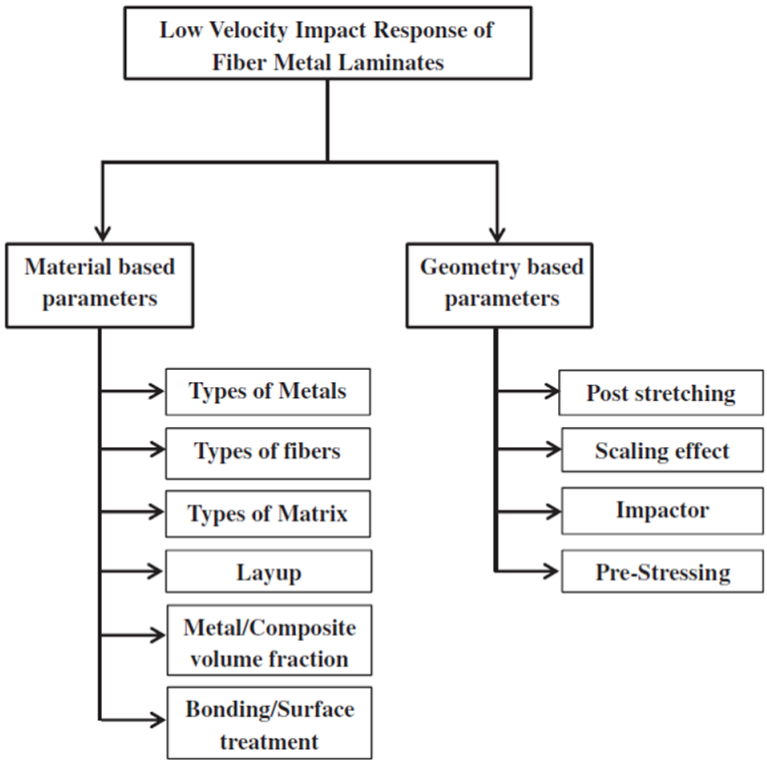

Figure 2.4 Material and geometry event-related parameters that influence the impact response of FMLs [97].

Material related parameters such as type of metal and composite-reinforced constituents, Metal Volume Fraction (MVF), and lay-up configuration of FMLs affect the overall stiffness and thereby have a significant effect on the dynamic response of the impacted structure. Geometry-related parameters such as the size of the panel, boundary conditions as well as characteristics of the impactor and loading rate also need to be taken into consideration in order to fully characterise the damage development in FMLs. In this literature review, a selection of critical parameters relevant to this PhD project are discussed in further detail.

2.1.6.1 EFFECT OF LAY-UP CONFIGURATION ON IMPACT RESISTANCE OF FMLs

The choice of lay-up, configuration and composition of FMLs are dependent on specific design requirements for the aerospace structure being considered, with each having its own advantages and disadvantages. Difficulties in directly comparing relevant research into the effect of stacking sequence and configuration of FMLs stem from the different impact test conditions used by researchers. A review of previous experimental investigations showed that specimens were generally small, with different boundary conditions and shapes including rectangular, square or

circular test areas [30, 35, 36, 39, 41-43, 63, 71, 72, 92]. Thus, this section aims to evaluate trends from literature on the property-dependent nature of FMLs.

Vlot [35] reported that due to their relatively low strain-to-failure value (~2%), ARALL and CARALL predominantly show fibre failure when subject to impact, irrespective of their lay-up configuration. Alternatively, the higher strain-to-failure (5%) of GLARE often exhibits both fibre and aluminium failure, and is highly dependent on the lay-up configuration [35]. Seyed Yaghoubi et al. [98] considered the effect of lay-up configuration on the low energy impact behaviour of GLARE 5 3/2, concluding that the quasi-isotropic [0°/45°/−45°/90°] configuration had better impact damage tolerance compared to angle-ply [45°/-45°/45°/-45°] and cross-ply [0°/90°/90°/0°] configurations. The worst performing configuration was unidirectional $[0°]_4$. These trends are consistent with results reported by Lui and Liaw [38] and Liaw et al. [37]. The latter study attributed the high impact resistance of cross-ply configuration to having fibres orientated in both directions, such that the increased number of adjacent plies with different ply orientations allow more energy to be dissipated through delamination cracking [38]. Additional energy absorption mechanisms include plastic deformation, debonding and crack initiation [38]. Increasing the number of GFRP plies in GLARE specimens subject to low velocity impact results in smaller damage width and higher specific energy to induce first cracking in the aluminium surface layers [42, 57].

Researchers have also investigated the effect of the total thickness of the impacted FML panel either through the substitution of a thicker metal layer or the addition of extra internal metal layers to the FML. Seyed Yaghoubi et al. [78] experimentally studied the influence of panel thickness of GLARE specimens, finding that failure modes changed with increasing panel thickness. GLARE 5 2/1 (t = 1.12 mm) exhibited debonding with aluminium cracking, while debonding, fibre fracture and aluminium cracking were observed in thicker GLARE 5 3/2 (t = 1.93 mm) specimens. FMLs with thicker aluminium layers offer increased impact resistance compared to thin aluminium layers [48, 58, 68]. However, Abdullah and Cantwell [68] identified a threshold aluminium thickness after which the perforation energy begins to decrease. Furthermore, the weight penalty with increasing aluminium thickness should be considered [48].

Several researchers have experimentally evaluated FML specimens subject to low velocity impacts, by comparing the stacking sequence having varying number of aluminium and ply layers [48, 57, 68, 71, 77, 78, 92, 99, 100]. Similar to the volume fractions of fibres and matrix in fibre-reinforced composites, a parameter referred to as the Metal Volume Fraction (MVF) of FMLs,

defined as the ratio of the total thickness of the metal layers to the total thickness of the laminate is investigated. Laliberte et al. [92] conducted experimental tests on three types of GLARE; GLARE 3 2/1, GLARE 4 2/1 and GLARE 5 2/1 with thicknesses of 0.85 mm (MVF = 0.70), 0.98 mm (MVF = 0.61), and 1.11 mm (MVF = 0.54), respectively. While multiple cracks were observed in the 0° and 90° directions in GLARE 3 2/1, GLARE 4 2/1 formed cracks perpendicular to the fibre direction. The study also reported that an increase in impact energy led to an increase in crack length of GLARE 4 2/1, however no changes in crack length were observed for GLARE 3 2/1. The greatest energy absorption was found with GLARE 5 2/1 due to the presence of more GFRP plies. Absorbed energy increased with impact energy due to resulting damage mechanisms such as plastic deformation, matrix cracking, delamination and fibre cracking [92]. In a similar study, Vlot and Krull [57] concluded that by increasing the glass/epoxy content in GLARE there is increased damage resistance. Wu et al. [71] investigated GLARE 4 3/2 and GLARE 5 2/1 at low velocity impact, concluding that although similar damage modes were reported for both FMLs, a difference in the shape of the rear crater damage area was found. GLARE 4 3/2 specimens exhibited a spherical rear crater damage area compared to an elliptical rear crater damage area in GLARE 5 2/1 [71].

The trends observed by researchers reveal that the lay-up configuration has a significant influence on the impact response of FMLs and subsequent damage mechanisms. There are only a limited number of published studies that identify the damage modes present in the composite constituent of the impacted FML specimens [35, 63, 71, 77, 78, 92, 100-102]. These studies are not comprehensive, hence there is a need to further investigate and characterise the damage mechanisms that are present in each of the FML material constituents. More experimental investigations are required to fully characterise the damage initiation and progression of FMLs under impact loads by varying the energy, in conjunction with lay-up configuration.

2.1.6.2 EFFECT OF STRAIN RATE SENSITIVITY ON THE IMPACT RESPONSE OF FMLs

During an impact event, dynamic loads are applied at a high strain rate to these materials, typically in the range of 10 s^{-1} to 1000 s^{-1}. Low velocity impacts such as dropped tools at velocities of approximately 10 ms^{-1} can generate strain rates in the order of 100 s^{-1}, whereas higher velocity impacts in the order of 100 ms^{-1}, such as runway debris, can cause strain rates ~1000 s^{-1} [103]. Bustow et al. [104] noted that no strong strain rate dependency was reported for high-strength

aluminium alloys (Al 7075-T73) at high strain rates. However other studies such as Kawata et al. [105] reported a decrease (1% to 4%) of the strength of Al 2024-T4 and Al 7075-T651, while Davies and Magee [106] showed a 3% increase in the strength for 7075-T6 in a range of strain rates up to 1000 s^{-1} .

Researchers [28, 107-109] have investigated the strain rate sensitivity of GFRP, showing that with an increase in strain rate there is an increase in the tensile strength and failure strain. Gilat et al. [107] attributed this behaviour to the fibre and matrix properties of the GFRP prepreg. Additionally, research conducted by Reyes [110] and Reyes and Cantwell [94] on the strain rate effects at the metal/composite interface of FMLs concluded that strain rate sensitivity is evident in the composite and adhesive material used to bond FMLs.

The effect of strain rate on the properties of FMLs and their constituents therefore need to be considered. Vlot [30] investigated the strain rate sensitivity on the tensile properties of FMLs including GLARE and ARALL. The results concluded that the tensile strength of GLARE increased by over 20% while ARALL exhibited only a minor increase at increasing strain rates in the range of 4×10^{-4} s^{-1} to 69 s^{-1}. Vlot [30] concluded that the rate sensitivity behaviour of GLARE was primarily determined by the rate sensitive behaviour of the GFRP prepreg. In a similar study, Soltani et al. [111] evaluated the quasi-static stress-strain curves from tensile tests on GLARE 2 3/2-0.4 and its constituents. Several researchers [112-114] have investigated the strain rate sensitivity of FMLs utilising other fibres such as carbon and Kevlar, concluding that hybrid metal/composite materials exhibit strain rate sensitivity.

McCarthy et al. [115] performed a series of tensile strength tests on GLARE 3 3/3-0.4 with fibres aligned at 0°/90° and -45°/-45° to the loading axis. Strain rate sensitivity was observed in both laminates. In particular, the 0°/90° tests showed an increase in the failure strain for quasi-static to high (3300 s^{-1}) rates, correlating to an increase in ultimate load capacity. Little evidence of rate dependency was observed between quasi-static and medium (100 s^{-1}) rates. The authors concluded that a threshold therefore exists, above which GLARE begins to exhibit a rate sensitive response.

Given the rate sensitivity of GLARE, it is necessary to define appropriate material properties and damage constitutive models for the computational analysis of the impact behaviour of FMLs. Research on the impact resistance of FMLs at static, low velocity (up to 10 m/s) and high velocity (up to 100 m/s) conducted by Vlot et al. [103] showed that GLARE exhibited higher impact resistance compared to monolithic aluminium 2024-T3 or carbon/epoxy composites, attributed to

the strain rate dependent behaviour of the glass fibres. Similarly, Vlot and Krull [57] reported that the impact damage resistance of FMLs increase with the glass/epoxy content due to the strain rate sensitivity of the glass fibres. More recently, research studies have concluded that for strain rates not exceeding ~10 s^{-1}, the low velocity impact responses of FMLs are comparable to those of quasi-static responses given that the impact mass is much larger than the mass of the FML panel [72, 91, 116-118].

2.1.6.3 EFFECT OF PRELOAD ON THE IMPACT RESPONSE OF FMLs

Although extensive experimental investigations have been conducted on the damage of FMLs in a stress-free loading condition, the literature on the effect of preload on the impact resistance of FMLs is very limited. Early work by Vlot [30, 41, 119] experimentally investigated the impact response of ARALL under tensile loading. Using a hydraulic testing machine, ARALL specimens were preloaded in tension in the rolling direction of the aluminium (in the 0° ply direction). The applied tensile stresses were increased from 0 MPa to 350 MPa, with the maximum value below the yield stress of the aluminium. The preloaded FML specimens were then subjected to low energy impact events. Vlot concluded that cracking of the aluminium layers occurred sooner when specimens were under preload. Also, a significant increase in the crack length was found at high preload levels (greater than 150 MPa). However, the maximum central permanent deflection and contact time decreased with increasing tensile preload level. At low impact energies of 0.13 J (elastic deformation response), the maximum contact force increased in the presence of preload, as the specimen responded more rigidly to the impact event [30]. At higher impact energies between 6.12 J and 9.39 J (plastic deformation response), preload had more influence of the force-time and force-deflection curves, as seen in Figure 2.5. The shape of the damage in ARALL is also influenced by preload. While the aluminium crack in ARALL typically extends parallel to the fibre orientation, the crack was found to grow perpendicular to the fibre direction and loading with the addition of tensile preload, thereby increasing the stress concentration of the FML under impact loads [119].

To date, research into the effect of preload on FMLs is limited to experimental investigations into ARALL. It is also worth noting that published research into preload has only considered tension, and does not other stress states such as compression. Additionally, the limited published literature does not address the damage processes and corresponding damage modes initiated during impact.

In particular, the lack of research conducted on other FML types, such as GLARE, calls for an in-depth study to be undertaken. Not only is further research into the impact response of FMLs under preload important for its use in aerospace structures, but also research is needed to extend our scientific understanding of the fundamental damage mechanisms that control the impact damage tolerance of these materials.

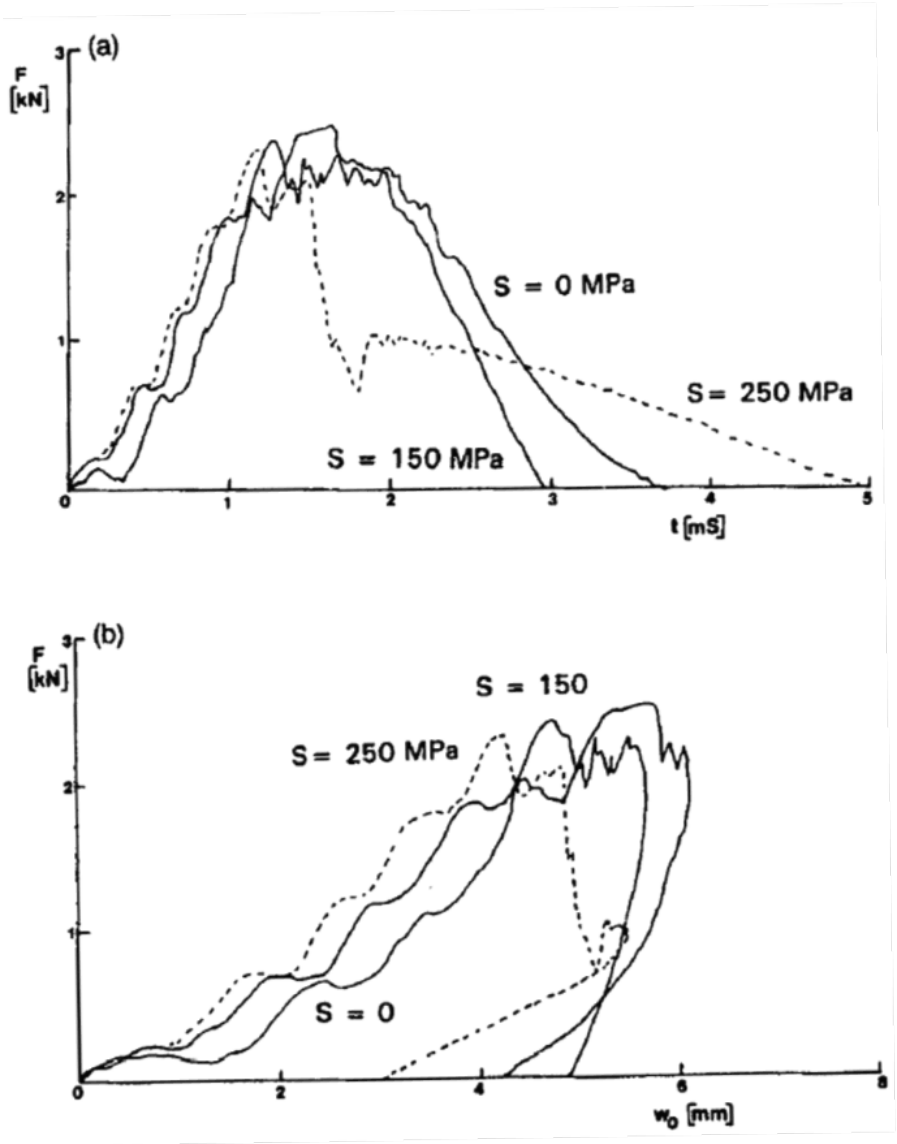

Figure 2.5 a) Force-time and b) force-deflection curves for ARALL 1 subject to an impact energy of 6.12 J and different levels of tensile loading [119].

2.2 NUMERICAL INVESTIGATION OF THE LOW VELOCITY RESPONSE OF FMLs

2.2.1 INTRODUCTION

As described above, impact dynamics of an FML specimen is complex resulting in a number of damage modes. The behaviour of FMLs under low velocity impact is dependent on a number of factors including impact velocity, lay-up configuration, thickness, type of material, boundary conditions, shape of impactor etc. [120]. Due to these factors, and the likelihood of damage extending beyond visible damage, experimental investigations are limited in their ability to determine the number, extent and mechanics involved in the impact process of FMLs. In addition, experimental investigations can be time consuming and expensive. Therefore, robust and efficient numerical analysis tools have been utilised by a number of researchers in recent years to investigate FMLs under impact. Finite Element (FE) models can be quick and inexpensive to develop, and importantly, allow for an in-depth understanding into the impact damage mechanisms of FMLs that are often not captured by experimental tests. This section presents a comprehensive overview of numerical studies into the low-velocity impact behaviour of FMLs, and clearly demonstrates the difficulties of modelling the multiple damage mechanisms of each of the FML constituents and their interactions.

2.2.2 MODELLING STRATEGY

Numerical models allow for the simulation of the the dynamic, non-linear and transient behaviour of the FML specimen under a localised impact load, generally relying on the following approaches [121]:

(i) damage mechanics (dependent on degradation of a plate by reducing the material stiffness due to damage);
(ii) fracture mechanics (applied to model a plate with pre-existing damage and dependent on energy release rate);
(iii) failure criteria (dependent on equivalent stress);
(iv) plasticity or yield surface approach.

In the case of FE modelling of FMLs subject to low velocity impact, most researchers use commercial FE software codes of Abaqus and LS-DYNA. Modelling FMLs under dynamic impact load is particularly complex when considering the individual metal and composite constituents.

Given the layered structure and different material characteristics of FMLs, Iannucci [121] noted that analogous information needed to be incorporated for modelling the impact behaviour accurately, including:

(i) damage mechanics (dependent on degradation of a plate by reducing the material stiffness due to damage);
(ii) material model including plasticity effects to provide post-yield response of metal layer;
(iii) appropriate material model having information about all possible failure of composite layer (eg., Hashin failure criteria in Abaqus);
(iv) material model to capture delamination initiation and its growth;
(v) interface elements to model layered structures and its sensitivity to debonding.

The heterogeneous nature of FMLs means that the constitutive models of the FE analysis are dependent on the scale on which the modelling is performed. Linde et al. [122] discusses three approaches for modelling the different failure modes of the metal and GFRP prepreg constituents. Firstly, the microscale approach models the individual properties of the fibre and matrix constituents. Second, the mesoscale approach considers the individual plies of each of the constituents. In this approach, the composite plies are considered as homogenous materials, however the interfaces between plies are considered separately. Thirdly, the macroscale approach, where FML constituents including the interfaces are considered as a complete homogenised laminate.

The accuracy of the FE models is primarily attributed to the choice of elements selected to model the individual metal and composite constituents of the FML [48]. Many researchers [9, 48, 72, 123, 124] utilise hexahedral solid elements for the metal layers. To represent the GFRP plies, a choice of solid, conventional shell and continuum shell elements are available. 3D solid elements are capable of representing the 3D geometry and stress state of the GFRP plies. Shell elements are commonly used to represent composite layers when the thickness of each ply is much smaller than their span length. A conventional 2D shell element is four-noded with displacement and rotational degrees of freedom at each integration point. It is based on the first-order shear deformation theory and is suitable for structures undergoing large bending deformation, such as the case in impact scenarios. However, this method for full composite failure analysis based on an intralaminar failure model does not allow for delamination between plies to be modelled.

Continuum shell elements, having kinematic and constitutive behaviour similar to that of conventional shell elements, combine the planar nature of 2D shell elements with the 3D geometry

of solid elements. It should be noted however that the planar stress assumption associated with the use of continuum shell elements has been argued to not be suitable for modelling composites during an impact scenario due to the complex through-thickness stresses [125].

Tita [126] developed a Vectorized User Material Subroutine (VUMAT) utilising quadrilateral, full integration S4 shell elements to model the plane stress state and eight-noded linear brick solid element (C3D8) to analyse the 3D stress state of clamped circular CFRP laminates at various impact energies. This was later implemented in Abaqus by a VUMAT subroutine, and has been used by numerous researchers [48, 72, 124, 125, 127-131] to capture the failure modes of FMLs subject to low velocity impact. Similarly, Setoodeh [132] developed an FE code IMPLW3D using a 3D elasticity-based approach coupled with Reddy's layer-wise laminated plate of both thick and thin composites in an impact scenario. However, the code was not easily implemented within commercially available FE software such as Abaqus or LS-DYNA. In a 2014 publication presenting a comprehensive review of past and current research work on FMLs subject to low velocity impact, Chai and Manikandan [97] cautioned that no efficient user-defined FE model was found for the impact analysis of FMLs.

In a detailed numerical study, Seo et al. [125] investigated the efficiency of 2D and 3D based modelling elements by comparing three distinct composite constitutive models namely:

(i) elastic-plastic metal and composite layer with no failure criteria,
(ii) elastic-plastic 3D solid element metal layer and continuum shell element composite layer with in-built Abaqus Hashin failure criteria, and
(iii) elastic-plastic 3D solid element metal layer and 3D solid element composite layer with VUMAT 3D Hashin failure model.

Seo et al. [125] stated that implementation of the Hashin failure model for fibre-reinforced composites within Abaqus/Explicit is limited to plane stress elements such as shell or continuum shell elements, and therefore neglects through-thickness stresses. The damage progression applies only to the in-plane properties and does not affect the out-of-plane properties of the ply. This implies that the material remains rigid [133] in the out-of-plane direction regardless of the extent of damage. Chai et al. [97] notes that although interlaminar damage is the major phenomenon for FMLs subject to impact, most analytical models of FMLs are formulated based on the plane stress assumption.

Seo et al. [125] concluded that at low impact energies resulting in Barely Visible Impact Damage (BVID) and Clearly Visible Impact Damage (CVID), there are no significant differences between

the 2D and 3D constitutive modelling approaches. They also noted that BVID cases corresponded to a limiting case whereby planar failure mechanisms dominate [125]. Overall, Seo et al. [125] resolved that while the 3D failure model was more conservative compared to the 2D failure model, it was evident that the correlation to experimental results at BVID and CVID impact energies were still good.

Sadighi [48] performed FE analysis to compare solid elements and shell elements for the composite layers of FMLs. The FE results showed that solid elements gave better correlation with the experimental results than shell elements. In contrast, Song [9] numerically investigated the impact performance of CARALL using solid elements for the metal layers and shell element for the CFRP layers incorporating the 2D in-built Abaqus/Explicit stress-based Hashin damage criteria. The model gave good agreement of the impact force-time histories compared to the experimental results. Khalili et al. [134] evaluated the effect of element type in the modelling of composite structures subjected to low velocity impacts, and concluded that continuum shell elements (SC8R) were suitable for modelling quasi-static and dynamic impact problems for both thin and thick composite structures. Rathnasabapathy et al. [135] used hexahedral continuum shell elements (SC8R) to model the composite layer in a validation study using the experimental impact results of Wu [71] for GLARE 5 2/1. The model captured the total damage area and allowed for predictions of the intralaminar damage associated with impact on a ply-based level.

In summary, while some researchers argue that the composite plies of the FML structure must be modelled using solid elements with 3D failure model to simulate the through-thickness behaviour during impact, other studies have shown that by using shell elements and incorporating the 2D in-built Abaqus/Explicit stress-based Hashin damage criteria, FE models are able to accurately capture the dynamic impact event and subsequent damage to the composite layers of the FML.

2.2.3 MODELLING DAMAGE AND FAILURE MECHANISMS OF FMLs

2.2.3.1 PLASTIC DEFORMATION

Guan et al. [136] and Fan et al. [137] used elasto-plastic material with rate-dependent behaviour for aluminium layers when modelling GLARE 3-2/1, 4-2/1, 5-2/1 and aluminium/woven GFRP FML specimens in 2/1, 3/2, 4/3 configurations respectively, subject to low velocity impact. Shear and tensile failure criteria were used to simulate the failure processes in the aluminium layers. The FE results showed good correlation with the experimental impact results in terms of maximum permanent displacement. The authors demonstrated high correlation of force-time history and

energy causing FML perforation. The study by Fan et al. [137] assumed that the aluminium layers in the FML dominated the impact response, and did not include delamination modelling between the composite plies. The FE model was shown to predict the perforation stage of the impact event, comparing well (within 10%) with the experimental results as shown in Figure 2.6. However, the inability of the model to capture interlaminar and intralaminar damage to the composite plies means that there was not a comprehensive overview on the role of each of the FML constituents during the impact event.

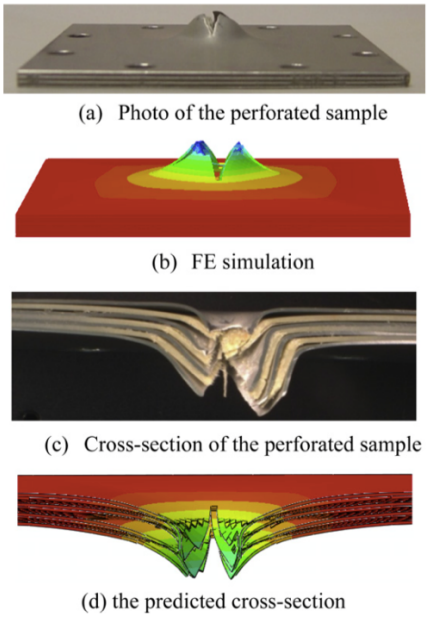

Figure 2.6 The failure mode and central cross-sections of the failed FML 4/3 plate (consisting of 8-ply composite cores) subjected to low velocity impact [137].

A numerical model developed by Mohotti et al. [138] based on the Lagrangian-based finite-element approach in LS-DYNA was used to study elastomer composites (polyurea) in FMLs under low-velocity impact loading. The polyurea was modelled using the Mooney-Rivlin material model and the aluminium alloy was modelled with the Johnson-Cook material model. No perforation of the FML plate was considered and no debonding was found between the polyurea coating and aluminium layer.

2.2.3.2 INTRALAMINAR DAMAGE

Intralaminar damage is a key damage mode to the composite constituent of FMLs. Capturing the initiation and progression of matrix cracking and fibre failure damage mechanisms is important to gain a greater understanding of the impact response of the FMLs.

Song et al. [9] conducted FE analysis into the effect of impact energy on CARALL using the 2D stress-based Hashin damage model for the composite constituent. Figure 2.7 shows the Von Mises stress distribution for the individual CFRP layers. A peanut-shaped stress contour along the fibre direction was computed for each of the ply layers, corresponding with the shape of matrix failure area [9]. This study by Song et al. [9] is one of few studies that demonstrate ply-by-ply analysis of the composite constituents of the FML structure under impact load.

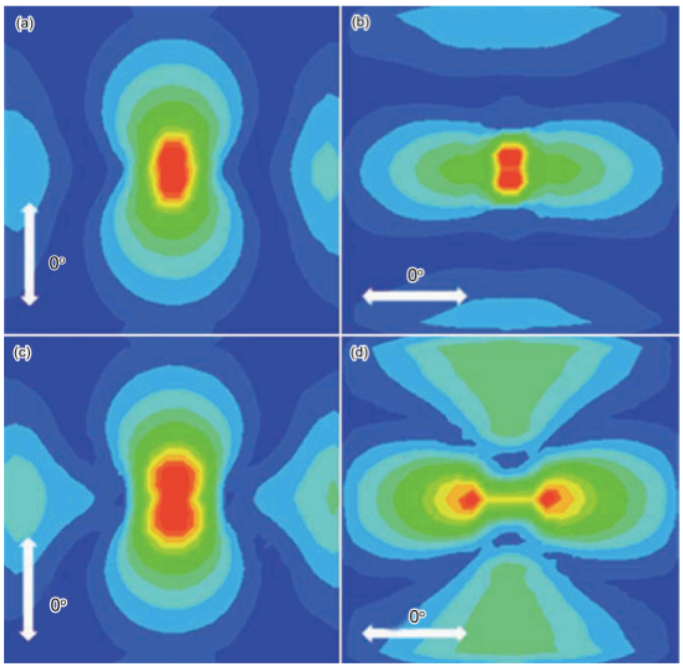

Figure 2.7 Von Mises stress distribution of individual CFRP layers for a) 0°, b) 90°, c) 0°, d) 90° ply direction of CARALL specimen subject to low velocity impact [9].

Seo [125] conducted an FE comparative study using the 2D and 3D failure criteria in Abaqus, comparing the force-time history, maximum deflection, and damage progression caused by low velocity impact on GLARE 5-2/1 and GLARE 4-3/2. The numerically damage shape using the 3D model was predicted to be larger than the 2D model for both FMLs. Seo [125] also noted that the initiation of composite failure in the 3D model occurs earlier compared to the 2D model. This FE study is one of the few publications that show intralaminar damage to the FML composite layers under impact. However, only the final stage of the composite plies were recorded, and the results do not discuss the damage progression of the fibre tension failure mode during the impact event. In FMLs, it is important to understand the damage initiation and progression during the impact event on a ply-by-ply basis to gather insight into the damage sequence and the possible interactions between damage modes. To date, this has not been studied in detail.

Zhu and Chai [72] implemented the 3D stress-based Hashin failure criteria to simulate failure in the GFRP layers and the Johnson-Cook plasticity model for the aluminium layers for two GLARE configurations (2/1 and 2/2). Numerical predictions of low velocity impacts showed good agreement with the experimental results. The authors showed numerically that the impact energy was dissipated by delamination, fibre failure, aluminium cracking and plastic deformation. Plastic deformation was computed to be the main energy absorption mechanism, initiating at the impact region and extending when the impact energy increases and controlling the stiffness and deflection of FML specimen.

In a recent study, Bienias [124] developed an FE model to investigate the damage response of FML laminates with the 2/1, 3/2 and 4/3 lay-up configurations subject to low velocity impact. Damage to the aluminium layers of the FMLs was modelled using the 'Ductile Criterion' in Abaqus/Explicit, such that the occurrence of metal damage is a function of stress triaxiality and plastic strain rate. The composite plies were modelling using the VUMAT subroutine in Abaqus/Explicit based on the 3D stress-strain based approach. Figure 2.8 (a) 2/1; (b) 3/2 and (c) 4/3 shows cross-section contour plots of the GLARE FMLs. State variables SDV3 and DUCTCRT represent matrix damage in the composite plies and ductile failure of the aluminium layers. Thus far, limited research has been done on mapping damage modes and tracking the sequence of damage.

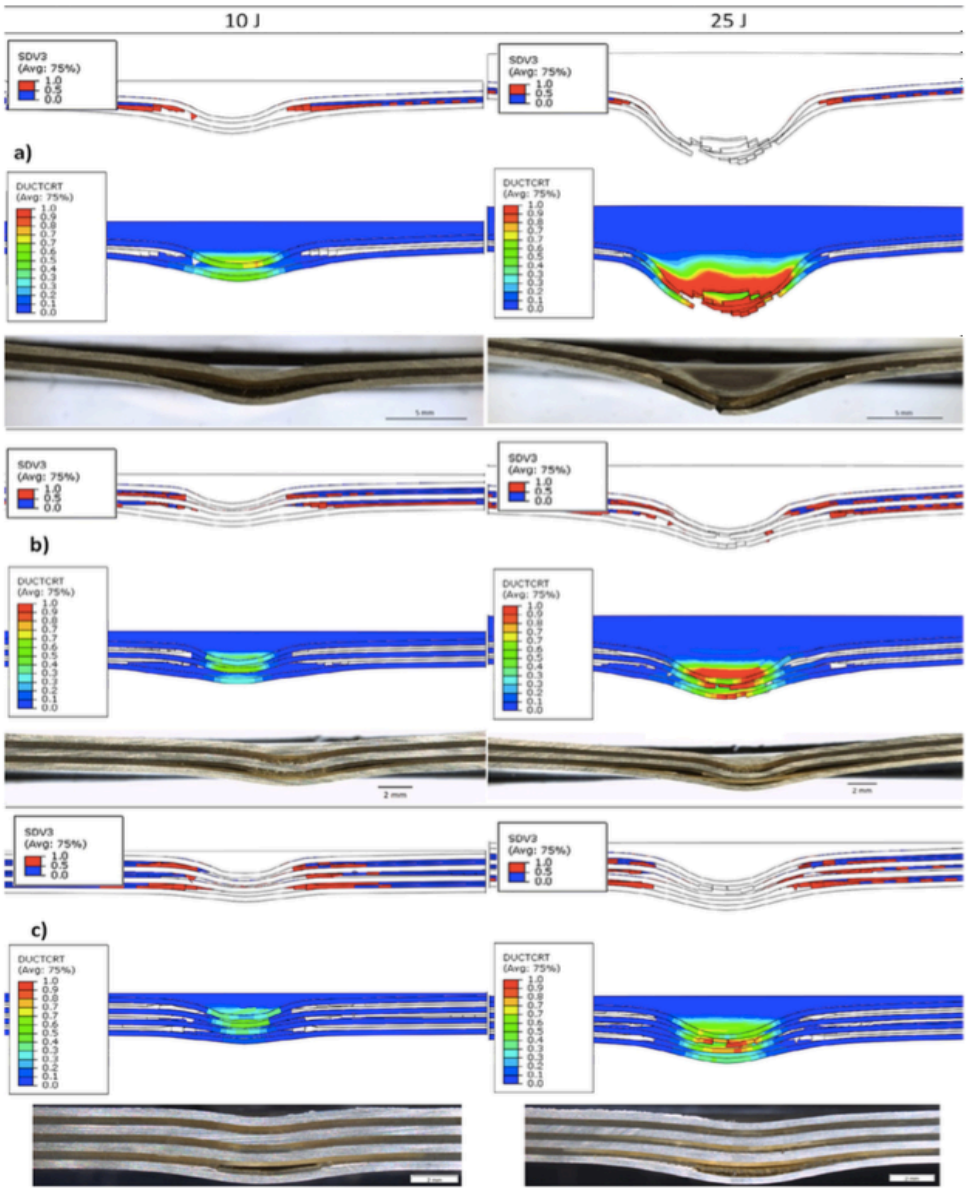

Figure 2.8 Numerically predicted impact damage contours (SDV3 and DUCTCRT for matrix damage and metal failure respectivly) of FML laminates with a) 2/1; b) 3/2 and c) 4/3 lay-ups [124].

2.2.3.3 DELAMINATION

Delamination is a critical failure mechanism for FMLs subject to impact events. As such, FE models that simulate the low velocity impact of FMLs must be capable of predicting the delamination on a ply-by-ply level in order to better understand the mechanisms by which delamination contributes to failure.

Laliberte et al. [128] developed a user-defined material subroutine in LS-DYNA to study the

failure mechanisms in GLARE 3-2/1, GLARE 4-2/1 and GLARE 5-2/1 using continuum damage mechanics. Three types of interface models were implemented and compared: tied interface (elastic-plastic aluminium, elastic GFRP), simple-tie break (elastic-plastic aluminium, elastic GFRP) and tiebreak (elastic-plastic aluminium and damageable GFRP), and showed that tiebreak provided better predictions of delamination damage. Hashin failure criteria were applied to each GFRP ply to compute damage initiation under impact loading. The behaviour of the interfacial regions was modelled using a traction-separation law. Depending on how the interface between the aluminium/GFRP was simulated, the predicted absorbed energy, peak force, and permanent dent depth could vary by as much as 50% from the experimental values. The study concluded that fibre failure and degradation of the composite plies were the main energy absorption mechanisms. Delamination, though not the main damage mode, should be studied because even minor delamination could affect the post-impact mechanical properties of GLARE [128].

Nakatani [53] developed an explicit FE model using the Cohesive Zone Model (CZM) to simulate delamination between composite plies to titanium/GFRP FML specimens subject to low velocity impact, closely replicating experimental results reported by Cortes et al. [12]. The use of the CZM combines strength-based criteria to predict damage initiation with fracture mechanics energy criteria to simulate damage propagation. The Johnson-Cook strain rate-dependent plasticity model was applied to the titanium layers, and orthotropic elasticity was used for the GFRP layers. Nakatani [53] reported that delamination and damage was dependent on the titanium layer on the non-impacted side of the FML, such that if cracks were initiated in the titanium layer, then the delamination pattern to the GFRP layers would change. These findings further reiterate the necessity to model the individual layers of the FML specimen to understand the interactions between damage modes. A similar study using CZM was conducted by Lopes [139] on CFRP plates, achieving satisfactory results compared to experimental post-impact damage inspections using C-scan ultrasonics.

Manikandan and Chai [130] used two non-interactive damage models to simulate the damage in composites plies to an aluminium glass/epoxy composite FML. This included an intraply damage model based on the continuum damage mechanics (CDM) approach and an interply damage model based on CZM at the interfaces of two dissimilar materials to account for delamination. The CDM approach accounts for fibre fracture and matrix cracking [130]. The FE models were able to compute the final intralaminar and interlaminar damage shapes in agreement with experimental observations, as well as the peak impact load, contact time and maximum impactor displacement. In a similar study, Zhou et al. [140] modelled the interfaces between the composite plies using

eight-node 3D cohesive elements (COH3D8) to predict delamination damage. A reasonable agreement was shown in the deformation failure modes.

It is evident from the studies discussed in this section that the intralaminar and interlaminar damage to the composite plies of FML specimens under low velocity impact are not easily captured. These phenomena can only be fully incorporated and understood through a ply-by-ply analysis of the damage initiation and progression. The development of a proficient numerical modelling methodology is therefore needed to capture the above mentioned damage and dynamic effects. The FE model must be capable of analysing the material models for anisotropic plasticity, crack and delamination growth with suitable failure criteria for the metal and composite constituents of the FML. Though the individual failure mechanisms of FMLs under impact are well known, a comprehensive map of all damage modes, sequence of damage initiation and progression, and interaction between damage modes is not sufficiently understood.

2.2.4 MODELLING PRELOAD AND IMPACT

Aircraft fuselage and wing structures are required to withstand in-plane loads up to design limit load, typically reaching values of 4000 με to 6000 με. As reported in Section 2.1.6.3, experimental research has proven that the combined effects of impact and preload has a significant influence on the failure behaviour and damage processes of FMLs, however this research is very limited. This section gives an overview of the few numerical studies undertaken on the effect of tension preload [141-145] and compression preload [146-151] of composite materials. These studies form the basis of the modelling methodology undertaken in this PhD project on the numerical investigation of preload on FMLs subject to low velocity impact.

Recent research into the effects of impact and preload [28, 29, 141, 145, 152-158] has shown that the presence of tension preload significantly influences the failure behaviour and damage processes of composite panels by reducing the impact tolerance and altering the failure modes. Pickett et al. [141] modelled the combined impact and preload response of three carbon/epoxy laminates having different fibres, resins and lay-up patterns. The FE model implemented a multi-layered thin shell element in the explicit FE code PAM-CRASH^{TM}, ensuring each composite ply was represented using an orthotropic elasto-plastic material model. Preload up to 0.25% strain was imposed at the loading tabs in both the positive and negative directions. The loading tabs are then held fixed for the impact simulation. The carbon/epoxy laminates exhibited transverse cracks when impacted at high preloads. Mikkor et al. [28] also used the explicit FE code PAM-CRASH^{TM}

to analyse the ballistic impact response of preloaded composites under various parameters such as preload magnitude, impact velocity and impact specimen geometry. However, the FE model did not consider delamination as a potential failure mode. A Bi-Phase ply composite model was used that has limited capabilities to treat transverse matrix and shear failure. It was found that changes to the failure behaviour depended on the magnitude of preloading.

Compressive preloading conditions are critical as plate buckling becomes an issue for thin FML structures. The application of compressive preload leads to a "softening effect" on structural stiffness (observed by global deflection), resulting in a more severe dynamic panel response in the forms of stress waves and global deflection compared to an unloaded panel [159]. The higher bending deformations, in contrast to a stiffening effect from a tensile preload, induce greater delamination damage due to initial buckling deformation. To evaluate the effect of compression preload prior to impact, Heimbs et al. [150] impacted compressively prestressed carbon/epoxy laminates. An explicit solver without dynamic relaxation was used in LS-DYNA for both the preloading and impact loading to ensure numerical stability of the composite panel. The displacement-controlled compressive prestress was applied, followed by the impact event until springback. The model predicted catastrophic failure of the carbon/epoxy laminates. Chai [151] conducted a similar investigation of low velocity testing in conjunction with compressive preload on stiffened carbon/epoxy panels. Shear cracks were observed leading to catastrophic failure at 30% of the ultimate compressive strength.

To date, only experimental investigations into the effect of preload have been conducted on FMLs subject to low velocity impact. A gap in research therefore exists to understand the failure processes of tension and compression preloaded FMLs that replicate realistic loading conditions.

2.3 POST-IMPACT RESIDUAL STRENGTH OF FMLs

2.3.1 INTRODUCTION

Compression-After-Impact (CAI) is an accepted standard for quantifying damage tolerance, and is defined as the ability of the impacted structure to resist the formation of damage and the ability to sustain further service load. Recent studies show that a reduction of compressive strength up to 60% can occur in composites when no obvious visible defect is identified [160]. This is particularly important when considering low velocity impacts that result in Barely Visible Impact Damage (BVID), that is difficult to detect from visual inspection.

Numerous studies have reported on the buckling and failure behaviour of impacted composites subject to uniaxial compression, and shown that they are influenced by the specimen geometry [148, 161, 162] and the impact damage [163-167]. A large number of studies into the residual compressive strength of impacted composite structures have been performed, however only a handful of studies have investigated the CAI strength of FMLs. To date, no literature exists on the CAI strength of FMLs subject to combined preload and impact. Therefore, work is still necessary to analyse and characterise the phenomenological correlation between the reduction in compressive strength and the impact damage to FMLs. This section reviews published research into the CAI strength of FMLs, and the damage mechanisms during post-impact compression loading.

2.3.2 RESIDUAL STRENGTH TESTING OF FMLs

In order to evaluate the damage tolerance of a structure after impact, a standard uniaxial compression test method was developed by Boeing and adopted by the ASTM to quantify the membrane-dominated response [160]. Literature on CAI experimental tests performed on thin composite and FML specimens commonly report that no standard currently exists, with many studies using a modified version of the ASTM D7137 standard [168] for CAI testing of monolithic composites (designed for 5 mm thick specimens). Specimen thickness below 5 mm are often prone to global buckling due to the high span-to-thickness ratio leading to deformation occurring in areas located far from the impact site. Hoogsteden [169] used a modified Boeing compression fixture to measure the CAI residual strength on 1.346 mm thick ARALL specimens, but without success. Global buckling of the impacted specimens occurred upon application of the compression load, before impact-induced damage regions had a chance to initiate failure. Jakubczak et al. [170] investigated an alternative CAI test fixture for CAI tests of thin FML specimens. In the suggested solution all degrees of freedom were removed in order to generate stress in the central part of the specimen, thereby enforcing local buckling in the impact damage area. Alternatively, another CAI test fixture based on the work by Sánchez-Sáez. et al. [171] uses a two-piece compression holder with a free zone in the impact axis. Jakubczak et al. concluded that using the latter design for FML specimens (1.1 mm thick) leads to a stress concentration and subsequent first buckling mode in the impact damage region.

2.3.3 EFFECT OF DAMAGE MODES ON COMPRESSIVE RESIDUAL STRENGTH OF FMLs

A reduction to the residual compressive strength of an impacted structure can usually be attributed to multiple damage mechanisms. A number of studies show that during CAI testing, the uniaxial compression load results in delamination as the dominant failure mode. Since much of the energy absorbed during impact is via the formation of delaminations, the CAI strength ultimately depends on the energy dissipated by the specimen during the impact event. Compared to residual tensile and flexural performance, the reduction to the compressive strength due to BVID is significant [172, 173]. CAI shows particular sensitivity to the size of the induced delamination. A majority of researchers agree that the presence of impact-induced delamination plays a key role in reducing the flexural stiffness of the laminate due to the formation of sub-laminates [146, 165, 166, 171, 174-179]. Sub-laminates have a lower bending stiffness than the original laminate and are less resistant to buckling loads [180]. Abrate [33] showed that under a compressive load, delamination can cause buckling in one of three modes: global buckling, local buckling (buckling of the thinner sub-laminate), or a mixed mode (combination of global and local buckling). In thin laminates, failure modes change from global to local to mixed mode as the delamination length increases [33]. This observation is supported by Homan [181] when investigating the CAI strength of GLARE 4-5/4, whereby global buckling initiated by local buckling in the impact-induced crater (dent) region.

A number of researchers including Cromer [160] have shown a correlation between the size of the delaminated area and CAI strength. Dhaliwal and Newaz [182] experimentally investigated the CAI residual strengths for three configurations of CARALL subject to low velocity impacts in the range of 14 J to 31 J, as shown in Figure 2.9. It was found that at higher impact energies (21 J to 31 J), local buckling of specimens stemming from delamination in the impact damage zone led to stiffness degradation of the CARALL and a subsequent reduction in the CAI strength by 28% to 41%. At lower impact energies (14 J), local buckling was not recorded, and CARALL specimens failed due to end crushing.

Only two publications, namely by Dhaliwal and Newaz [182] and Homan [181] who examined CARALL and GLARE 4-5/4 respectively, have investigated the correlation between the delamination damage mode and the residual compressive strength of FMLs. Thus, further investigation is necessary to study the influence of increasing impact energy and resulting delamination damage on the CAI strength of FMLs.

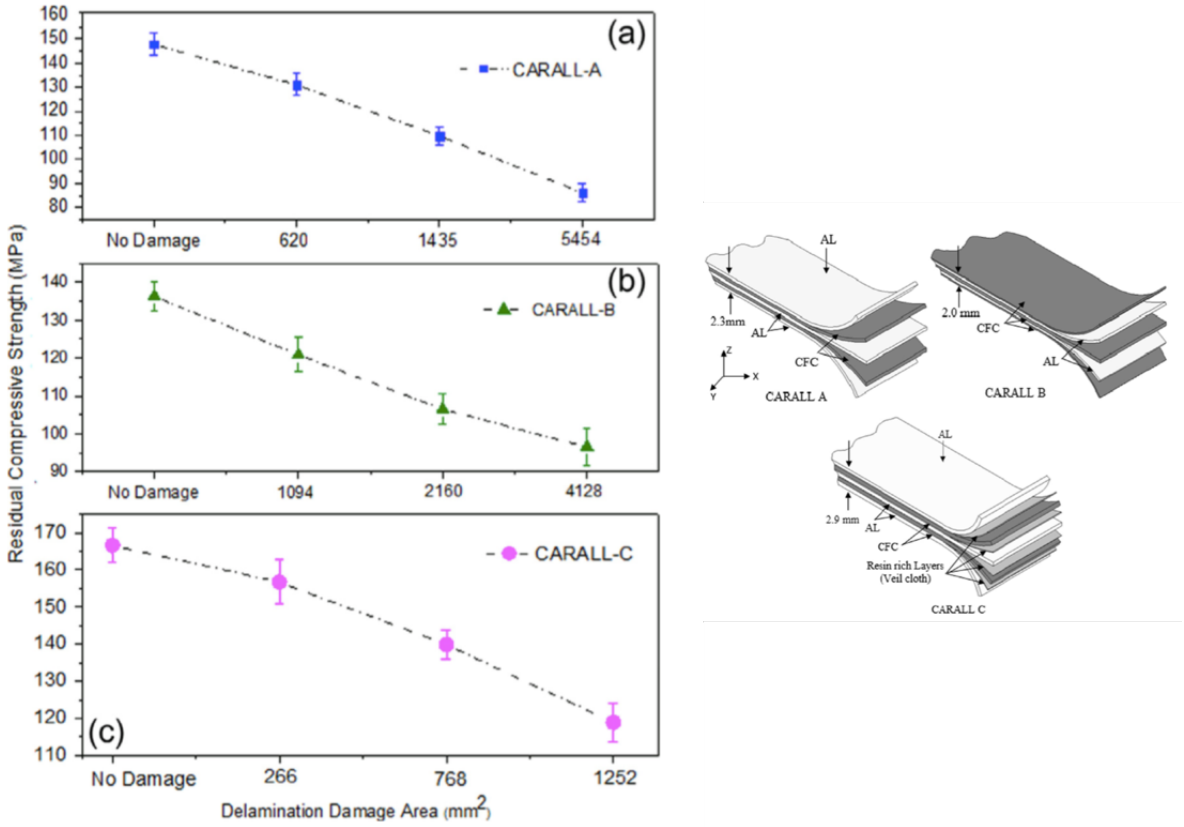

Figure 2.9 Residual compressive strength as a function of impact-induced damage area for a) CARALL A, b) CARALL B and c) CARALL C configurations [182].

Similar to the effects of delamination, impact-induced debonding in FMLs is a result of interfacial shear stresses induced by bending and weak adhesive bonds at the metal/composite interface. Dhaliwal and Newaz [182] studied the effect of debonding (effect of interfacial bond strength) at the interfaces of aluminium/carbon fibre layers of CARALL specimens. The results showed that an addition of resin-rich veil cloth layers led to an increase in the adhesive strength at interfaces of the aluminium/CFC layers, with to a 30% to 35% increase to the residual compressive strength after impact loading. It can therefore be concluded that debonding of the metal/composite interfaces in FMLs is important to the CAI strength.

Furthermore, not only may the delamination and debonding cause weakening, matrix cracking concentrates around the impact region, increasing in proportion to the impact energy level. The number of matrix cracks that induce delamination and debonding within the FML specimen will therefore play a key role in determining the residual strength.

Delamination and debonding damage modes are not sufficient to cause final failure of the FML

under CAI tests, since in most cases neither of these damage modes propagate over the entire width of the specimen. Buckling may be accompanied by fibre failure, especially in the 0° plies, which can grow stably, usually in the direction transverse to the loading direction. Localised contact forces from either impact or indentation can cause surface fibre cracks. Permanent indentation and back-face bulging can lead to fibre fracture crack propagation in the transverse direction. Bull et al. [183] performed CAI experiments using X-ray computed tomography (CT) scanning to gain a visual insight into the damage progression. They observed that a crack near the front surface 0° fibre plies propagates perpendicular to the loading direction under compression, causing stress redistribution in the 0° plies, and thereby lowering the residual compressive strength. In a similar study, Rivallant et al. [184] noted the role of fibre failure in CAI when assessing composite laminates. To date, no research has been published on the correlation between fibre failure due to impact and residual strength of FMLs.

Kilic [185] determined that damage width is the most important factor governing CAI performance of composite materials. While this statement may be valid for composite laminates, it does not necessarily apply to FMLs. As detailed in Section 2.1.4, plastic deformation in the form of front and rear crater damage and cracking of the metal layers are key damage mechanisms induced by low velocity impact, helping to absorb a significant amount of the impact energy. Few studies have considered the role of plastic deformation of the metal FML layers in relation to the residual compressive strength. Aminanda et al. [162] conducted an experimental and numerical CAI analysis on sandwich structures of 15 mm thick Nomex honeycomb core and 0.5 mm thick brass metallic skins. The study concluded that CAI strength decreases with an increase of the maximum indentation depth, hence the damage in the core due to indentation is more important. Takatoya [186] performed an experimental CAI analysis on titanium alloy foils and graphite fibre-reinforced plastic hybrid laminate, and concluded that for low impact the energy was mainly absorbed by plastic deformation of the foil, and this resulted in a higher residual strength. Homan [181] experimentally performed CAI tests on GLARE 4-4/5 and found a 2% decrease in compressive residual strength due to impact dent and 10% decrease due to through crack. A large gap in understanding the role of plastic deformation of FMLs subject to low velocity impact therefore exists in literature.

To date, no research has been published on the CAI strength of FMLs subject to low velocity impact under tension or compression preload. FML structures in aircraft fuselage and wing applications must withstand in-plane loads typically reaching a pre-tension strain level of 4000 με

to 5000 με. While the literature is limited, Section 2.1.6.3 details published results that show the detrimental effects of preload on the damage to FMLs resulting from low velocity impact. In order to have a complete understanding of the damage tolerance of FMLs subject to low velocity impact that replicate realistic loading conditions it is essential to identify and characterise the phenomenological correlation between the CAI strength and the impact damage under preloading conditions.

2.4 SUMMARY AND OUTSTANDING RESEARCH ISSUES

To date, most research conducted on FMLs subject to low velocity impact have been limited to experimental studies. While this research provides useful insights into the initiation of damage, often it is limited to quantification of damage after the impact has taken place. It is evident that experimental observations are limited in their ability to visually detect interior damage to composite layers of the FML, sometimes extending well beyond the impacted region. The findings of the published experimental tests provide the basis for the research work performed in this PhD project. A key gap in literature is identified as the lack of knowledge in providing a detailed insight into the damage initiation and progression of the damage modes within each of the FML constituents, the sequence in which they occur, and the way in which the damage modes interact.

A critical analysis of the FE modelling strategy and modelling of damage modes in FMLs subject to low velocity impact has been presented. Following a detailed review, current numerical models are shown to be limited in their ability to predict the amount of internal damage at a ply-by-ply level. This is particularly important for low velocity impacts that result in BVID. BVID is often difficult to visually inspect, however often results in extensive damage in the form of matrix cracking, fibre failure and delamination that initiates at the impact region, and propagates to cover a wider area of the composite plies.

A majority of the experimental and numerical studies were also identified to be conducted under stress-free conditions, not representative of real-world aircraft applications. The effect of preload on the impact behaviour of FMLs is a key area that necessitates further investigation. Only a limited number of publications investigated the effect of tension and compression preload on the impact response of FMLs. Of those papers preload was found to intensify damage modes. Therefore, an in-depth investigation is needed to further investigate the influence of preload on the damage initiation and progression, and identify and characterise the role they play in low velocity impact at a ply-by-ply level.

Finally, a detailed analysis of the current knowledge of post-impact strength of FMLs was conducted. Only a few publications investigated the CAI strength of FMLs, with little insight into the role of damage mechanisms. Furthermore, no research has been published on the CAI strength of FMLs subject to low velocity impact under tension or compression preload.

Not only is further research into the impact dynamics of FMLs important for their use in aircraft structures, but to also deepen our scientific understanding of the fundamental damage mechanisms, the sequence in which they occur, their interactions, and their role in the degradation of FMLs subject to low velocity impact.

CHAPTER 3 : EXPERIMENTAL AND NUMERICAL ANALYSIS OF IMPACT LOADING AND DAMAGE TO FIBRE METAL LAMINATES

ABSTRACT

Experimental and numerical analysis is presented in this research chapter to characterise the dynamic force response, deformation and failure modes that occur with FMLs when subjected to low velocity impact. This study extends on published research to develop and validate an FE analysis methodology to simulate the dynamic impact response and damage mechanisms of FMLs. Emphasis on identifying the various failure modes, the sequence in which they occur, and the way in which they interact, allow novel insight into the contribution of the different failure modes to the impact response of FMLs.

Parametric numerical studies into the FE model construction, mesh type and impact contact behaviour are performed. Particular attention to the damage modelling approach is given to ensure that all damage modes in the FML constituents are accurately captured. Plastic deformation of the aluminium layers as well as matrix cracking, fibre failure and delamination of the glass fibre reinforced polymer (GFRP) composite layers are critical failure modes that are simulated using a ply-based damage modelling approach. Interfacial debonding between the aluminium and GFRP layers is also an important failure mode.

The numerical analysis is validated using experimental results obtained from impact tests conducted on FML coupons. Low velocity impact tests were performed at four energy levels on two FML configurations. Destructive and non-destructive characterisation of the impacted specimens revealed plastic deformation of the aluminium layers in the form of front and rear crater damage as well as permanent central plastic deflection. Cross-sectional micrographs provided further insights into the damage within the FML specimen, revealing that the extent of damage within the composite in the form of intralaminar and interlaminar cracking was far greater than the visible damage.

FE predictions were consistent with experimental findings, and validate the damage analysis used in the modelling methodology. The FE predictions provided important insights into the damage initiation and propagation at a ply-by-ply level in order to improve our understanding and predictive capabilities of the complex impact damage mechanisms in FMLs.

3.1 INTRODUCTION

Impact damage is a key concern for aerospace structures, and as described previously is likely to occur during maintenance, manufacture and in-flight leading to internal damage to the structure. Therefore, understanding the failure mechanisms of FMLs under impact loading is of primary importance in order to assess the damage tolerance of these materials when used in aerospace structures. The inability to visually detect interior damage in FMLs, which can extend well beyond the impacted region, remains an important safety issue to the aerospace industry. This chapter addresses the key impact damage mechanisms in each of the FML constituents, in the forms of:

(i) plastic deformation of the metal layers;
(ii) matrix cracking and fibre failure in the composite plies;
(iii) delamination between composite plies; and
(iv) debonding between the metal and composite layers.

As reported in Chapter 2, there have been many experimental and numerical studies conducted on the impact behaviour of FMLs. However, only a limited amount of research has been performed on the development of an accurate numerical model to predict the dynamic response and damage mechanisms of FMLs under impact. FE analysis is frequently used as a reliable method to gain insight into the impact damage mechanisms of other materials that are often difficult and time consuming to detect through experimental observations. The numerical modelling of FMLs under dynamic impact events requires a mechanistically-accurate FE model that incorporates the responses of each of the FML constituents. In order to model the impact behaviour accurately, several FE capabilities are required including:

(i) material model including plasticity effects of the metal layers;
(ii) appropriate damage models to capture damage initiation and progression within the composite layers; and
(iii) contact algorithms to model the layered nature of FMLs and the separation of ply layers and interfaces.

To date, limited research has been conducted into modelling the impact response of FMLs incorporating a combination of all the above mentioned FE capabilities. The research presented in this chapter aims to further this by developing a numerical model that incorporates the different material characteristics and appropriate damage models of each of the FML constituents. In particular, the FE modelling methodology out-lined in this chapter focuses on ply-by-ply analysis of the complex damage modes in the GFRP constituent of the FML in order to effectively predict both intralaminar and interlaminar damage mechanisms.

This research focuses on the experimental and numerical investigation into the impact response of FMLs. Experimental tests at various impact energies were conducted to investigate the impact performance and failure mechanisms of FMLs. The experimental analysis provides the benchmark behaviour of FMLs and is used to demonstrate the applicability and accuracy of the FE methodology.

3.2 MATERIALS AND EXPERIMENTAL TECHNIQUES

The manufacturing of FMLs requires particular attention due to the hybrid nature of the layered structure. Variations in the constituents and configuration of the metal and composite layers allow numerous types of FMLs to be produced, however the applicable manufacturing processes for FMLs are limited [187]. FMLs require several manufacturing steps that allow the metal and composite layers to be correctly assembled and bonded.

3.2.1 SURFACE PRE-TREATMENT FOR ALUMINIUM LAYERS

In order to improve the adhesive bonding between the layers of metal and fibre-reinforced laminate, the metal surfaces are pre-treated prior to the bonding process. The surface treatment of the metal layers is aimed at increasing the surface roughness and aid the formation of a high strength and durable adhesive bond with the GFRP layers. The degree to which the metal must be pre-treated is relative to the service application and desired ultimate bond strength. When maximum strength is not required, simple surface cleaning by degreasing is usually adequate. In this work, the interface between the metal and composite plays an important role in the load transfer in FML structures, as shown by Botelho et al. [16] and Papanicolaou et al. [188]. To ensure maximum strength, good bond reproducibility, and maximum resistance to deterioration at the interface, a thorough surface treatment is necessary [189]. Numerous methods have employed

the use of mechanical abrasions and/or chemical etches to prepare the metal surface prior to bonding [190].

In this study, rolled sheets of aircraft grade aluminium 2024-T3 with a thickness of 0.406 mm was chosen for the metal layers to the FMLs. Based on abrasive-blasting and silane pre-treatment procedures developed by Rider et al. [191], Diaz-Benito et al. [192] and Park et al. [193], a modified method was developed with the main aim of finding a practical treatment to remove contamination and the existing oxide layer to produce a microscopically rough surface.

Initial mechanical abrasive techniques using sandblasting led to severe warping of the metal layers due to the thin sheet thickness of the aluminium 2024-T3. Instead, a light-weight pneumatically operated orbital sander with aluminium oxide sand paper (40 grit) was used to mechanically abrade and remove the oxide layer from the aluminium. It is worth noting that an oxide layer will immediately reform as soon as the oxide layer is removed, and therefore it is essential to produce a surface with a 'fresh' oxide layer free from contamination. To remove all contamination from the surface that inhibit the formation of chemical bonds, the aluminium surfaces were subjected to a series of degreasing steps prior to the application of a silane treatment. The water-break test (ASTM F22 – 02 [194]) was performed as a quick and non-destructive method to evaluate the hydrophilic state of the abraded aluminium surface to be bonded. Using distilled water, this test is used to detect hydrophobic contaminants on the aluminium. A film of water on a clean surface will appear as a continuous sheet while a break in the water sheet in the form of discrete and disconnected water beads occurs as an indication of contaminants. The water-break test was particularly important in the proceeding step of silane treatment to ensure the even distribution of the silane solution over the aluminium.

Park et al. [195] noted that in addition to surface roughness, a stable oxide layer is a critical parameter to ensure a strong and durable bond. Aluminium alloys pre-treated with a silane solution have been shown to improve adhesion and anti-corrosion performance of the metal surface [196], attributed to the formation of stable, covalent bonds between the metal (oxide) and the silane agent [10]. Jovanovic et al. [197] investigated the use of γ-methacryloxypropyltrimethoxysilane (MPS) to enhance the adhesive properties and corrosion stability of treated aluminium surfaces. MPS (ABCR supplied by GmH&Co KG) was chosen therefore for the silane pre-treatment of the aluminium sheets used to produce the FML test specimens. In this treatment process, an aqueous solution at 1% by volume of organo-silane in distilled water was used. Upon passing the water-break test, the aluminium sheets were evenly coated with the silane agent, and subsequently cured

in the oven at 110ºC for 60 minutes. Details of the solvent degreasing, abrasion and silane treatment steps prior to the application of the adhesive are summarised in Table 3.1.

In order to evaluate the above mentioned pre-treatment method to promote roughness, an optical surface profilometer was used to measure the surface finish of the aluminium. The Alicona IF-Profiler 3D profilometer measures the surface roughness (Ra) by using concentrator optics to illuminate the surfaces from different angles. The surface roughness is therefore calculated by extracting a linear profile of the aluminium surface. Figure 3.1 illustrates the differences in the 2D surface roughness profiles of the aluminium 2024-T3 using a) a combination of the orbital sander and application of the silane solution and b) only the pneumatically operated orbital sander. The resulting measured surface roughness confirmed that the application of the silane solution increased the surface roughness of the pre-treated aluminium offering improved conditions for adhesion.

Order of pre-treatment process	Description	
Step 1	Mechanical abrasion	1.1 Using a light weight pneumatically operated orbital sander, sand the aluminium with aluminium oxide sand paper (40 grit)
Step 2	Solvent degrease the bonding surface	2.1 Clean surface with distilled/deionised water. Wipe clean along the rolling direction of the aluminium 2.2 Perform the water-break test. Using a spray bottle completely wet the surface with distilled/deionised water. Hold the specimen at a 45º angle to observe if water breaks from the surface in any region. Any breakage in the form of water beading or blotchy areas indicate that contaminants are still on the surface 2.3 Dry surface using a hot air gun
Step 3	Application of silane solution to bonding surface	3.1 Prepare organo-silane coupling agent (1% γ-methacryloxypropyltrimethoxysilane in distilled/deionised water) 3.2 Using a mechanical stirred, stir solution for approximately 1 hr or until solution is clear 3.3 Apply solution to the bonding surface for 10-15 minutes, ensuring that the surface does not dry as this leads to a thick silane layer. Typical application methods include submerging the surface (dipping) or brushing with soaked tissues 3.4 Remove any excess solution 3.5 Dry in oven for 1 hour at 110ºC. Upon removal from the oven, allow the panel to cool. Proceed to the adhesive bonding process to ensure no contaminants in the air are deposited on the chemically clean surface

Table 3.1 Surface pre-treatment for aluminium substrates.

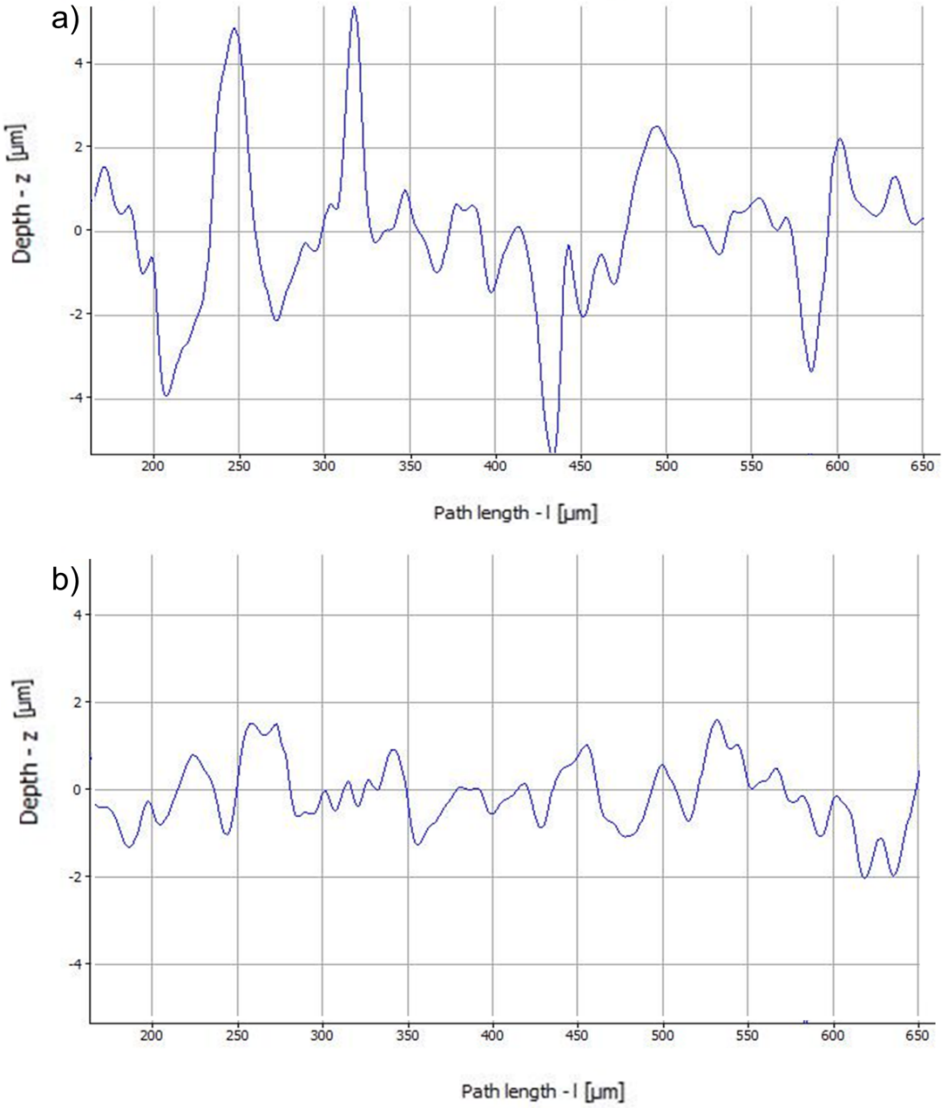

Figure 3.1 2D surface 60 2023-T3 surfaces a) orbital sander and silane solution, b) orbital sander.

3.2.2 MANUFACTURING OF FML PANELS

Unidirectional GFRP laminate (MTM57/E-GLASS-300 supplied by Lavender CE Pty Ltd) was chosen for the composite component of the FMLs. The experimental and numerical investigation is conducted on two types of FML: (i) FML 1 2/1-0.4 and (ii) FML 2 3/2-0.4 which are shown in Figure 3.2. Following the conventional terminology scheme for FMLs (as described in Chapter 1), the lay-up scheme for the FML panels are referred to as FML X 2/1-0.4, where FML X refers to the name of the FML configuration and 2/1-0.4 represents two layers of aluminium sheets (0.406 mm in thickness per sheet) and one GFRP laminate layer. The GFRP lay-up configurations were therefore (i) [0°/90°/90°/0°] and (ii) [0°/90°], having a nominal cured thickness of 0.295 mm

per ply. Both lay-ups were chosen to replicate commercially available GLARE configurations that employ S2-glass epoxy composite prepreg. As with all FML grades, the composite lay-up can be varied depending on the desired FML configuration and variant. After the conventional composite lay-up process, each laminate panel was debulked to ensure no air gaps or voids.

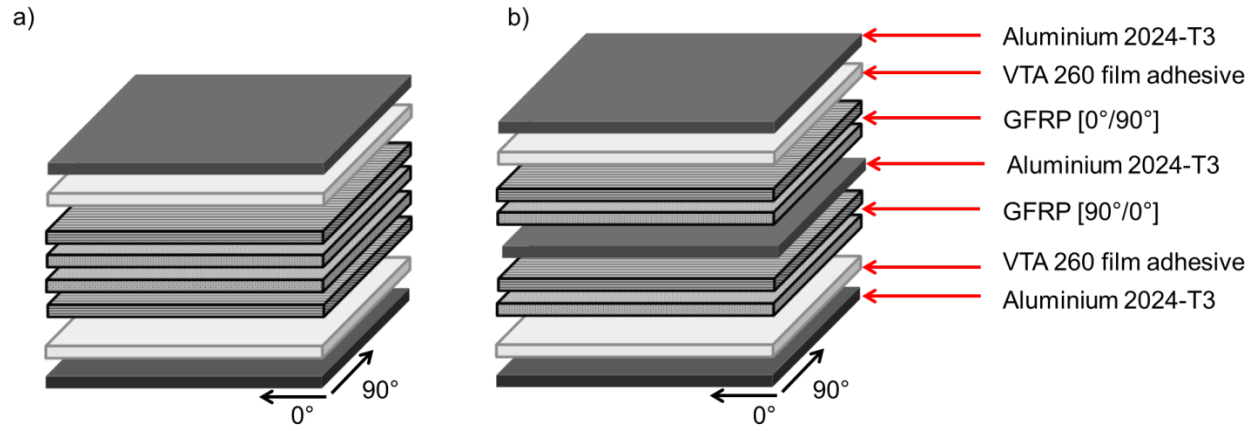

Figure 3.2 Schematic of the stacking arrangement for a) FML 1 2/1-0.4 (t = 2.59 mm) and b) FML 2 3/2-0.4 (t = 3.59 mm).

3.2.3 FML PANEL CONSTRUCTION

The FML panels were prepared using a hand lay-up technique. All aluminium sheets used in the FML specimens were pre-treated and coated with MPS silane solution prior to bonding with the GFRP composite. Due to the susceptibility of an FML layered structure to undergo debonding between the metal and composite layers [198], an epoxy-based structural adhesive (VTA260/PK13-313 supplied by Lavender CE Pty Ltd) with a cure temperature of 120°C was chosen to create a strong bond at the metal and composite interfaces.

All FML panels were fabricated with a size of 300 mm × 40 mm. The assembled FML panels were debulked prior to curing using release film, airweave and a vacuum bag. The assembled FML panels were then cured in an autoclave at 120°C and 0.62 MPa for 115 minutes. This is the cure and consolidation cycle recommended by the manufacturers of the GFRP prepreg and film adhesive. In this way, the composite laminates and adhesive layers were co-cured in a single cure cycle. The final thickness of the cured FML 1 2/1-0.4 and FML 2 3/2-0.4 was 2.59 and 3.59 mm, respectively.

3.2.4 EXPERIMENTAL IMPACT TESTING

A series of low velocity impact tests were conducted to evaluate the deformation and damage response of the FMLs. Impact tests were performed using an instrumented drop-weight impact rig fitted with a spherical steel impactor of 12.7 mm in diameter and mass of 2.09 kg. A 300 mm × 40 mm FML test specimen was clamped between two hydraulic grips exposing an impact region of 200 mm × 40 mm, as shown in Figure 3.3. Aluminium tabs were bonded on the ends of each specimen to decrease the crushing stresses induced by clamping of the hydraulic grips. The hydraulic grips lock into the aluminium tabs to increase friction and prevent slipping of the specimen under loading. Different impact energies were achieved by adjusting the impactor drop height. A digital data acquisition computer system recorded the impact force-time history during each test. Tests for each impact energy parameter were repeated four times to assess the variability in the impact response.

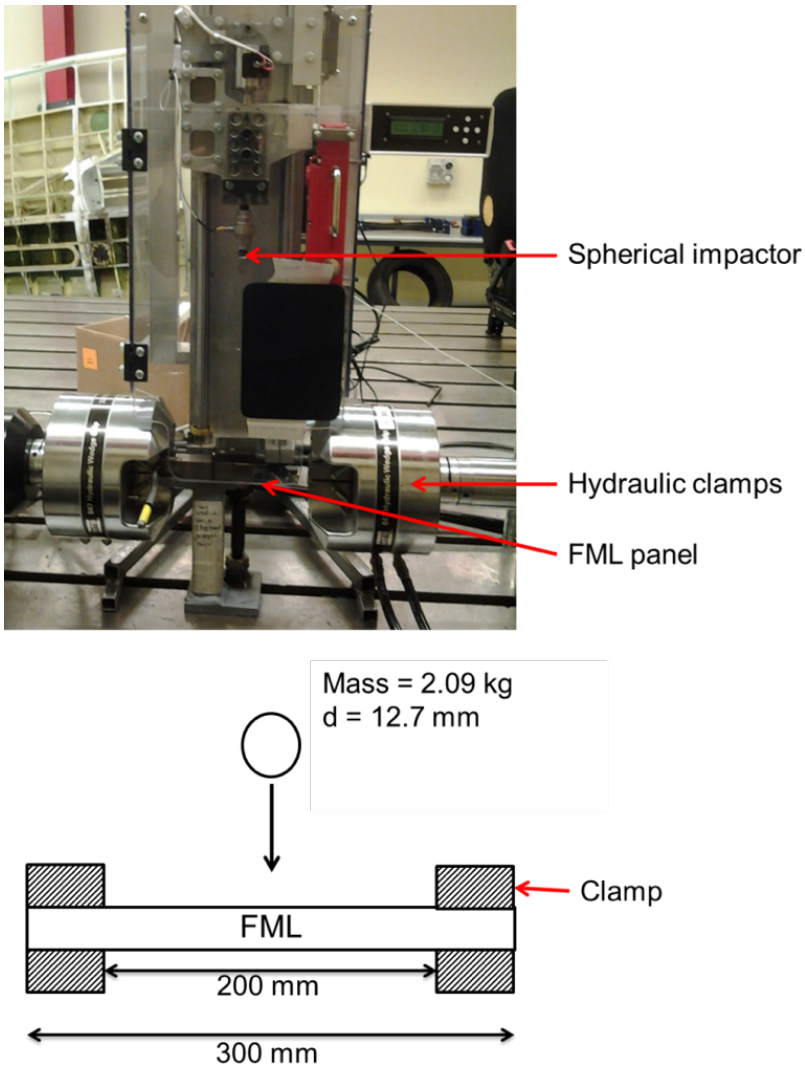

Figure 3.3 Impact drop-weight rig and schematic of impact boundary conditions.

3.3 FINITE ELEMENT MODELLING METHODOLOGY

A FE analysis methodology was developed to compute the deformation response and to predict the failure modes of the FMLs subject to impact. The damage modes considered in the FE model were (i) plastic deformation of the metal layers, (ii) matrix cracking and fibre failure in the composite plies, (iii) delamination between the composite plies, and (iv) debonding of the metal and composite layers. As reported in Chapter 2, experimental analysis has been the preferred method for determining the damage initiation and progression in FMLs subject to impact by measuring the overall damage shape of the fractured surfaces. However, due to the rapid nature of the impact event and the multiple failure modes induced, it is not always possible to experimentally observe the failure mechanisms and the sequence in which they occur. The development of an FE model can therefore be used to reduce the number of time consuming and expensive experimental tests required. Comparisons with experimental tests enable the validation of the FE model.

An FE model was developed using Abaqus/Explicit 6.11 [199]. The methodology takes into account three modelling parameters; namely the choice of element, material and mechanical behaviour, and relevant failure criteria for each of the FML constituents. Appropriate geometric dimensions and boundary conditions were defined to represent the experimental conditions. A brief description of the methods and procedures used is given. In the next section, the evaluation of the accuracy of the element type, mesh pattern, impactor modelling and analysis of FML panel is presented.

3.3.1 SOLVER

The explicit solver available in Abaqus 6.11 was chosen for the FE model of the FMLs as it is suited for simulating high speed dynamic events such as hard body impact. The explicit non-linear algorithm uses an explicit central difference time integration rule to obtain displacements at a series of time increments [200]. The Abaqus/Explicit solver is ideally suited to capture the range of complex non-linear aspects in the impact event, which include a large number of contact constraints rapidly changing, extensive plasticity, and possible structural collapse [201].

3.3.2 MODELLING STRATEGY

Detailed analysis of FMLs requires a three-dimensional modelling approach in order to accurately capture each of the failure modes. In particular, due to the need to analyse the material behaviour

at the ply level, as well as the separation of the layers, the mesoscale approach is applied to the modelling of FMLs. In addition to limiting the number of elements used, the selection of a mesoscale level analysis allows an ease of modelling when considering other FML configurations [81]. The capability of the ply-based mesoscale approach to model the interface between individual plies and the adhesive bondlines between metal and composite layers makes it an attractive choice in capturing delamination and debonding respectively, while still allowing the model to be computationally efficient.

Figure 3.4 illustrates the constituents of the FMLs, which are each individually able to undergo damage subject to low velocity impact exceeding a threshold energy. This figure serves as the base on which the modelling strategy was developed in order to accurately predict the force response and damage to the FMLs. The modelling strategy for each of the FML constituents and corresponding failure mechanisms are discussed in detail in the subsequent sections.

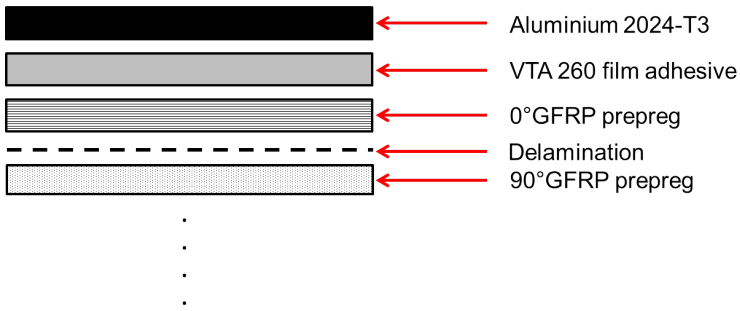

Figure 3.4 Schematic of FML showing modelling strategy (Note: not to scale).

3.3.3 ALUMINIUM 2024-T3

To model the aluminium layers, eight-noded hexahedral solid reduced integration elements (C3D8R) were chosen. Each metal layer was modelled with one element in the through-thickness direction. These elements were chosen to accurately model the 3D stress state of the aluminium 2024-T3, as well as the capability of applying the Johnson-Cook material model to calculate the elastic-plastic response of the aluminium layers. The Johnson-Cook model accounts for the variation of the strain rate dependent yield stress and failure strain of the aluminium [202]. The Johnson-Cook model is an elasto-viscoplastic model that defines the flow stress as a function of equivalent plastic strain hardening, strain rate hardening and temperature softening. The Johnson-Cook model is capable of capturing the elastic-plastic behaviour of the FML. Given that the Johnson-Cook model captures plasticity of the metal, it is chosen as suitable selection to model the aluminium alloy of the FML under impact loading. The Johnson-Cook model has been widely

used by researchers to simulate crash and impact analysis; showing advantages over other bi-linear and plastic constitutive models, particularly in predicting the stress–strain behaviour of metallic materials loaded at low to medium strain rates [138]. The equivalent stress is represented with the following equation [203]:

$$\sigma_Y = (A + B\varepsilon^n)\left(1 + C\ln\frac{\dot{\varepsilon}}{\dot{\varepsilon}_0}\right)(1 - T^{*m}) \tag{3.1}$$

where σ_Y is the effective stress, ε is the effective plastic strain, $\dot{\varepsilon}$ is the effective plastic strain rate, $\dot{\varepsilon}_0$ is the reference strain rate (typically normalised to 1.0 s^{-1}), n is the work hardening exponent, A, B, C and m are material constants, and T^{*m} is the homologous temperature. Temperature variation was not considered in this investigation, due to the low energy of the impact scenario, and was therefore taken as zero. Based on a cumulative damage law, the Johnson-Cook material model defines damage as:

$$D = \sum \frac{\Delta\varepsilon}{\varepsilon_f} \tag{3.2}$$

in which the effective plastic strain at failure, ε_f, is determined by:

$$\varepsilon_f = [D_1 + D_2\exp(D_3\sigma^*)](1 + D_4\, ln\,\dot{\varepsilon}^*)(1 + D_5T^*) \tag{3.3}$$

σ^* is the stress triaxiality defined as the mean stress normalised by the effective stress. The parameters D_1, D_2, D_3, D_4 and D_5 are fracture constants. Failure of the elements is assumed to occur when $D = 1$ [204]. The material model parameters for aluminium 2024-T3 are listed in Table 3.2.

Parameter	Value	Unit
ρ	2770	kg/m^3
v	0.33	-
E	73084	MPa
A	2650	MPa
B	4260	MPa
n	0.24	-
C	0.015	-
m	1.0	-
D_1	0.13	-
D_2	0.13	-
D_3	-1.5	-

D_4	0.011	-
D_5	0	-

Table 3.2 Johnson-Cook material model parameters for aluminium 2024-T3 [203].

3.3.4 GFRP LAMINATE

The choice of elements to represent the GFRP layers is crucial in order to accurately predict their response when the FML is subject to low velocity impact. As discussed in Chapter 2 (section 2.2.2), numerous researchers have investigated the influence of element types to analyse the response and subsequent damage modes of the GFRP constituent of FMLs under low velocity impact [9, 48, 125, 126, 134]. Moreover, researchers have evaluated the implementation of progression damage and failure models to accurately predict the initiation and progression of damage mechanisms, that often occur concurrently.

Previous studies have shown the successful application of solid-like shell or continuum shell elements to accurately replicate the structural behaviour of the GFRP layers to FMLs subject to low energy impacts [9, 53, 70, 99, 125, 137]. Based on this, eight-noded reduced integration continuum shell elements (SC8R) with three integration points in the through-thickness direction were used for each composite ply in this work. Given the importance to accurately predict the failure mechanisms within the GFRP plies, the use of continuum shell elements is necessitated in order to successfully apply the in-built Abaqus/Explicit progressive damage and failure model.

Damage in the unidirectional GFRP layers was modelled using the Abaqus/Explicit damage model for fibre reinforced laminated materials to capture in-plane ply failure modes. This model uses a progressive failure analysis of the GFRP, which is critical in accurately capturing the complex response under impact. Prior to damage initiation, the GFRP is modelled as an orthotropic elastic material. The stress-strain relations can be written as:

$$\begin{Bmatrix} \varepsilon_{11} \\ \varepsilon_{22} \\ \varepsilon_{33} \\ \gamma_{12} \\ \gamma_{13} \\ \gamma_{23} \end{Bmatrix} = \begin{bmatrix} 1/E_1 & -\nu_{21}/E_2 & -\nu_{31}/E_3 & 0 & 0 & 0 \\ -\nu_{12}/E_1 & 1/E_2 & -\nu_{31}/E_3 & 0 & 0 & 0 \\ -\nu_{13}/E_1 & -\nu_{23}/E_2 & 1/E_3 & 0 & 0 & 0 \\ 0 & 0 & 0 & 1/G_{12} & 0 & 0 \\ 0 & 0 & 0 & 0 & 1/G_{13} & 0 \\ 0 & 0 & 0 & 0 & 0 & 1/G_{23} \end{bmatrix} \begin{Bmatrix} \sigma_{11} \\ \sigma_{22} \\ \sigma_{33} \\ \sigma_{12} \\ \sigma_{13} \\ \sigma_{23} \end{Bmatrix} \quad (3.4)$$

where E_i is the Young's Modulus in the i-direction, G_{ij} is the shear modulus in the i–j plane, v_{ij} is the Poisson's ratio in the j-direction when the laminate is stressed in the i-direction. v_{ij} and v_{ji} are related by $v_{ij}/E_i = v_{ji}/E_j$. The subscripts 1, 2 and 3 refer to the x, y and z directions.

In order to successfully predict damage initiation, the damage model utilises the Hashin failure criteria [199] to identify failure initiation in the fibre (*f*) and in-plane transverse matrix (*m*) directions in tension (*t*) or compression (*c*). Damage initiation is defined as the onset of degradation at a material point. Expressed in terms of ply stress σ_{ij} and material strengths, the initiation criteria are given as follows:

$$F_f^t = \left(\frac{\tilde{\sigma}_{11}}{X_T}\right)^2 + \alpha\left(\frac{\tilde{\sigma}_{12}}{S_L}\right)^2, \qquad \tilde{\sigma}_{11} \geq 0 \tag{3.5}$$

$$F_f^c = \left(\frac{\tilde{\sigma}_{11}}{X_C}\right)^2, \qquad \tilde{\sigma}_{11} \leq 0 \tag{3.6}$$

$$F_m^t = \left(\frac{\tilde{\sigma}_{22}}{Y_T}\right)^2 + \left(\frac{\tilde{\sigma}_{12}}{S_L}\right)^2, \qquad \tilde{\sigma}_{11} \geq 0 \tag{3.7}$$

$$F_m^c = \left(\frac{\tilde{\sigma}_{22}}{2S_T}\right)^2 + \left[\left(\frac{Y_C}{2S_T}\right)^2 - 1\right]\frac{\tilde{\sigma}_{22}}{Y_C} + \left(\frac{\tilde{\sigma}_{12}}{S_L}\right)^2, \qquad \tilde{\sigma}_{11} \geq 0 \tag{3.8}$$

where X_T, X_C and Y_T, Y_C denote the tensile and compressive strengths in the longitudinal and transverse directions, and S_L, S_T are the longitudinal and transverse shear strengths respectively. The damage model introduces scalar damage variables that degrade the initial material properties of the composite. The coefficient α refers to the contribution of the shear stress to the fibre tensile initiation criterion. The coefficient can be specified to obtain the model proposed by Hashin and Rotem [205] or Hashin [206] by setting $\alpha = 0$ or 1 respectively. In this study, $\alpha = 0$ and $S_T = 0.5Y_C$ are set to achieve the model proposed by Hashin and Rotem [205], and therefore the assumption that there is no shear stress contribution to the initiation of the fibre tensile failure is applied [137, 207]. The damage variables F^t_f, F^c_f, F^t_m, F^c_m indicate whether the corresponding failure criteria are satisfied. Damage initiation occurs when any of these damage variables reach unity.

Following failure initiation, further loading causes degradation of the material stiffness coefficients. The material response in terms of apparent stress, σ is expressed by relating the strain, ε to the damage elasticity matrix, C_d:

$$\sigma = C_\mathrm{d}\varepsilon \tag{3.9}$$

$$C_\mathrm{d} = \frac{1}{D}\begin{bmatrix} (1-d_f)E_1 & (1-d_f)(1-d_m)\upsilon_{21}E_1 & 0 \\ (1-d_f)(1-d_m)\upsilon_{12}E_2 & (1-d_m)E_2 & 0 \\ 0 & 0 & (1-d_s)G_{12} \end{bmatrix} \tag{3.10}$$

$$D = 1 - (1 - d_f)(1 - d_m)\upsilon_{12}\upsilon_{21} \tag{3.11}$$

$$d_f = \begin{cases} d_f^t, & \text{if } \tilde{\sigma}_{11} \geq 0, \\ d_f^c, & \text{if } \tilde{\sigma}_{11} < 0, \end{cases} \tag{3.12}$$

$$d_m = \begin{cases} d_m^t, & \text{if } \tilde{\sigma}_{22} \geq 0, \\ d_m^c, & \text{if } \tilde{\sigma}_{22} < 0, \end{cases} \tag{3.13}$$

$$d_s = 1 - (1 - d_f^t)\,(1 - d_f^c)(1 - d_m^t)(1 - d_m^c) \tag{3.14}$$

where D is the overall damage variable. d_f, d_m and d_s define the current state of the fibre and matrix damage respectively, expressed in terms of damage variables d^t_f, d^c_f, d^t_m, d^c_m, d_s for fibre, matrix and shear in tension and compression.

The reduction to the stiffness properties is controlled according to a linear stress-displacement law (linear evolution law), governed by the area under the stress-displacement curve or equivalent fracture energy, G^F dissipated during the damage process in each mode. This linear evolution law is based on the approach developed by Camanho and Dávila [208] in the modelling of delamination using cohesive elements. An explanation of the linear stress-displacement law is given in Section 3.3.5. The mixed-mode, energy-based damage evolution law based on a power law fracture criterion with linear softening is selected for damage propagation. Thus, failure under mixed-mode conditions is governed by a power law of the energies required to cause failure in individual (normal or shear) modes [209]. G^F_{ft}, G^F_{fc}, G^F_{mt}, and G^F_{mc} correspond to the fracture energies for fibre tension, fibre compression, matrix tension and matrix compression, and these were specified to induce energy dissipated during damage.

As discussed in Chapter 2, research studies [72, 91, 116-118] concluded the low velocity impact responses of FMLs are comparable to those of quasi-static responses, given that the impact mass is much larger than the mass of the FML panel and that strain rates do not exceed 100 s^{-1}. In the present work, only low velocity impacts are investigated, and as such the FML panels considered in this study are assumed to undergo quasi-static deformation processes. Therefore, the Hashin failure criteria are independent of strain rate effects in the composite material, and quasi-static elastic and strength properties are assumed.

Longitudinal and transverse material properties for the GFRP were attained through experimental tensile testing of uniaxial loaded specimens using a 50 kN Instron testing machine according to

ASTM D3039/D3039M test method [210]. Unidirectional GFRP specimens consisting of eight plies and having the dimensions of 175 mm × 25 mm (longitudinal) and 250 mm × 15 mm (transverse) were manufactured with fibre orientations in the 0° or 90° directions with respect to the loading. Table 3.3 provides a summary of average mechanical properties of MTM57/E-GLASS-300 prepreg recorded over six tests. The repeatability of the experimental results was good, with the coefficient of variation less than 8% for the E_{11} E_{22} and S_{11} values. The S_{22} values had a coefficient of variation of 14.3%, which is typical for this property [211]. The orthotropic properties for the unidirectional GFRP are given in Table 3.3 respectively. Some material parameters were taken from values in literature [212-215].

Parameter	Value	Units	Source
ρ	1.78	g/cm^3	[215]
E_{11}	34160	MPa	Test
$E_{22} = E_{33}$	7870	MPa	Test
$G_{12} = G_{13}$	6300	MPa	[213]
G_{23}	5000	MPa	[213]
$\nu_{12}=\nu_{13}$	0.29	-	Test
ν_{23}	0.31	-	[213]
X_T	817.5	MPa	Test
X_C	880	MPa	[214]
Y_T	47.34	MPa	Test
Y_C	160	MPa	[212]
$S_L = S_T$	55	MPa	[214]
$G^F_{ft} = G^F_{fc}$	150	J/m^2	[212]
$G^F_{mt} = G^F_{mc}$	100	J/m^2	[212]

Table 3.3 Material properties of unidirectional MTM57/E-GLASS-300.

3.3.5 VTA260 FILM ADHESIVE

To analyse debonding between the aluminium and GFRP layers in an FML, a single layer of eight-noded three-dimensional cohesive elements (COH3D8) were used to represent the film adhesive. The formulation of cohesive elements is based on the Cohesive Zone Model (CZM) approach, and is commonly used to analyse delamination fracture in laminated materials. The CZM approach is characterised by the properties of the adhesive material, crack initiation conditions and crack

evolution function [216]. Cohesive elements at the aluminium-GFRP interface employed traction and shear strength properties corresponding to the adhesive properties.

The traction load-crack separation law defines the relationship between the relative displacement (gap opening) of the connected substrates, and the traction load generated between them across the interface [217]. Figure 3.5 shows a typical bi-linear traction-separation law where the *x*-axis and *y*-axis represent the displacement and stress, respectively. In this figure, t_0 represents the interfacial strength, δ_0 is the critical separation, δ_{fail} is the separation at failure, and the area under the curve represents the critical strain energy release rate, G^c.

The failure mechanism of the traction-separation law assumes an initially linear elastic behaviour, followed by three stages, namely: damage initiation; damage evolution; and element deletion [199]. Damage initiation occurs when the element reaches the strength limit (peak traction) of the material. After the element passes the damage initiation criteria, the stiffness of the element decreases linearly with increasing crack separation during the damage evolution stage. When the interface reaches zero stiffness, the element is removed and a frictionless contact is applied.

Under mixed-mode fracture, the cohesive input properties that are required to define the bi-linear traction-separation law include the initial stiffness (K), interfacial strength (t) and fracture energy (G_c), in each of its three deformation modes, i.e. the normal tensile component and two perpendicular shear components. The traction-separation cohesive law is therefore characterised in terms of peak failure stress, $t^0{}_n$ and $t^0{}_s$ and fracture energies $G^c{}_n$ and $G^c{}_s$ where n and s refer to the normal (Mode 1) and in-plane shear (Mode 2) directions. The out-of-plane shear, $t^0{}_t$ (Mode 3) values were taken as equal to the Mode 2 values [218, 219]. The stiffness parameters, K_{nn}, K_{ss} and K_{tt} are the moduli of the cohesive material divided by its thickness [204].

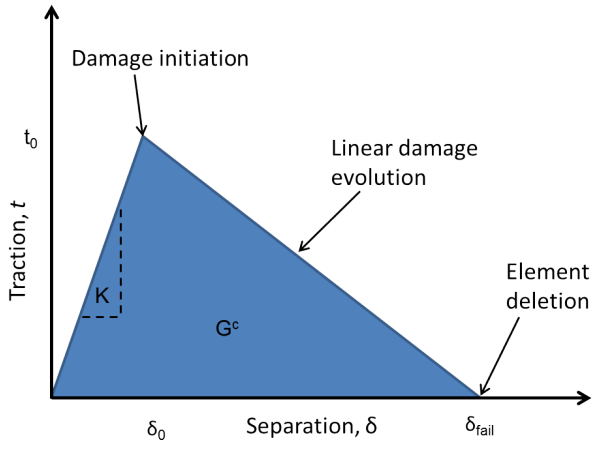

Figure 3.5 Bilinear traction-separation law used to model the adhesive film in FMLs.

The linear elastic behaviour of the traction-separation law is defined in terms of the elastic constitutive stiffness matrix, K, which relates the nominal traction stress vector, t, to the nominal strain vector, ϵ :

$$t = \begin{Bmatrix} t_n \\ t_s \\ t_t \end{Bmatrix} = \begin{bmatrix} K_{nn} & 0 & 0 \\ 0 & K_{ss} & 0 \\ 0 & 0 & K_{tt} \end{bmatrix} \begin{Bmatrix} \epsilon_n \\ \epsilon_s \\ \epsilon_t \end{Bmatrix} = K\epsilon \tag{3.15}$$

Regardless of the true thickness of the cohesive layer, the default choice of the constitutive thickness of the cohesive layer in terms of traction-separation is 1.0. The elastic constitutive stiffness matrix and density is therefore determined by using the true thickness of the adhesive layer t_c as $K=E/t_c$ and $\rho=\rho_c t_c$ [220].

A damage initiation criterion of the cohesive layer is expressed as a quadratic nominal stress criterion defined as:

$$\left\{\frac{\langle t_n \rangle}{t_n^0}\right\}^2 + \left\{\frac{\langle t_s \rangle}{t_s^0}\right\}^2 + \left\{\frac{\langle t_t \rangle}{t_t^0}\right\}^2 = 1 \tag{3.16}$$

where t_n, t_s and t_t are the normal stress and shear stresses in the cohesive layers. Following damage initiation, damage evolution is controlled by the energy dissipated as work of separation during the decohesion process. The dependence of the fracture energy on the mode mixity is defined by the linear softening law:

$$\left\{\frac{G_n}{G_n^c}\right\} + \left\{\frac{G_s}{G_s^c}\right\} + \left\{\frac{G_t}{G_t^c}\right\} = 1 \tag{3.17}$$

where G_n, G_s and G_t represent the work done under the traction load and its corresponding separation in the normal, in-plane and out-of-plane shear directions.

In order to capture damage propagation, the elastic stiffness that defines the element constitutive equation needs to be increased to avoid inaccurate representation of the mechanical behaviour of the interface. The stiffness of the cohesive layer is required to be sufficiently high for composite materials to ensure adequate load transfer between bonded layers [216, 221]. This also allows for the prevention of the reduction of material elasticity at the bond interface due to excessive distortion of the cohesive elements without giving rise to numerical errors related to incorrect stress oscillations. While the appropriate value for the stiffness (penalty parameter) is dependent on the geometry and lay-up of the specimen, the present investigation employs a value of $K = 1 \times 10^6$ N/mm as suggested by Camanho et al. [221] for graphite/epoxy specimens. Jofre and Julián [211] used similar values when modelling adhesively bonded steel/CFRP joints. These properties

were also employed in the delamination model. The cohesive interface properties of the adhesive were modelled using the density and mechanical properties given in Table 3.4.

Parameter	Value	Units
ρ	1.2	g/cm^3
E	3000	MPa
ν_{12}	0.35	-
G	1100	MPa
K_{nn}	1×10^6	N/mm
K_{ss}	1×10^6	N/mm
K_{tt}	1×10^6	N/mm
t^0_n	65.8	MPa
t^0_s	38	MPa
t^0_t	38	MPa
G^c_n	1302	J/m^2
G^c_s	7750	J/m^2
G^c_t	758	J/m^2

Table 3.4 Mechanical properties of the VTA 260 adhesive layer [223].

3.3.6 DELAMINATION

As described in Chapter 2, several strategies to accurately model delamination between the GFRP plies have been investigated in previous research, including the use of cohesive elements, tie constraints and surface-based cohesive surfaces, as illustrated in Figure 3.6. Each of these methods takes into consideration the transverse shear stresses, that are important when modelling delamination failure.

In this work a surface-based cohesive interaction law was applied at the interface between ply boundaries. The application of surface-based cohesive behaviour is similar to that of cohesive elements, as described in section 3.3.5, and allows the user to define the interaction between two surfaces without generating additional elements. Surface-based cohesive behaviour is primarily intended for situations in which the interface thickness is negligibly small [199], and is therefore appropriate in modelling the thin resin-rich interface between the composite plies in FMLs.

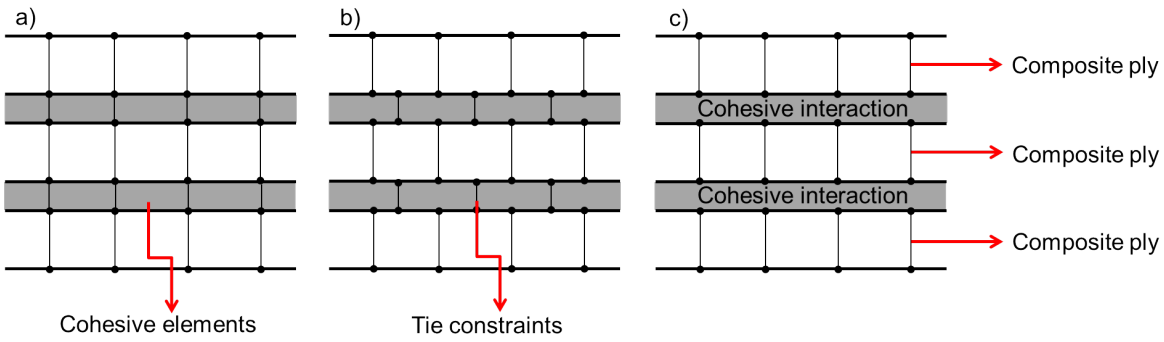

Figure 3.6 Strategies for modelling delamination: a) cohesive elements with a regular mesh, b) tie constraints with non-coincident nodes, c) surface-based cohesive interactions.

The use of surface-based cohesive behaviour requires the user to specify the master and slave surfaces for the deformable bodies, as well as the interaction behaviour between the two surfaces. In the FE model of the FMLs, the general contact algorithm in Abaqus/Explicit is used in conjunction with traction-separation laws as previously described to pair two adjacent composite surfaces and capture delamination between each ply. In addition, a friction coefficient of $\mu = 0.5$ is defined between composite ply surfaces [129, 222].

The interlaminar damage initiation properties are given in Table 3.5. The present analysis uses properties from Phadnis et al. [223] for E-glass/epoxy composites. Similar properties are expected for the S-glass/epoxy prepreg used in FMLs. A variation of the damage initiation parameters within 15% from the sourced values given in Table 3.5 did not significantly influence the overall analysis results. Damage progression was modelled using a mixed-mode energy-based damage evolution law based on a power law, where G_{Ic} and G_{IIc} are the fracture toughness values for Mode 1 and Mode 2 interlaminar loading, and η is the power coefficient.

Parameter	**Value**	**Units**
t^0_n	35	MPa
t^0_s	65	MPa
t^0_t	65	MPa
G_{Ic}	504	J/m^2
G_{IIc}	1566	J/m^2
G_{IIIc}	1566	J/m^2
η	1	-

Table 3.5 Interlaminar damage properties [86].

3.3.7 IMPACTOR

Contact between the impactor and FML specimen is simulated using the general contact algorithm in Abaqus/Explicit, whereby contact between multiple regions of the FE model can be defined using a single interaction. Used to define an all-inclusive surface interaction, the general contact algorithm is used for the impact scenario to allow the impactor to interact with the internal constituents of the FML plate as the elements erode. Tangential behaviour with a penalty contact formulation between contacting surfaces was defined to account for friction forces. The Coulomb friction model was used such that the tangential motion between the impactor and FML plate is zero until the shear component of the surface traction reaches a critical value, τ_{max}, dependent on the normal contact pressure, P, and the friction coefficient, μ [129, 222, 224]. A friction coefficient of $\mu = 0.3$ was used between the impactor and FML plate [129, 222]. In addition, the use of a friction coefficient improved the convergence behaviour of the FE model.

The impactor was assumed to have infinite rigidity and was modelled as a fully rigid body. This assumption was considered valid due to the negligible deformation of the hardened steel impactor. The spherical impactor with a diameter of 12.7 mm and mass of 2.09 kg was modelled at the position “just before impact”, as shown in Figure 3.7.

3.3.8 GEOMETRY AND BOUNDARY CONDITIONS

Figure 3.7 describes the geometry and boundary conditions of the FE model to replicate the experimental impact tests performed on the FMLs. The exposed impact region was 200 mm × 40 mm for the FML specimens, which were supported between two hydraulic clamps. The boundary conditions were defined to be fully clamped, with no translation or rotation at the supports.

The initial velocity of the impactor is prescribed to the reference point on the impactor in the vertical (z) direction to simulate the impact velocities of the experimental tests.

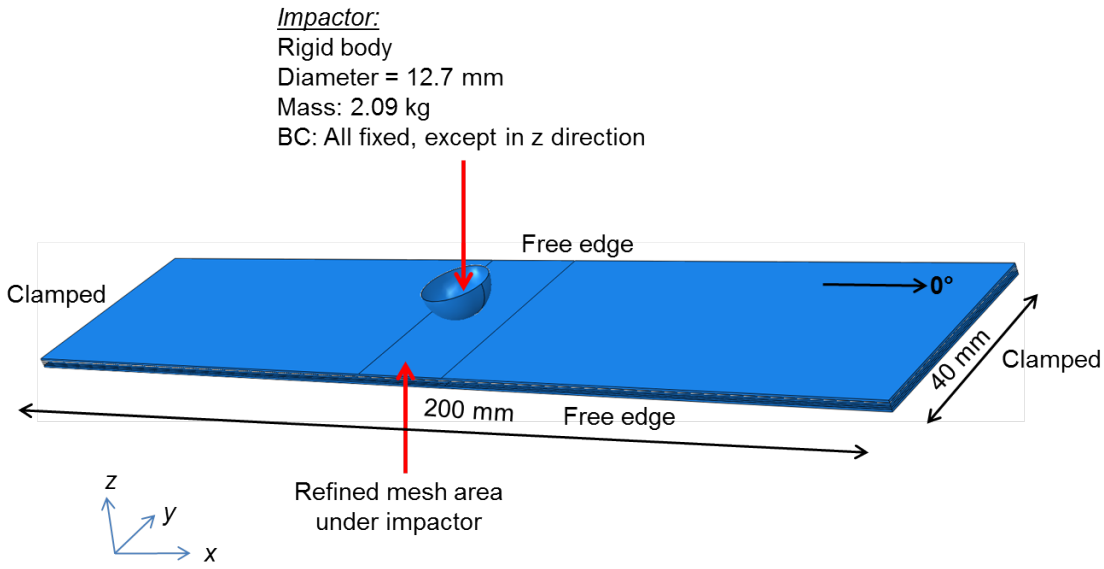

Figure 3.7 Geometry and boundary conditions (BCs) of FML panel subject to impact.

3.3.9 ANALYSIS CONTROLS

3.3.9.1 HOUR-GLASSING AND DAMPING

Due to the implementation of first-order reduced integration elements, mesh stability issues can arise which are commonly referred to as 'hour-glassing'. Hour-glassing occurs when elements distort in a way that the strain at the integration point of the element is zero. As such, the strain in bending is not detected. This in turn leads to zero stresses resisting deformation of the plate induced by uncontrolled distortion of the mesh. In order to prevent the effects of hour-glassing, an enhanced stiffness relaxation formulation is employed [129, 222]. Additionally, a distortion control in Abaqus/Explicit was used to prevent negative volume elements or elements undergoing excessive distortion that may result due to the dynamic loading conditions or the rate of material degradation. The distortion control utilises a penalty load when the element is inverted to a predefined proportion of the original element size [224].

Moreover, damping associated with volumetric straining in the form of bulk viscosity was employed in the FE model to control high frequency oscillations resulting from high velocity dynamic events such as impact tests. Two forms of bulk viscosity are available in Abaqus/Explicit, namely linear and quadratic [199], that describe the relationship between bulk viscosity, pressure and volumetric strain. In addition to reducing the overall stable time increments of FE simulations, the linear and quadratic bulk viscosities are introduced to dampen ringing at high element

frequencies and prevent elements from collapsing under high velocity gradients. Default damping coefficients of 0.06 and 1.2 were used for the linear and quadratic damping, respectively [199].

3.3.9.2 ELEMENT DELETION

Abaqus/Explicit allows for the removal of elements upon the detection of fully degraded elements, whereby the element no longer contributes to the stiffness of the model. Elements are removed when the scalar damage variable reaches the default value of 0.99. The elements are deleted prior to the damage variables reaching unity to avoid sudden element distortions resulting from the absence of residual stress [224]. A parametric study was conducted to investigate the influence of the maximum degradation scalar damage variable. Results showed minimal effect of varying the scalar damage variable due to the non-penetration of the impacted FML specimen for the range of low velocities considered in this research study. The Abaqus/Explicit STATUS output variable is used to indicate if an element is active. A value of 1.0 indicates that the element is still active, while a value of zero indicates a degraded or deleted element.

3.4 MODEL VALIDATION

3.4.1 IMPACT OF ALUMINIUM PLATES

To validate the FE modelling approach proposed in section 3.3.3 for aluminium panels subject to low velocity impact, the behaviour of a single monolithic aluminium layer is first considered. A series of impact tests were conducted to evaluate the impact response of single layer 300 mm × 40 mm monolithic aluminium 2024-T3 specimens of 0.406 mm thickness using the experimental technique described previously.

The experimental findings were verified with the numerical analysis by comparing the maximum plastic deformation, force-time histories, and peak loads for low velocity impacts. Figure 3.8 shows a comparison of the experimentally recorded and numerically predicted contact force-time histories of the aluminium plate impacted at 5 J. In this figure, and in subsequent force-time figures presented, a single experimental result is shown as a representation of all repeat tests. The FE analysis was run for an extended period of time to allow for elastic recovery of the aluminium plate for comparison with experimental data. Very close predictions were obtained for both the peak force (within 3%) and the time at peak load. Slight over-estimation of the impact duration by

the FE model can be attributed to the assumptions of perfect boundary conditions for the aluminium plate and the rigidity of the impactor [225].

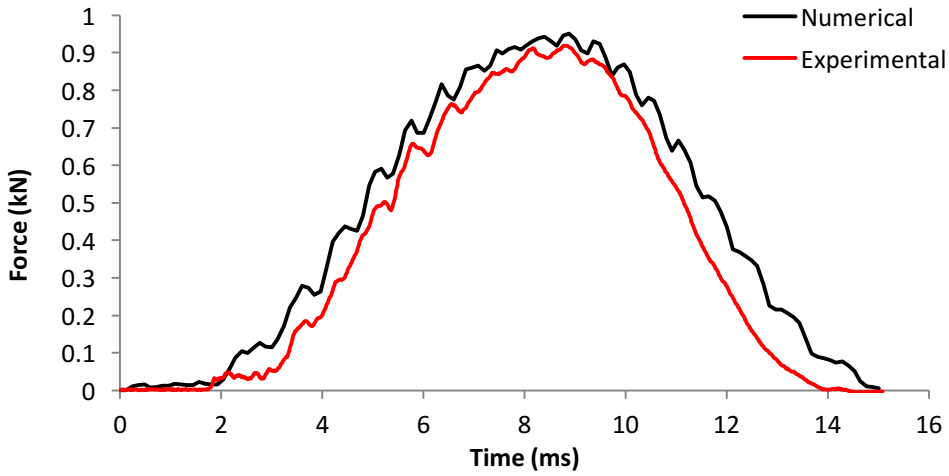

Figure 3.8 Experimental and numerical force-time histories of aluminium plate impacted at 5 J.

Figure 3.9a compares the experimentally measured and numerically predicted central permanent deflection of the impacted aluminium plates. The error bars represent standard deviation. The central permanent deflection occurs as a result of plastic deformation of the aluminium. The FE predictions demonstrate excellent agreement with the experimental results, showing a 2.3% difference between the measured and predicted permanent deflections. In order to evaluate the absorbed energy of the impact event, the ratio of the kinetic energy of the impactor before and after impact, defined as the energy restitution coefficient (E) is considered, as shown in Figure 3.9b. The predicted E values of the monolithic aluminium plate are in good agreement with the experimental results with approximately 14% difference between the results.

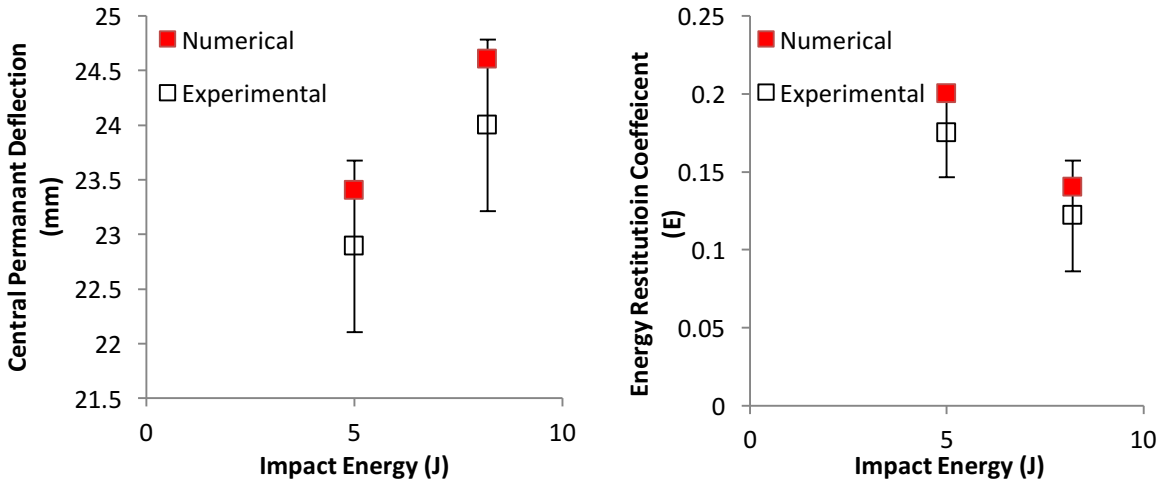

Figure 3.9 a) Central permanent deflection and b) Energy restitution coefficient results for aluminium 2024-T3.

3.4.2 IMPACT OF GFRP LAMINATE

To ensure that the FE modelling approach incorporating progressive damage analysis is capable of predicting the various internal damage modes of the composite layers to the FML, the impact response, including impact force histories and damage modes are assessed. A series of impact tests were conducted to evaluate the impact response of 300 mm × 40 mm composite panels consisting of four layers of GFRP in a [0°/90°/90°/0°] configuration using the experimental techniques described previously. Comparisons were made with the experimental results, and the adequacy of the FE approach was evaluated. The experimental and numerical force-time histories for an impact energy of 5 J are compared in Figure 3.10. The numerical force-time curve and impact duration show excellent agreement with the experimental results. A 1.4% difference between the measured and FE predictions of the peak force was found.

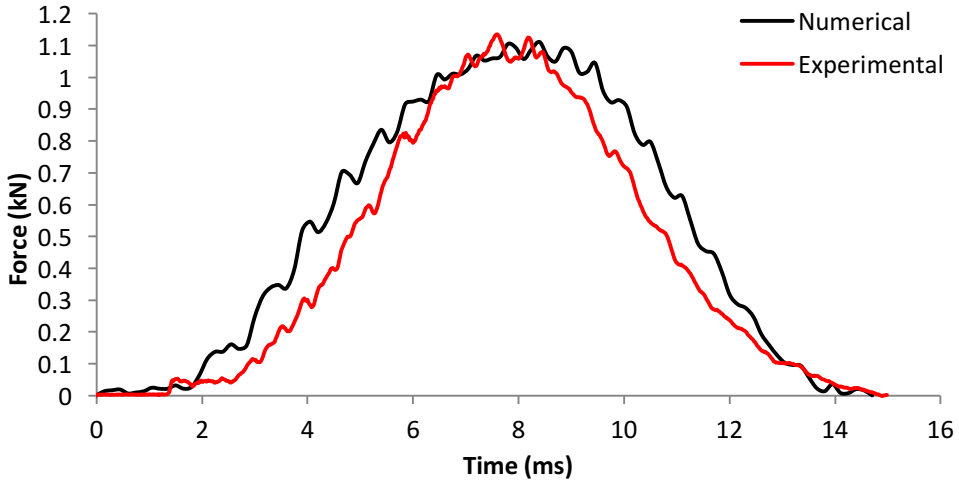

Figure 3.10 Experimental and numerical force-time results of GFRP laminate impacted at 5 J.

The extent of damage to the GFRP laminate analysed around the impact site is shown in Figure 3.11. The FE model allows the intralaminar damage of the impacted composite to be investigated on a ply-by-ply basis. Figure 3.11 shows damage contour plots for fibre compression, fibre tension, matrix compression and matrix tension in the individual plies of the laminate, where Ply 1 is on the impacted side of the material. The damage index varies between 0 (undamaged, blue) and 1 (fully damaged, red). These aspects are also used in all subsequent similar figures.

Of particular importance is the prediction of delamination initiation and progression in the impacted GFRP laminate using the FE model. Figure 3.12 shows the superposition of the numerically predicted delamination compared to experimental observation. The experimental damaged region was observed using the back illumination technique. As the GFRP specimens are thin and translucent, a light source was placed behind the specimen to view the overall damage

area as shown in Figure 3.12. Delamination areas are visible due to the separation between plies of different fibre orientations and are represented as dark areas in the image. Figure 3.12 and subsequent figures showing experimentally observed delamination are a representation of all repeat tests.

The predicted delaminations at each ply interface are identified by failure of the surface-based cohesive contact interaction, using the variable CSDMG (cohesive surface damage) in Abaqus/Explicit. The variable CSDMG illustrates the stiffness degradation and is represented by damage indices ranging from 0 (no damage, grey) to 1 (complete damage, blue), where the contours from all delamination interfaces have been combined. The FE model shows very good agreement in the size and typical peanut shape of the interlaminar damage. A 6.7% difference in the predicted delamination damage area compared to experimental observations was recorded; falling within the experimental scatter.

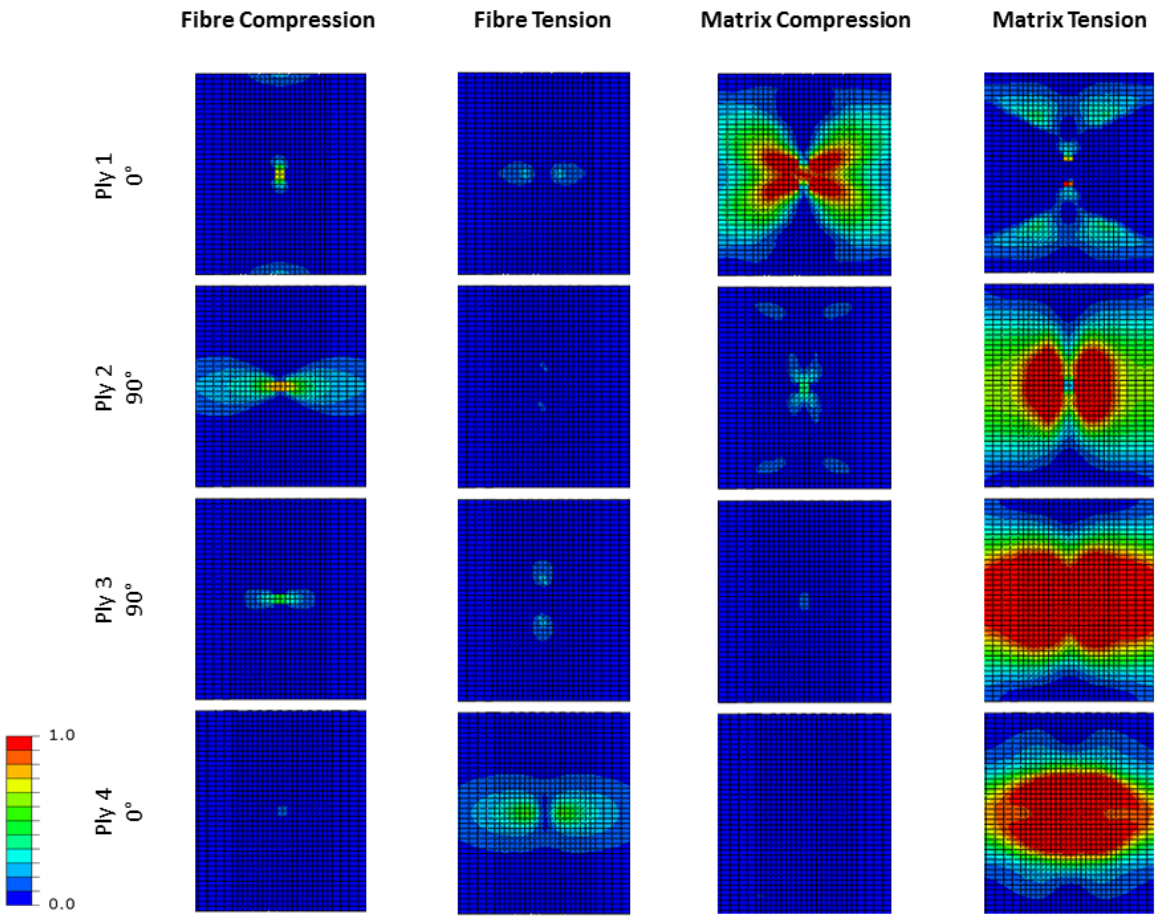

Figure 3.11 Numerically predicted damage contours in the GFRP laminate impacted at 5 J.

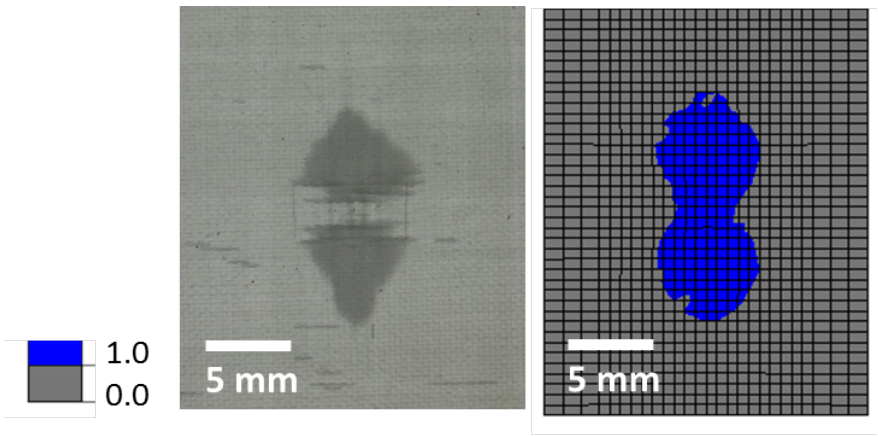

Figure 3.12 Experimental observation (left) and superimposed numerical delamination damage (right) of GFRP laminate impacted at 5 J.

3.4.3 MESH DEPENDENCE STUDY

Mesh sensitivity studies were conducted to examine the influence of varying mesh density on the simulation of low velocity impact to an FML panel. Three mesh sizes were investigated in order of increasing number of elements: coarse, medium and fine meshes, as shown in Figure 3.13. The material properties and impact conditions were kept constant, and only the mesh density was varied. As the principal region of interest was the area directly under and close to the impact site, the FML panel geometry was partitioned in Abaqus/CAE to include a central region of increased mesh density. For all three mesh density cases, a single layer of elements in the through-thickness direction was adopted for each layer of the FML panel to minimise the computational expense.

Table 3.6 provides details of the model characteristics for each mesh size. The results of the analyses and comparison with experimental results are presented as a percentage difference (% Diff). Numerical simulations were carried out to test the ability of the mesh cases to predict the peak loads and force-time histories for low velocity impact of the FML 1 2/1-0.4 specimen, as well its ability to predict both the orientation and shape of delamination compared to experimental observations. These aspects demonstrate that the combination of intralaminar and interlaminar failure analysis in the FE model was able to accurately capture the damage mechanisms of FML specimens resulting from low velocity impacts.

Figure 3.14 shows the force-time curves for all mesh cases, where the area under the curve defines the dissipated energy. Contact duration was found to be independent of the number of elements as the mechanical responses are almost identical for the three mesh density test cases. Experimental peak force for FML 1 2/1 subject to an impact energy of 5 J was measured to be 1.67 kN. The

numerical model marginally over-predicted the peak load for all cases. However, with an increase in mesh density there was a reduction and convergence of maximum load. Although the percentage differences between the predicted and experimentally recorded peak loads were between 5.4% to 6.1%, the increase in the mesh density had a significant effect on the simulation time, resulting in approximately double the simulation time between the medium and fine mesh densities. Given the increase in mesh size between the medium and fine mesh cases (approximately 2.5 times the mesh density), this increase in simulation run time is expected.

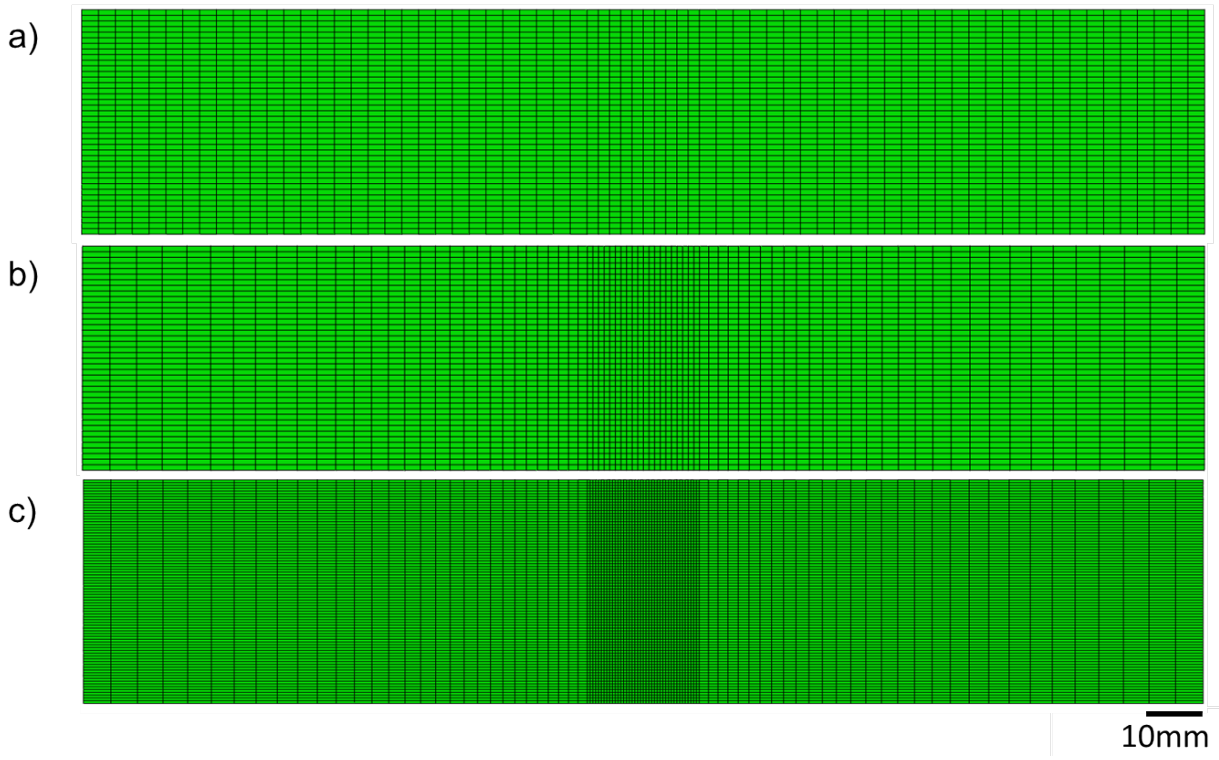

Figure 3.13 a) Coarse, b) medium and c) fine mesh densities for impact of FMLs.

Mesh density	**Number of elements**	**Number of nodes**	**Peak force (kN)**	**% Diff**	**Delamination area (mm^2)**	**% Diff**	**Simulation time (hours)**
Coarse	16803	34934	1.78	6.1	7.92	61	19
Medium	19203	39854	1.77	5.8	5.28	7.7	44
Fine	48003	98174	1.76	5.4	4.91	0.2	74

Table 3.6 Mesh density study results.

The influence of mesh density on the numerical predictions of the orientation and shape of delamination is also investigated. Experimental observations attained using optical microscopy

showed delamination area of 4.9 mm^2 when impacted at 5 J. Table 3.6 shows the predicted delamination areas and percentage differences compared to the experimental result. Although all mesh cases over-predicted the delamination area, the medium and fine mesh sizes were able to capture a similar delamination area, shape and orientation, revealing the characteristic circular shaped delamination between dissimilar plies directly under the impactor. A detailed analysis of the delamination shape and orientation prediction of FMLs subject to low velocity impact will be discussed in section 3.5.5.

Based on the ability of the model to predict the peak force as well as the delamination shape and size, while compromising on the simulation running time, the medium size mesh density was chosen for the low velocity impact analysis of the FMLs.

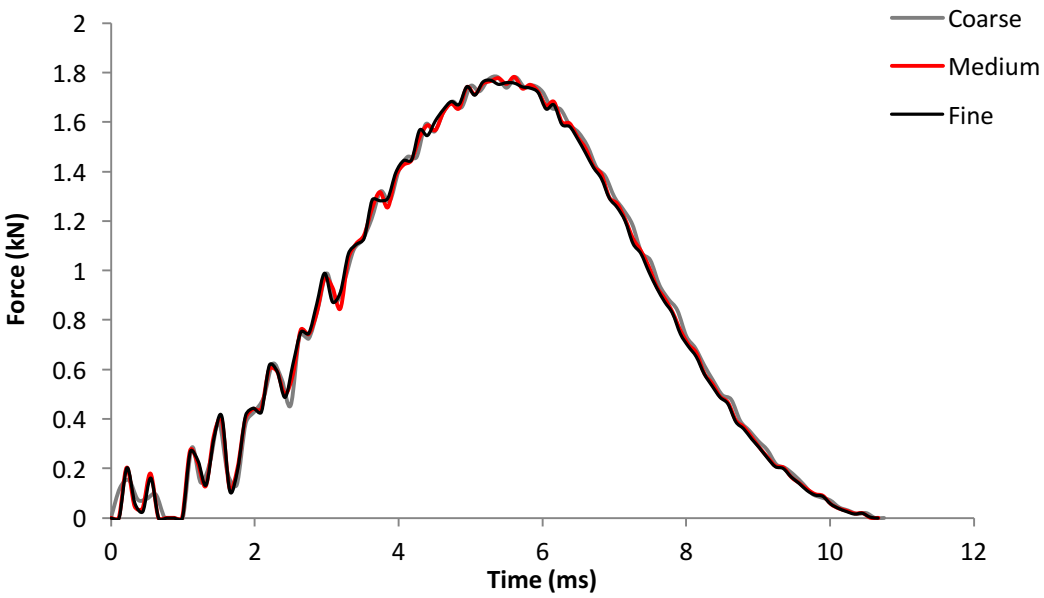

Figure 3.14 Force-time curve for FML 1 2/1-0.4 panel.

3.5 LOW VELOCITY IMPACT BEHAVIOUR OF FMLs

3.5.1 INTRODUCTION

The following section investigates the dynamic response of two FML configurations subject to low velocity impacts. The developed FE model is used to investigate the influence of increasing impact energy on the initiation and progression of various damage modes. The experimental and numerical investigation is conducted on FML test coupons FML 1 2/1-0.4 and FML 2 3/2-0.4. The experimental and FE predictions will be described by comparing several parameters including the force-time histories, peak impact force, and plastic deformation of the FML. Additionally, a

series of destructive and non-destructive post-impact analyses are carried out on the FML specimens to determine the damage modes in each of the FML layers. A summary of the damage modes found in experimental and numerical investigations of FMLs subject to low velocity impacts are described in Chapter 2. This section focuses on further increasing the understanding of the role of each damage mechanism in the degradation of FMLs subject to low velocity impact. Particular attention is given to the sequence of damage initiation and progression, as well as the interaction of the various damage mechanisms, which has not been systematically studied before.

3.5.2 POST-IMPACT DAMAGE EVALUATION

In this research, experimental damage measurements were carried out during post-impact analysis. In order to evaluate the crater damage on the front (impacted) and rear (non-impacted) surfaces of the FMLs, two different methods were used: (i) a digital calliper was put in contact with the indented FML and the diameter of crater damage was measured and (ii) an image processing package - ImageJ [226] - was used to analyse the damage area. The results obtained from both methods were similar. As such, the following discussions reference procedures specified using the image processing method.

The permanent central plastic deformation is a measurement of the centre of the dent, and was carried out during the post-damage inspection stage of the analysis. This measurement is critical when assessing the impact damage of FMLs in aerospace applications such as leading edges of aircraft due to their ability to create a turbulent airflow at increased dent depths.

Delamination area of the composite layers to the impacted FML specimens is also investigated. Difficulties in using ultrasonic methods for non-destructive evaluation (such as C-scan ultrasonics) of damage can arise due to the acoustic impedance mismatches of the two constituents of the FML as described in section 2.1.4.4, rendering it challenging to perform an accurate analysis of the failure modes.

In addition, X-ray micro-computed tomography (XμCT) that uses X-rays to create 3D images of the damage within the FML samples was trailed at LaTrobe University, Melbourne, Australia. The XμCT system employs a conical-shaped beam of X-rays that are passed through the damaged specimen as it is rotated from -90° to +90°. These 2D tomographic projections or ‘virtual slices’, as seen for example in Figure 3.15, are captured by the imaging detector and then combined and reconstructed using algorithms to build a 3D image of the FML specimen, as shown in Figure 3.16. Although this method provides the benefit of non-destructive inspection of the damage within the FML specimen, due to the layered nature of the FML specimens, there were some issues

with image quality. These included image segmentation and volume rendering, whereby the layers of the FML panel were difficult to separate. In addition, noise that appears as grain on the image was due to the thin slice thickness of the FML panels. Recently, Léonard et al. [227] demonstrated the successful use of XμCT on the impact damage characterisation of CARALL specimens. However, it was noted that obtaining a good contrast between the low density composite and cracks/voids was difficult.

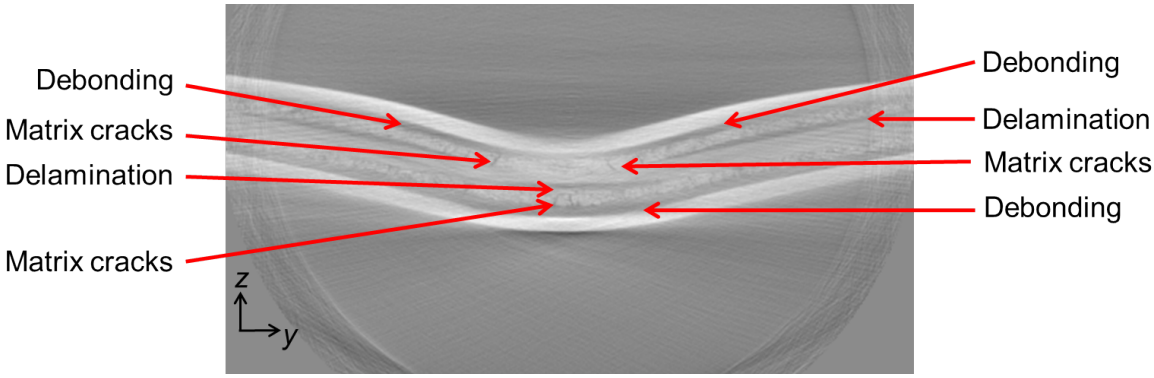

Figure 3.15 2D XμCT projections of Y-Z cross-section of impact damage to FML 1 2/1.

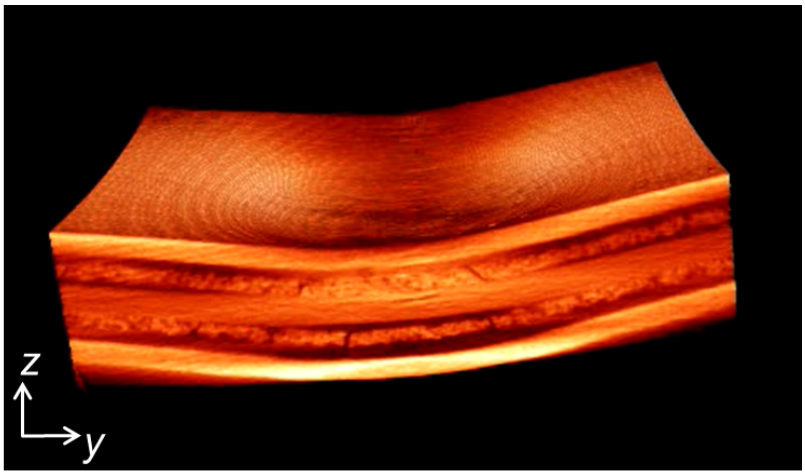

Figure 3.16 Reconstructed 3D image of Y-Z cross-section of impact damage to FML 1 2/1.

In order to gain better insight into the damage of the GFRP laminate in this research, the external aluminium layers were removed, and the post-impact examination of the GFRP laminate was conducted using optical microscopy. A back illumination technique was used to apply a light source to the upper surface of the GFRP in order to clearly view the damage.

Cross-sections of the impacted FML were taken across the width (Y-Z plane) of the specimen with reference to the coordinate system in Figure 3.7. Each damage mode will be explained in detail with reference to post-impact experimental observations.

3.5.3 DAMAGE MODES

At low impact energies, significant damage to the FML specimens occurred in the forms of plastic deformation to the aluminium layers as well as intralaminar and interlaminar damage to the GFRP plies and debonding between the metal and composite layers. During the impact event, the high contact pressure induced by the impactor produced compressive stress waves within the FML. The waves propagate through the FML until they reach the rear aluminium layer (non-impacted side), where they are reflected as tensile waves. The flexure of the impacted FML specimen and the tensile stress wave are largely responsible for the interlaminar and intralaminar damage of the GFRP plies, as well as adhesive failure [82].

Although the sequence of damage modes could not be verified experimentally, it is clear that the resulting damage modes are linked such that the onset of a damage mode triggers others. A summary of the damage modes for FML 1 2/1 and FML 2 3/2 subject to the impact energy of 19.5 J are presented in Figure 3.17 and Figure 3.18, respectively.

At low impact energies (5 J and 8.2 J), plasticity occurred in the metal layers and was visible as regions of permanent deformation in the form of front and rear crater damage, as well as central plastic deformation of the impacted specimens. FML 1 2/1 and FML 2 3/2 exhibited visible front crater damage in the form of a localised circular indentation due to the spherical shape of the impactor. The rear surface of the aluminium developed local damage in a roughly elliptical shape with the long axis orientated along the 0° direction (rolling direction of the aluminium). The elliptical (rather than circular) rear crater damage demonstrates the influence of the cross-ply laminate made from orthotropic plies which produce higher stresses along the outer 0° ply in the 0° direction.

No visible cracks on either the front or the rear aluminium surfaces of the FML 1 2/1 and FML 2 3/2 specimens were observed at low impact energies. However, with an increase in impact energy (12.8 J and 19.5 J) front and rear crater damage increased in size, resulting in a prominent peak on the rear crater. A hairline crack occurred on the front aluminium surface of FML 1 2/1 at 19.5 J, equivalent in length of the impactor diameter. Rear aluminium cracking initiated at an impact

energy of 12.8 J for both FML configurations. This occurred as a result of tension in the rear aluminium layer that allows the crack to initiate and grow. All cracks formed perpendicular to the 0° direction along the longitudinal axis, and a clear progression of crack length occurred with increasing impact energy.

Although a similar trend was observed in FML 2 3/2, the resulting rear aluminium crack length was approximately 30% smaller than observed in FML 1 2/1. This is due to the increased thickness of FML 2 3/2 with the addition of the middle aluminium layer which increases the stiffness of the overall FML thereby decreasing the flexural deformation of the specimen under impact. Post-impact observations of the FML 2 3/2 specimen impacted at 19.5 J revealed a crack in the middle aluminium layer directly under the impact region, as seen in Figure 3.18. At an impact energy of 19.5 J, FML 1 2/1 specimens exhibited a large increase in front and rear crater damage areas compared to FML 3 3/2. This was due to the significant impact energy absorption that occurred through crack formation of the middle layer of the FML 2 3/2 specimen. As the impactor initiated a crack in the middle aluminium layer, the impactor was slowed down such that the impact force was applied over a larger area. Thus, less energy was available to cause plastic deformation to the outer aluminium layers.

In addition to metal plasticity, matrix cracking and delamination in the GFRP layers constitute typical damage mechanisms in FMLs. These damage modes are generally known to be linked, particularly when FMLs are subject to bending load such as that induced during low velocity impact [228]. Matrix cracking was observed in numerous locations in the GFRP layers in both FML configurations. Due to the c-sectioning across the width (Y-Z plane) of the specimens with reference to the coordinate system in Figure 3.7, matrix cracks were only visible in the 0° plies (Plies 1 and 4).

At low impact energies (5 J and 8.2 J), matrix cracks were located in the outer 0° ply (Ply 4) in the FML 1 2/1 specimen. This was due to the flexural response of the FML under impact that induced significant tensile bending stresses on the non-impacted side of the specimen. Matrix cracks were orientated at an angle from the mid-surface, indicating that transverse shear stresses had a significant role in their formation [33]. Similar observations have been noted for FML 2 3/2; however, a decrease in the extent of matrix cracking was observed because of the higher flexural rigidity of this FML configuration.

In the low impact energy range (5 J and 8.2 J), delamination in the FML 1 2/1 specimen only occurred near the outer surface in the 90°/0° interface (Plies 3 and 4), extending away from the impact region. Delaminations were introduced as a result of the orthotropic properties of the individual GFRP plies and bending stiffness mismatch between plies (i.e. different bending rigidities of sub-laminates above and below a given interface) [33, 229]. In addition, matrix cracks in Ply 4 propagating toward Ply 3 induced delamination at the ply interface between these two plies with their different fibre orientations (90°/0° interface). This was evidenced by cross-sectional observations that show transverse matrix cracks located towards the edges of the delamination region in both FML configurations. Similar observations have been reported for polymer matrix composites impacted at low velocities [230-232]. In contrast, although the FML 2 3/2 exhibited matrix cracks in the same ply location as the FML 1 2/1, no delamination was observed. This was once again due to the ability of the additional aluminium layer of FML 2 3/2 to absorb impact energy, such that greater energy was required to initiate the delamination damage mode.

At higher impact energies (above 8.2 J), an increase in the number and severity of matrix cracks were recorded for both FML configurations. Similar to low impact energies, matrix cracks were observed in the outer 0° ply (Ply 4), but also occurred under the edge of the impactor on the inner 0° ply (Ply 1). This is attributed to the high interlaminar shear and transverse normal tensile stresses [232] through the material as a result of contact forces. The matrix cracks can induce interlaminar delamination due to opening stresses. Delamination occurred between the 0°/90° and 90°/0° interfaces. Delamination near the outer surface (90°/0° interface) increased in length for both FML configurations with increasing impact energy. Delamination at the upper surface (0°/90° interface) was initiated, extending away from the impact region for both FML configurations.

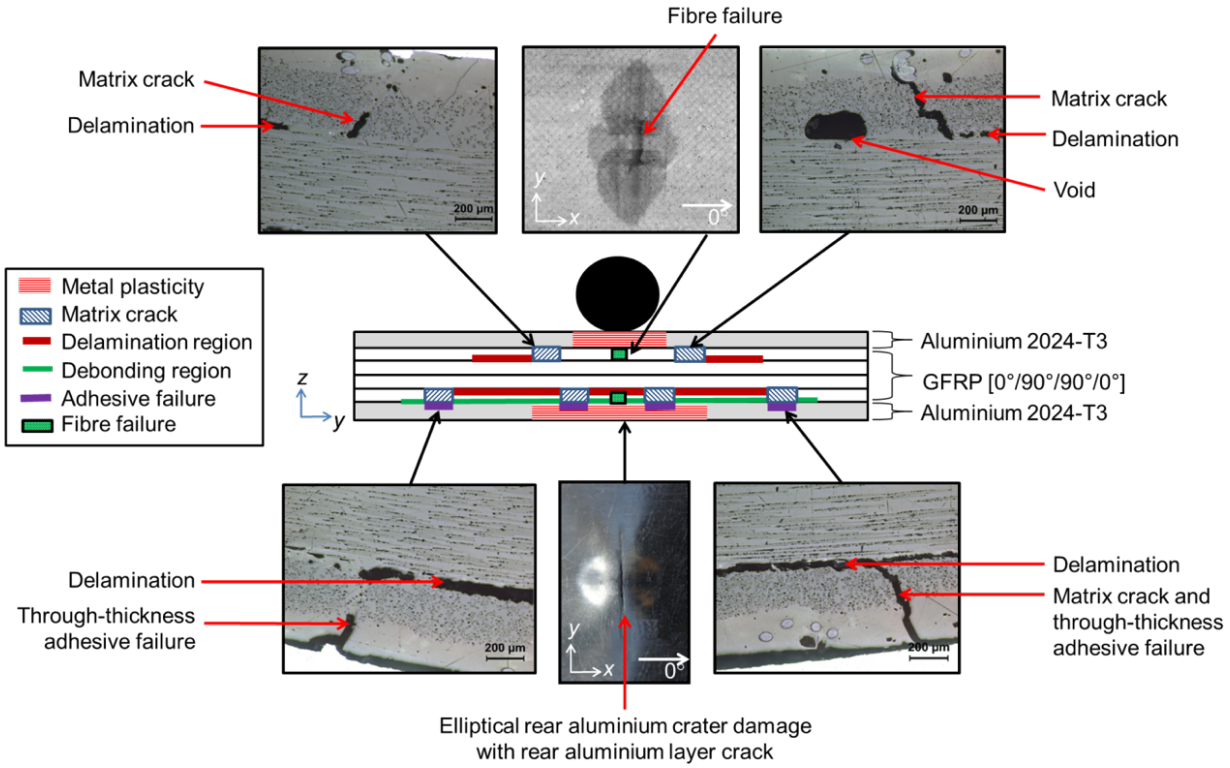

Figure 3.17 Y-Z cross-section of damage mechanisms of FML 1 2/1 impacted at 19.5 J (fibre splitting and aluminium damage images from X-Y plane).

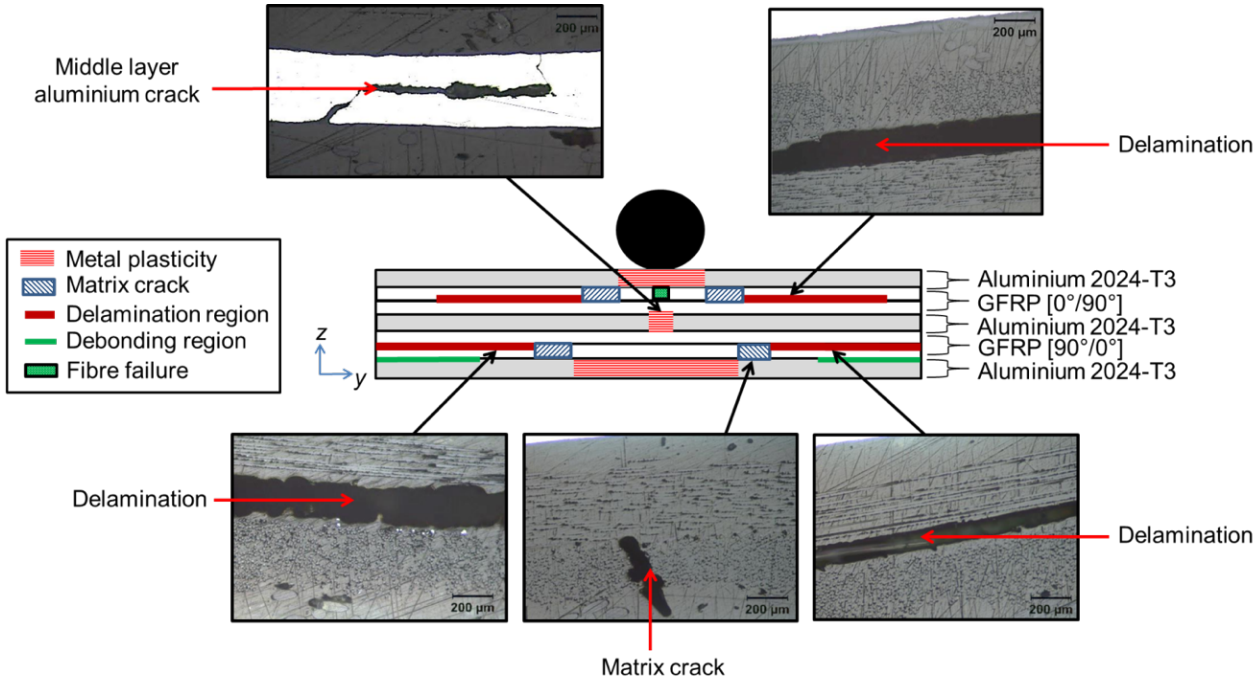

Figure 3.18 Y-Z cross-section of damage mechanisms of FML 2 3/2 impacted at 19.5 J.

Figure 3.19 shows the size and shape of the delaminations in FML 1 2/1 for two impact energies. Research has shown that delaminations typically extend in the direction of the lower or outermost ply reinforcement [27], and as such the optical microscopy images aid in identifying the ply interface where delamination occurs. At an impact energy of 8.2 J, delamination was confined to a relatively small area surrounding the impact region. The shape of the delamination was approximately circular, and about the same diameter as the impactor. With an increase in impact energy to 19.5 J, the delamination area was larger than the size of the visible crater area on the front aluminium surface, extending beyond the impact region. The delamination area exhibited a 'peanut shape' aligned in the 90° direction at the 0°/90° interface (Plies 1 and 2), as well as a roughly elliptical delamination area aligned in the 0° direction, directly under the impactor in the 90°/0° interface (Plies 3 and 4). Similar experimental observations have been reported by Bagnoli et al. [77] and Wu et al. [71] on GLARE specimens subject to impact energies between 7 and 40 J.

At high impact energies, the occurrence of small cracks in the adhesive were observed on the outer adhesive surface of the FML 1 2/1 specimen. Matrix cracks at the outer 0° ply (Ply 4) extend to the adjacent adhesive layer, resulting in through-thickness transverse failure of the adhesive layer. No adhesive failure was observed in the FML 2 3/2 specimens.

The initiation point of fibre failure was difficult to experimentally identify during the impact event. Fibre failure on the impacted side of the FML specimen was the result of the compressive bending strains induced during impact. Fibre failure near the rear surface was due to tensile bending strains on the non-impacted side of the FML. With an increase in the applied strain, the transverse stresses lead to longitudinal splitting cracks along the 0° plies. Optical microscopy images of FML 1 2/1 in Figure 3.19 show evidence of vertical fibre crack in the 0° plies, indicated by the dark vertical line in the GFRP. An increase in impact energy resulted in a significant increase in the size of fibre failure. At 8.2 J, fibre failure was concentrated in a localised region around the impact region, perpendicular to the 0° direction, as indicated in Figure 3.19a. This was due to the high stress and indentation effects caused by the shear force induced by the impactor and bending stresses in the non-impacted GFRP surface. Fibre failure length was recorded to be approximately equal to the diameter of the impactor when impacted at 19.5 J. In addition to local stresses induced by the impactor, the increase in fibre failure length was attributed to bending stresses in the FML away from the impact region. Minor fibre failure was detected in the FML 2 3/2 specimen through microscopic observations, however due to the middle aluminium layer of the FML 2 3/2 specimens accurate readings could not be made.

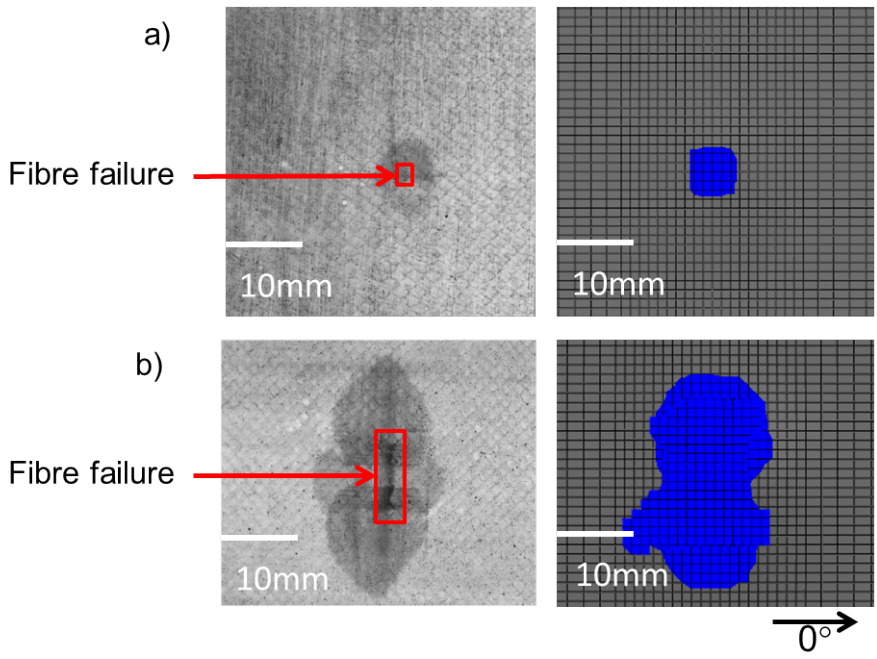

Figure 3.19 Optical microscopy images (left) and FE predictions (right) of the GFRP delamination and fibre failure damage for FML 1 2/1-04 at a) 8.2 J and b) 19.5 J.

Sinmazçelik et al. [10] reported that the effectiveness of FML relies on the level of the bonding integrity between the metal and the composite layers. The bonding interface must possess sufficient interfacial strength to distribute the impact load between two characteristically different materials. Debonding between the rear aluminium and adhesive/GFRP layers was observed near the non-impacted side of the FML 1 2/1 specimen. At low impact energy of 8.2 J, FML 1 2/1 exhibited minor debonding equal to the length of delamination on the outer surface of the GFRP (90°/0° interface), directly under the impact region. Prominent debonding between the rear aluminium layer and adhesive/GFRP occurred with increasing impact energy for FML 1 2/1, as seen in Figure 3.17. No debonding occurred at low impact energies in the FML 2 3/2 specimen. With an increase in impact energy, minor debonding was observed on the non-impacted side of the FML 2 3/2 specimen directly under the delamination on the outer surface (90°/0° interface), extending to the edges of the specimen width. No debonding of the middle aluminium layers was observed.

The results presented above, and similar experimental observations of critical damage modes of FMLs subjected to low velocity impact reported in published literature validate the FML manufacturing method detailed in Chapter 3, providing a sufficiently strong bond between the aluminium and GFRP constituents of the FML. While the resulting damage modes due to low velocity impact are dependent on adhesive bond strength, the experimental observations reveal

that it is not the most prominent factor that dictates the initiation and progression of the damage modes. Rather, adhesive failure was a result of interfacial shear stresses induced by bending at the metal/GFRP interface, often stemming from matrix cracking in the impact region.

3.5.4 EFFECT OF IMPACT ENERGY AND FML CONFIGURATION

The response to impact as described in terms of force-time histories produced by low velocity impacts on the FML 1 2/1 and FML 2 3/2 materials is shown in Figure 3.20 for low (8.2 J) and high (19.5 J) energies. All experimental curves show pronounced oscillations deriving from dynamic phenomena such as dynamic resonances and vibrations due to coupling between the specimen and its support. At low impact energies, elastic-like behaviour of the FML specimens was found, corresponding to the relatively smooth force-time histories as seen in Figure 3.20 a and c. At higher impact energies, the force-time curve for FML 1 2/1 showed the initial elastic phase was interrupted by sudden load drop at the maximum peak load, as seen in Figure 3.20b. The sharp load drop in FML 1 2/1 was likely induced by cracking of the rear aluminium layer. In comparison, smaller load drops following peak load, seen in Figure 3.20d, were exhibited in FML 2 3/2 corresponding to decreased extent of damage compared to FML 1 2/1 when impacted at similar impact energies. Additionally, damage mechanisms such as delamination and fibre failure in the GFRP plies can cause load drops in the force-time histories, corresponding to propagation of damage resulting in the loss of local rigidity. This behaviour was observed by Vlot [41] who investigated the low velocity impact damage of GLARE. Vlot concluded that the sharp load drop was dictated by the first cracking on the rear aluminium layer in the rolling direction, after which discrete load drops were indicative of delamination and failure of the GFRP plies. The occurrence of small load drops correlate with the existence of delamination and fibre failure, as previously noted.

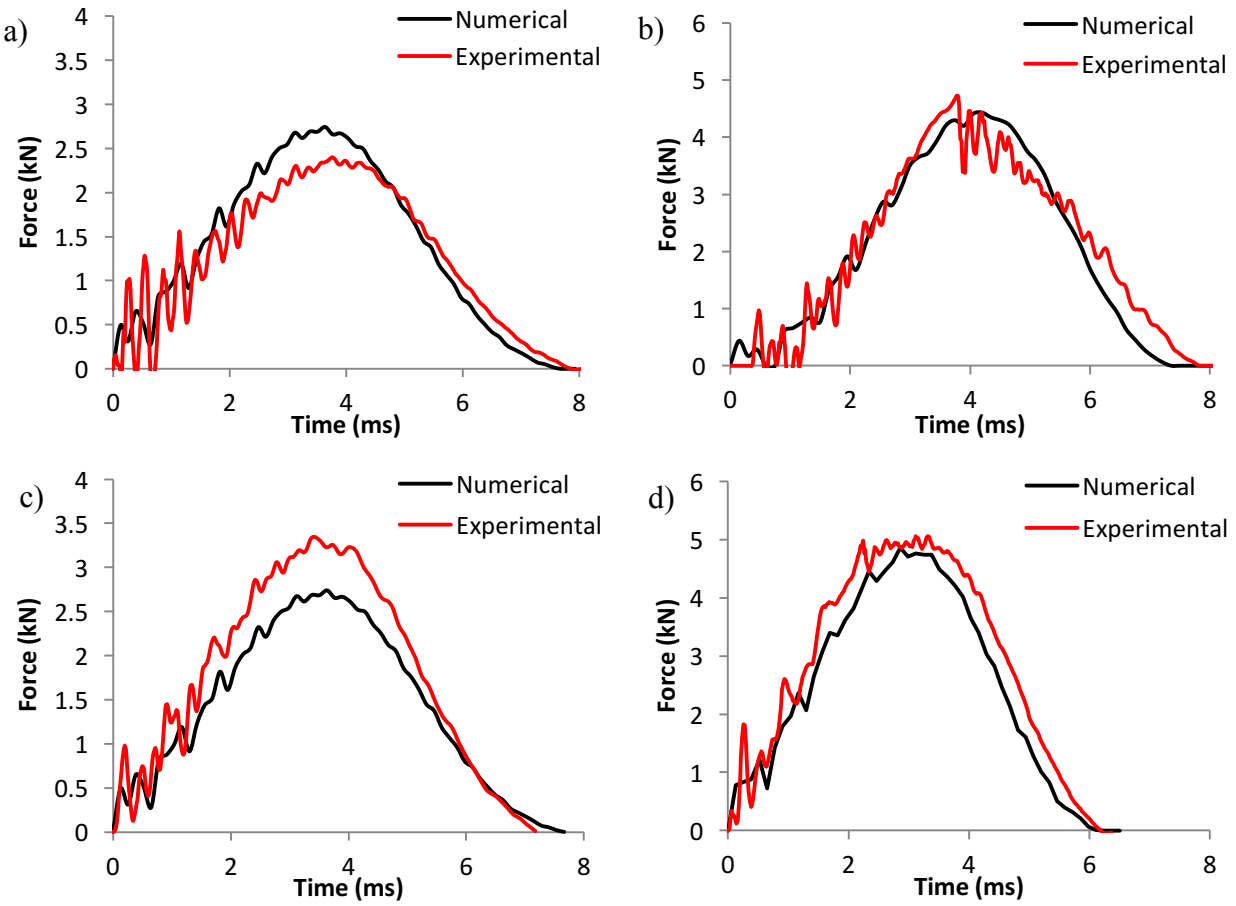

Figure 3.20 Force-time results for FML 1 2/1-0.4 a) 8.2 J and b) 19.5 J, and FML 2 3/2-0.4 at c) 8.2 J and d) 19.5 J.

A detailed summary of the experimental results is presented in Figure 3.21 and Figure 3.22 for the FML 1 2/1 and FML 2 3/2 configurations, respectively. In general, increasing the impact energy resulted in a quasi-linear increase in the peak force and all key damage metrics. At low impact energies (5 J and 8.2 J) the FML 1 2/1 material experienced plastic deformation of the aluminium that plays a dominant role in absorbing the energy. With an increase in impact energy from 5 J to 8.2 J, a ~300% and 800% increase in the front and rear crater damage areas were recorded, respectively. Plastic central deformation was found to increase, and delamination and debonding damage modes were induced at 8.2 J directly under the impactor. The initiation and growth of these damage modes, particularly within the GFRP plies, allowed the FML 1 2/1 material to absorb more energy at higher impact forces, reflected in the ~3% reduction in the energy restitution coefficient at 8.2 J. A similar trend occurred with the FML 2 3/2 specimen. It is noted, however, that delamination was not initiated at 5 J and very minor delamination at the 90°/0° interface was detected at 8.2 J. This was due to the increased thickness of the FML with the addition of the middle aluminium layer. As the impactor strikes the FML 2 3/2 specimen, the impact force was

absorbed over a larger volume of material per unit thickness. More energy was therefore required to delaminate the GFRP fibres. In addition, no debonding was found to initiate at this impact energy range.

Absorbed energy during an impact event is partially dissipated as heat and vibrations, but also plays a fundamental role in the development of damage such as permanent plastic deflection, delamination, fibre breakage and intralaminar splitting [233]. At high impact energies, the FML panels undergo notable permanent central deflection due to the plastic behaviour of the aluminium. Additionally, rear aluminium cracking was induced in both FML constituents. High absorbed energy values also correlate to a large increase in the amount of localised interlaminar and intralaminar damage at high impact energies. This is evidenced by the significant increase in the extent and number of failure modes, as seen in Figure 3.17 and Figure 3.18, and the subsequent decrease in energy restitution coefficient of the FML specimens.

At 12.8 J, the delamination damage area increased by 222% in FML 1 2/1, occurring at the 90°/0 (Plies 1 and 2) and 0°/90° (Plies 3 and 4) interfaces. Additionally, the debonding length at the rear aluminium layer and adhesive/GFRP increased by nearly 20%. A combination of these two damage modes allowed the FML 1 2/1 specimen to act as a number of separate layers. The separation of layers allowed for the effective in-plane redistribution of short transverse loads into the laminate, thereby increasing the energy absorbed at higher impact energies, as noted by Vlot and Krull [57] and Moriniere et al. [234].

The significant increase in the extent of intralaminar and interlaminar damage modes of the GFRP, and the introduction of rear aluminium cracking initiated at this impact energy corresponded to the noticeable decrease in the energy adsorption coefficient of 27%. Although rear aluminium cracking was initiated in the FML 2 3/2 material at this impact energy, only an 8% decrease was measured in the energy adsorption coefficient. This was due to the significant differences in delamination damage area of 80% between the FML 1 2/1, as well as the lack of debonding that occurred in the FML 2 3/2 specimen; illustrating the effectiveness of these damage mechanisms in energy absorption.

At 19.5 J, FML 1 2/1 experienced a significant decrease in energy restitution coefficient of 37.5% occurred from 12.8 J. This was due to an increase in the number and severity of all damage modes. In particular, central plastic deformation, front crater damage and rear crater damage areas increased by 63%, 192% and 130%, respectively. Additionally, FML1 2/1 exhibited a rear

aluminium crack length increase from 7 mm to 18 mm at 12.8 J and 19.5 J. At this impact energy, front aluminium cracking in the form of a hairline crack was initiated. The high impact energy was absorbed through increased metal plasticity of the aluminium layers. A large increase in delamination area of 112% and debonding lengths was also recorded.

In comparison, metal plasticity in the form of central plastic deformation, and front and rear crater damage area for FML 2 3/2 plateaued at high impact energies and was the result of the increased stiffness of the FML configuration due to the additional aluminium layer. Under high impact loads, FML2 3/2 was unable to undergo larger bending strains to induce large plastic deformations and debonding within the impacted specimen. A visual inspection of the front and rear crater damage areas shows a significant difference between FML 1 2/1 and FML 2 3/2. Similarly, the delamination damage area between FML 1 2/1 and FML 2 3/2 showed a difference of 20% when subjected to the same impact energy of 19.5 J. The cracking of the middle layer of aluminium directly under the impactor in FML 2 3/2, as shown in Figure 3.18, acted as the primary energy absorbing mechanism, however this was less efficient at absorbing impact energy compared to FML 1 2/1. In addition, the decrease in the number and extent of damage mechanisms in FML 2 3/2 compared to FML 1 2/1 reveal that significant differences in impact resistance properties exist between the two types of FML specimens. This is reflected in the ~50% difference in the energy restitution coefficient between FML 1 2/1 and FML 2 3/2 at 19.5 J.

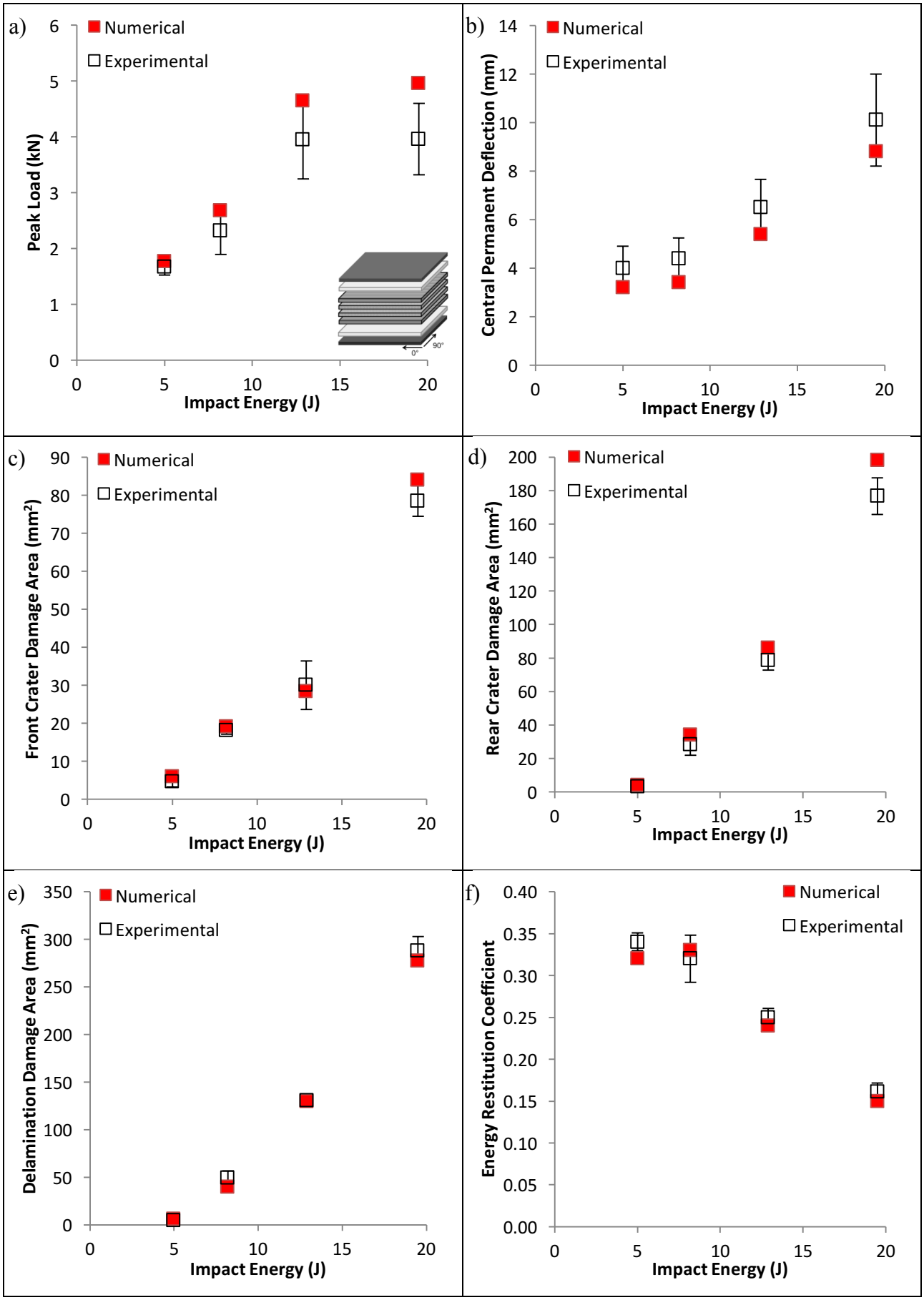

Figure 3.21 FML 1 2/1 Experimental and numerical results.

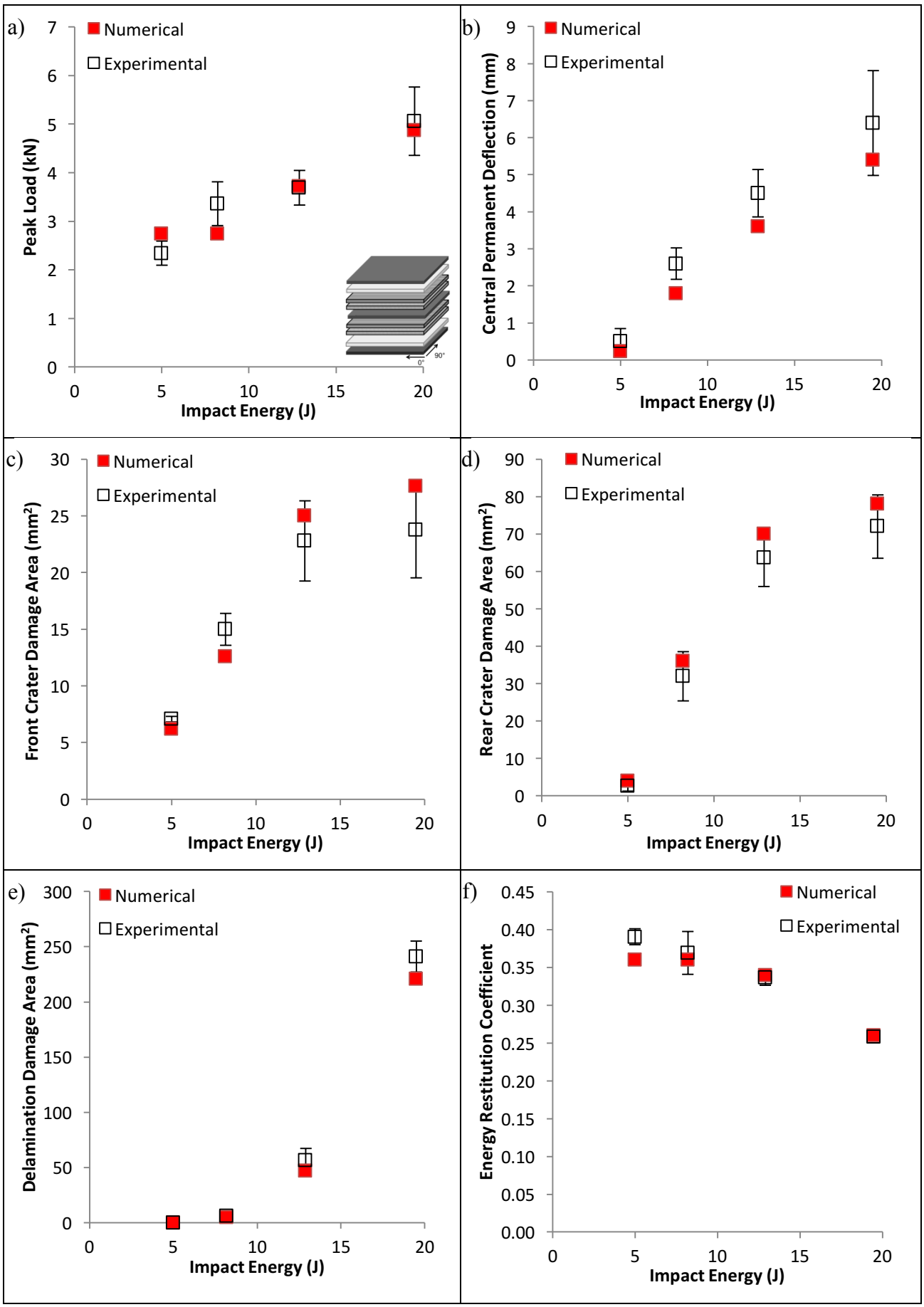

Figure 3.22 FML 2 3/2 Experimental and numerical results.

3.5.5 COMPARISON BETWEEN EXPERIMENTAL AND NUMERICAL RESULTS

There is good agreement between the experimental and numerical results as shown in Figure 3.21 and Figure 3.22, with the FE predictions almost always within the experimental error. In particular, both quantitative and qualitative predictions of the effect of impact energy and FML configuration on damage initiation and progression showed a high degree of accuracy for all damage modes.

Comparison of the force-time histories for both FML configurations showed good agreement between the experimental measurements and FE predictions. However, the FE predictions did not replicate the sharp load drop in the FML 1 2/1 specimen at 19.5 J, as seen in Figure 3.20b. This is likely induced by cracking of the rear aluminium layer to the impacted FML specimen. Although the FE model captured the progressive softening from plasticity, cracking was difficult to predict using the FE model due to the brittle intermetallic phase in the aluminium. Cracks often initiate and grow along a row of fine intermetallic precipitates (known as stringers) aligned in the rolling direction of the aluminium sheet. Stringers can promote rapid crack growth and results in a significant load drop under impact loading that cannot be captured with the FE model. Despite this, the force-time histories for both FML configurations in terms of peak load and contact time highlights good agreement between the experimental recordings and FE predictions.

Front and rear crater damage areas were all predicted closely, demonstrating that the FE model captured the metal plasticity damage mechanism for both FML configurations. However, the FE model under-predicted the permanent deflection, in particular for the FML 2 3/2 material. The reason for this discrepancy may be due to the clamped boundary conditions in the FE model that may not have been completely replicated in the experimental tests.

The delamination predictions were also a key aspect of comparison, in terms of size, area and location. The model under-predicted the size of the delamination between the outer GFRP plies (90°/0° interface) orientated in the 0° direction at high impact energies (12.5 and 19.5 J). This is likely due to the highly complex interaction of damage modes, particularly the extensive matrix cracking and delamination. Despite this, the FE predictions still showed good agreement with the experimental results for the delamination damage area and orientation.

3.5.6 DAMAGE PATTERNS AND SEQUENCE

Caprino et al. [60] determined the sequence of failure modes with increasing impact energy for GLARE 5 2/1 [Al/0°/90°/Al/90°/0°/Al]. The work correlated the failure modes of the FML to the

impact force-displacement curve measured experimentally. However, their proposed method of determining failure mode initiation and progression is difficult to apply in experiments. The FE modelling methodology developed in this research offers a detailed ply-based analysis of the various damage modes and when they occur in FMLs. This allowed for the sequence and interaction of damage modes to be studied to an extent not possible with experimental impact testing.

Figure 3.23 shows the impact force-time results of FML 1 2/1 subject to low (8.2 J) and high (19.5 J) impact energies, with the initiation of damage modes indicated in each ply (P) from the front (1) to the rear (4) ply.

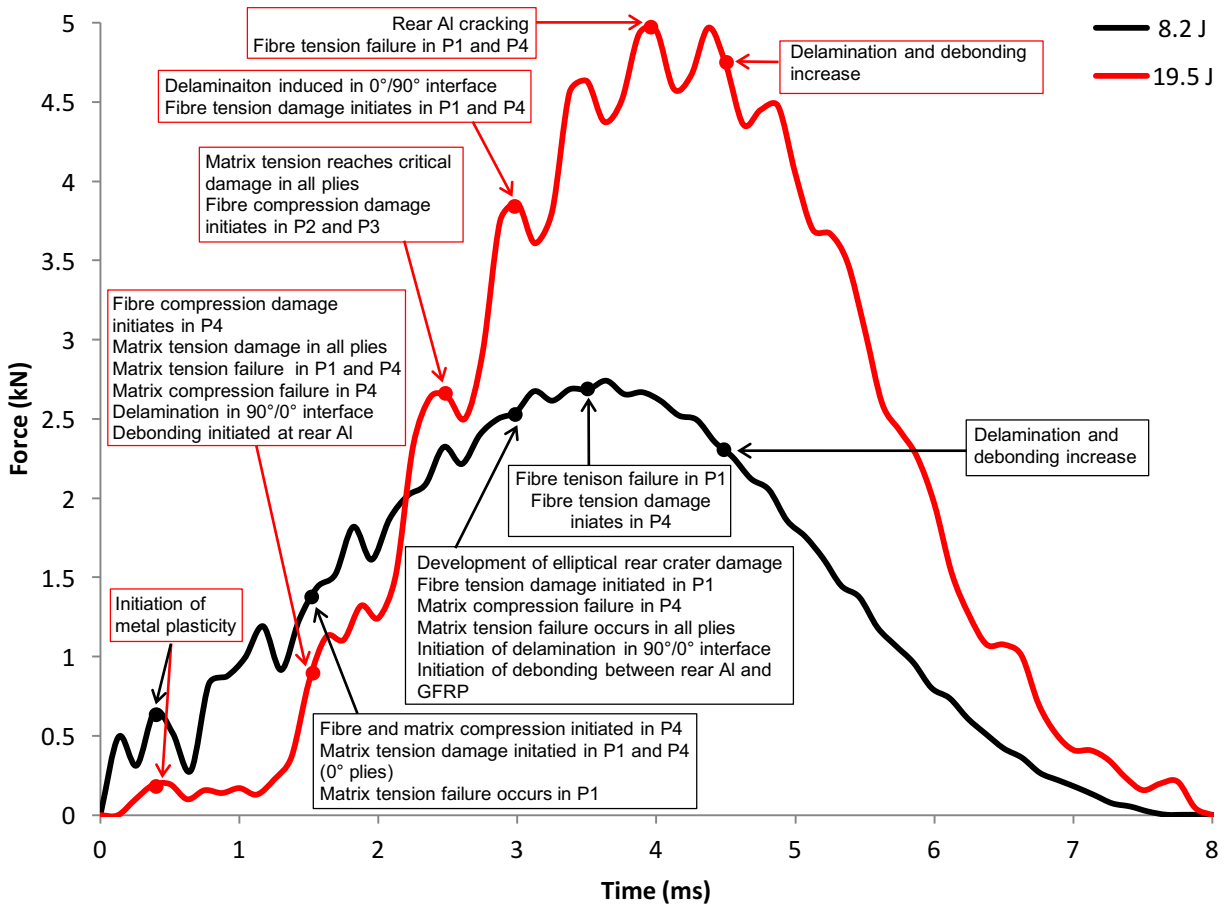

Figure 3.23 Force-time histories of FML 1 2/1 for two energy levels showing predicted initiation and failure of damage modes.

Figure 3.24 and Figure 3.25 shows ply-by-ply FE predictions of the failure contours for each of the GFRP plies and ply interfaces of the FML 1 2/1 material impacted at 8.2 J at the end of the impact simulation. Similarly, Figure 3.26 and Figure 3.27 show the FE predictions for the FML 1

2/1 material impacted at 19.5 J. As noted previously, the damage index varies between 0 (undamaged, blue) and 1 (fully damaged, red) in the FE model. To make it clearer to the reader, a distinction is made between damage initiation (damage index > 0) and failure (damage index = 1).

At low impact energies (8.2 J), the first mode of failure occurs at the surface of the aluminium layers in the form of plasticity as the impactor makes contact with the FML. The numerical model predicts high plastic strain in the front and rear aluminium layers in a circular shape directly under the impact region resulting from the spherically-shaped impactor.

At t = 1.5 ms, fibre and matrix compression initiated in Ply 4 (0°) directly under the impact region. Additionally, matrix tension damage initiated in the 0° plies (Plies 1 and 4), reaching a failure value (fully damaged) in P1 under the impactor. No fibre tension damage was initiated in any of the GFRP plies at this stage of the impact.

At t = 3.0 ms, high strains occurred at the rear aluminium layer, taking an elliptical shape with the long axis orientated in the 0° direction due to the high stresses produced along the outer ply of the GFRP in the 0° direction. This reflects the formation of the elliptical rear aluminium crater damage shape experimentally observed in FML1 2/1. Fibre compression damage initiated in Plies 2 and 3 in a localised region immediately under the impactor. Fibre compression damage extended in P4, but did not reach the critical failure value. Matrix tension failure occurred in all plies under the impactor. Similarly, matrix compression failure occurred in the outer GFRP ply (Ply 4) corresponding to experimentally detected matrix cracking in this ply. These matrix cracks led to the initiation of delamination at the 90°/0° ply interface, as seen in Figure 3.25. Additionally, debonding between the rear aluminium layer and GFRP/adhesive was initiated under the impactor resulting in a debonding length of ~2 mm.

Maximum impactor depth occurred at t = 3.5 ms, when the force-time curve reached peak load. Plastic strain on the front and rear aluminium layers was increased by 50%. Fibre tension failure occurred in Ply 1 extending to a length of 2 mm. This corresponded to fibre fracture detected through optical microscopy images, as shown in Figure 3.19. Fibre tension damage also initiated in P4. Matrix compression and tension failure increased in damage size in their respective plies.

At t = 4.5 ms, the delamination and debonding lengths were predicted to increase by 40%. No significant damage initiation or failure progression was found to occur when the impactor rebounded and the impacted FML specimen stabilised.

Similar to low impact energy, at high impact energy permanent deformation damage occurred at the surface of the aluminium layers of the FML, as high plastic strains were predicted directly under the impactor. At t = 0.5 ms, plastic strain was predicted to develop in a spherical and elliptical shape on the front and rear aluminium layers, respectively. At t = 1.5 ms after initiation of impact, fibre compression damage initiated in Ply 4 in a circular shape under the impactor. Matrix tensile damage in the GFRP plies at this time interval was predicted to occur in all plies, reaching the critical failure value in the 0° plies (Plies 1 and 4). Matrix compression failure occurred in Ply 4 under the impact region, in turn initiating delamination at the 90°/0° ply interface, as seen in Figure 3.27. Debonding between the rear aluminium layer and adhesive/GFRP also initiated at this time step.

Following this, at t = 2.5 ms, fibre compression damage was initiated in Plies 2 and 3 perpendicular to the fibre direction. Predicted matrix tensile failure grew at all ply levels approximately perpendicular to the fibre orientation, reaching complete failure. The extensive matrix tension failure corresponding to matrix cracking was predicted to grow, extending beyond the visible crater damage. It can therefore be concluded that even before the impactor reached the maximum penetration depth, damage in the form of matrix cracking had extended well beyond the impact region. Additionally, matrix compression failure grew in Ply 4.

At t = 3.0 ms, fibre failure initiated in the 0° plies (Plies 1 and 4). Matrix compression failure (Ply 4) and matrix tension failure (all plies) extended beyond the front and rear crater damage areas, allowing a delamination to form along the 0°/90° ply interface in a peanut-like shape. Delamination of the 90°/0° ply interface and debonding was predicted to further increase. Fibre compression damage grew further covering a larger damage area, however did not reach critical failure values.

As the FML specimen reached its maximum displacement at t = 4.0 ms, a significant load drop after peak force occurred in the force-time curve. Plastic strain to the rear aluminium layer increased by 75%. The high tensile stress at the non-impacted side of the FML caused the rear aluminium sheet to crack perpendicular to the 0° direction, as observed in experimental post-impact analysis. Fibre tension failure in Ply 1 and Ply 4 occurred directly under the impacted region and extended perpendicular to the fibre orientation. A critical failure length of 7 mm was predicted, correlating well with experimental observations, as seen in Figure 3.19. Significant debonding is predicted between the rear aluminium layer and GFRP plies consistent with the

cross-sectional micrographs, as shown in Figure 3.17. No further damage initiation or failure occurred when the impactor rebounded, which was expected.

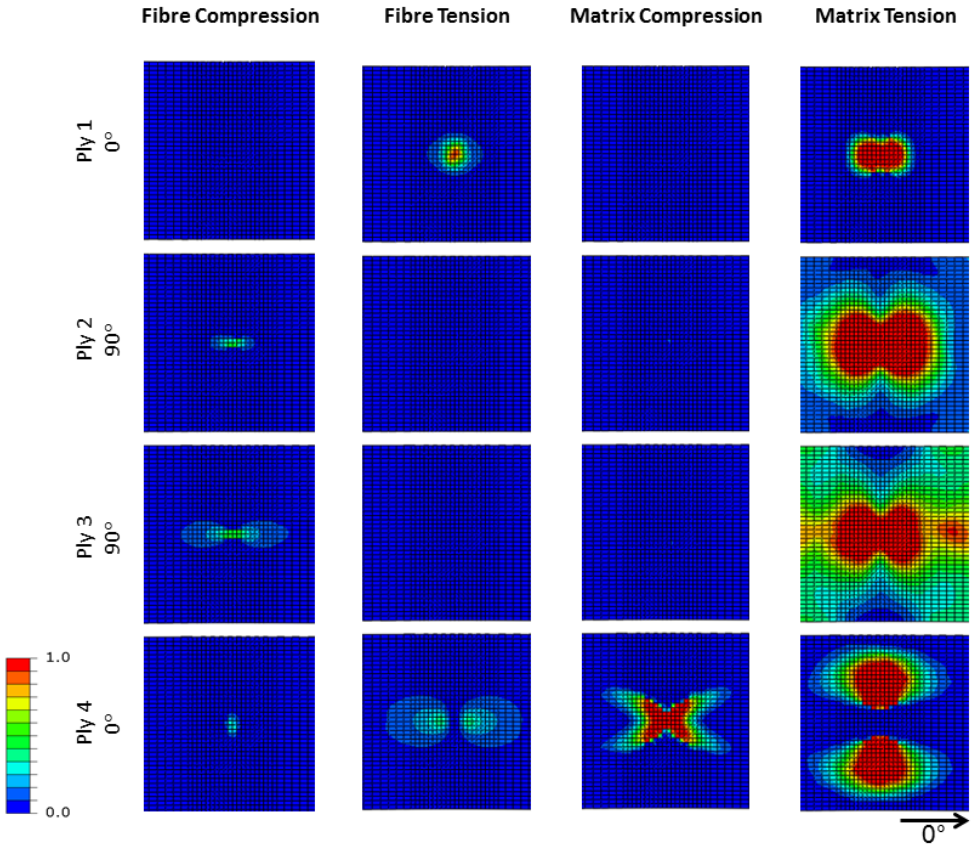

Figure 3.24 Numerically predicted damage contours of FML 1 2/1-0.4 impacted at 8.2 J.

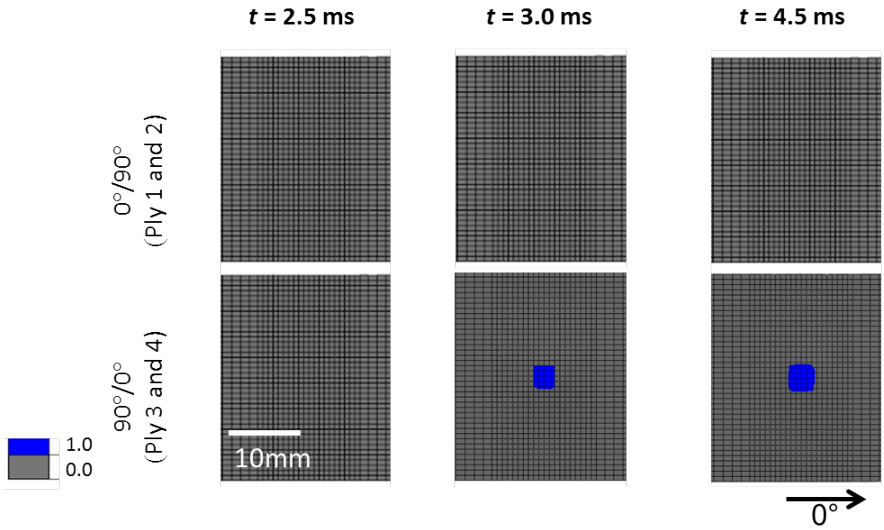

Figure 3.25 Numerically predicted delamination contours of FML 1 2/1 impacted at 8.2 J.

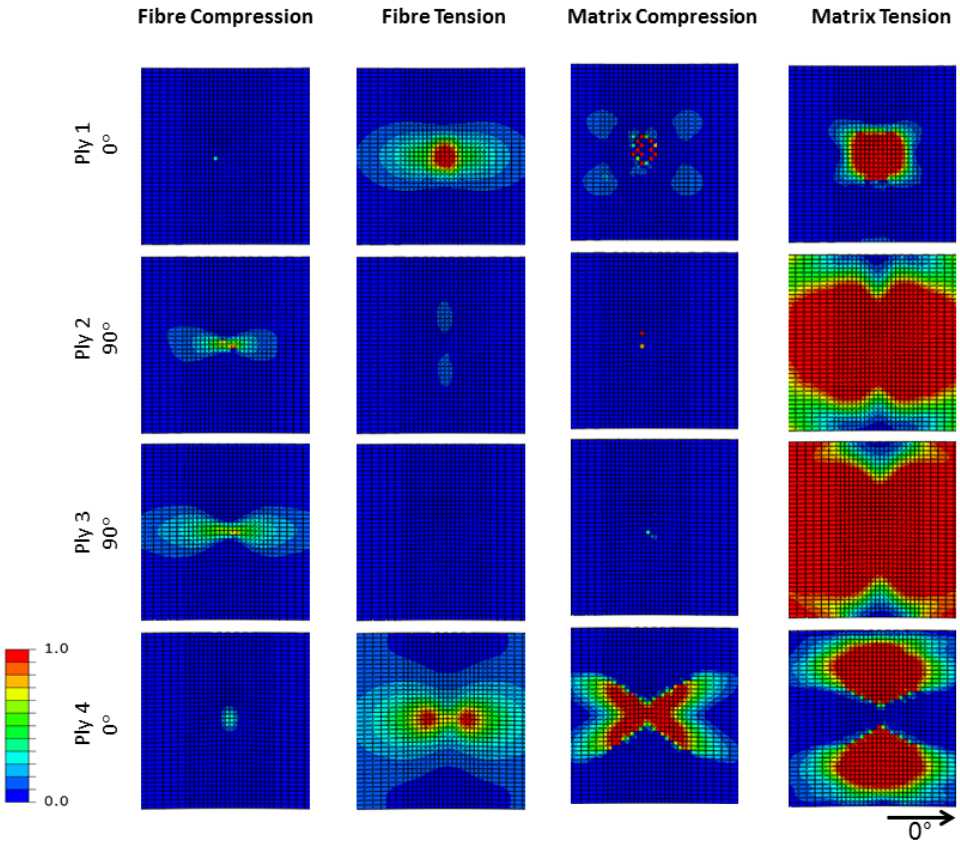

Figure 3.26 Numerically predicted damage contours of FML 1 2/1-0.4 impacted at 19.5 J.

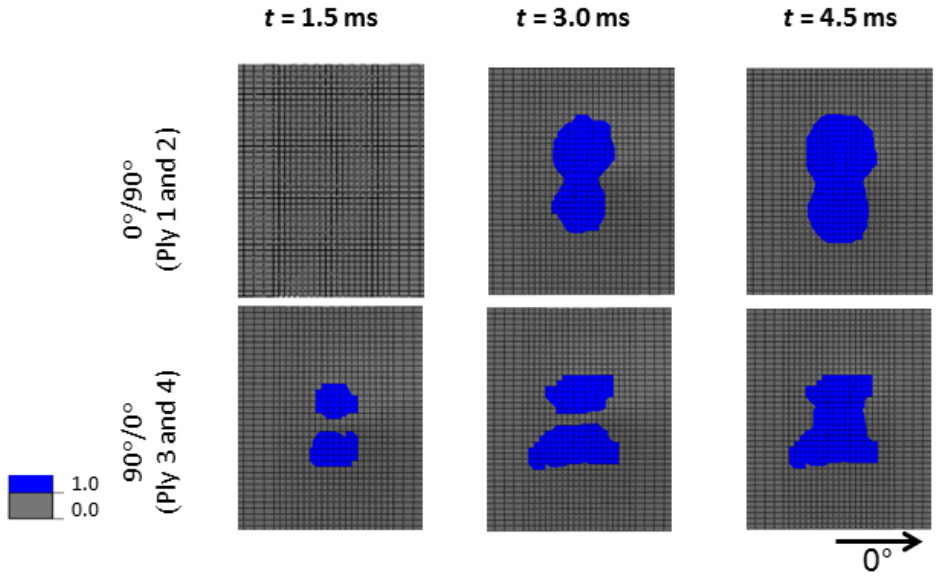

Figure 3.27 Numerically predicted delamination contours of FML 1 2/1 impacted at 19.5 J.

Ply-based FE analysis of the damage patterns and sequence for the FML 2 3/2 specimen subject to low velocity impact was also investigated. With the exception of cracking in the middle aluminium layer at 19.5 J, the FE analysis of damage initiation and propagation at low and high

impact energies showed similar trends to FML 1 2/1. Maximum strain in the middle aluminium layer occurred at t = 2.05 ms after initiation of impact, correlating to the drop in the force-time curve after peak load, as seen in Figure 3.20d. In addition, the FE model predicted the overall reduction to the number and severity of damage modes exhibited in FML 2 3/2, as recorded experimentally, when compared to the thinner FML 1 2/1.

3.6 CONCLUSION

An experimental investigation was conducted to evaluate and characterise the complex damage modes that occur within FMLs subject to low velocity impact. The investigation revealed that plasticity of the surface aluminium layers was the dominant energy absorbing mechanism at low impact energies (5 J and 8.2 J). In addition to metal plasticity, several damage modes occurred, namely matrix cracking, fibre failure, delamination and debonding. However, these damage modes were considered minor as they did not extend beyond the visible front and rear aluminium crater damage areas. With an increase in impact energy (12.8 J to 19.5 J), both FML configurations exhibited extensive metal plasticity in the form of front and rear crater damage, as well as aluminium cracking. Extensive intralaminar and interlaminar damage to the GFRP layers beyond the impact region was also observed.

Detailed post-impact analysis through cross-sectioning and optical microscopy revealed the extent of the damage modes present in FMLs, allowing insight into the location of damage modes. Moreover, links between damage modes were identified, such as the initiation of delamination at matrix cracks. Cross-sectional images taken across the width (Y-Z plane) of the impacted FML specimens showed matrix cracks located in the 0° plies. Upon reaching the ply interface, matrix cracks triggered delamination due to shear stresses at the interface between two adjacent plies having different fibre orientations. This phenomenon is evidenced by cross-sectional observations of transverse matrix cracks located towards the edges of the delamination region in both FML configurations. Post-impact analyses on the FMLs provided further insights into the various damage modes in each of the layers, which has not been extensively studied before.

The effects of increasing impact energy and FML configuration were studied in detail. Damage in the form of plastic indentation, debonding at the aluminium and composite interface, as well as interlaminar and intralaminar damage to the GFRP plies contributed to the impact energy absorption of FMLs. Increasing impact energy caused a quasi-linear increase in peak force and all

the key damage metrics for both FML materials. This growing extent of damage modes in the FMLs with increasing impact energy can therefore be related to the increase in the absorbed energy. FML 2 3/2 recorded lower damage and peak force compared to FML 1 2/1. In particular, cracking of the internal (middle) aluminium layer and lower number of damage modes occurring at high impact energies (19.5 J) was observed. This was due to the increased stiffness from the additional aluminium layer in the FML 2 3/2 material, and as such, FML 2 3/2 was less effective at absorbing impact energy compared to FML 1 2/1.

A FE modelling methodology was developed to gain an understanding of the dynamic response and damage of FMLs subject to low velocity impact. The ply-based model provided important insights into the damage initiation and progression, as well as the sequence and interaction of key damage modes. FE predictions showed excellent agreement with experimental measurements of the impact duration, peak contact force, and plastic deformation of both FML materials. In addition, the FE model accurately captured the internal damage to the GFRP laminate, allowing insights into complex intralaminar and interlaminar damage modes that are otherwise difficult/impossible to identify using experimental techniques. The computed projected damage areas for the FMLs showed good agreement with experimental results, sufficiently capturing the delamination shape and location.

At low impact energies (5 J and 8.2 J), FE modelling of damage initiation and progression in FML 1 2/1 showed that all the intralaminar damage modes were initiated in the GFRP plies, although they do not extent beyond the impact region. Matrix cracking in Ply 4 led to the initiation of delamination along the 90°/0° ply interface as well as debonding of the rear aluminium layer and adhesive/GFRP directly under the impact region. Although extensive metal plasticity did not occur at this impact energy range, fibre failure in Ply 1 and Ply 4 was initiated, corresponding to minor drops in the force-time curve.

At higher impact energies (12.8 J and 19.5 J), intralaminar damage in FML1 2/1 initiated soon after initial contact with the impactor. Matrix cracking in Ply 1 and Ply 4 extended beyond the impact region leading to delamination along the 0°/90° and 90°/0° ply interfaces, as well as debonding under the impactor. Rear aluminium cracking and fibre failure corresponded to the drop in peak force, and subsequent load drops were associated with an increase in damage modes. Delamination and debonding continued to increase as the impactor rebounded.

The FE predictions reproduced key failure modes that were experimentally observable during post-impact analysis. The ability of the FE model to accurately analyse the impact event provided insights into the initiation and progression of various damage modes at the ply-level; which is not readily achieved by experimental testing and post-impact observation. In-depth analysis of the induced damage, and in particular, links between damage modes allowed greater understanding of the processes that govern the overall impact resistance of FMLs. Particular emphasis was given to increasing the understanding of the sequence of damage initiation and progression on a ply-based level, which has not been systematically studied before. The modelling methodology is demonstrated to be capable of a high level of accuracy capturing all damage modes to an extent not previously reported in published literature.

CHAPTER 4 : EFFECT OF TENSILE PRELOAD ON THE IMPACT RESPONSE OF FIBRE METAL LAMINATES

ABSTRACT

Following the study of the dynamic response of FMLs subject to low velocity impact presented in Chapter 3, the work described in this chapter aims to investigate the influence of tensile preload on the damage initiation and progression in FMLs subject to low velocity impact. Investigation of the influence of combined tensile preload and impact loading on composites has been extensively studied, however only three publications have considered the effect of preload on the damage response on FMLs. Furthermore, these studies have been limited to experimental investigations from which only basic damage parameters were recorded. In this work, an experimental and numerical investigation is conducted to provide a ply-by-ply insight into the identification, characterisation, sequence and interaction of damage modes that lead to the degradation of FMLs subject to low velocity impact under tensile preload.

Tensile preloading is shown to have a significant influence on the impact response due to the increase in rigidity and overall flexural stiffness of the FMLs, referred to as a 'stiffening effect'. This is evidenced by the decrease in bending deformation of the tension preloaded FML compared to unloaded cases. The contact duration of the impact event decreased as impact-induced stress waves propagate faster under tensile preload, indicating that incipient damage occurs earlier, and more extensive interlaminar and intralaminar damage within the GFRP plies propagate from the impact region. Front crater damage area (BVID) of the FML decreased, while delamination damage area increased linearly with the tension preload level, covering a larger area of the impacted specimen compared to the unloaded case. A downward trend of the energy restitution coefficient indicted that more energy was absorbed by the FML at higher tension preload levels. The FE model is shown to accurately capture the coupling of intralaminar and interlaminar damage modes, and the sequence in which they occur when a FML is subject to combined tensile and impact loading.

4.1 INTRODUCTION

Many studies have been conducted on the impact behaviour of FMLs (as reported in Chapter 2), although most of these studies have been carried out on test specimens under stress-free conditions representing unloaded structures. However, aircraft fuselage and wing structures need to withstand in-plane quasi-static loads up to design limit load, reaching a preload of 4000 με to 6000 με. Hence, foreign body impacts typically occur on loaded aircraft structures which may influence the damage tolerance.

Recent research into the combined effects of impact and preload [28, 29, 141, 145, 152-158] has shown that preload does significantly influence the failure behaviour and damage processes of fibre-reinforced composite panels. The studies found that the preload decreased the impact tolerance and altered the failure modes of composites. As a result, the preload led to earlier catastrophic failure of the laminate. However, limited research into the effect of tensile preload on the impact damage response of FMLs has been published [30, 41, 119]. Therefore, it is essential to investigate the effect of preload on the low velocity impact response of FMLs that closely replicate realistic loading conditions.

Experimental investigations by Vlot [30, 41, 119] showed that the damage shape in ARALL was influenced by tensile preload. Tensile preload caused a higher effective stiffness on the FML specimen and shorter impactor contact duration. In addition, cracking of the aluminium layers in ARALL was reported to grow perpendicular to the preloading direction, thereby increasing the stress concentration of the FML specimen under impact loads. These studies were limited to experimental investigations only. To date, no studies have identified nor characterised the critical failure modes of FMLs under tensile preload using combined experimental and numerical techniques. A gap in research therefore exists to understand the failure processes of tensile preloaded FMLs subject to low velocity impact.

This chapter presents an experimental and numerical investigation into the effect of tensile preload on the low velocity impact response of FMLs. The investigation is conducted on FML 1 2/1-0.4 [Al/0°/90°/90°/0°/Al] test coupons, and a series of parameters including force-time histories, peak force and plastic deformation is evaluated. Particular emphasis is given to characterisation of the damage modes present in the FML through experimental observations and FE predictions.

The aims of this chapter are to:

(i) investigate the influence of tensile preload on the damage initiation and progression of various failure modes in FMLs;
(ii) comprehensively identify and characterise damage modes and the role they play in the degradation of FMLs subject to low velocity impact under tensile preload;
(iii) develop an FE model capable of predicting failure processes on a ply-by-ply level; and
(iv) understand the sequence of failure and the way in which damage modes interact under tensile preload.

4.2 EXPERIMENTAL AND NUMERICAL TECHNIQUES

4.2.1 EXPERIMENTAL SET-UP

A series of impact tests was performed to evaluate the deformation and damage response of FMLs under tensile preload. The experiments were conducted on the FML 1 2/1-0.4 specimen configuration. The instrumented drop-weight impact rig used for low velocity impact testing, as shown in Figure 3.4 and described in Chapter 3, was used with no changes to the impactor and test specimen dimensions. Horizontal hydraulic actuators (50 kN load capacity) capable of applying in-plane loading allowed the FML specimens to be placed under a constant tensile load. Preload was exerted as displacement-control along the long axis of the FML, which was also the 0° fibre direction and rolling direction of the aluminium. The load was held constant during the impact event. Aluminium tabs were bonded on to the ends of each specimen to minimise crushing stresses caused by clamping of the grips. The length of the specimens between the clamps was long enough to assure a uniaxial stress field in the impact region.

Similar to Chapter 3, the overall damage area was measured using a back-illumination technique in order to measure the cumulative delamination of the GFRP plies observed on all interfaces of the FML sample. Delaminations are visible due to the debonding between adjacent plies with different fibre orientations.

This study was designed considering realistic operational loads an aircraft may experience. Aircraft fuselage skins typically experience an operational preload of about 1500 με during their service life, while wing skins can reach peak strains in the region of 3000 με to 4500 με [235]. In addition, tension preload was considered relative to the FML 1 2/1 ultimate tensile strength (σ_{ult} = 272.3 MPa), and was applied in increments of 2000 με (20% of σ_{ult}) up to 8000 με (65% of σ_{ult}). Four different impact energies (5 J, 8.2 J, 12.8 J, 19.5 J) were used by adjusting the impactor drop

height. Tests for each impact energy and tensile preload increment were repeated four times to assess the variability in the impact damage response.

4.2.2 NUMERICAL MODEL

4.2.2.1 GEOMETRY AND BOUNDARY CONDITIONS

The FML 1 2/1-0.4 specimen configuration were modelled to replicate the experimental tests. To account for the tensile preloading at various strain levels using the FE model, prescribed displacement was applied to the FML specimen. The conversion of preload to displacement was done using the following equation:

$$\Delta L = \varepsilon \times L \tag{4.1}$$

where ΔL and L represent the applied displacement and the length of span respectively, and ε is the strain.

Based on the capability of the FE modelling methodology detailed in Chapter 3 to successfully capture all damage modes for unloaded FMLs subject to low velocity impact, the damage modes considered were not changed from those specified in Chapter 3. Preloading conditions were applied as the initial step prior to impact in the FE model.

4.2.2.2 RAMP-UP TECHNIQUE

Preload was applied to the FML model specimen by implementing a preloading step (Step 1) in Abaqus/Explicit. The rate of preload was controlled by using the smooth step definition method defined through the *AMPLITUDE function in order to minimise the inertia effect in explicit analyses, as seen in Figure 4.1. To reduce oscillations and inertia effects during the preloading step, a ‘minimum time’ was determined. The ramp-up portion of the analysis was done over a relatively long time period (t_1 = 3 ms) during which displacements in the longitudinal direction were prescribed. The displacement was then held constant ($t_2 = t_3$) to model uniaxial preloading conditions during impact duration (Step 2).

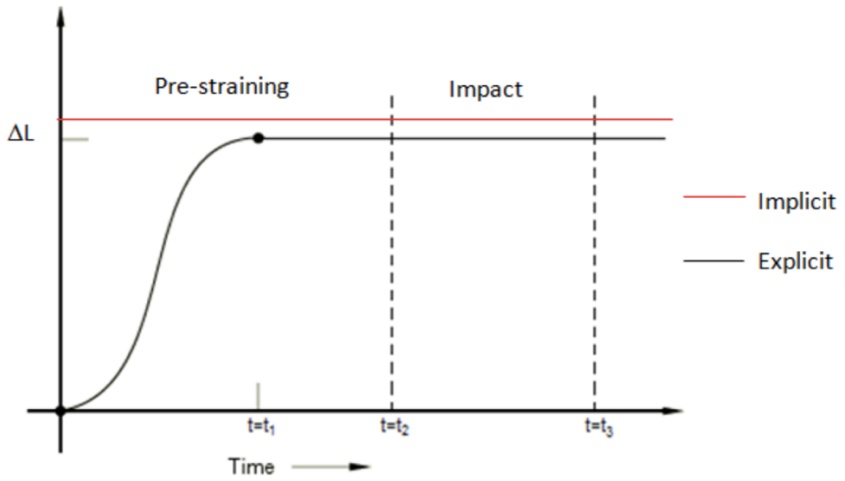

Figure 4.1 Smooth step definition used to apply preload to the FE model of the FML [142].

4.3 RESULTS AND DISCUSSION

4.3.1 DAMAGE MODES

This section provides a description of each of the damage modes identified from the experimental impact tests performed on the FML under tensile preload. Detailed characterisation of a wide range of damage metrics, including the progression of the metrics as the impact energy and preload increase, is given in the following section. A representative summary of the damage modes that was observed experimentally is shown in Figure 4.2 and Figure 4.3, for FML 1 2/1 subject to an impact energy of 19.5 J at tensile preload levels of 4000 με and 8000 με, respectively. Due to C-sectioning across the width (Y-Z plane) of the specimen, matrix cracks are only visible in the 0° direction.

With the introduction of tensile preload, significant impact damage occured to the FML in the aluminium layers in the form of plasticity and to the GFRP plies in the forms of interlaminar and intralaminar damage. It is clear even at lower tensile preloads that the failure mechanisms and the amount of damage was different compared to unloaded impact scenarios. The tensile preload produced a ‘stiffening effect’, which increased the rigidity and flexural stiffness, as evidenced by the decrease in deflection of the impacted FML specimens. At higher tension preload levels, less bending deformation of the impacted FML was observed compared to unloaded cases.

Similar to the unloaded impact conditions, the sequence of damage modes could not be verified experimentally, however the resulting damage modes were linked such that the onset of one damage mode triggered others.

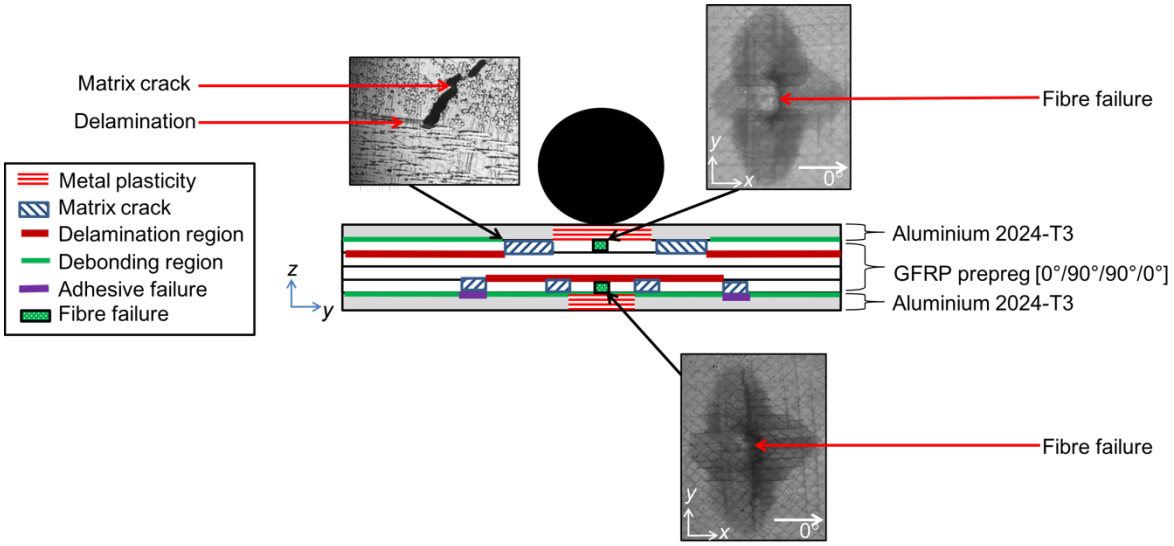

Figure 4.2 Y-Z cross-section of damage mechanisms of FML 1 2/1 impacted at 19.5 J at 4000 με.

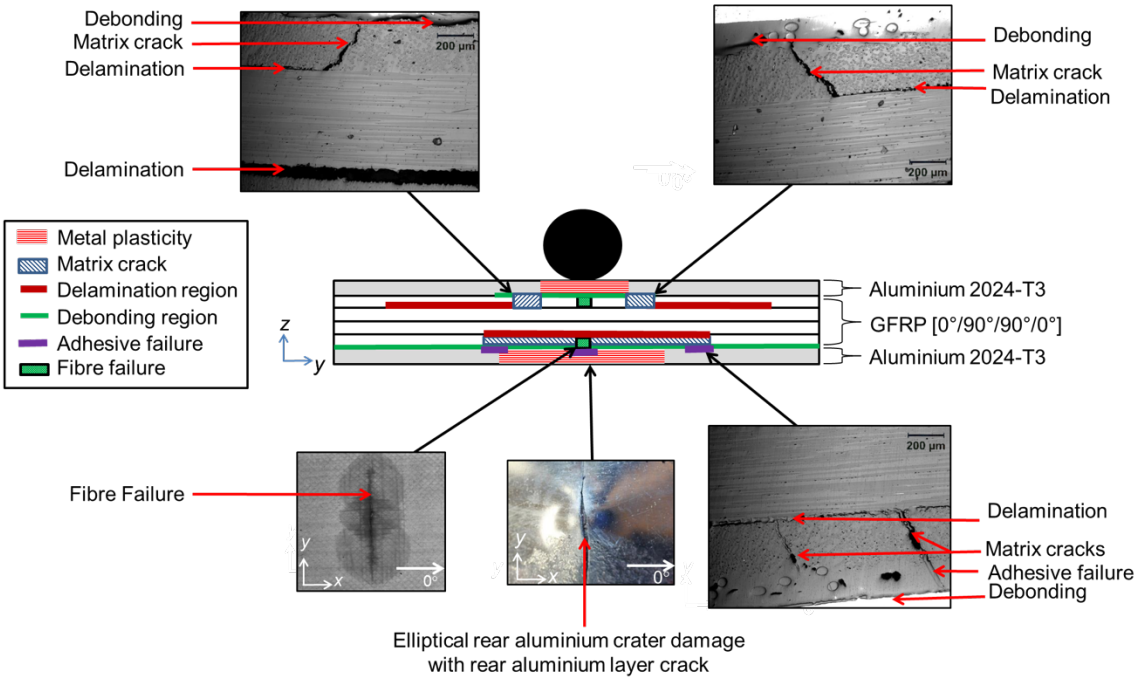

Figure 4.3 Y-Z cross-section of damage mechanisms of FML 1 2/1 impacted at 19.5 J at 8000 με.

Metal plasticity in the form of front and rear crater damage, as well as central permanent deflection was observed. Front crater damage was observed in the form of a localised circular indentation

governed by the impactor shape. The rear crater damage was roughly elliptical in shape. These results are similar to those of an impacted unloaded FML panel. Front and rear hairline cracks were initiated at higher impact energies (12.8 J and 19.5 J) perpendicular to the 0° direction along the longitudinal axis of the panel.

In addition to metal plasticity, interlaminar and intralaminar damage mechanisms were observed in the FML subject to tensile preload. Matrix cracking occurred due to tension stresses within the ply transverse to the fibre direction, and was the primary damage mode for uniaxial tension [236]. Matrix cracks were orientated at an angle from the mid-surface under the edge of the impactor on the inner 0° (Ply 1) and the outer 0° (Ply 4) plies, indicating the role of transverse shear stresses similar to unloaded impact observations. Matrix cracks nucleated other forms of damage, such as delamination, caused by interlaminar shear stresses when the microcrack propagated within the resin-rich region between plies. Fibre failure occurred perpendicular to the 0° directly under the impact region on the impacted side of the FML specimen. Similar to the unloaded specimens, this was due to the high stress and indentation effects caused by shear stresses induced by the impactor.

Delamination occurred at the 0°/90° interface (Plies 1 and 2), initiating from the matrix cracks and extending away from the impact region. In addition, delamination occurred at the 90°/0° interface (Plies 3 and 4), directly under the impact region. Due to the stacking sequence of the GFRP plies in the FML specimen, tensile preloading induced shearing between plies with different orientations. The sum of this shear and the shear due to the impact promoted the increase in delamination damage. The delaminated area had a typical ‘peanut shape’, with its long axis perpendicular to the 0° direction. In addition, at the 90°/0° interface, a roughly elliptical delamination area was observed aligned in the 0° direction. This agrees with literature regarding experimental research of GFRP laminates subject to low-velocity impact, where damage contours in composite layers are usually oriented in accordance with the direction of the bottom layer in a specified interface of composite [27, 237].

In the case of high preload levels, the link between the matrix cracking and delamination was visible, as delamination was seen to propagate from the edges of the matrix cracks. This was due to the reduction in global bending deflection with the application of the tensile preload, allowing local matrix cracks to increasingly occur and thus lateral propagation of the delaminations. With an increase in preload to 8000 με, as seen in Figure 4.3, delamination initiating from the micro-cracks was also observed further from the impact region in the 0°/90° interface (Plies 1 and 2) and 90°/0° interface (Plies 3 and 4), extending nearly the entire width of the specimen. This is credited

to the high interlaminar shear stresses and transverse normal tensile stresses in addition to the increased flexural stiffening effect of the tensile preload.

Minor debonding initiated between the outer aluminium layer and adhesive/GFRP plies. Small cracks in the adhesive were observed on the outer adhesive layer, extending from matrix cracks at the outer 0° ply (Ply 4) adjacent to the impactor. Initiation of debonding between the rear aluminium surface and GFRP laminate is linked to matrix cracking and this debonding region, as it was not the adhesive that failed, but instead the interface between the GFRP ply and adhesive layer. Adhesive failure was more prominent at higher impact energies and higher tensile preload levels, stemming from matrix cracks away from the impactor in the outer GFRP ply (Ply 4).

Fibre failure occurred on the impacted and rear sides of the FML specimen. The latter is particularly important as the tensile preload adds to the tensile bending strains on the non-impacted side of the FML, growing the fibre crack perpendicular to the 0° direction. At high preload levels, fibre failure increased compared to lower preload levels and unloaded specimen, approximately equal to the diameter of the impactor, caused by the addition of the tensile preload and local stresses induced by the impactor.

4.3.2 EFFECT OF TENSILE PRELOAD WITH INCREASING IMPACT ENERGY

The effect of tensile preload on the force-time response produced by low velocity impacts on FML 1 2/1 is shown in Figure 4.4 for low impact energy (8.2 J) and high impact energy (19.5 J) levels. The tension preloads are 4000 με and 8000 με. The experimental curves exhibit oscillations due to dynamic resonances and vibrations between the specimen and support. However, some of the load drops also suggest the possibility of failures in the FML panel caused by the addition of the tensile stress and also the increase in the structural stiffness induced by the application of tensile preload.

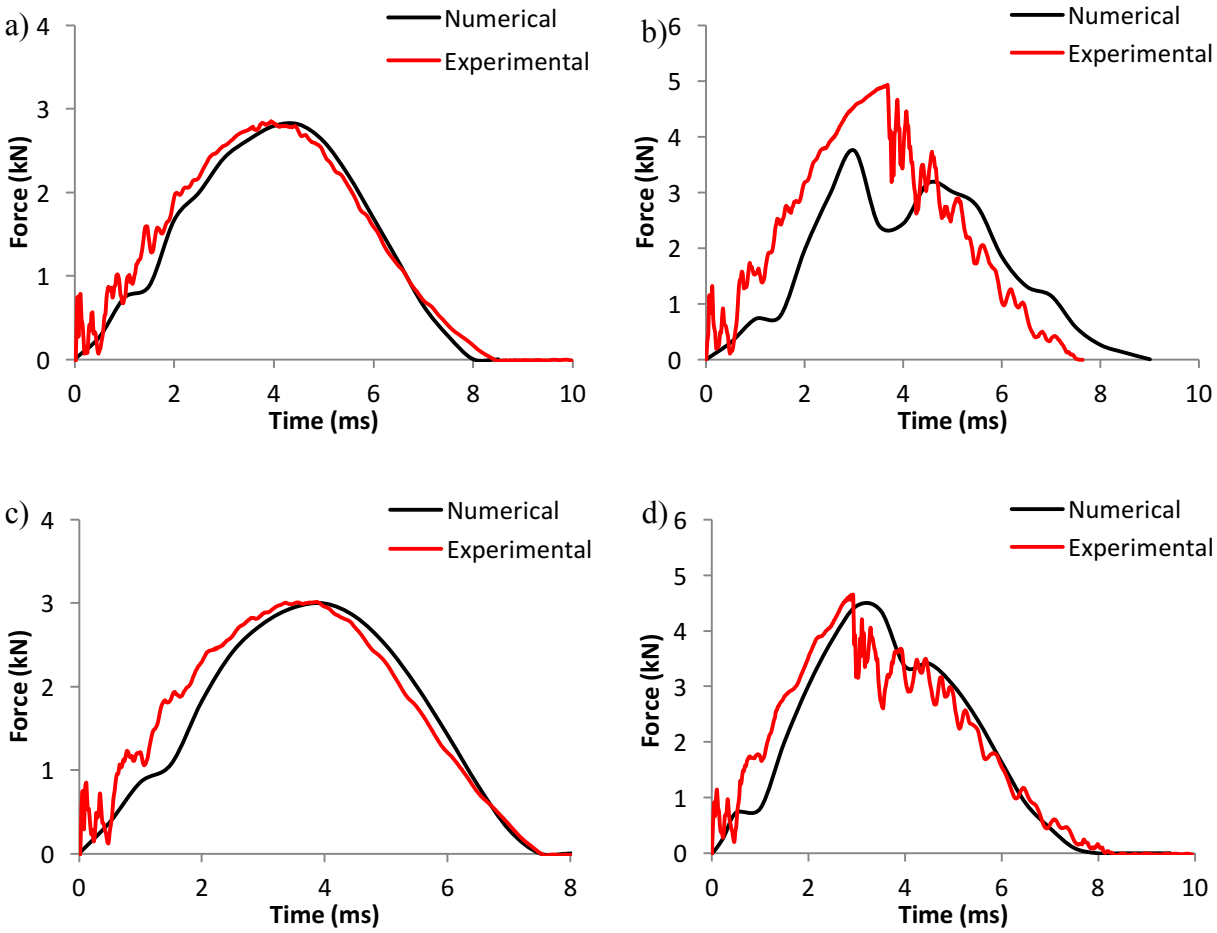

Figure 4.4 Force-time histories for at 4000 με a) 8.2 J, b) 19.5 J and 8000 με c) 8.2 J, d) 19.5 J.

The force-time history for the low energy impacts display a characteristic bell-shaped curve. In contrast to force-time curves for the unloaded case that showed an initial elastic behaviour of the specimen, a sharp load drop occurred at t = 0.5 ms, and a smaller but significant load drop at t = 1.5 ms. While it is difficult to assess the damage initiation through experimental tests, these load drops are likely to be indicative of metal plasticity damage as well as the loss of local rigidity of the FML due to the onset of interlaminar and intralaminar damage. It is important to note that these damage mechanisms were initiated earlier when specimens were preloaded in tension. A thorough analysis of the damage pattern and sequence will be addressed in Section 4.3.4 with the aid of numerical analysis. Overall, at low impact energy, elastic-like behaviour of the FML specimen was observed indicated by the relatively smooth force-time curve to peak force, with only minor plasticity damage to the front and rear aluminium layers. At the higher impact energy, the force-time curves present a similar trend of load drops as for the low energy impacts. The peak force is associated with a sudden drop in force after the initial peak, induced by cracking of the front and rear aluminium layers. In comparison to unloaded cases, the load drop was significantly larger in tension preload which indicates increased damage.

Previous studies [156, 238, 239] into the effect of tensile preload on low velocity impact of composites, including GFRP, reported that the contact duration decreased due to the stiffening effect of the tensile preload. Table 4.1 shows the experimental and numerical contact duration of the combined tension preloading and impact event. An average ~10% and ~8% reduction in the total contact duration of the impact event was measured by increasing the strain from 4000 με and 8000 με at the low impact energy (8.2 J) and high impact energy (19.5 J) respectively. This is believed to occur because the tensile in-plane loads induces a faster response [145]. As such, impact-induced stress waves propagated faster under tensile preload, which helped spread out the impact energy more quickly from the impact point. This was evidenced by a 24% increase in total delamination area, extending beyond the impact point. Kim [142] noted the importance of the relationship between contact duration and preload levels, as the area under the force-time curves represent the impulse energy transferred to the panel during impact.

		No preload (ms)	**4000 με (ms)**	**8000 με (ms)**
8.2 J	Experimental	7.7	8.4	7.5
	Numerical	7.6	8.3	7.5
19.5 J	Experimental	7.7	7.5	7.8
	Numerical	7.2	9.0	7.8

Table 4.1 Experimental and numerical recordings of contact duration of tension and impact tests.

A detailed summary of the experimental results is presented in Figure 4.5, Figure 4.6, Figure 4.7 and Figure 4.8. These figures are explained in detail over the following paragraphs. Figure 4.5 (top left) shows the values of peak force, which is an essential parameter in the evaluation of the FML resistance to dynamic loads. With the introduction of tension preload, an increase in peak load was measured due to the stiffening effect on the FML panel. These results are consistent with those of previous studies [143, 153, 154, 157, 159, 239, 240] for composite plates. The effect of the tensile preload was more prominent at the lower impact energies (5 J and 8.2 J), giving rise to an increase of peak load of 46% and 23% at 5 J and 8.2 J respectively. At higher impact energies, this effect decreased significantly, with no significant increase to the peak load recorded at 12.8 J and 19.5 J. At these higher impact energies, aluminium cracking is initiated, and a threshold is reached such that the FML undergoes increased damage rather than further response from the FML.

Figure 4.5 shows the extent of front (bottom left) and rear (bottom right) crater damage. At low impact energies (5 J and 8.2 J), preload had a minimal effect on the front rear crater damage. However, for FML specimens subject to high impact energy (12.8 J and 19.5 J), the visible front

crater damage area decreased by 20% and 26% from no preload impact to 4000 με tensile preload at 12.8 J to 19.5 J respectively. This again was due to the stiffening effect induced by the tensile preload. A further decrease of 28% and 18% was measured from 4000 με to 8000 με at 12.8 J to 19.5 J respectively. This was due to the stiffening effect brought on by the tensile preload thereby decreasing the flexural deformation of the specimen under impact, as evidenced by a reduction of central permanent deformation

An opposite trend was seen for rear crater damage to the tension side of the impacted specimen, where the damage area doubled from the unloaded case to 2000 με at 5 J, and showed a further increase of 54% between 2000 με to 8000 με. At higher impact energies, an increase of 41% and 6% in rear crater damage area was measured from the unloaded case to 2000 με at 12.8 J to 19.5 J respectively, with a further 17% and 75% between 2000 με to 8000 με respectively.

The central permanent deflection is shown in Figure 4.5 (top right), where in general the deflection decreased with preload. This is observed from experimental and numerical results for all impact energies, and was a result of the increase in panel stiffness with preload. It is interesting to note that the largest decrease in central permanent deflection (or largest increase in stiffness) occurred when moving from no preload to low preload. This effect was noticeably higher at high impact energies, with a 15% and 25% reduction in deflection for 12.8 J and 19.5 J respectively. For lower impact energies of 5 J and 8.2 J the corresponding reduction in deflection was only 7% and 9% respectively. For all impact energies, further increases in preload showed only minor reductions in deflection.

Front and rear cracking of the aluminium layers increased with increasing preload, as seen in Figure 4.6. At high preload levels, a significant increase in front and rear aluminium cracking occurred, with a 150% increase in the rear aluminium cracking from the unloaded impact to 8000 με subject to 19.5 J. This is a result of increased tension strain in the rear aluminium layer of the FML specimen that allowed the crack to open and propagate. Similarly, front aluminium cracking increased by approximately 125% at 8000 με compared to the unloaded case at 19.5 J. This observation supports the finding that significant plastic deformation of the aluminium layers of the FML specimen aids in impact energy absorption.

Figure 4.7 shows the delamination area with increasing preload level, where an increase in interlaminar damage in the GFRP plies was measured. This is due to the interaction between matrix cracking and interlaminar damage, which covered a larger area of the preloaded FML

specimens compared to the unloaded cases. Figure 4.7 shows an approximately linear increase in delamination damage with increasing preload, most notably at the lowest (5 J) and highest (19.5 J) impact energies. The introduction of the tension preload to 2000 με caused an 85% and 45% increase in delamination area for 5 J and 19.5 J respectively. A further increase in tension preload from 2000 με to 8000 με caused a 150% and 73% increase in delamination damage area for 5 J and 19.5 J respectively.

Significant delamination was induced at lower impact energies (5 J) with the application of tensile preload. At this energy level, it is important to note that although the visible impact damage to the exterior aluminium layers of the FML was minor, commonly classified as BVID during inspection, delamination to the GFRP was significant. At 8.2 J, the delamination area was increased by 32% and initiated at both the 0°/90° interface (Plies 1 and 2) and 90°/0° interface (Plies 3 and 4). Although front crater damage and central permanent deflection decreased, the interlaminar and interlaminar damage mechanisms played an important role in energy absorption.

The initiation and evolution of damage modes upon impact allowed the FML specimen to absorb energy; reflected in the downward trend of the energy restitution coefficient, as shown in Figure 4.8. This indicates more energy was absorbed with increasing tension preload. At high impact energies (12.8 J and 19.5 J), the introduction of the tension preload caused a 12% and 15% reduction in the energy restitution coefficient. At high impact energy levels, critical failure modes to the FML occurred such as plastic deformation, fibre failure, adhesive failure and delamination, correlating to a large increase in the absorbed energy values. At a tension preload of 8000 με however, the energy restitution coefficient was similar to that of an unloaded impact case. In the case of high preload level, the large increase in the rear crater damage area as well as front and rear cracking of the aluminium layers constituted a major energy absorption mode.

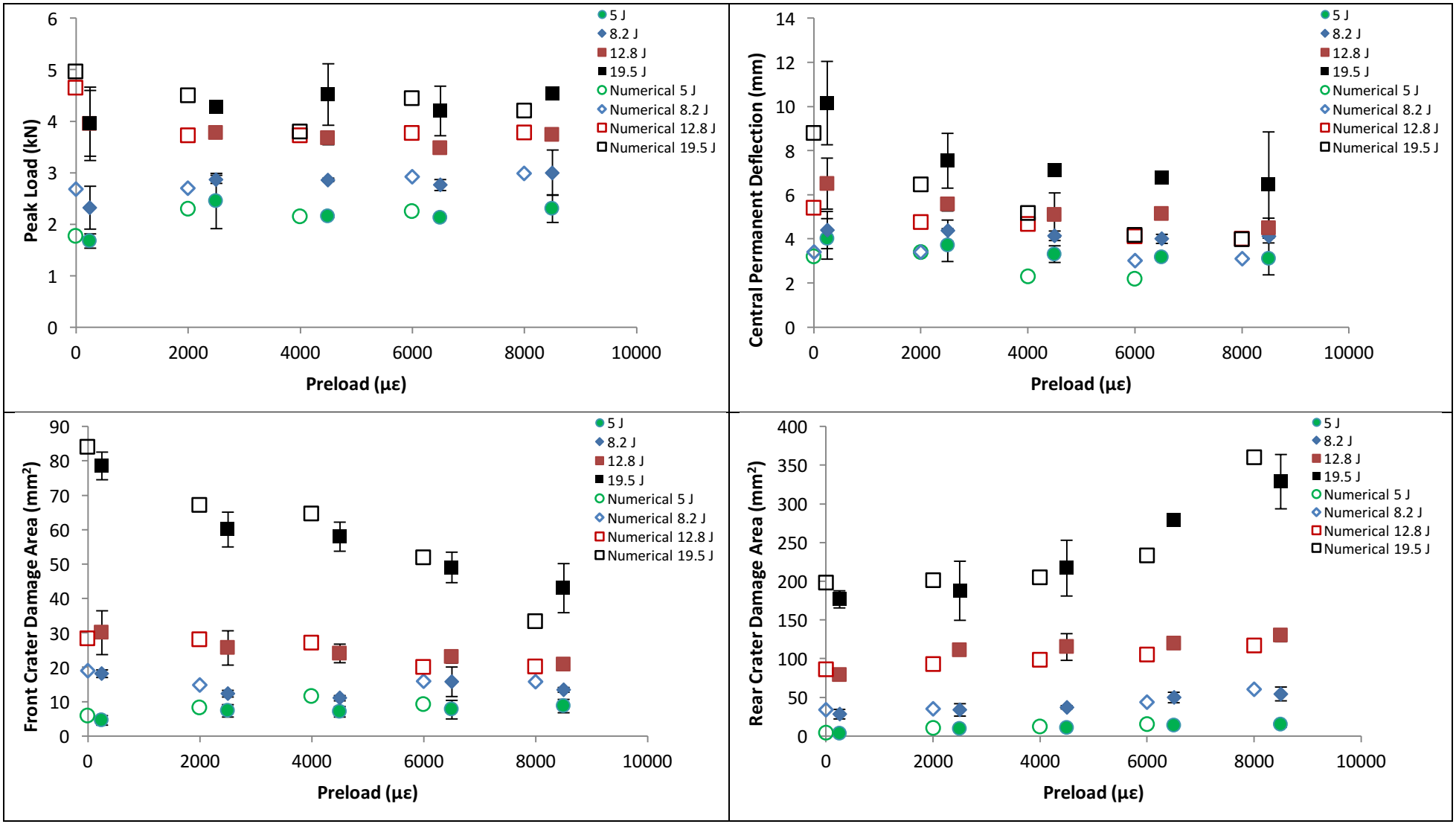

Figure 4.5 Experimental and numerical results with increasing tension preload. For clarity numerical results have been off-set on the x-axis.

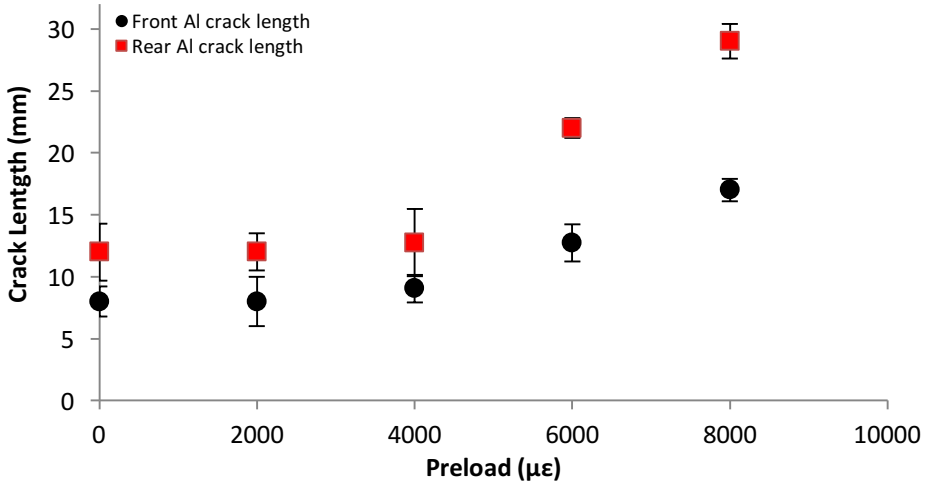

Figure 4.6 Front and rear crack lengths for FML 1 2/1-04 subject to 19.5 J with increasing preload.

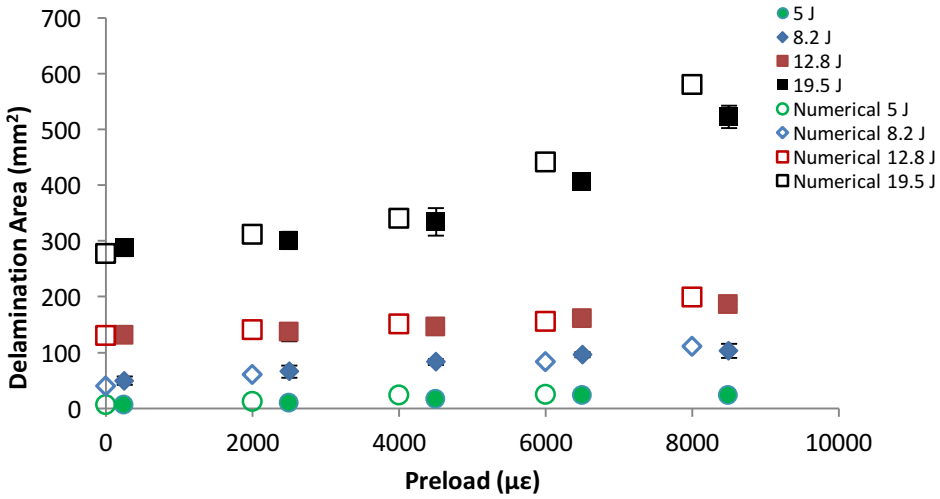

Figure 4.7 Delamination area with increasing tension preload.

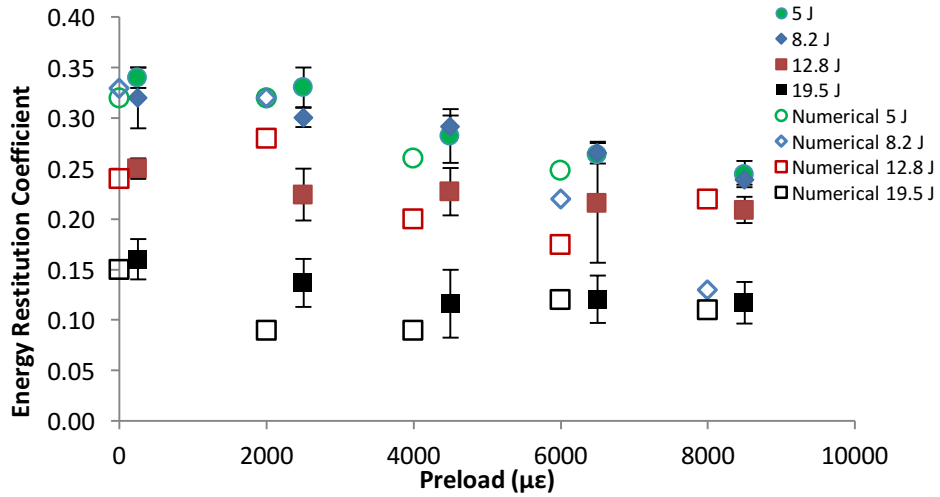

Figure 4.8 Energy restitution coefficient with increasing tension preload.

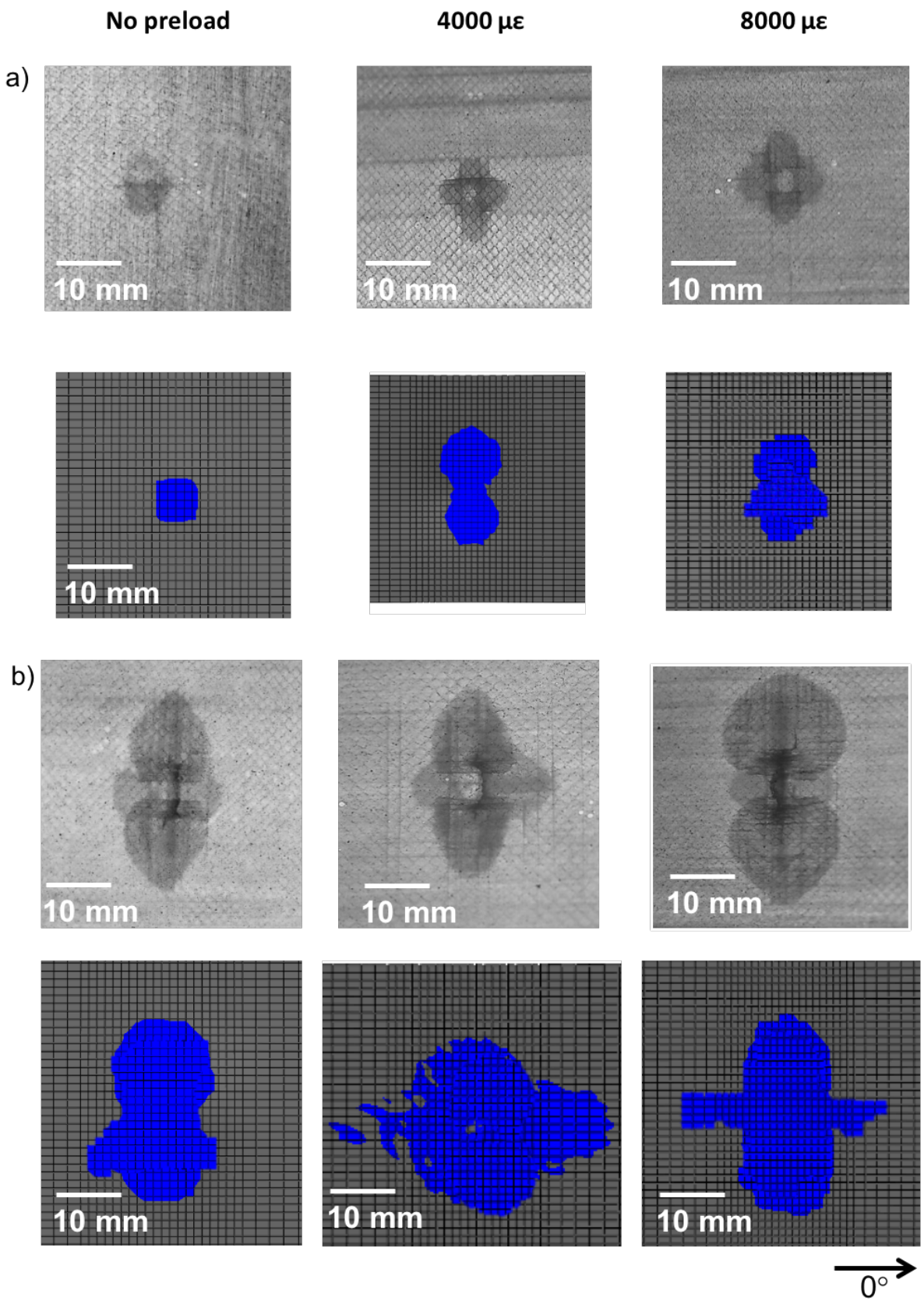

Figure 4.9 Optical microscopy images and FE predictions of the GFRP delamination and fibre failure damage for FML 1 2/1-04 subject to a) 8.2 J and b) 19.5 J with increasing preload.

4.3.3 COMPARISON BETWEEN EXPERIMENTAL AND NUMERICAL RESULTS

A comparison of the experimental results and FE predictions for the critical damage metrics of the FML is shown in Figure 4.4 to Figure 4.9. For ease of comparison, the FE predictions in Figure 4.5, Figure 4.7, and Figure 4.8 have been slightly off-set on the x-axis. Overall, the FE predictions show high degree of accuracy with the experimental results, and are within the experimental error. The effect of tension preload on the impact response of FML 1 2/1 was accurately analysed, showing a good agreement with all damage metrics.

Force-time histories (Figure 4.10) showed good correlation between experimental measurements and FE predictions. At low impact energies (5 J and 8.2 J) shown in Figure 4.4a and Figure 4.4c, the FE model accurately replicated the bell–shape of the force-time curve and the initial load drop at approximately t = 1.5 ms. At high impact energies (12.8 J and 19.5 J) shown in Figure 4.4b and Figure 4.4d, the model accurately simulated the sharp load drop immediately after peak force was reached, which is characteristic of cracking to the aluminium layers due to stiffness degradation. It is interesting to note that due to the increased bending stiffness of the FML specimen from the tensile preload, the FE force-time histories showed a decrease in oscillations compared to an unloaded specimen.

The FE predictions under-estimated the central permanent deflection by approximately 10%. Front and rear crater damage were predicted, once again demonstrating the capability of the FE model to analyse plastic deformation to the aluminium layers of the FML. However, the FE model did not explicitly capture the initiation and growth of cracking to the aluminium layers that was observed in the experimental analysis, and instead this region is represented as an area of plasticity and associated material softening.

FE predictions of delamination damage are compared to experimental observations in terms of size, area, shape and location in Figure 4.9. The FE model over-predicted slightly the size of internal damage (by 9%), although the shape of the delamination area was captured well. The analysis of delamination area shows that the significant increase in delamination area under the impactor was accurately predicted using the FE model at both the 0°/90° interface (Plies 1 and 2) and 90°/0° interface (Plies 3 and 4). At high impact energies and high tension preload, the model under-predicted the delamination area at the 90°/0° interface (Plies 3 and 4).

The FE model predicted most damage metrics and damage mechanisms, and captured all qualitative trends.

4.3.4 DAMAGE PATTERN AND SEQUENCE

As demonstrated in Chapter 3, the FE model allows for detailed ply-based analysis of the various damage modes for FMLs. Until now, limited research has been done to analyse the ply-by-ply damage that initiates in impacted FML specimens under tensile preload. Moreover, no research has been conducted to characterise the effect of tensile preload on the sequence (damage initiation and progression) of failure modes upon impact, and the interaction of these failure mechanisms.

Figure 4.10 shows the force-time curves of FML 1 2/1 subjected to low (8.2 J) and high (19.5 J) energy impact at 4000 με and 8000 με preload. The graph is annotated with key points indicating the initiation of damage in each ply (P) from the front (1) to the rear (4) ply that correlated to the numerically predicted failure contours of each GFRP ply and ply interface.

The FE model allows a ply-by-ply analysis in order to investigate the sequence of damage with respect to the force-time history. Analysis of the stress distributions on a ply-level give insight into the influence of preload on the formation and propagation of flexural waves that govern the impact response and influence the damage mechanisms. Schueler et al. [241] studied the effects of tensile preloads on the high velocity impact response of composite plates and concluded that the deformation behaviour is affected by stress stiffening, with a non-linear geometric effect that leads to an increase in the out-of-plane stiffness when in-plane tensile stress is applied. Using this theory in a preload and impact scenario, the flexural waves generated by the impact are smaller in amplitude but move more rapidly through the FML panel.

Similar to the unloaded case, the initiation of metal plasticity is the first damage mode to occur when the impactor makes contact with the FML specimen. At this time step, a difference in the plastic strain on the rear aluminium layer is already calculated at 4000 με and 8000 με preload levels, and later result in an increase in rear crater damage area at higher preload levels.

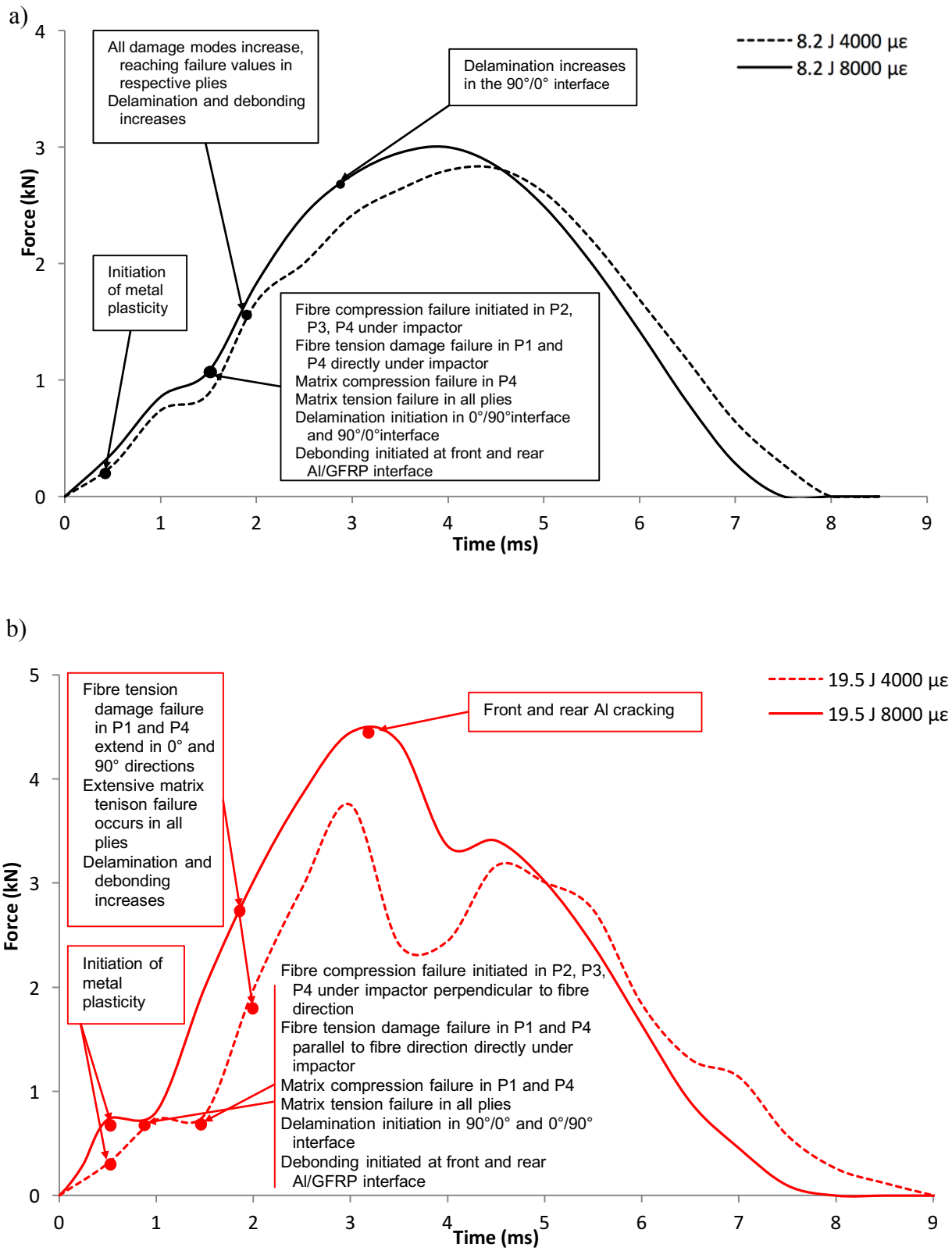

Figure 4.10 Force-time histories of predicted initiation and failure of damage modes of FML 1 2/1 subject to tensile preload of 4000 με and 8000 με at a) 8.2 J and b) 19.5 J.

Figure 4.11 and Figure 4.12 show the ply-by-ply FE prediction of the final failure contours for each of the GFRP plies and ply interfaces impacted at 8.2 J at 8000 με. At t = 1.5 ms, all damage modes within the GFRP layers are triggered including matrix cracking, fibre failure, delamination, and debonding of the metal/GFRP interfaces. This is indicated in the force-time curve by the significant load drop. As described above, damage occurs sooner as the impact waves propagate faster under tensile preload compared to unloaded specimens. This is evident when comparing the force-time curves of 4000 με and 8000 με, as seen in Figure 4.10, whereby at higher preloaded levels, the contact duration was reduced by 6% and 4% at impact energies of 8.2 J and 19.5 J respectively.

At low impact energies (8.2 J) subject to the highest tensile preload of 8000 με at this time step, fibre compression failure was initiated (damage index > 0) in Ply 2, Ply 3 and Ply 4 directly under the impact region, however does not reach the critical failure value (damage index = 1). Fibre tension damage in the 0° plies (Ply 1 and Ply 4) was initiated, leading to fibre failure directly under the impact region. Additionally, matrix compression failure was initiated in the 0° plies. Matrix tension failure occurred in all GFRP plies, corresponding to experimentally detected cracking in the 0° plies (Ply 1 and Ply 4). Delamination was predicted using the FE model to initiate at the 0°/90° and 90°/0° ply interfaces. This correlates with experimentally observed post-damage inspection showing delamination damage along the 0°/90° interface (Plies 1 and 2), initiating from the micro-cracks and extending away from the impact region and 90°/0° interface (Plies 3 and 4). The FE model also predicted debonding at the front and rear Al/GFRP interfaces. In comparison to the unloaded specimens analysed in Chapter 3, damage occurred sooner as the impact waves propagated faster under tensile preload.

Following this, at t = 2 ms all damage modes increased, reaching failure values (damage index = 1, corresponding stiffness properties completely reduced) in their respective plies. Delamination increased at t = 3 ms at the 90°/0° ply interface. At t = 3.5 ms, the impactor reached its maximum indentation depth, corresponding to the peak force being reached on the force-time curve. Plastic strain to the front and rear aluminium layers increased directly below the impactor agreeing with front and rear crater damage. The force-time curves were relatively smooth indicating an elastic response to the impact without aluminium cracking. No further damage or failure progression occurred as the impactor rebounded and lost contact with the FML surface.

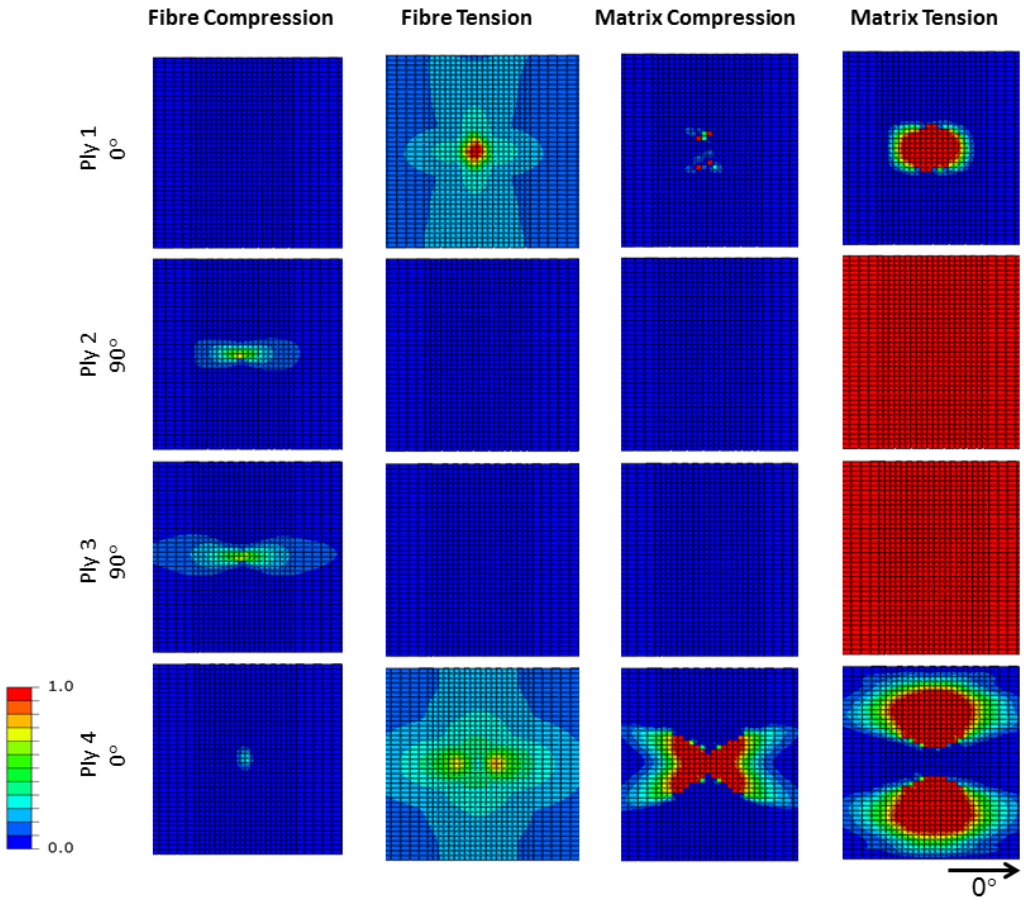

Figure 4.11 Numerically predicted damage contours of FML 1 2/1-0.4 impacted at 8.2 J at 8000 με.

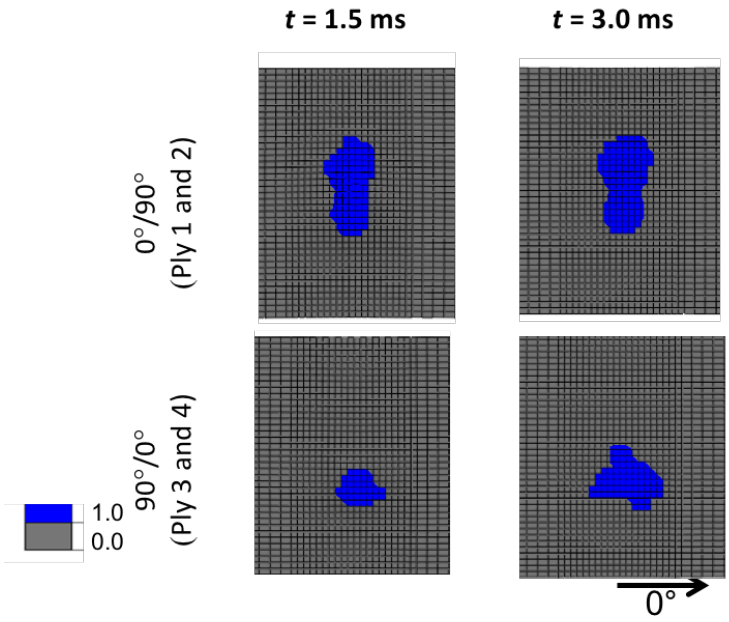

Figure 4.12 Numerically predicted delamination contours of FML 1 2/1 impacted at 8.2 J at 8000 με.

Figure 4.13 and Figure 4.14 show the numerically predicted ply-based damage contours at high impact energies (19.5 J) subject to a preload of 4000 με and 8000 με, and the predicted delamination at 8000 με respectively.

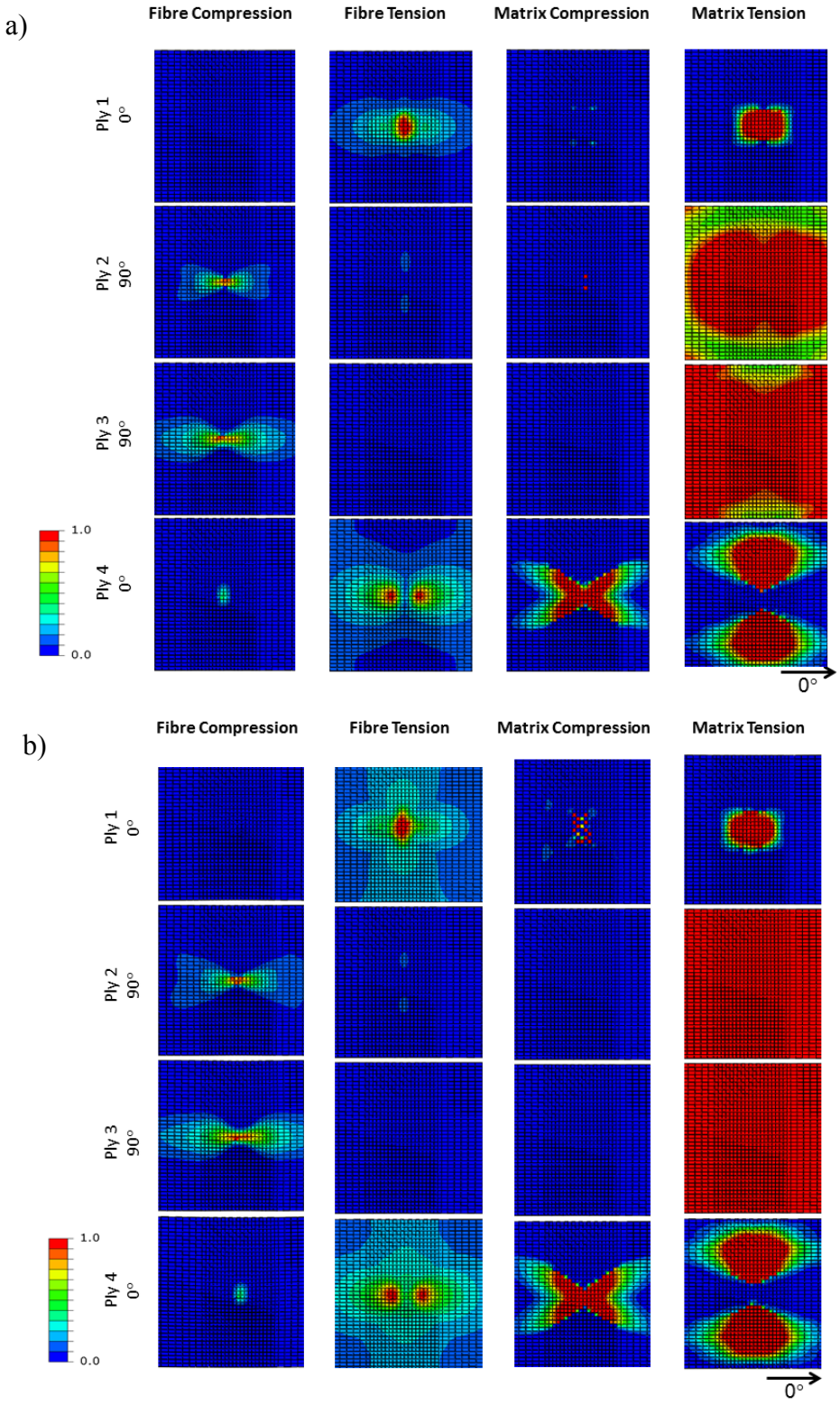

Figure 4.13 Numerically predicted damage contours of FML 1 2/1-0.4 impacted at 19.5 J at a) 4000 με and b) 8000 με.

It is clear that the damage modes were more widespread, and developed much earlier compared to an unloaded impact due to a higher peak force (14%) and shorter contact time (6%) which was induced by the stiffening effect of the FML specimen under tensile preload.

At t = 0.5 ms after initiation of impact, high plastic strains were predicted directly under the impactor. At this time step, permanent deformation damage occurred on the surface of the aluminium layers of the FML. The FE predictions showed that with an increase in preload, there was no significant increase in the plastic strain on the front aluminium. However, plastic strain on the rear aluminium surface increased with the preload level. This agrees with the experimentally observed measured increase in rear crater damage area with increasing tensile preload.

At t = 1.0 ms, a similar trend of damage initiation occurred at high impact energies, as was predicted at lower impact energies. At high preload levels, the main differences were that matrix compression initiated in both 0° plies (Ply 1 and Ply 4), and delamination occurred at both ply interfaces (0°/90° and 90°/0° ply interface). Debonding was initiated at the front and rear Al/GFRP interfaces. Figure 4.10 showed that damage was initiated earlier at high preload levels (8000 με) when compared to lower preload levels (4000 με), reflected in a drop in the force-time curve. As described previously, this was due to the impact-induced stress waves that propagated faster under tensile preload, helping to spread out the impact energy.

At t = 2 ms after impact initiation, extensive matrix tension failure occurred in all plies corresponding to matrix cracking that extended beyond the impact region. Similar to the unloaded impact conditions, it can be concluded that before the FML panel reached its maximum displacement, matrix cracking was a significant form of damage in the GFRP plies, extending beyond the visible crater damage. At high tension preload levels, this damage was predicted using the FE model to initiate earlier. With an increase in preload level to 8000 με, fibre tension failure in the P1 and P4 extended in the 0° and 90° directions. These predictions correlate to the fibre failure found in the experimental studies. Delamination and debonding lengths were also predicted to increase.

The impactor reached its maximum penetration depth and thus peak load at t = 3 ms and t = 4 ms for 4000 με and 8000 με respectively, as represented by the large load drop in the force-time curves. High tensile stresses were predicted in the rear aluminium layer using the FE model. This caused the rear aluminium layer to crack perpendicular to the 0° direction, as experimentally

observed. Debonding was predicted to increase, particularly between the rear aluminium and GFRP layers.

By comparing the FE predictions of the damage modes, there was an increase in some damage metrics with increasing tensile preload, primarily the matrix cracking in the 90° plies that induced extensive delamination and debonding regions, which were larger than the visible front and rear crater damage. Fibre tension also increased correlating to the increased fibre failure lengths in the 0° plies.

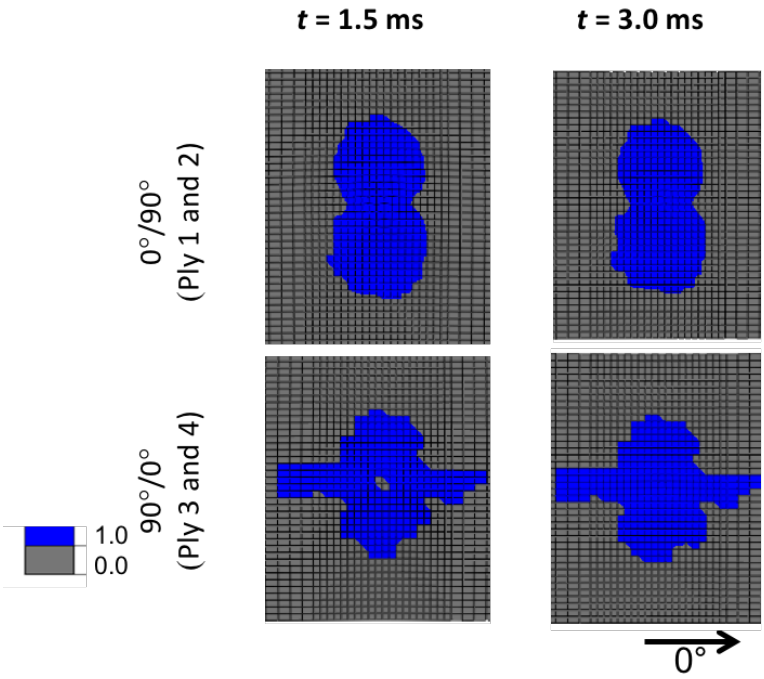

Figure 4.14 Numerically predicted delamination contours of FML 1 2/1 impacted at 19.5 J at 8000 με.

4.4 CONCLUSION

Tensile preloading has a strong influence on the impact response of FML specimens, and therefore should be considered in relevant structures and load cases. This is of particular interest due to the tendency of impact to produce internal damage with little or no exterior visibility (ie. BVID), as can be seen by the downward trend of front crater damage area with an increase in tensile preload. In addition, the resulting interlaminar and intralaminar damage is observed to propagate away from the impact region, leading to a decrease to the structural integrity of an aircraft structure.

An experimental and numerical investigation was conducted to evaluate the influence of tensile preload on the damage initiation and progression in FMLs subject to low velocity impact. This

chapter provided a ply-by-ply insight into the identification, characterisation, sequence and interaction of damage modes and the role they play in the degradation of FMLs subject to low velocity impact under tensile preload.

Upon the application of tension preload, the rigidity of the FML specimen increased giving rise to a 'stiffening effect', whereby the overall flexural stiffness of the panel was increased, as evidenced by the decrease in deflection of the impacted structure. With an increase in preloading, the stiffness of the specimen increased leading to less bending deformation of the FML compared to unloaded cases. This reduced the contact duration both experimentally and numerically as the impact-induced stress waves propagated faster under tensile preload, thereby spreading out the impact energy more quickly from the impact region.

Experimental results and FE predictions showed that damage modes included plastic deformation, aluminium cracking, debonding of the aluminium and GFRP/adhesive interface, adhesive failure, as well as interlaminar and intralaminar damage of the GFRP plies. As a result of the stiffening effect of the tension preload, the peak force increased whereas the contact times and deflection decreased when compared to an FML specimen without preload. Although rear crater damage, rear aluminium cracking and delamination increased with the tensile preload level, particularly for high impact energies (12.5 J and greater), the amount of front crater damage decreased.

The FE model showed excellent agreement with experimental measurements, and accurately captured the damage to the GFRP plies, allowing detailed insight into the sequence and interaction of interlaminar and intralaminar damage modes, otherwise impossible to identify through experimental tests. The FE predictions replicated the experimentally observed failure modes, damage location and severity. The FE model fills a gap to provide better understanding of the increase in complexity of damage modes induced by the addition of tensile preload, and the sequence of damage initiation and progression.

The research presented in this chapter has made a number of original contributions to the existing body of knowledge on the impact response of FMLs:

(i) Characterise the experimentally observed phenomena and key failure mechanisms of tensile preloading, and the role it plays in the degradation of FMLs subject to low velocity impact.
(ii) Utilisation of the validated FE modelling methodology to study the influence of increasing tensile preload on the damage initiation and progression of FML subject to low velocity

impact on a ply-based level. Provide insight into the sequence of failure and interactions between damage modes, previously not studied in-depth before.

CHAPTER 5 : EFFECT OF COMPRESSION PRELOAD ON THE IMPACT RESPONSE OF FIBRE METAL LAMINATES

ABSTRACT

Previously published research has shown that an applied axial compressive preload can have a significant influence on the failure behaviour and damage processes of fibre-reinforced composite panels. However, the effect on the impact response of FMLs has not been investigated. A gap in research therefore exists to investigate the effect of compression preload on the response of FMLs subject to low velocity impact.

In this study, compressive preload is applied to FMLs in increments of 2000 με (50% of critical buckling load of the FML specimen, P_{cr}) up to 8000 με (170% of P_{cr}) to account for aerospace structures that operate near their critical buckling load or even in the post-buckling region. Compressive preloading led to a "softening effect" that reduced the overall flexural stiffness of the FML, evidenced by the increase in deflection of the impacted material. Rear crater damage increases significantly with the introduction of compressive preload. The initiation and propagation of the rear aluminium crack was also measured and closely related to the resulting rear crater damage. As the impact energy increased, the compressive preload level needed to initiate a rear crack decreased. Plastic deformation of the aluminium layers of the FML was identified as a key energy absorbing damage mode, evidenced by the downward trend of the energy restitution coefficient with increasing preload levels. In addition, interlaminar damage in the form of extensive delamination and intralaminar damage (matrix cracking) appeared to be more localised, occurring directly under the impact region. Fibre failure on the back surface also occurred due to the "softening effect" induced by the compressive preload. Propagation of delamination was higher for preloaded specimens, extending beyond the visibly detectable damage in the front aluminium layer.

A reduction (~40% decrease compared to the unloaded case) in the contact duration was found both experimentally and numerically as the impact-induced stress waves propagated faster under

the compressive preload, helping to spread out the impact energy quickly from the impact region. All damage mechanisms were shown to be induced soon after initiation of impact.

This chapter assessed the critical failure modes through experimental and numerical studies by providing a ply-by-ply insight into the identification, characterisation, sequence and interaction of damage modes of the FML structure that led to the degradation of FMLs subject to low velocity impact under compressive preload. The FE model yielded accurate and consistent results with respect to predicting the presence, location, and extent of all critical failure modes.

5.1 INTRODUCTION

Aircraft structures under compression loading are commonly exposed to low velocity impact threats, often generated by impacting stones propelled by the tires. Similar to all BVID, damage can be difficult to detect during routine visual inspections and it may propagate undetected leading to structural failure, particularly under compressive loads. Therefore, there is strong interest in investigating the influence of compressive preload on the impact response of aerospace structures. According to Nettles [242], compression preloading is of greater concern than tensile preloading as damaged composites are more susceptible to compressive failures, especially when considering damage in the forms of debonding and delamination which can lead to premature buckling.

Many researchers [28, 145, 146, 150, 154, 157, 159, 242-250] have studied the effect of compression preload on the impact response of laminated composites. These studies have reported that interlaminar and intralaminar damage are key failure mechanisms, including delamination, matrix cracking and fibre breakage that lead to significant reductions in the residual strength and stiffness. These damage mechanisms are made further complex due to plate buckling, particularly in the case of relatively thin composite structures. Chiu et al. [157] showed that the introduction of a compressive preload decreases the flexural stiffness of a composite plate leading to an increase in deflection that increases delamination.

Compressive preloading conditions are critical as plate buckling becomes an issue for thin FML structures. The application of compressive preload leads to a “softening effect” on structural stiffness (observed by global deflection), resulting in a severe dynamic panel response in the form of stress waves and global deflection compared to an unloaded panel [159]. The higher bending deformations, may induce delamination damage, and act in combination with buckling-driven deformation.

There is currently a scarcity of research on the effect of compressive preloading on the impact response of FMLs. It is expected that the impact behaviour of FMLs will have a greater complexity than laminated composites due to the number of different failure modes in and between the individual constituents, as well as interaction between the damage mechanisms. To date, no studies have identified and characterised the damage to FMLs subject to combined impact and compression preload. Moreover, no work has been done to investigate how compressive preload affects the sequence of damage initiation and damage propagation.

Therefore, a need exists to study the influence that compressive preload has on the impact response of FMLs, and how this loading may alter the failure modes. In the present work, FML 1 2/1-0.4 [Al/0°/90°/90°/0°/Al] test coupons were used for the experimental testing and numerical simulation.

By utilising the validated FE model described in Chapters 3 and 4, it is possible to characterise and understand the parameters that govern the impact mechanics of compression preloaded FML structures to complement the experimental results.

The aims of this chapter are to:

(i) investigate the influence of compressive preload on the structural response and failure modes of FMLs subject to low velocity impact;
(ii) understand the sequence of damage initiation and propagation in the individual constituents of the FML, as well as the interaction between failure modes;
(iii) characterise the impact damage modes on a ply-by-ply level.

5.2 EXPERIMENTAL AND NUMERICAL MODEL

5.2.1 EXPERIMENTAL METHODOLOGY

In this study, a benchmark FML 1 2/1-0.4 specimen was preloaded under uniaxial compression until plate buckling was detected by analysing the strain gauge data. The experimental results (shown in Figure 5.1) were compared to analytical calculations as well as the critical buckling load for FMLs reported in literature. In this specific case, the critical buckling load, P_{cr} was 8.91 kN for the FML 1 2/1 specimen. Similar buckling loads were reported by Remmers and de Borst [251] and Remmers [252].

Compression preload was considered as a fraction of ultimate load and buckling load of the FML,

and was applied in increments of 2000 με (0.5 P_{cr}) up to 8000 με (1.7 P_{cr}). While the investigated compression preload range is admittedly wide, some aerospace structures operate near their critical buckling load or even in the post-buckling region. It was concluded that due to the lack of published research, there is a need to study the effect of higher preload. An example of this is runway debris hitting aircraft wing skins that can experience peak strains in the region of 3000 με to 4500 με [235].

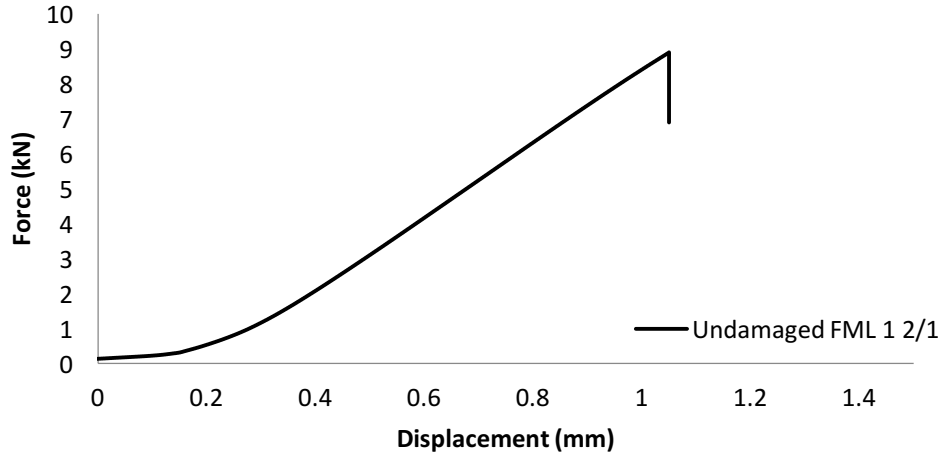

Figure 5.1 Experimental load-displacement curve for FML 1 2/1 under uniaxial compression.

Figure 5.2 illustrates a Y-Z cross-section of the experimental setup for the combined impact and preload testing, including the removable anti-buckling rig. A central circular cut-out (diameter of 40 mm) was cut from the anti-buckling rig, exposing an adequate target area of the FML test specimen to the impactor.

A specially designed anti-buckling test rig that allowed for uniaxial compressive preloading of the FML specimens was used. The lateral ends were simply supported at the front and back surface via rounded steel supports providing a linear contact located 10 mm from the specimen edges. These supports restrict any translation of the specimen along its normal direction but enable its rotation along the length axis. The specimen length between the clamps was long enough to assure a uniaxial stress field in the impact region which was unaffected by end restraint conditions. Compression preload was exerted as displacement control along the long axis of the FML (0° fibre direction and rolling direction of the aluminium) and held constant during the impact event.

The instrumented drop-weight rig as described in Chapter 3 was used for low velocity impact testing. For direct comparison to the unloaded FML impact experimental tests presented in Chapter 3, the same impact energy levels were used. Minor adjustments were made to the length

of the specimen to accommodate the anti-buckling rig with no changes to the impactor dimensions, as shown in Figure 5.2. Aluminium tabs were bonded to the longitudinal ends of each FML test specimen in order to minimise crushing stresses caused by clamping of the grips.

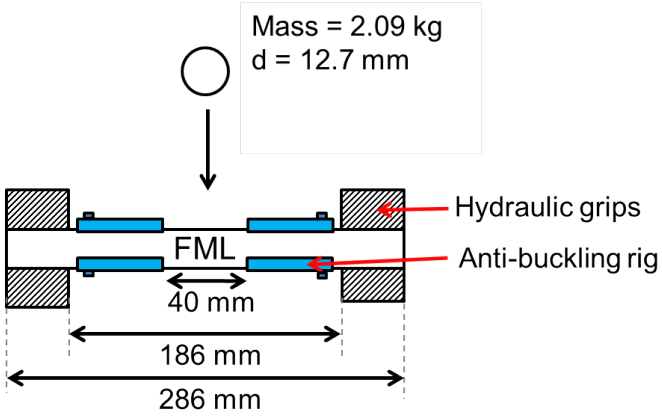

Figure 5.2 Y-Z Cross-section of the experimental setup including anti-buckling rig.

5.2.2 FE MODELLING

The boundary conditions of the FE model were adjusted to account for the anti-buckling rig. Due to the linear contact of 10 mm from the specimen lateral edges, simply supported boundary conditions were applied at the lateral ends of the FE specimen, and fully constrained nodes at the longitudinal ends.

Compressive preloading was performed within the Explicit calculation step by implementing the Ramp-Up technique in Abaqus/Explicit, as described in Chapter 4.2.4. This approach was used to avoid oscillations, but has a relatively expensive computational cost ascribed to the preloading step.

5.3 RESULTS AND DISCUSSION

5.3.1 DAMAGE MODES

In this section, post-test damage assessment of the FML specimens was performed, and descriptions of each of the damage modes are identified. Later sections detail the damage characterisation and progression of impact damage with increasing compressive preload.

Metal plasticity to the aluminium layers in the form of front and rear crater damage was found to be localised directly under the impactor. Front crater damage was localised directly under the impact region in a roughly circular shape. Rear crater damage was elliptical in shape with its long axis along the 0° direction (rolling direction of the aluminium). This is different to the direction of rear crater damage in the unloaded FML, as described in the previous chapter. An example of metal plasticity to the front and rear aluminium layers of the impacted FML at 19.5 J with compressive preload of 8000 με is presented in Figure 5.3a and b respectively. Cracking of the aluminium layer of the FML is initiated at a lower impact energy (8.2 J) under compressive preloading compared to the unloaded case where aluminium cracking was first recorded at 19.5 J.

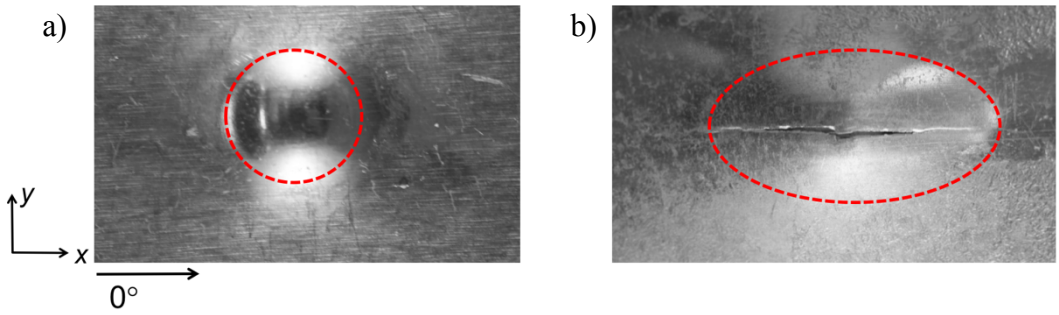

Figure 5.3 Metal plasticity to the a) front (circular shape) and b) rear (elliptical shape) aluminium layers of the impacted FML at 19.5 J with compressive preload of 8000 με.

In order to inspect the interlaminar and intralaminar damage mechanisms, Y-Z cross-sections of the impacted FML specimens subject to compression preload were considered, as shown in Figure 5.4 and Figure 5.5 for FML 1 2/1 impacted at 8.2 J and 19.5 J subject to 8000 με respectively. Due to C-sectioning across the width (Y-Z plane) of the specimens, matrix cracks are only visible in the 0° direction. Localised internal matrix cracks in the outer 0° ply (Ply 4) at the boundary of delamination at the 90°/0° interface (Plies 3 and 4) of the FML were observed, further evidence of the "softening effect" of the compressive preload, in contrast to a stiffening effect of the tensile preload. This corresponds to results that were also reported in other studies that look into CFRP laminates [253, 254]. At higher preload levels, matrix cracks initiate other damage modes, such as adhesive failure, which can be seen to be an extension of the matrix cracks. Adhesive failure is more prominent at higher impact energies, stemming from matrix cracks in the outer GFRP ply (Ply 4). Debonding was significant at higher impact energies, as a large debonding region formed between the rear aluminium layer and GFRP/adhesive layer.

At lower impact energies (5 J and 8.2 J), fibre failure was detected in the outer 0° ply (Ply 4), similar to that of the unloaded case. However, under compressive preloading, fibre failure was

more prominent (longer in length) compared to the unloaded case. At higher impact energies (12.8 J and 19.5 J), fibre failure length was approximately the same length as the rear aluminium crack on the non-impacted side of the impacted FML.

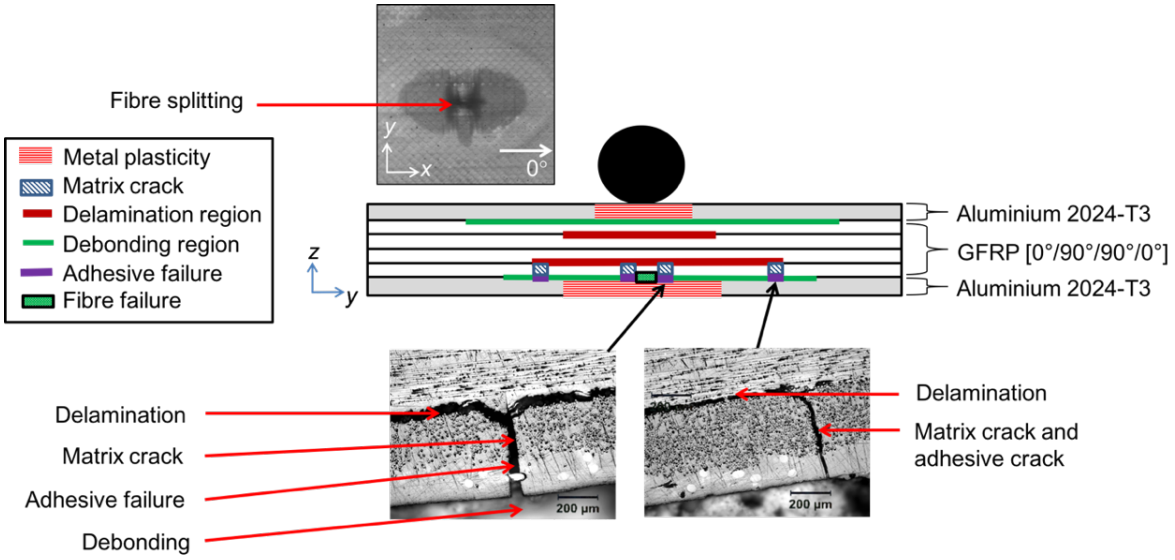

Figure 5.4 Y-Z cross-section of damage mechanisms of FML 1 2/1 impacted at 8.2 J with compressive preload of 8000 με.

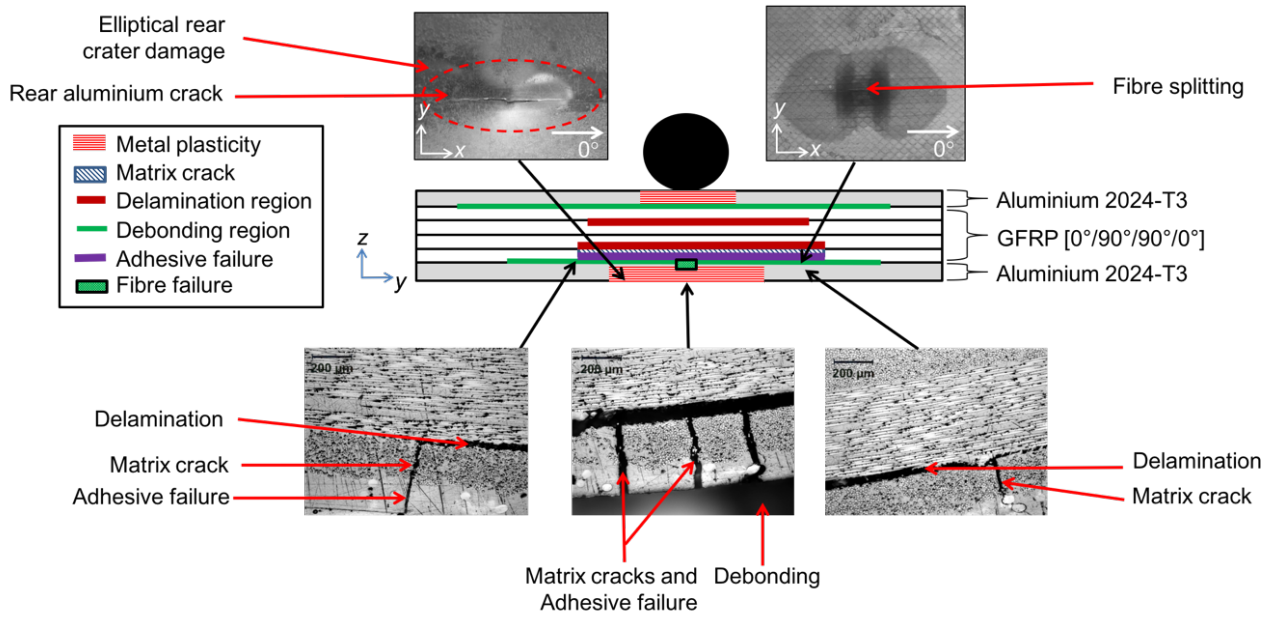

Figure 5.5 Y-Z cross-section of damage mechanisms of FML 1 2/1 impacted at 19.5 J with compressive preload of 8000 με.

Delamination forms in a typical peanut shape occurring in the 90°/0° interface (Plies 3 and 4). As the compressive preload increases to 8000 με, delamination is initiated directly under the impactor in the 0°/90° interface (Plies 1 and 2).

Debonding can be seen to be extensive between the top and bottom aluminium layers and adhesive/GFRP plies. Small cracks in the adhesive layer propagating from matrix cracks in the outer 0° (Ply 4), led to the initiation of debonding region between the outer aluminium layer and adhesive, extending nearly the width of the specimen, and significantly wider compared to the debonding in the upper region of the specimen (impact side).

At a compressive preload of 8000 με, fibre failure was observed in the outer 0° (Ply 4), typically representative of the onset of delaminations and/or matrix cracks. The fibre splitting failure was orientated in the 0° (rolling direction of the aluminium), associated to the aluminium cracking on the non-impacted side of the FML specimen.

5.3.2 EFFECT OF COMPRESSION PRELOAD WITH INCREASING IMPACT ENERGY

The influence of compressive preload on the force-time response of the FML at low impact energy (8.2 J) and high impact energy (19.5 J) at preload of 4000 με and 8000 με is shown in Figure 5.6. The impact response and dynamic resonance of the FML specimen is characterised by oscillations after first contact with the impactor, captured by the experimental results. It is interesting to note that due to the reduced stiffness of the FML specimen arising from the compressive preload, the force-time histories show an increase in oscillations compared to an unloaded specimen. This is attributed to metal plasticity damage as well as the loss of local rigidity of the FML due to the onset of interlaminar and intralaminar damage.

At higher impact energies (19.5 J), as the impacted FML specimen deflects back upwards, the contact force increased steeply. A significant load drop is seen to occur at $t = 1.0$ ms, characteristic of initiation of cracking of the aluminium layers in the FML, followed by further drops in the force-time curve resulting from oscillations and material damage induced by the application of compressive preload. Upon reaching peak force, the force-time curve drops to zero, suggesting no further damage modes are propagated. However, the FE model predicts that this is not the case, and further damage evolution occurs as the impactor rebounds. A comprehensive investigation of this effect is provided in Section 5.4.

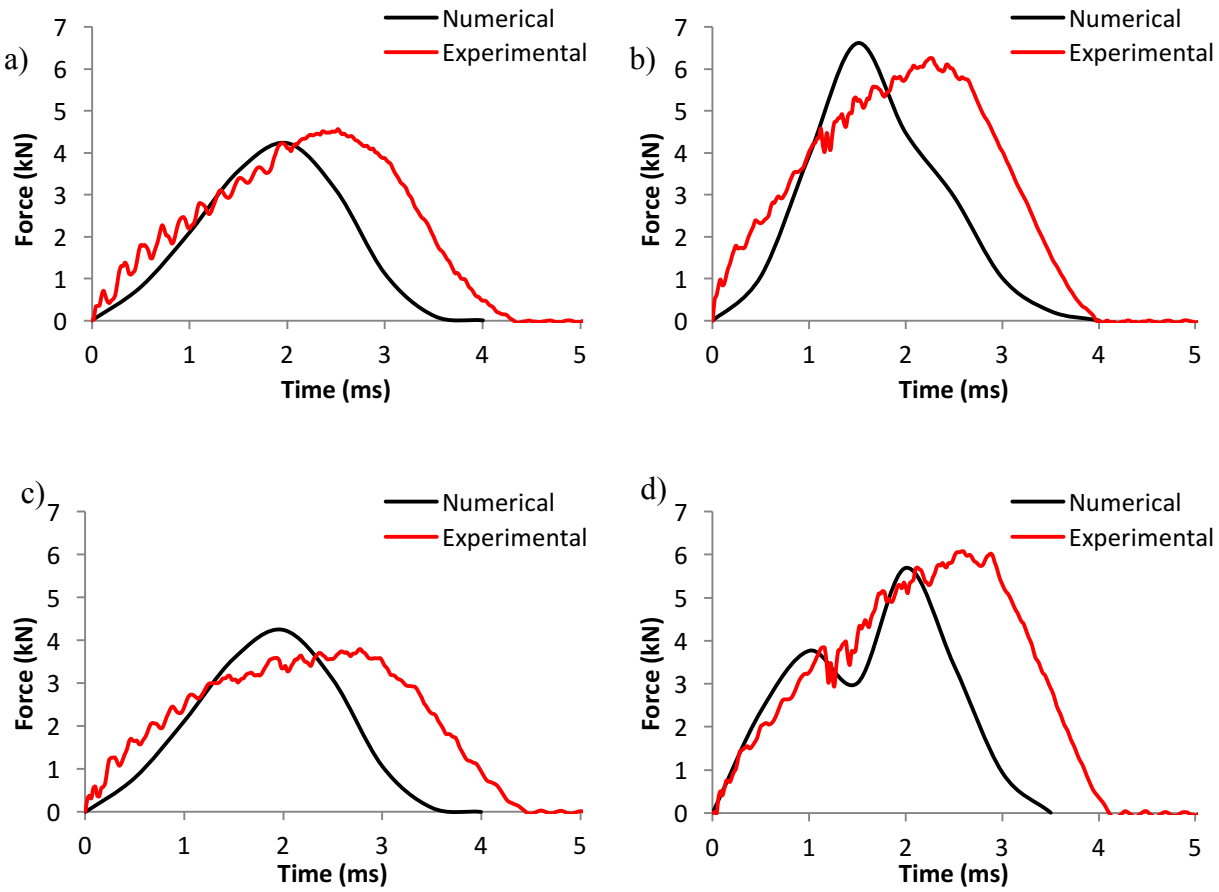

Figure 5.6 Force-time histories at 4000 με a) 8.2 J, b) 19.5 J and 8000 με c) 8.2 J, d) 19.5 J.

An important point to note is that the experimental and numerical force-time curves both show a reduction in contact time by up to 50% compared to unloaded case, as shown in Table 5.1. This indicates that impact-induced stress waves propagate faster under compressive preload to initiate incipient damage earlier. Previously published results have differing results on the effect of compressive preload on the impact contact duration of laminates. While some studies [235, 255] found that contact force histories are almost identical regardless of the applied compressive force, other studies [144, 145, 159, 242, 249, 256] report that the contact time increased with the compressive preload level which then appeared to 'soften' the impact response [249, 256]. Pickett et. al. [141] and Loktev [257] studied the effect of compressive preload on the impact response of carbon/epoxy laminates and an orthotropic Uflyand-Mindlin plate respectively, and found that the compressive preload altered the failure modes and led to shorter duration of the impact event. Loktev [257] attributed this to a positive pre-stressed moment causing a stiffening response that reduced the contact duration.

In the experimental tests and numerical model studied in this section the FML test specimen is

loaded above the critical buckling load (170% P_{cr}); however, the anti-buckling rig severely limits the lateral deformation of the specimen. No buckling or deflection of the specimen was observed during the experimental or numerical investigations. A comparison of the force-time histories between experimental tests and FE predictions showed that the FE model accurately capturing the bell–shaped curves of the force-time curve at low impact energies, and sharp load drop in the FML specimen exposed to parameters of high impact energy and preload. However, the FE results show a shorter contact duration than experimentally measured. A similar finding was recorded by Heimbs et al. [150] when studying CFRP plates subject to combined impact and compression preload.

		No preload (ms)	**4000 με (ms)**	**8000 με (ms)**
8.2 J	Experimental	7.76	4.3	4.36
	Numerical	7.62	4.0	4.0
19.5 J	Experimental	7.78	4.08	4.06
	Numerical	7.2	3.96	3.5

Table 5.1 Experimental and numerical recordings of contact duration of compression and impact tests.

Figure 5.7 compares the experimental results and FE predictions of the effect of compressive preload on the peak force of the impacted FML. For ease of comparison, the FE predictions have been slightly off-set on the x-axis. The results show that peak force increases with the introduction of compressive preload level, however no further change is recorded with increased compressive preload. This is because peak force is limited by the onset of damage, as reported by Whittingham et al. [235] when analysing carbon-fibre/epoxy laminated plates subject to compressive preload.

Upon impact, the increase in the extent and number of damage modes causes the FML specimen to absorb more impact energy. At low impact energies (5 J and 8.2 J), the introduction of compressive preload of 2000 με causes a significant increase in peak load (116%). This ‘spike’ induced by the preload is less notable as higher impact energies (12.8 J and 19.5 J), where experimental and numerical results show a small, but significant increase in peak load of 42% at 2000 με. With a further increase in compressive preload from 2000 με and 8000 με, no significant changes (4% increase) in the peak load is recorded.

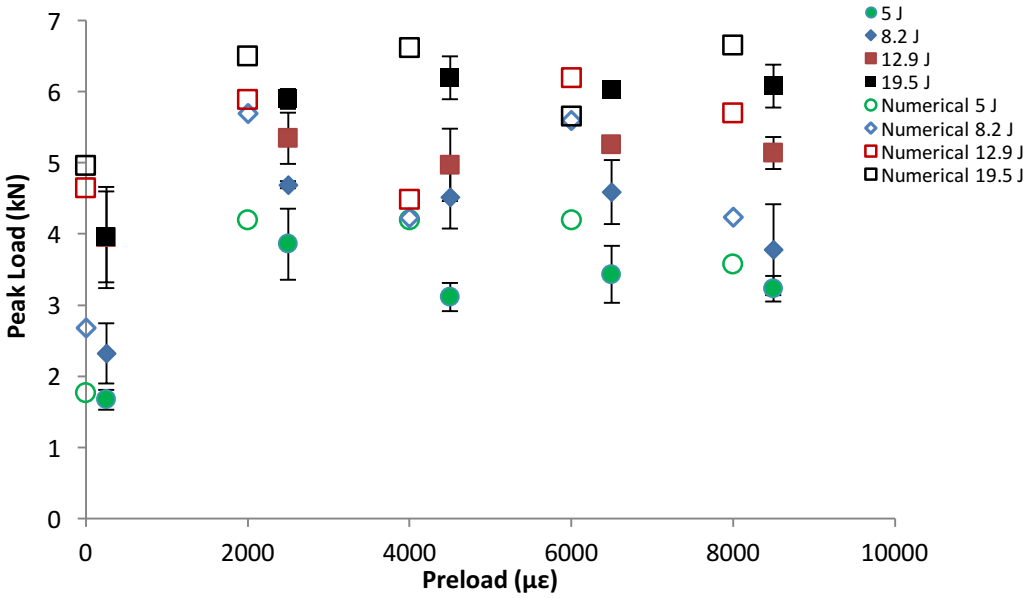

Figure 5.7 Experimental and numerical peak force results with increasing compressive preload.

Figure 5.8 compares the experimental results and FE predictions for the plastic deformation metrics of the impacted FML. At low impact energies (5 J), the front crater damage area is spherical in shape, determined by the shape of the impactor. With the introduction of the compressive preload (2000 με), the front crater damage area increased by 211%. In comparison, at the medium impact energy range (8.2 J and 12.8 J), this effect becomes less with an average increase of 24%. With an increase in preload (4000 με to 8000 με), no substantial increase in front crater damage occurred. In contrast, at the highest impact energy (19.5 J), the front crater damage size decreased by 41%. At this impact energy, several failure modes occur simultaneously including debonding between the front aluminium layer and GFRP/adhesive plies. Rapid propagation of the debonding occurs in conjunction with rear crater damage and rear crack growth leading to increased energy absorption. With a further increase in compression preload, little change was found to the front crater damage area size.

Rear crater damage increases significantly with the introduction of compressive preload. Once again, low impact energies are more sensitive to preload. At 5 J and 8.2 J, the rear crater damage area increased by 2870% and 522% respectively, when subject to a 2000 με compression preload compared to the unloaded case. When the impact energy was increased to 12.8 J, the damage area increased by 264%. This trend follows until 19.5 J, where the rear crater damage increases by 116%. The reduced influence of the compression preload at higher impact energies can be attributed to the presence of other damage modes which become more significant. At low impact energies, the FML is less susceptible to an increase in rear crater damage with compressive

preload. Conversely, for high impact energies (12.8 J to 19.5 J), an increase in preload from 2000 με to 8000 με shows an upward trend whereby rear crater damage increases by 24%. Numerical predictions are shown to match within 5% of the experimental results.

The initiation and propagation of the rear aluminium crack is closely related to the resulting front and rear crater damage areas. As described previously, no cracking occurred along on the front aluminium layer (closest to impactor). However, significant rear cracking occurred in the 0° direction (ie. rolling direction), contrary to the unloaded and tensile preloaded cases. As the impact energy increased, the compressive preload level needed to initiate a rear crack decreased. This indicated that under compressive preloading, one of the critical damage and energy absorbing modes is plastic deformation of the rear aluminium layer. The growth of the crack length at high impact energies (12.8 J to 19.5 J) reaches a plateau value above 4000 με, increasing marginally by 4% and 6% for 12.8 J and 19.5 J respectively.

Central permanent deflection, governed by the "softening effect" of the FML specimen, increased with the introduction of compressive preload of 2000 με for 5 J, 8.2 J and 12.8 J by 20%, 55% and 14% respectively. Further increase in preload levels does not show a significant increase in central permanent deflection. At the highest impact energy (19.5 J), the opposite effect occurred whereby central permanent deflection decreased by 21% with the introduction of the compressive preload of 2000 με. This may be due to the initiation and propagation of other critical failure modes, such as the delamination, fibre splitting and severe debonding of the front and rear aluminium layer and GFRP/adhesive layer, as shown in Figure 5.5, as well as simultaneous plastic deformation failure modes that occurred such as an increase in rear crater damage area and cracking of the rear aluminium layer.

The FE analysis of the plastic deformation of the impacted FML allow us to identify and characterise experimentally observed phenomena and key failure mechanisms brought about by the introduction of compressive preload, and the effect it has on the damage tolerance and degradation of the impacted FML specimen. The FE predictions are shown to have a good agreement with the experimentally measured damage metrics.

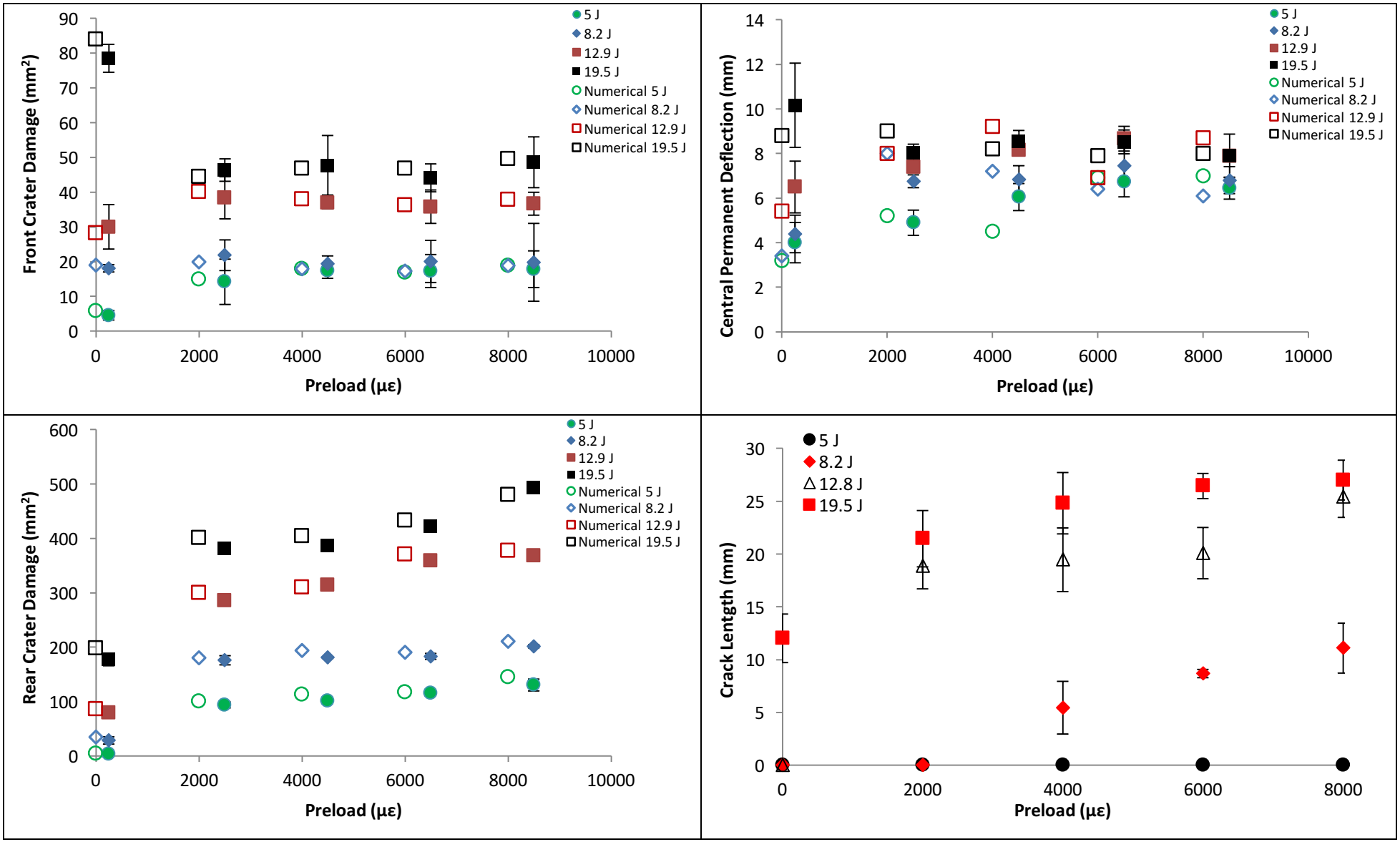

Figure 5.8 Experimental and numerical results with increasing compression preload. For clarity the numerical results have been off-set on the x-axis.

Figure 5.9 shows an approximately linear increase in delamination damage area with increasing compressive preload induced by high interlaminar stresses at the ply interface caused by the impact. At low impact energies (5 J to 8.2 J), experimental and numerical results both show that the preload causes relatively small increases of 27% and 9% to the delamination damage area, respectively. However, further increase in preload causes a significant increase by 180% and 142% between 2000 με and 8000 με for 5 J and 8.2 J respectively. This is due to the initiation of delaminations on both ply interfaces at the higher preload levels. At higher impact energies (12.8 J to 19.5 J), a reverse trend is observed, whereby compressive preload of 2000 με causes a rapid increase in delamination area of 180% and 114% respectively, followed by an increase of 26% and 53% between 2000 με and 8000 με for 12.8 J and 19.5 J respectively.

In addition to the resulting "softening effect" of the FML, the rapid increase in delamination area is brought about by an "additional buckling effect" [157]. As the impactor rebounds, the FML specimen is still under a uniaxial compressive stress, such that the specimen undergoes deflections from the bending moment induced by the compressive load, which causes the delamination damage area to enlarge.

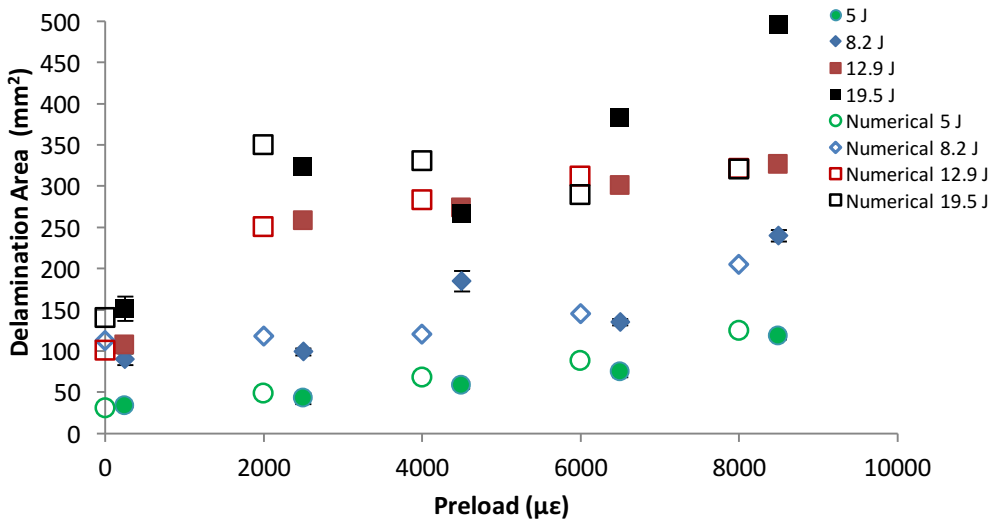

Figure 5.9 Delamination area with increasing impact energy and preload.

An important point to note is that upon visual inspection, the front crater damage area (BVID) is not representative of the damage within the GFRP constituents. As shown in Figure 5.8, only a small increase was detected in the front crater damage area with an increase in compressive preload, and does not reflect the size, orientation or extent of the delamination region that extends well beyond the impact location. This highlights the need for a predictive FE model in order to characterise the damage modes on a ply-by-ply level.

Due to the compressive stresses experienced by the FML, the experimental observations reveal that the majority of failure mechanisms occur away from the impact point. A close comparison between the rear crater damage area and delamination damage of 10% further validates this correlation. Figure 5.10 shows the size, shape and location of delamination damage at both the 0°/90° interface (Plies 1 and 2) and 90°/0° interface (Plies 3 and 4) of the FML specimen subject to an impact energy of 19.5 J with increasing preload. Optical microscopy images show the effect of increasing compressive preload on the delamination damage to the impacted FML. The delamination areas are approximately ellipsoidal in shape. In contrast to the unloaded and tensile preload cases, the major axes of the delamination profiles under compressive preload were aligned in the longitudinal direction (0° direction) occurring at the 90°/0° interface (Plies 3 and 4). These results correlate to the fibre splitting and rear crater damage observed experimentally. Similar results have been recorded by Chiu et al. [157] when investigating the effect of compressive preload on graphite/epoxy laminates. At low impact energy (5 J and 8.2 J), the addition of the compressive preload changes the shape of the delamination area from circular (unloaded case) to a peanut shape occurring along the 90°/0° interface (Plies 3 and 4). With an increase in preload level, more matrix cracks developed in the outer 0° ply (Ply 4) above the delamination zone, leading to a growth in delamination until the its length equalled the span of the matrix cracks. As the compressive preload increased to 8000 με, delamination was initiated directly under the impactor in the 0°/90° interface (Plies 1 and 2) in an ellipsoidal shape. Delamination area at this impact energy rang increased upon the application of compressive preload of 2000 με. No increase in fibre splitting length was recorded with an increase in compressive preload.

At higher impact energies (12.8 J and 19.5 J), an ellipsoidal-shaped delamination area occurred along both ply interfaces. With an increase in compressive preload, delamination at the 90°/0° interface (Plies 3 and 4) was the most dominant.

The FE model predictions of the total delamination area compare well with the experimental results. At 4000 με, the FE model predicts the total damage area within 20% of the experimental values, as well as the shape and orientation of the delaminations along each ply interface. With an increase in preload to 8000 με, the FE model under-predicts the total delamination area by mostly under-predicting the growth of delamination damage along the 90°/0° interface (Plies 3 and 4). As described in Chapter 4, this is likely due to limitations of the shell element formulation of the FE model to simulate the through-thickness properties of the FML for the impact event. Overall however, the FE methodology is shown to have a reasonable degree of accuracy; capturing all

damage mechanisms and trends well and allowing insight into damage mechanisms that are not detectable using visual inspection.

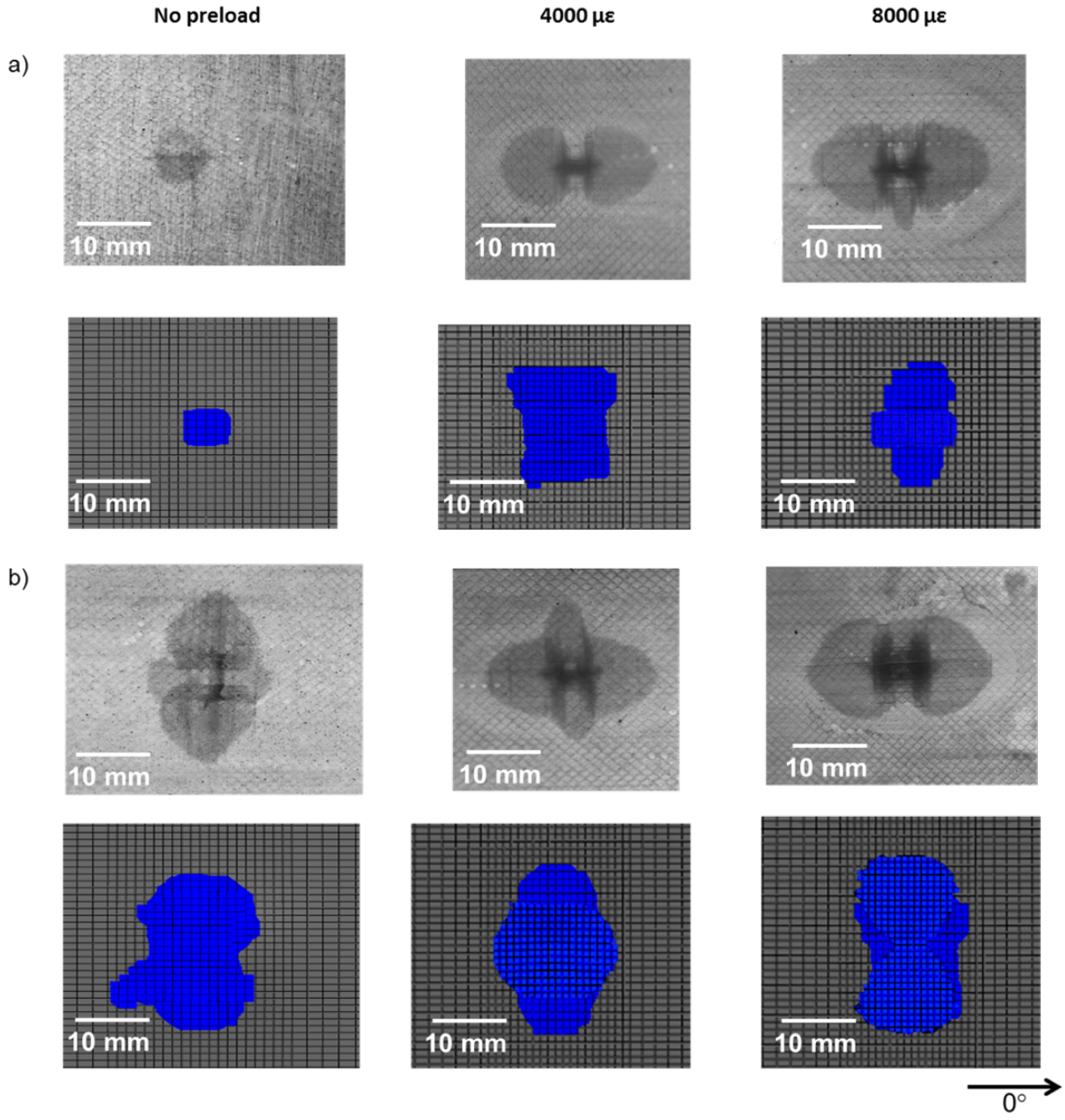

Figure 5.10 Optical microscopy images and FE prediction of the GFRP delamination and fibre failure damage of FML 1 2/1-0.4 subject to a) 8.2 J and b)19.5 J with increasing compression preload.

The increase in softening of the FML that permits large bending strains under compressive preload aided the initiation and evolution of damage modes upon impact. Similar to the unloaded and tensile preload cases, these damage modes absorb energy and this was evidenced by the downward trend of the energy restitution coefficient with increasing impact energy, as shown in Figure 5.11. A similar trend was reported by Heimbs et al. [150] when studying low velocity impacts on CFRP

plates subject to compressive preload of 80% of the buckling load. At low impact energies (5 J and 8.2 J), a 10% increase of energy was absorbed and less energy was returned as elastic springback compared to the unloaded FML, attributed to the fibre splitting, rear aluminium cracking and extensive delamination. At high impact energies (12.8 J and 19.5 J), this increase was minimal (2%) with the application of compression preload, however significantly increases (25%) between 2000 με and 8000 με. At high impact energies (19.5 J), the FE model slightly over-predicted the coefficient of restitution, possibly due to the under-prediction of the total delamination area at this energy range, and the inability of the FE model to capture the cracking of the rear aluminium layer. The FE predictions however are shown to have good agreement, within the experimental error.

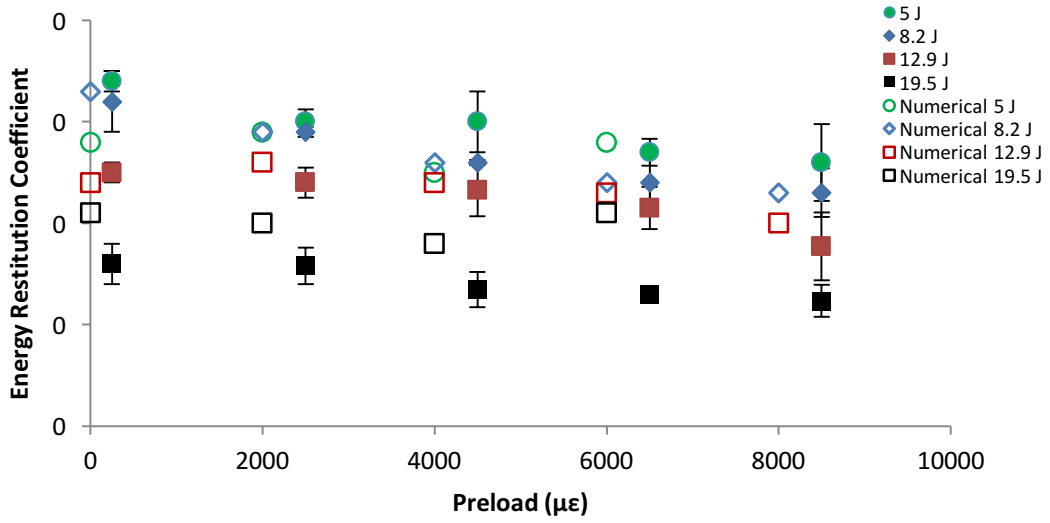

Figure 5.11 Energy restitution coefficient with increasing impact energy and compression preload.

5.3.3 DAMAGE PATTERN AND SEQUENCE

In case of compressive preload, out-of-plane bending deflection is critical, particularly when considering thin specimens. The FE model demonstrates that the global deflection of the preloaded FML specimen was higher than that of the unloaded case. The increased bending deformation of the FML specimen gives rise to an increase in energy-absorbing failure mechanisms, including increased interlaminar damage. Figure 5.12 shows the FE force-time curves of the FML subject to low (8.2 J) and high (19.5 J) energy impacts at 4000 με and 8000 με preload levels. The graph is annotated with key points indicating the initiation of damage in each ply (P) from the front (1) to the rear (4) ply that correlated to the numerically predicted failure contours of each GFRP ply and ply interface.

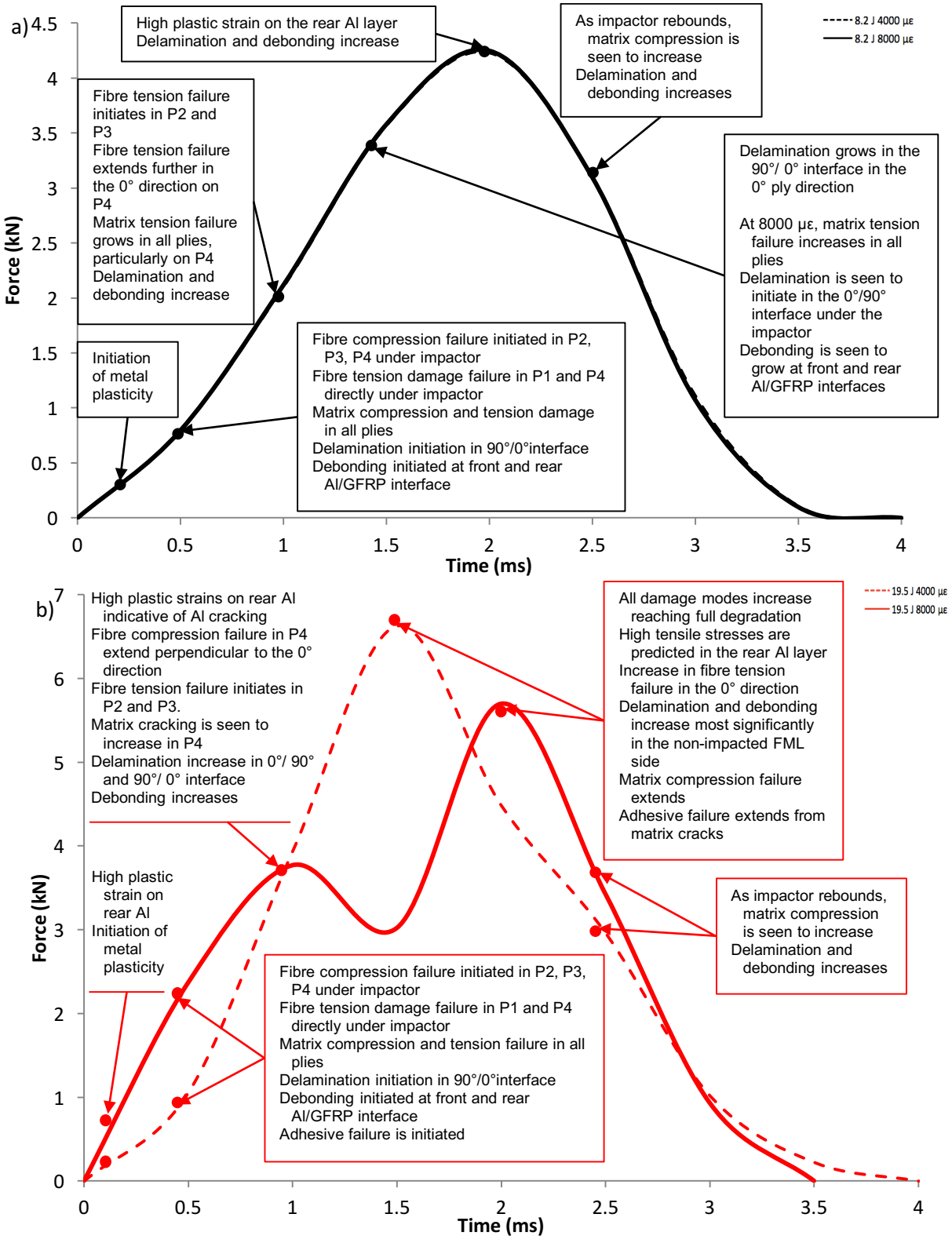

Figure 5.12 Force-time histories and predicted initiation and failure of damage modes of FML 1 2/1 subject to compression preload of 4000 με and 8000 με at a) 8.2 J and b) 19.5 J.

The contact duration for the high velocity impact at 19.5 J was reduced by 43% and 48% at 4000 με and 8000 με respectively, indicating that damage occurred more rapidly than the unloaded condition. Higher peak forces (as shown in Figure 5.7) also indicated that the damage modes were more extensive and widespread. At low impact energy (8.2 J), the FE force-time histories were exactly the same for 4000 με and 8000 με. At this impact energy, experimental results show little influence of increasing compressive preload (after the application of the initial preload) on the plastic deformation of the impact FML specimen (i.e. front crater damage, rear crater damager and central plastic deformation) which govern the force-time curve.

Upon initial contact between the impactor and preloaded FML, initiation of metal plasticity occurred. Plastic strain developed directly under the impactor on the front and rear aluminium layers of the FML, corresponding to the initiation of front and rear crater damage as experimentally observed. At t = 0.5 ms, fibre compression failure initiated within P2, P3 and P4 directly under the impactor. In addition, fibre tensile failure developed in P1 and P4 under the impactor and in the 0° plies. Matrix tension and compression failure initiated in all plies. Delamination initiated at the 90°/0° interface (Plies 3 and 4) under the impact region induced by matrix micro-cracking, and propagated within the "resin-rich" region between the plies. The intralaminar damage (matrix cracking) was predicted to be more localised under the impact region, and distributed through several plies. Debonding initiated at the front and rear aluminium/GFRP interfaces.

At t = 1 ms, fibre tension failure initiated in P2 and P3 and extended further in the 0° direction on P4, indicating the initiation of fibre splitting under the impactor. Matrix tension failure occurred in all plies, with the most extensive in P4, extending beyond the impact region. Delamination and debonding further increased at the front and rear aluminium/GFRP interfaces.

At t = 1.5 ms, delamination growth occurred along the 90°/0° interface in the 0° ply direction. For high preload levels, matrix tension failure increased in all plies, and delamination initiated at the 0°/90° interface (Plies 1 and 2) under the impact region. When the impactor reached its maximum depth at t = 2 ms, high plastic strain occurred on the rear aluminium layer. Delamination and debonding increased, but the growth levels "capped" by the matrix cracks at the bottom plies of the GFRP layers.

When the impactor rebounded it was caught to avoid multiple impacts to the specimen. The FE model indicated further extension of the damage modes, as the specimen was still under compressive load at this time. In particular, the high plastic strain on the rear crater damage caused

further growth in delamination and debonding damage. Overall, damage was predicted to initiate from the bottom plies on the rear side of the FML specimen (opposite to the impact region). Under plate bending induced by the compressive preload, the rear FML side was in tension, hence failure occurred in matrix tensile mode. More extensive damage modes were therefore experienced in the rear plies of the GFRP.

Figure 5.13 shows the ply-based damage contours at the highest impact energy (19.5 J) and compressive preload of 8000 με. Upon impact, a similar trend of damage initiation and progression occurred as low impact energies. The main differences however, were the extent and rapid progression of the failure modes. At t = 0.5 ms after initiation of impact, high plastic strains occurred at the front and rear aluminium layers, and this corresponded to the experimentally observed increase in rear crater damage area and rear aluminium cracking. Delamination damage initiated at the 0°/90° interface (Plies 1 and 2) and the 90°/0° interface (Plies 3 and 4). Debonding initiated at the front and rear aluminium/GFRP interfaces. Fibre compression initiated in P2, P3 and P4 directly under the impactor, as seen in Figure 5.13. Furthermore, fibre tensile damage occurred in P1 and P4 in the impact region. Matrix cracking initiated in all plies, under the impactor in the 0° plies (P1 and P4) and in an X-shape in the 90° plies (P3 and P4). Matrix tension damage initiated in a circular shape replicating the impactor in P1, while in P2, P3 and P4 damage grew in a perpendicular direction to the respective ply orientations, as shown in Figure 5.13.

At t = 1 ms, the force-time curves show a sharp load drop, which was indicative of cracking of the aluminium; in this case the rear aluminium layer. Fibre compression and tension failure in P4 extended perpendicular and parallel to the 0° direction respectively. Fibre tension failure also initiated in P2 and P3. Matrix cracking increased in P4, initiating and propagating delamination cracks along both the 0°/90° interface (Plies 1 and 2), and the 90°/0° interface (Plies 3 and 4) oriented perpendicular and parallel to the 0° direction respectively.

At t = 1.5 ms and 2 ms (4000 με and 8000 με respectively), all damage modes increased and reached the failure values in their respective plies. High tensile stresses were predicted in the rear aluminium layer as well as an increase in fibre tension in the 0° direction, and this correlated with the fibre failure that occurred in the experimental studies. Delamination and debonding lengths were also predicted to increase, most significantly in the non-impacted FML side. Matrix compression failure extended in an X-shape away from the impact region, further allowing matrix cracking to develop as a significant form of damage in the GFRP plies, extending beyond the visible crater damage. Matrix tension in each ply further increased perpendicular to the ply

direction. Similar to low impact energy, further extension of the damage modes in the form of delamination and debonding occurred as the impactor rebounded.

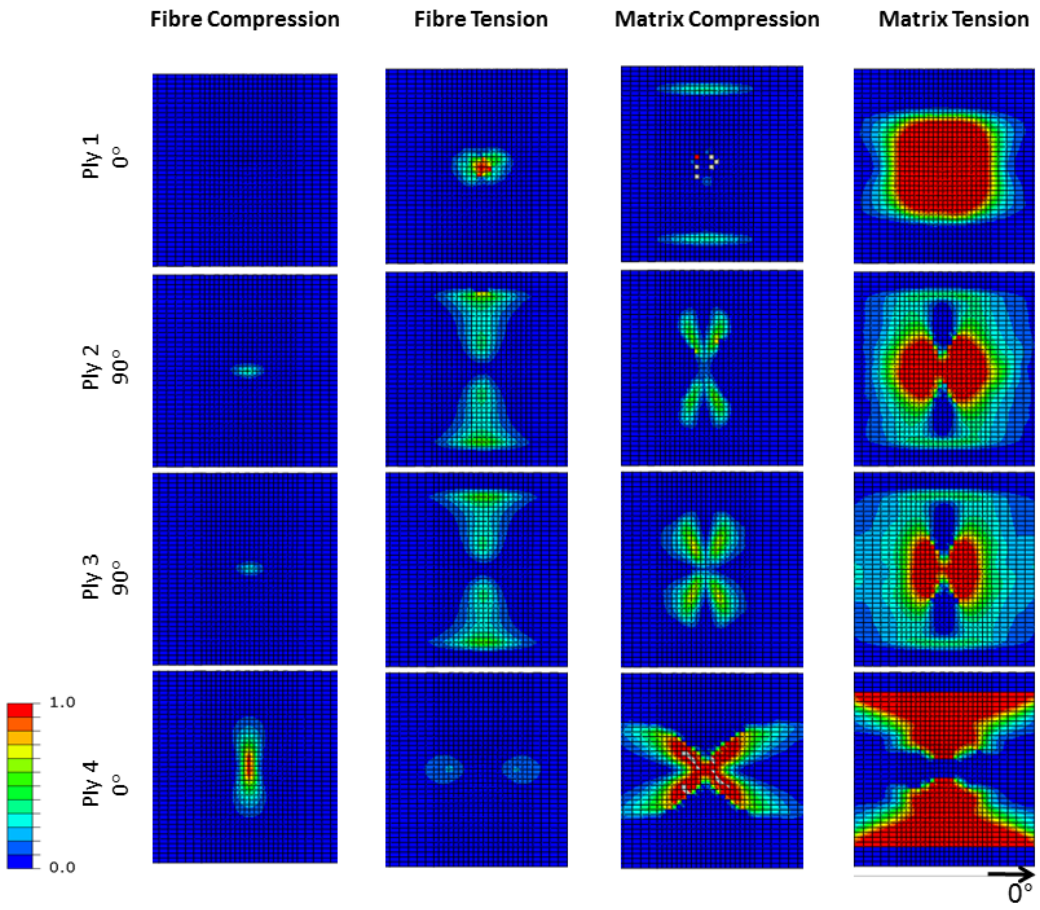

Figure 5.13 Numerically predicted damage contours of FML 1 2/1-0.4 impacted at 19.5 J at 8000 με compressive preload.

5.4 CONCLUSION

In this study, an experimental and numerical investigation was conducted to evaluate the influence of compression preload on the damage initiation and progression in FMLs, providing a ply-by-ply insight into the identification, characterisation, sequence and interaction of damage modes. While a number of publications have studied the effect of compression preload on composites, to date, there are no published research studies for FMLs.

Compressive preloading has a significant effect on the failure modes of FMLs subject to low velocity impact damage. Compressive preloading leads to a “softening effect” such that the overall flexural stiffness of the FML specimen decreases, evidenced by the increase in deflection of the

impacted material. A reduction in the contact duration was found both experimentally and numerically as the impact-induced stress waves propagated faster under the compressive preload, helping to spread out the impact energy quickly from the impact region. However, the numerical simulations under-predicted the contact duration by ~15%.

The decrease in the FML stiffness increased the plastic deformation to the aluminium layers under impact loading, with a larger area of front and rear crater damage and rear aluminium cracking. In addition, interlaminar damage in the forms of extensive delamination and intralaminar damage (matrix cracking) appeared to be more localised, occurring directly under the impact region. Fibre failure on the back surface also occurred due to the "softening effect" induced by the compressive preload.

The FE predictions are showed good agreement with the experimentally observed failure modes, damage location and severity. The ply-by-ply analysis of the damage modes induced by compressive preloading provided an insight into the sequence of damage initiation and progression, allowing for direct correlation with the damage in the individual layers to the FML. This was particularly evident when analysing the relation between matrix cracking, adhesive failure, delamination, and debonding of the GFRP/adhesive interfaces. The model also revealed that damage growth continued for a short period following the impact event.

This chapter has made a number of original contributions to the existing body of knowledge on the impact response of FMLs:

(i) identification of the influence of compressive preload on the dynamic response of FMLs subject to low velocity impact;
(ii) characterisation of the experimentally observed damage modes and trends in resulting damage with increasing preload levels;
(iii) insight into the interlaminar and intralaminar failure modes as a result of compressive preload, and the interaction between failure modes using a ply-based FE modelling approach, not detectable through non-destructive testing or visual inspection; and
(iv) understanding of the initiation and progression sequence of the failure modes, including damage to the impacted specimen as the impactor rebounds.

CHAPTER 6 : EXPERIMENTAL INVESTIGATION INTO THE COMPRESSIVE RESIDUAL STRENGTH OF IMPACTED FMLs

ABSTRACT

This chapter presents an experimental study into the Compression-After-Impact (CAI) properties of FMLs. The study includes the investigation into the influence of tension and compression preloading coupled with low velocity impact. The experiments revealed that impact damage can significantly reduce the compressive strength of the FML specimen. Compression failure of impacted FMLs is due to the propagation of impact-induced damage mechanisms such as plastic deformation (front and rear aluminium cracking), debonding, matrix and fibre microcracking, delamination, as well as the interactions between these damage mechanisms. The presence of impact-induced cracks in the aluminium layers of the FML, as well as fibre failure in a transverse direction to loading (0° direction) were identified as critical failure mechanisms that resulted in a significant detrimental effect on the residual compressive strength of the FML specimen. Damage growth during CAI is triggered by impact-induced sub-laminate buckling, causing fibre and delamination damage growth. Global buckling of the FML specimen and local buckling of the delaminated sub-laminates are accompanied by a transverse crack on the impact face of the FML specimen.

Experimental investigation into the combine preload and impact revealed that residual compressive strength decreased with increasing tensile preload. An increase in delamination damage and debonding region led to the reduction of CAI strength. Additionally, the increase of aluminium cracking and fibre failure due to tensile preload created a ‘weak point’ from which CAI damage initiated.

For a combined compressive preload and impact, compressive preload had a more detrimental effect in reducing CAI strength of the FML at low impact energies. This is due to the increased front and rear crater damage area as well as delamination damage. Aluminium cracking and fibre failure initiated at lower impact energies and preload levels, contributing to the reduction in CAI

strength. Buckling of the FML occurred earlier compared to the unloaded case. At high impact energies, compressive preload led to a minimal reduction in residual compressive strength due to the near perforation of the FML specimen including significant aluminium cracking and fibre failure. As such, CAI strength of the FML plateaued above compressive preload of 2000 με.

6.1 INTRODUCTION

As demonstrated in previous chapters of this thesis, damage in the form of delamination, debonding, matrix cracking and fibre breakage in FMLs typically extends well beyond the impacted region. Among the mechanical properties reduced by the impact, the compression strength is one of the most significant. Compression-After-Impact (CAI) strength is a widely accepted measure for evaluating the damage tolerance of a structure. A reduction to the compressive strength of up to 60% can occur in composite laminates with no obvious visible damage [160].

Research into the CAI strength of FMLs is very limited and lags similar research performed on composite materials. Thus far only eight published research studies have assessed the residual compressive strength of FMLs subject to impact damage, including CARALL [182], ARALL [169, 258], GLARE and aluminium/GFRP hybrids [18, 162, 170, 259] and titanium/graphite FRP [186]. However, these studies only consider the effect of delamination and debonding damage modes on the CAI strength of FMLs, as detailed in the Chapter 2. Thus, a gap in research exists to provide a complete understanding of all the damage modes, including metal plasticity, on the residual compressive strength of FMLs subject to low impact energies. Also, no investigations into the effect of tension and compression preloading during impact on the residual strength of FMLs has been conducted.

Research into the CAI strength of sandwich structures report that damage geometry and plastic deformation directly influence the compression-after-impact strength [148, 161, 162]. A loss of CAI strength can be due to multiple damage mechanisms and potentially coupling between them, including delamination, sub-laminate buckling, and matrix cracking and/or fibre failure.

Delamination has been identified as one of the key factors that reduce the CAI strength of composites laminates [146, 165, 166, 171, 174-179]. Numerous studies have shown a correlation between the size of the delamination region and the magnitude of the reduction in CAI strength of

composite materials subject to low velocity impact [160, 185]. Delamination initiated during impact can separate the specimen into multiple sub-laminates, as shown schematically in Figure 6.1. Under a axial compressive load a delamination can cause buckling in one of three modes [33]: (i) global instability (buckling of the laminate), (ii) local instability (buckling of the sub-laminate), or (iii) mixed-mode (combination of the global and local buckling). As the buckling stress of a sub-laminate is lower compared to the initial specimen, buckling or local buckling are likely to occur under CAI loading and lead to premature failure [171, 176, 178, 183, 260-262]. Furthermore, some studies [184, 262-264] identified the propagation of fibre failure in the impacted region as another damage mode that contributes to the loss of residual strength of a composite.

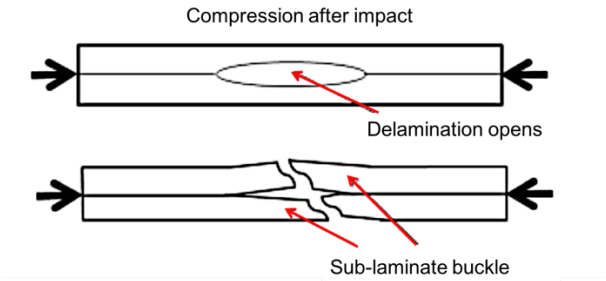

Figure 6.1 Damage response of laminate under compression loading [262].

Due to the limited amount of research published on the CAI strength of FMLs, an experimental study is undertaken to investigate the effect of different impact energies and preloading conditions on the residual compressive strength of FMLs. This study evaluates the effect of different layups, namely FML 1 2/1 and FML 2 3/2, on the CAI strength of FMLs. An evaluation of the impact-induced damage such as delamination, matrix cracks, fibre failure and metal plasticity was conducted to determine correlations with the CAI properties of FMLs.

The aims of this chapter are to:

(i) investigate the influence of increasing impact energy and resulting impact damage on the compressive residual strength of FMLs;
(ii) study the effect of tension and compression preloading on the compressive residual strength of FMLs subject to low velocity impact;
(iii) identify and characterise the phenomenological correlation of the reduction in compressive strength to the impact-induced damage;
(iv) determine the effect of FML lay-up on the CAI strength and failure mode.

6.2 EXPERIMENTAL METHODOLOGY

Currently there is no standard procedure for CAI testing of FMLs, with many researchers opting for a modified version of ASTM D7137 [168] for CAI testing of monolithic composite plates. In this study, the modified version of ASTM D7137 is used, however this standard mainly applies for test specimens thicker than 3 mm. In the case of the FML panels tested in this study, anti-buckling plates were used to inhibit buckling but not restrain out-of-plane rotations. CAI tests were carried out in a way to avoid global buckling of the impacted FML specimens but allow local buckling of the sub-laminates. The anti-buckling rig adapted to the geometry of the impacted specimens used in the study is shown in Figure 6.2. A square central opening (window), similar to that used by Sjoblom and Hwang [265] and Nettles and Hodge [266], was cut out of the anti-buckling rig to view failure at the impact region during compression loading.

The FML specimens were trimmed using a precision table grinder to meet the requirements of the test fixture. A compressive load was applied using a 50 kN Instron 5581 Universal Testing Machine. The FML specimens were compressed in the 0° direction at a constant crosshead displacement rate of 1 mm/min until failure. A spherical bearing was used to provide self-alignment during the load application to minimise unwanted bending moments. In cases where the impact-induced damage was not sufficient to initiate failure under CAI loading, the FML specimen showed a tendency to fail at the constraint ends due to the high stress concentration in this region.

The data acquisition system recorded the applied displacement and the corresponding reaction force. Strain gauges were not attached to the specimen, and therefore only residual compressive strength was recorded from the experimental tests. Three impacted FML specimens were tested at each loading condition to obtain an average reduction of residual strength caused by impact damage.

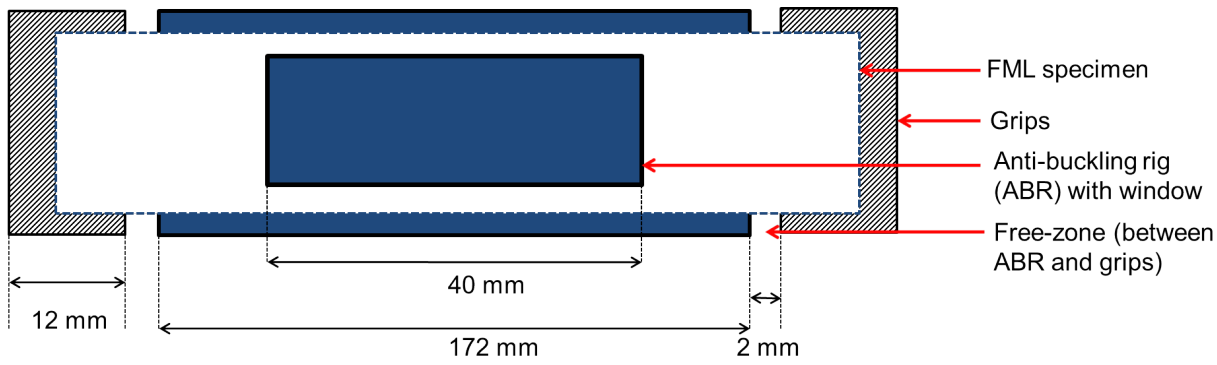

Figure 6.2 Schematic plane-view of adapted CAI anti-buckling rig for FML specimens.

6.3 RESULTS AND DISCUSSION

In this section, post-CAI damage assessment and force-displacement curves were used to investigate the influence of increasing impact energy on FML 1 2/1 and FML 2 3/2 specimens by analysing the failure progression and material degradation. Correlations between the impact damage modes and reduction in CAI strength is presented. Later sections detail the effects of tension and compression preloads on the CAI strength of FML 1 2/1.

6.3.1 EFFECT OF LOW VELOCITY IMPACT ON THE CAI STRENGTH OF FMLs (NO PRELOAD)

Examination of the FML 1 2/1 and FML 2 3/2 specimens following CAI testing revealed two distinct types of failure, as shown in Figure 6.3. At low impact energies (5 J and 8.2 J) whereby little or no damage was recorded, compression failure occurred at the "free-zone" between the grips and anti-buckling rig (shown in Figure 6.3a). This type of failure indicated that the extent of the impact was too small to trigger failure at the impact point. Instead, the region of high stress concentration in the free-zone causes failure. FMLs impacted at higher energies (12.8 J and 19.5 J) that resulted in multiple failure modes including large delaminations, aluminium cracking and fibre failure (as detailed in Table 6.1) failed under compression loading at the point of impact. CAI tests of the FMLs impacted at 19.5 J (Figure 6.3b) showed a region of local buckling from the impact dent, extending transversely to the direction of applied compression load (0° direction), across the complete specimen width. At higher impact energies (12.8 J and 19.5 J), cracking occurred to the front and rear aluminium layers. The hairline cracks grew perpendicular to the 0° direction. Fibre failure occurred at the rear surface of the FML in the 0° direction. The presence of aluminium cracking and fibre failure plays an important role in CAI rupture at the impacted region, and are key damage mechanisms controlling the compressive load bearing limit of the FMLs.

The FML 2 3/2 configuration subject to low impact energies (5 J and 8.2 J) did not show CAI failure; exceeding the compressive load limit of the CAI test (50 kN). For these cases, the CAI tests were manually stopped and the residual strength would could not be measured.

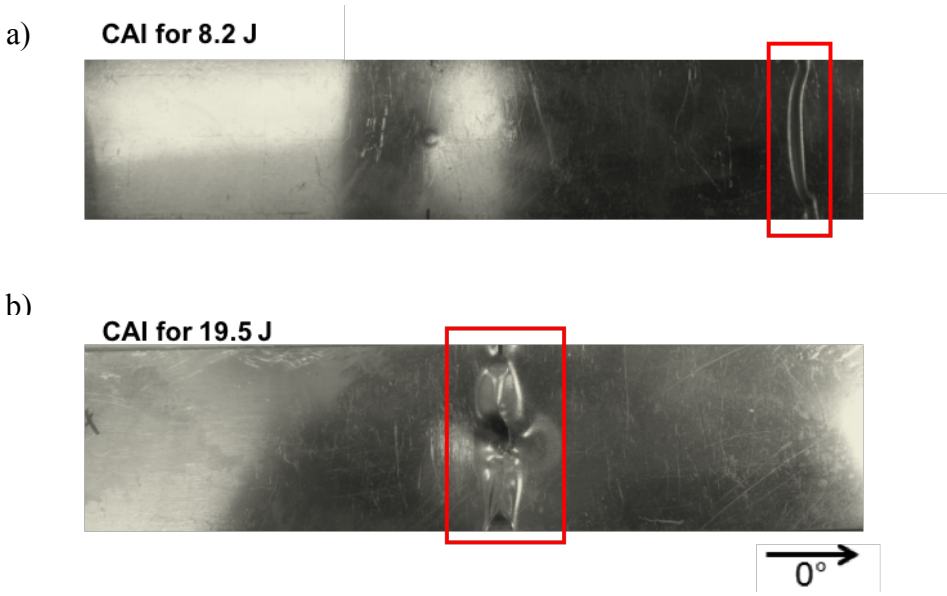

Figure 6.3 CAI experimental failure modes for FML 1 2/1 showing a) failure at free-zone between the clamp and anti-buckling rig (8.2 J) and b) failure at impact zone (19.5 J).

The curves of CAI load as a function of displacement for FML 1 2/1 and FML 2 3/2 are presented in Figure 6.4. All FMLs showed a similar trend that can be divided into two distinct phases. The first phase, shown by a linear slope indicates where the impact damage area does not significantly influence the FML membrane stiffness. The second phase corresponds to the evident loss of linearity due to the lateral deflection of the FMLs specimen, referred to by many researchers as the "knee-point". The compressive load capability of both FML 1 2/1 and FML 2 3/2 configurations reduced as impact energy was increased, evidenced by the decrease in slope of the force-displacement curve and decrease in displacement to failure. For FML 2 3/2, the force-displacement curves for all impact energies except that of 5 J displayed one or more load drops at the displacement of approximately $t = 1.8$ mm, which is indicative of failure progression. This was due to the growth of the rear aluminium cracks in the transverse direction to the applied compressive load (0°). Due to the smaller damage area due to the impact event, material degradation is gradual compared to the FML 1 2/1 specimen that fractures suddenly.

Figure 6.5 shows the effect of increasing impact energy on the CAI strength of FML 1 2/1 and FML 2 3/2. Both FMLs showed a slight downward trend in residual strength with increasing energy. A summary of impact-induced damage and observations of the CAI tests are shown in Table 6.1. FML 1 2/1 and FML 2 3/2 showed a decrease in residual compressive strength of 3% and 8% (not statistically significant) for specimens with impact-induced damage subject to 5 J respectively, and a further reduction of 20% and 25% with increasing impact energy up to 12.8 J.

At the highest impact energy of 19.5 J, no further reduction of residual strength was measured. Similar trends have been reported by Sánchez-Sáez et al. [171] for the CAI strength of thin composite laminates. It is clear that there is a correlation between the decrease in CAI strength with the increase in the presence and extent of damage resulting from increased impact energy.

The higher compressive strength of the FML 2 3/2 was due the additional stiffness of the extra aluminium layer. As reported in Chapter 3, the FML 2 3/2 was unable to undergo large bending strains, and thus impact-induced deformation and debonding was reduced. Interestingly, despite the additional aluminium layer in the FML 2 3/2, when this material was subject to higher impact energies (12.8 J and 19.5 J) its CAI strength was similar to FML 1 2/1, as seen in Figure 6.5.

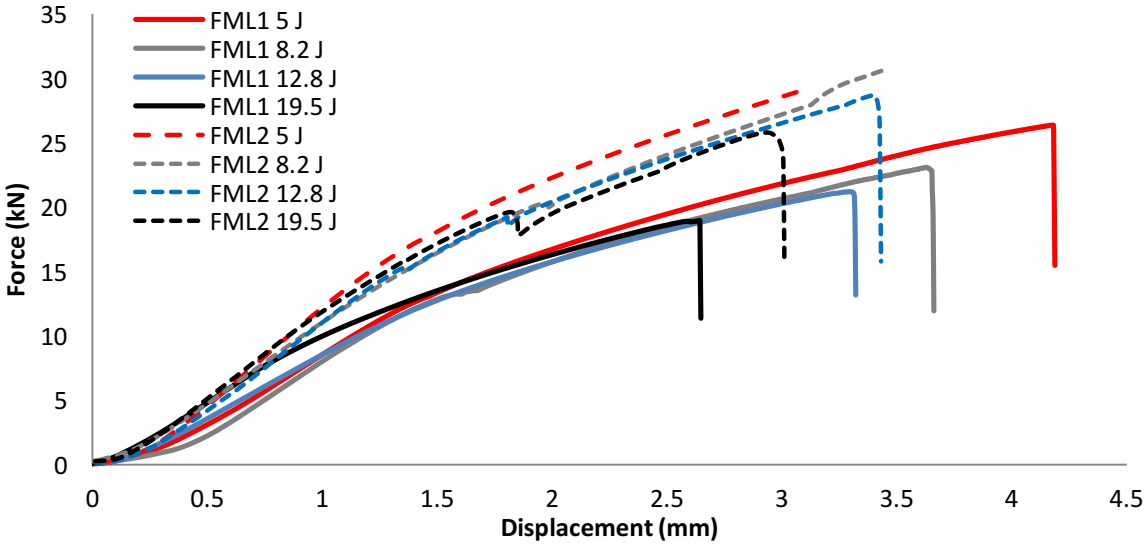

Figure 6.4 Experimental CAI force-displacement curves for of FML 1 2/1 and FML 2 3/2 at varying impact energies.

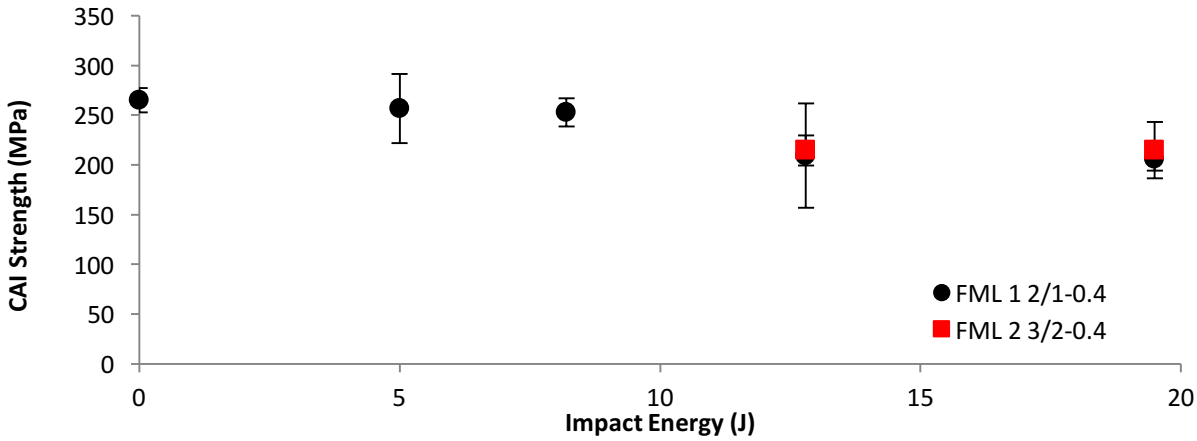

Figure 6.5 Experimental results of compressive residual strength with increasing impact energy for FML 1 2/1 and FML 2 3/2.

FML configuration	Impact energy (J)	Impact	Average CAI strength (MPa)	CAI failure location	CAI damage mechanisms
FML 1 2/1	0	-	265	Free-zone	• Buckle at free-zone
	5	• No visible cracks on front or rear aluminium surface • Delamination in 90°/0° ply interface	256	Free-zone	• Buckle at free-zone
	8.2	• No visible cracks on front or rear aluminium surface • Delamination in 90°/0° ply interface • Fibre failure initiated in 0°direction • Debonding between rear aluminium and adhesive/GFRP layers observed	252	Free-zone	• Buckle at free-zone
	12.8	• Rear aluminium cracking • Delamination in 90°/0° and 0°/90° ply interface • Fibre failure in 0°direction • Prominent debonding	209	Impact zone	• Local buckling along 0° direction • Rear cracking extends to width of specimen • Debonding between the rear aluminium and adhesive/GFRP layers • Minor sub-laminate buckling
	19.5	• Rear aluminium cracking • Hairline crack on front aluminium surface • Delamination in 90°/0° and 0°/90° ply interface • Fibre failure initiated in 0°direction • Prominent debonding	206	Impact zone	• Local buckling along 0° direction • Rear cracking extends to width of specimen • Rear aluminium crack extends along width of FML • Debonding between the front and rear aluminium and adhesive/GFRP layers • Extensive sub-laminate buckling

FML configuration	Impact energy (J)	Impact	Average CAI strength (MPa)	CAI failure location	CAI damage mechanisms
FML 2 3/2	0	-	-	Did not fail	-
	5	• No delamination	-	Did not fail	-
	8.2	• Rear aluminium cracking initiated	-	Did not fail	-
	12.8	• Rear aluminium cracking • Delamination in 90°/0° and 0°/90° ply interface • Minor debonding between rear aluminium and adhesive/GFRP layers observed	214	Impact zone	• Rear aluminium crack extends • No debonding between middle aluminium and adhesive/GFRP layer • Minor debonding between the rear aluminium and adhesive/GFRP layers • Sub-laminate buckling
	19.5	• Rear aluminium cracking • Crack in middle aluminium layer of FML • Delamination in 90°/0° and 0°/90° ply interface • Fibre failure observed • Debonding between rear aluminium and adhesive/GFRP layers observed	215	Impact zone	• Rear aluminium crack extends • Minor debonding between middle aluminium and adhesive/GFRP layer • Debonding between the rear aluminium and adhesive/GFRP layers • Sub-laminate buckling

Table 6.1 Summary of impact-induced damage mechanisms and CAI damage mechanisms for FML 1 2/1 and FML 2 3/2.

As reported in Chapter 3, the number and severity of matrix cracks that induce delamination increase at higher impact energies. At impact energies 12.8 J and 19.5 J, delaminations initiated between both ply interfaces (0°/90° and 90°/0° plies), extending away from the impact region with increasing impact energy. Furthermore, debonding occurred between the rear aluminium and adhesive/GFRP with increasing impact energy as a result of the interfacial shear stresses induced by bending.

Impact-induced delamination cracks within the GFRP and debonding between the metal and GFRP layers divided the FMLs into multiple sub-laminates within the impacted zone. Upon application of the compression load, sub-laminate buckling was initiated at a lower stress compared to the intact specimen. This leads to a combination of local buckling and sub-laminate buckling during CAI testing, as shown in Figure 6.6. The presence of sub-laminate buckling correlated with the reduction of residual compressive strength of the FMLs, suggesting that the sub-laminate buckling of the GFRP layer of the FML specimen plays an important role in final failure of the specimen.

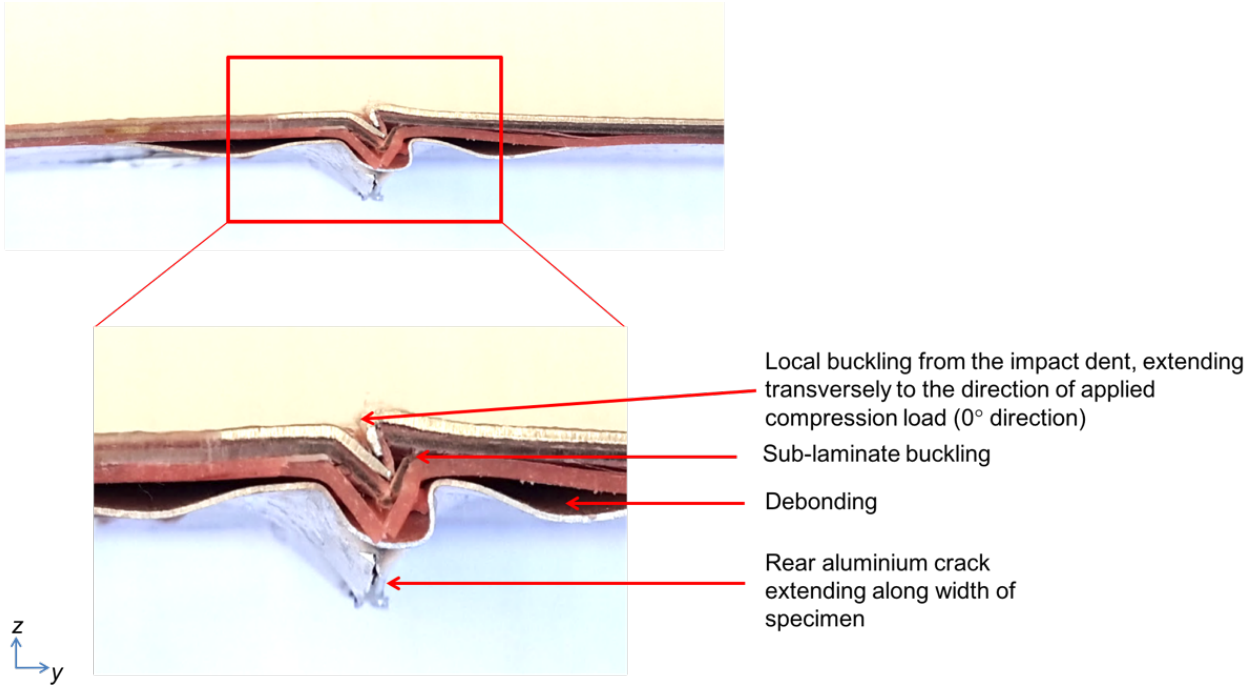

Figure 6.6 Cross-section of FML 1 2/1 impacted at 19.5 J showing CAI experimental test failure at the impact zone.

The extent of CAI failure mechanisms observed for FML 2 3/2 was far less than the FML 1 2/1. This is due to the smaller amount of delamination and metal plasticity damage induced by the

impact events. At the highest impact energy (19.5 J), FML 2 3/2 showed debonding between the middle aluminium and adhesive/GFRP layer as well as debonding between the rear aluminum and adhesive/GFRP layers. Minor sub-laminate buckling of the FML 2 3/2 was also observed during CAI testing, but not to the extent of FML 1 2/1. A small increase in rear aluminium cracks were observed with the application of the compressive load for CAI tests.

A plot of the CAI strength as a function of the experimentally measured impact-induced delamination area is presented in Figure 6.7. As delamination area increases over 50 mm^2, compressive residual strength reduced by 17% in FML 1 2/1, after which CAI strength plateaus with further increase in delamination area. At delamination area ≥ 50 mm^2, two distinct damage modes occurred, namely (i) delamination is initiated along the 90°/0° and 0°/90° ply interfaces leading to sub-laminate buckling and (ii) rear aluminium cracks are present leading to the progression of the crack in the transverse direction to the applied compressive load. This indicated that while each damage mode has a detrimental effect on the CAI strength, a combination of the damage modes led to failure of the FML. Similarly, for FML 2 3/2, CAI failure was first occurred when delamination damage area is 50 mm^2, after which no further reduction in CAI strength is recorded. Delamination area ≥ 50 mm^2 is therefore a good visual indicator of the compressive load-carrying capability of both FML configurations. Overall, Figure 6.7 shows that the FMLs have good impact damage tolerance.

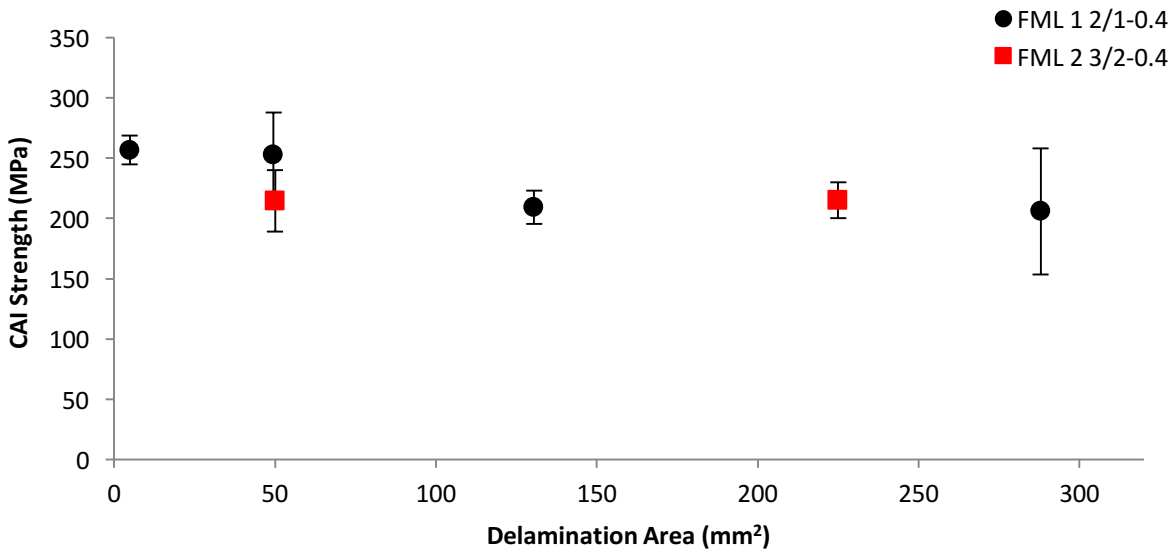

Figure 6.7 Experimental impact-induced delamination area as a function of CAI compressive residual strength.

6.3.2 EFFECT OF TENSILE PRELOAD ON THE CAI STRENGTH OF FMLs

The effect of tensile preload on the CAI strength of FMLs have not been previously reported. From the experimental and numerical results presented in Chapter 4, it is clear that often BVID is not an accurate indication of the extent of the impact damage to FMLs. This is particularly important for tension preloading conditions whereby front crater impact damage area was found to decrease with increasing tension preload levels whereas the overall damage was increased. It is therefore important to identify and characterise the phenomenological correlation between the impact-induced damage and the CAI strength of FMLs subject to tensile preload and low velocity impact conditions.

At low impact energies (5 J and 8.2 J), CAI failure occurred at the specimen free-zone up to 4000 με, and at the impact damage zone for tensile preload levels of 6000 με and 8000 με. The CAI force-displacement curves of FML 1 2/1 specimens following impact at 8.2 J and 19.5 J are shown in Figure 6.8. All FML specimens subject to higher impact energies (12.8 J and 19.5 J) failed at the impact damage zone. A similar failure location observation was observed by James [267] for composite sandwich panels, stating that fibre failure damage was the primary cause of the CAI failure.

Furthermore, it should be noted that the strain limit of aluminium is calculated to be 4600 με. As such, the application of the compression load during CAI tests for specimens at high preload levels (above the yield strain of the aluminium constituents ie. 6000 με and 8000 με) mean that the aluminium layers of the FML specimen undergo strain-hardening.

Figure 6.9 shows the CAI experimental test failure cross-section of FML 1 2/1 impacted at 19.5 J and tensile preload of 8000 με (strain-hardened). A significant decrease in plastic deformation at the point of CAI failure is observed when compared to the FML 1 2/1 unloaded specimen shown in Figure 6.6.

Although the plastic deformation at CAI failure was decreased, force-displacement curves for FML 1 2/1 specimens subject to 19.5 J (Figure 6.8b) showed a significant decrease in the compressive load-carrying capability, even if strain-hardened. Thus, it can be concluded that CAI strength is not solely governed by plastic deformation and cracking of the aluminum layers. Delamination and debonding propagating sub-laminate buckling under CAI loading are key contributors to CAI failure.

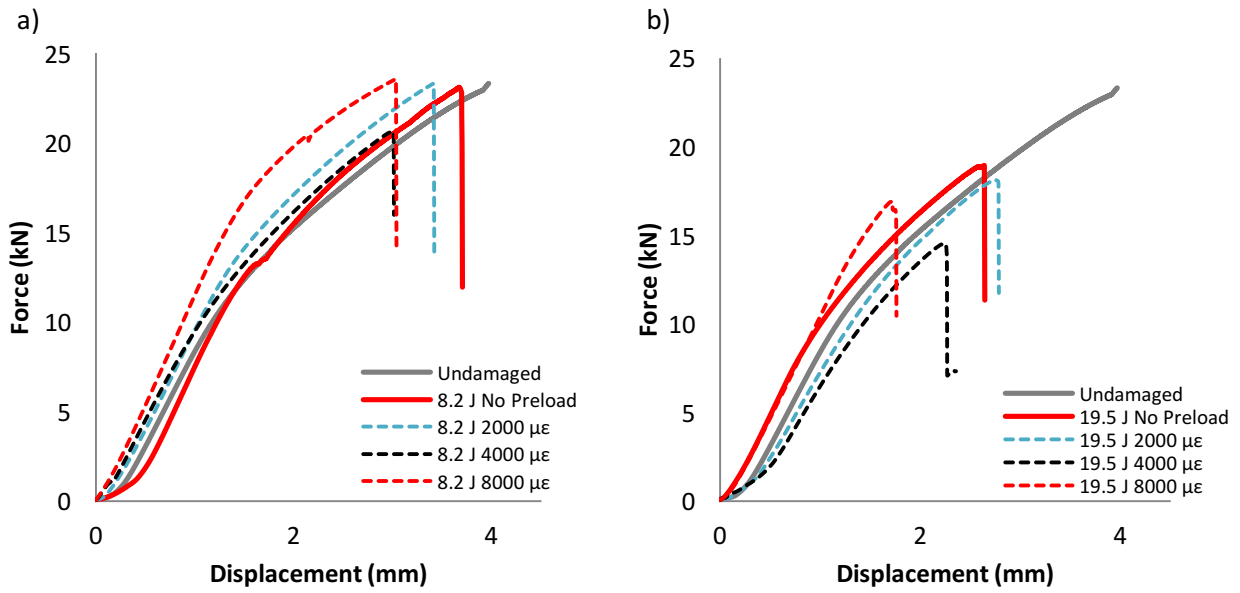

Figure 6.8 Experimental CAI force-displacement response of FML 1 2/1 at varying tensile preload levels for a) 8.2 J and b) 19.5 J impact energies.

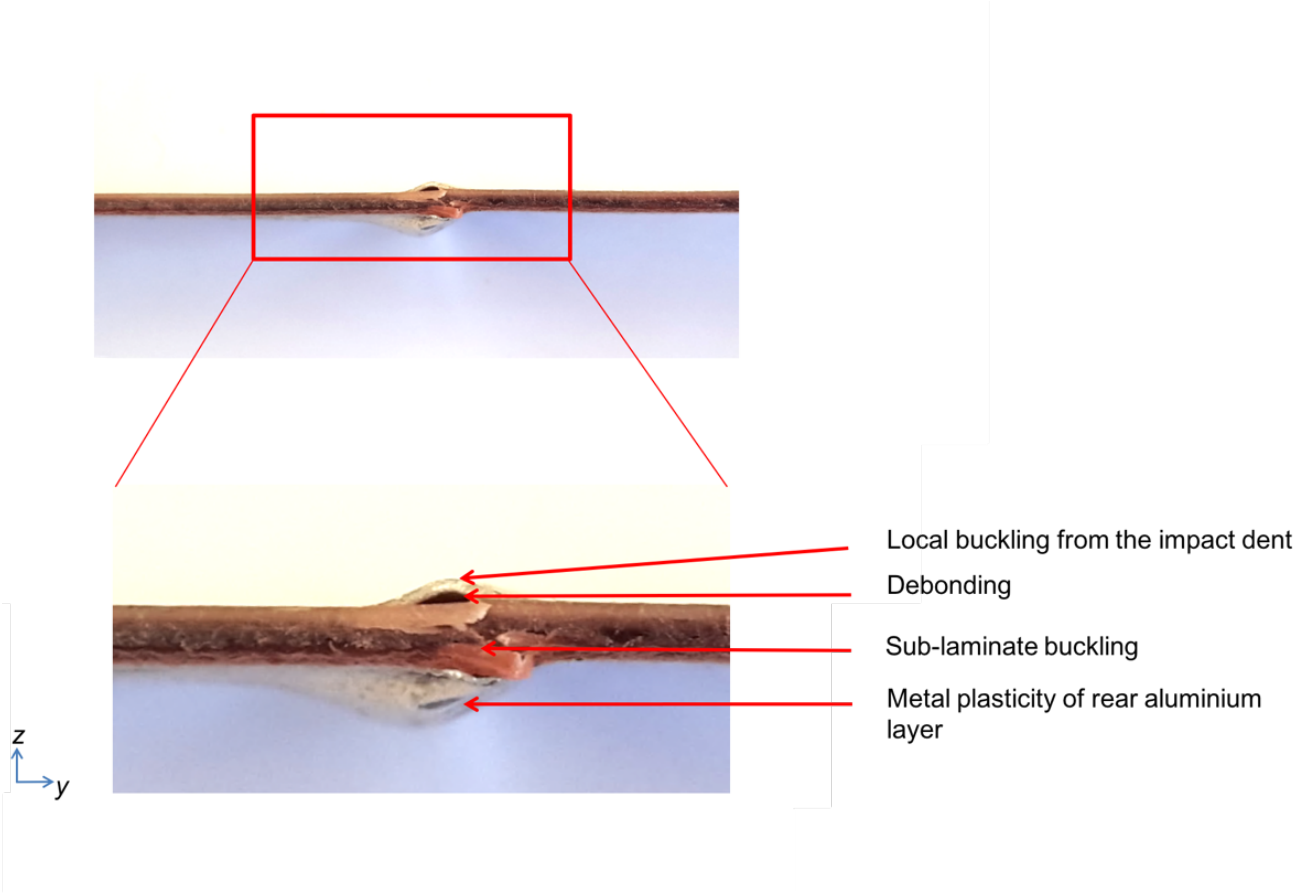

Figure 6.9 Cross-section of FML 1 2/1 impacted at 19.5 J and 8000 με tensile preload showing CAI experimental test failure.

Figure 6.10 shows the CAI strength of FML 1 2/1 with increasing tensile preload levels for a range of low velocity impact energies. The residual compressive strength decreased with increasing tensile preload. At low impact energies (5 J and 8.2 J), the application of the relatively low tensile preload of 2000 με led to no significant reduction (2.5% decrease) to the CAI strength of the FML. As reported in Chapter 4, at these impact energies and preload level, front and rear crater damage occurred, however there are no cracks within the aluminum layers (which is the same for the unloaded FML low impact energies). With an increase in tensile preload minor increases occurred to the front and rear crater damage area. However, at an impact energy of 8.2 J, the total delamination area increased by 67% from no preload case to 4000 με tensile preload and a further 24% from 4000 με and 8000 με (shown in Figure 4.7). Delamination damage occurred at the 0°/90° and 90°/0° interfaces. This corresponded to a decrease in CAI strength of 9% from no preload case to 4000 με and a further 7.6% from 4000 με and 8000 με. At these preloading levels, the initiation and growth of fibre failure perpendicular to the loading direction occurred. The fibre failure of the GFRP plies appears to create a 'weak-point' from which CAI damage propagation can originate. Yan [131] reported that the combination of matrix and fibre shear failure caused final failure of woven fibre-reinforced composites under compression loading, and a similar effect occurred for the FMLs impacted at 12.8 J.

For the FMLs subject to 19.5 J and tension preload of 2000 με, the front crater damage area decreased by 23% and no changes to the front and rear aluminium cracks occurred as shown in Figure 4.5 and Figure 4.6. However, compressive residual strength, shown in Figure 6.10, decreases by 24%. This is particularly important for low velocity impact that generate BVID, such that with a decrease in visible damage to the impacted side of the FML, significant decrease in CAI strength is seen to occur. With a further increase in tension preload, delamination area, front and rear crack lengths and fibre failure significantly increased, while front crater damage area decreased, as discussed in Chapter 4 and reported in Figure 4.6, Figure 4.7 and Figure 4.8. This corresponded to a 14% and 10% decrease in CAI strength at 4000 με and 8000 με respectively, as shown in Figure 6.10.

The impact-induced damage modes play an essential role in determining the residual compressive strength of an FML subject to tension preload, namely (i) growth of aluminum cracks and fibre failure, which both occur perpendicular to the loading (0°) direction and (ii) growth of delamination crack along the ply interfaces and debonding between the aluminum/GFRP plies that divide the intact FML specimen into multiple sub-laminates.

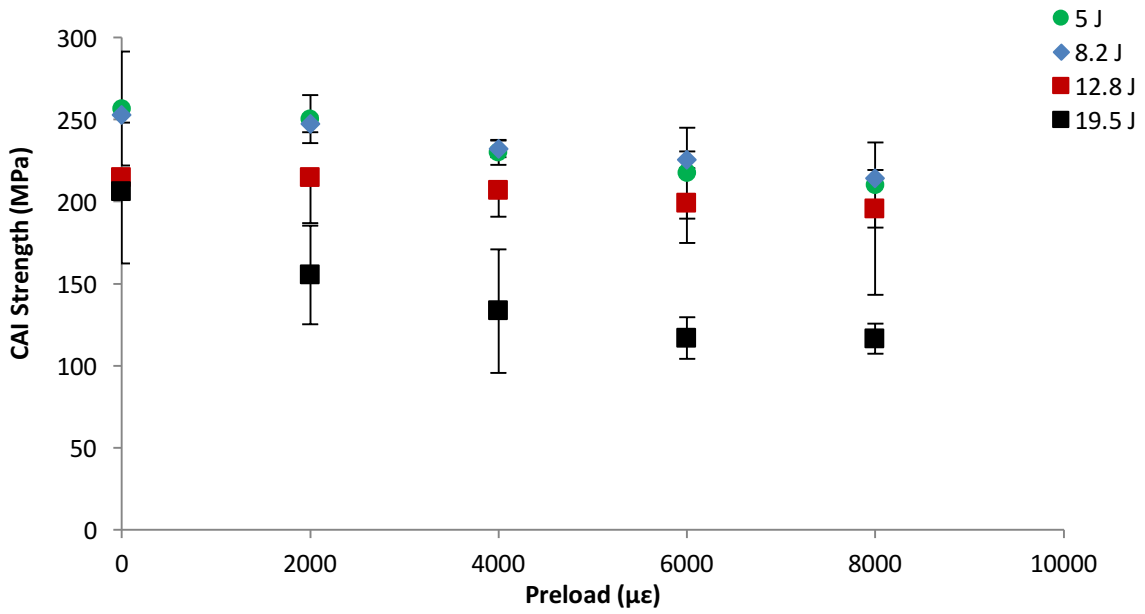

Figure 6.10 Experimental results of compressive residual strength with increasing tensile preload.

6.3.3 EFFECT OF COMPRESSION PRELOAD ON THE CAI STRENGTH OF FMLs

As reported in Chapter 5, compressive preloading conditions for thin FMLs subjected to impact is important due to plate buckling. The application of compressive preload led to a "softening effect" resulting in a more severe dynamic panel response in the form of stress waves leading to increased plastic deformation of the aluminium layers in the FML as well as greater delamination damage. To date, no research has been published on the residual compressive strength of FMLs subject to combined low velocity impact and compressive preloading.

Figure 6.11 illustrates the CAI force-displacement curves for 8.2 J and 19.5 J with increasing compressive preload. At low impact energy (5 J and 8.2 J), the introduction of compressive preload (2000 με) showed a clear reduction of CAI strength compared to the unloaded case. At these low impact energies an increase in the front and rear crater damage areas as well as delamination damage was recorded compared to the unloaded case. Rear aluminum cracking and fibre failure initiated at lower impact energies and preload levels, contributing to the reduction in CAI strength. The impact-induced damage modes were sufficient to reduce the CAI strength and caused buckling of the FML under CAI testing to initiate earlier (applied displacement before failure was lower) compared to the unloaded case. With a further increase in compressive preload levels, only

minor changes to the force-displacement curve were recorded. At higher impact energies (12.8 J and 19.5 J), the force-displacement curves show that the compressive preload level of 2000 με is similar to the unloaded case. However, with an increase in preload of 4000 με and above, buckling is initiated earlier.

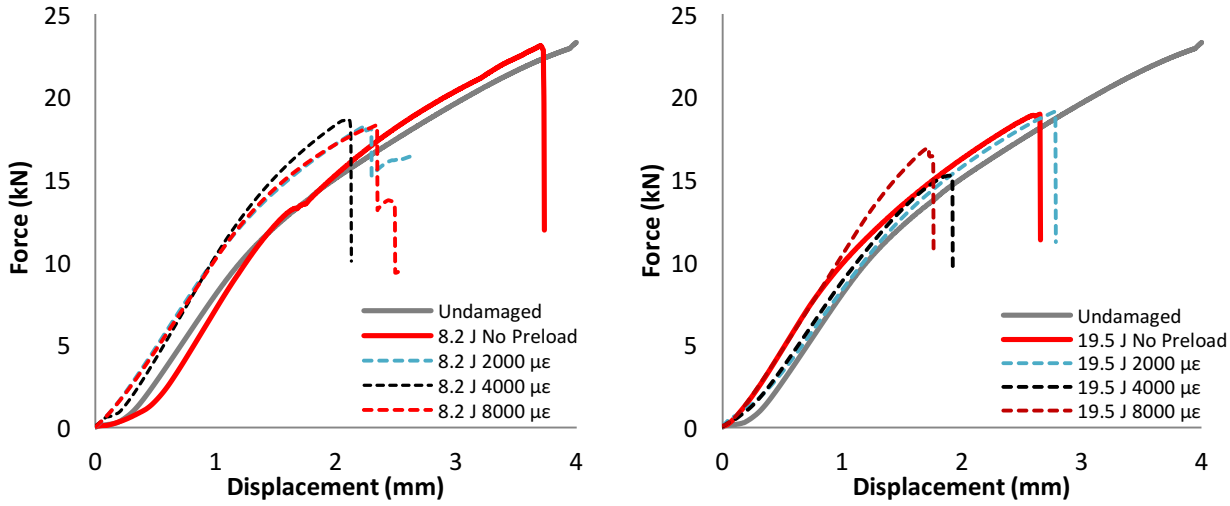

Figure 6.11 Experimental CAI force-displacement response of FML 1 2/1 at varying compressive preload levels for a) 8.2 J and b) 19.5 J impact energies.

These findings are further evidenced in Figure 6.12 showing the CAI strength with increasing preload levels. At low impact energies, compressive residual strength reduction of ~13% of FML 1 2/1 at 2000 με followed by a plateau in CAI strength with increasing compressive preload levels is recorded. At high impact energies (12.8 J and 19.5 J), the increase in compressive preload led to a minimal reduction in residual compressive strength (~7%) which plateaus above 2000 με due to the near perforation of the FML specimen.

Figure 6.13 shows the front and back face, and cross-section of CAI experimental test failure onto FML 1 2/1 subject to 19.5 J at 8000 με. As detailed in Chapter 5, FML under combined compressive preload and impact developed fibre failure and aluminium cracking occurred along the loading (0°) direction, in contrast to the tension and unloaded cases. As such, the region of local buckling from the impact dent on the front face of the FML extended transversely to the direction of applied compression load (0° direction) across the complete specimen width. Damage to the back face of the FML showed a bulge stemming from the debonding in this region. In comparison to the tension and unloaded cases, minor sub-laminate buckling was also recorded.

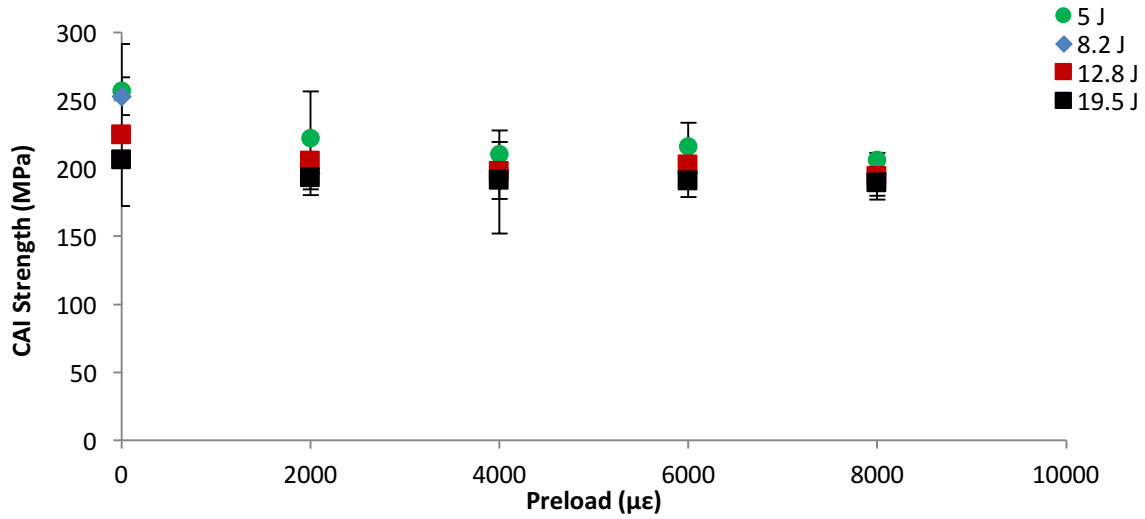

Figure 6.12 Experimental results of compressive residual strength with increasing compressive preload.

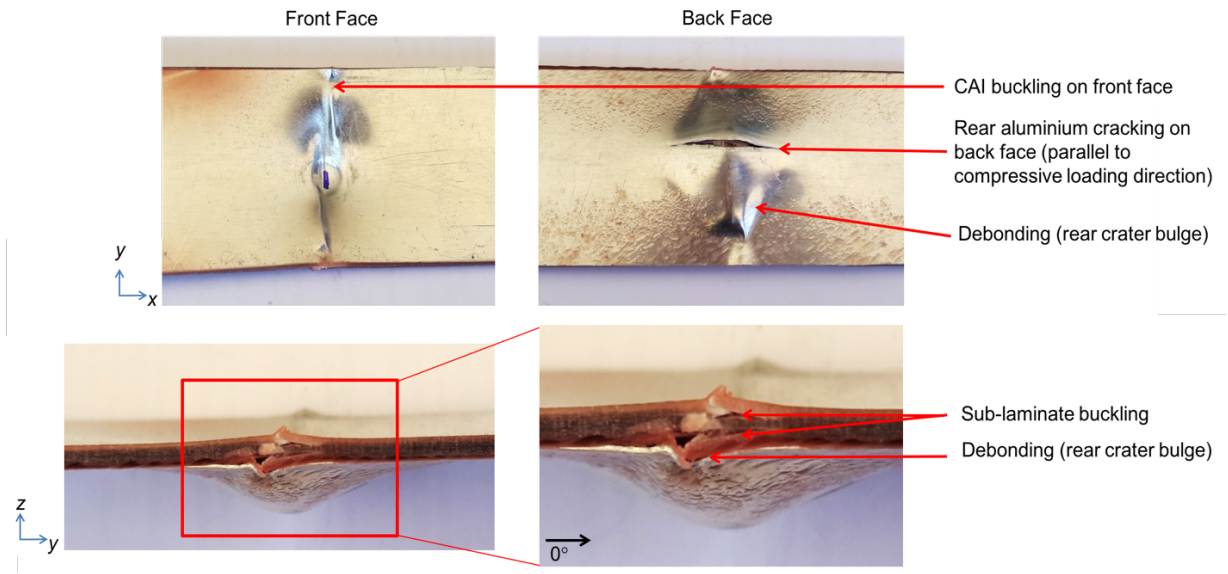

Figure 6.13 Front and back face, and cross-section of CAI experimental test failure onto FML 1 2/1 subject to compressive preload and impact.

6.4 CONCLUSION

An experimental investigation into the residual compressive strength of FMLs following impact loading was performed. Compressive failure was characterised by buckling at the impact damage region, directly under the impactor, or in cases where the damage was not sufficient to initiate failure at the impact damage region, failure at a point of high stress concentration near the constraint ends. The extent and severity of the damage due to the impact event was associated with

an increased loss of CAI strength. The presence of impact-induced cracks in the aluminum layers of the FML as well as fibre failure in a transverse direction to loading (0° direction) was identified as critical failure mechanisms that resulted in a detrimental effect on the CAI strength. Impact-induced delamination and debonding divided the FMLs into multiple sub-laminates initiating sub-laminate buckling from the impacted region, which contributed to the reduced CAI strength.

To date, no research has been conducted on the effect of tension or compression preload and impact on the residual compressive strength of FMLs. The residual compressive strength decreased with increasing tensile preload. With an increase in tensile preload levels, delamination damage and debonding was seen to increase propagating sub-laminate buckling, often extending away from the impact region. Additionally, higher tensile preload levels increased the presence of aluminium cracking and fibre failure of the FMLs, further reducing the CAI strength, with the latter creating a ‘weak point’ from which CAI damage initiated.

At low impact energy (5 J and 8.2 J), the introduction of compressive preload (2000 με) showed a clear reduction of CAI strength compared to the unloaded case, due to the increase in the front and rear crater damage areas as well as delamination damage. Aluminum cracking and fibre failure initiated at lower impact energies and preload levels, contributing to the reduction in CAI strength, and leading to buckling of the FML earlier compared to the unloaded case. With a further increase in compressive preload levels, only minor reductions of the CAI strength were recorded. At high impact energies (12.8 J and 19.5 J), the increase in compressive preload led to a minimal reduction in residual compressive strength which plateaued above 2000 με due to the near perforation of the FML with significant fibre failure and aluminium cracking.

CHAPTER 7 : MAJOR CONCLUSIONS AND FUTURE WORK

7.1 MAJOR CONCLUSIONS

This PhD thesis has presented an original and extensive research study into the deformation, damage and failure processes of FMLs subject to low velocity impact. The aim of this research was to develop a validated FE analysis methodology to identify and characterise the various damage modes, the role of each damage mechanism in the degradation of FMLs subject to low velocity impact, the sequence of damage initiation and progression in order to gain further insight into the interaction of the various failure mechanisms.

7.1.1 IMPACT OF FMLs UNDER STRESS-FREE CONDITIONS

The published literature demonstrated the difficulties of impact modelling FML structures due to the layered structure and different material properties of the metal and composite constituents. Experimental analysis has been the preferred method for determining the impact response of FMLs, however experimental tests pose a number of limitations. The research undertaken in this PhD project extended on published research to develop and validate a computationally efficient and predictive FE analysis methodology to provide a novel analysis of the complex dynamic response and of the multiple damage mechanisms of FMLs subject to low velocity impact. The damage modes considered in the FE model were (i) plastic deformation of the metal layers, (ii) matrix cracking and fibre failure in the composite plies, (iii) delamination between the composite plies, and (iv) debonding of the metal and composite interfaces.

At low impact energies (5 J and 8.2 J), the FE model predicted intralaminar damage modes were initiated in the GFRP plies of the FML 1 2/1, although they did not extent beyond the impact region. Matrix cracking led to the initiation of delamination as well as debonding of the rear aluminium layer and adhesive/GFRP directly under the impact region. Matrix cracking extended beyond the impact region leading to delamination under the impactor at higher impact energies (12.8 J and 19.5 J). The debonding length at the rear aluminium layer and adhesive/GFRP also increased at these impact energies. The combination of these two damage modes allowed the

separation of layers. As such, the FML 1 2/1 specimen acted as a number of separate layers so that effective in-plane redistribution of short transverse loads occurred thereby increasing the energy absorption capability. Front aluminium cracking in the form of a hairline crack was also initiated, increasing from 7 mm to 18 mm for 12.8 J to 19.5 J. At high impact energies, intralaminar damage initiated soon after initial contact with the impactor, and progressed rapidly beyond the visible damage of the aluminium layers of the FML. Links between damage modes were identified, such that matrix cracks triggered delamination due to shear stresses at the interface between adjacent plies having different fibre orientations. The modelling methodology demonstrated a high level of accuracy capturing all damage modes to an extent not previously reported in published literature.

In comparison, the damage modes for FML 2 3/2 plateaued at high impact energies due to the increased thickness with the addition of the middle aluminium layer. Under high impact loads, FML2 3/2 did not undergo relatively high bending strains needed to induce large plastic deformations and debonding. The decrease in the number and extent of damage mechanisms in FML 2 3/2 compared to FML 1 2/1 revealed that significant differences in impact resistance properties exist between the two types of FML specimens. This is reflected in the 50% difference in the energy restitution coefficient between FML 1 2/1 and FML 2 3/2 at 19.5 J. Cracking of the middle layer of aluminium directly under the impactor was observed, and acted as the primary energy absorbing mechanism, however this was less efficient at absorbing impact energy compared to the thinner FML 1 2/1.

Both quantitative and qualitative predictions of the effect of impact energy and FML configuration on damage initiation and progression showed a good degree of accuracy for all damage modes. Moreover, the ability of the FE model to accurately analyse the impact event provided novel insights into the initiation and progression of various damage modes at the ply-level. In-depth analysis of the damage, and in particular, links between damage modes allowed greater understanding of the processes that govern the overall impact resistance of FMLs. Particular emphasis was given to increasing the understanding of the sequence of damage initiation and progression on a ply-based level, which had not been systematically studied before.

7.1.2 IMPACT OF FMLs UNDER PRELOAD CONDITIONS

The literature review revealed that the majority of impact studies on FMLs have been carried out under stress-free conditions. While investigations into the influence of tension and compression preload conditions on the impact behaviour of composites has been extensively studied, less than

five publications have considered the effect of preload on the damage response on FMLs, and are limited to experimental investigations. Therefore, a gap exists to study the influence that preload has on the impact dynamics of FMLs, and how these loading conditions may alter the amount and types of damage. This PhD project therefore involved an experimental and numerical investigation to provide a ply-by-ply insight into the identification, characterisation, sequence and interaction of damage modes that lead to the degradation of FMLs subject to low velocity impact under preload. In this study, tension preload was considered relative to the FML 1 2/1 ultimate tensile strength and was applied from 20% of σ_{ult} up to 65% of σ_{ult}. Compressive preload was applied from 50% of P_{cr} up to 170% of P_{cr} to account for aerospace structures that operate near their critical buckling load or even in the post-buckling region.

Tensile preloading was shown to have a significant influence on the impact response due to the increase in rigidity and overall flexural stiffness of the FMLs. This 'stiffening effect' led to less bending deformation of the FML compared to the unloaded case, as evidenced by the decrease in deflection. Visible front crater damage area decreased by approximately 20% with the initiation of tension preload, and further decreased as the preload level was increased. Front and rear cracking of the aluminium layers also increased with the preload level as a result of increased tension in the layers that allowed the cracks to open.

The initiation and severity of damage modes such as plastic deformation, fibre failure, adhesive failure and delamination upon impact indicated more energy was absorbed with increasing tension preload, reflected in the downward trend of the energy restitution coefficient. Intralaminar and interlaminar damage was observed to propagate away from the impact region leading to a decrease in the structural integrity of an FML structure, underlining the necessity of the FE model to accurately capture and numerically predict all damage modes.

Under tension preload, matrix cracking and delaminations were identified as the critical damage modes in low energy impact (5 J and 8.2 J). At higher impact energies (12.8 J and 19.5 J), all damage modes were initiated before the impactor reached the maximum indentation depth. The FE model was shown to accurately capture the coupling of intralaminar matrix damage and interlaminar delamination. Tensile preload loaded the fibres and matrix during impact causing fibre and interply shear damage mechanisms that promoted delamination. Matrix cracks induced delamination between adjacent plies with different fibre directions, evidenced by the interaction

between matrix tension failure and delamination often extending the beyond visible front and rear crater damage.

In line with previous studies on the effect of tensile preload on the low velocity impact response of composites, the contact duration decreased as a result of the stiffening effect to the FML from the tensile preload, allowing impact-induced stress waves to propagate faster and indicating that incipient damage occurs earlier. The effect was captured by the FE model whereby damage progression was accelerated and damage modes were initiated sooner after the initial impact than stress-free conditions.

Conversely, the application of compressive preload led to a 'softening effect', such that the overall flexural stiffness of the FML specimen decreased. Central permanent deflection, governed by the 'softening effect', increased with the introduction of compressive preload. At the highest impact energy (19.5 J) however, the opposite effect occurred, whereby central permanent deflection decreased by ~20% with the introduction of the compressive preload due to the initiation and propagation of other critical failure modes, such as the delamination, fibre splitting and severe debonding of the front and rear aluminium layer and GFRP/adhesive layer.

The delamination area increased with the compressive preload level for all impact energies. The ply-based FE model predicted interlaminar damage in the form of extensive delamination and intralaminar damage. The FE model also provided new insights into the evolution of some damage modes brought about by an 'additional buckling effect' as the impactor rebounded. Further increases in damage modes were predicted as the FML specimen underwent increased deflections from the bending moment created by the compressive load once the impactor rebounded. Overall the FE methodology is shown to have a high degree of accuracy, capturing all damage mechanisms and trends well, and allowed insight into damage mechanisms that are not detectable using visual inspection.

7.1.3 CAI STRENGTH OF FMLs

Compression-After-Impact (CAI) testing is a widely accepted method for evaluating the damage tolerance of an aircraft structure. Published research into the CAI residual strength of FMLs is limited. Furthermore, to date no investigations on the effect of preload and impact on the residual strength of FMLs has been conducted. This PhD project assessed the level of degradation of FMLs

and provided further understanding of the effect of impact damage modes on the residual compressive strength of FMLs.

CAI failure of the FMLs was characterised by buckling at the impact damage region, directly under the impactor, or in cases where the damage was not sufficient, failure at a point of high stress concentration at the constraint ends. In general, an increase in impact energy and the corresponding increase in impact damage led to a reduction to the residual strength of the FMLs. When the compression load was applied, FML specimens with significant delamination and debonding experienced sub-laminate buckling whereby the material separated into multiple sub-laminates. This led to a combination of local buckling and sub-laminate buckling during CAI testing thereby decreasing the CAI strength of the FMLs. Aluminium cracking and fibre failure were also identified as critical damage mechanisms that reduced the residual strength of the FMLs. The higher CAI strength of the FML 2 3/2 was due to the additional stiffness provided by the middle aluminium layer.

For FML specimens subject to tension preloading conditions, their CAI strength decreased with an increase in preload levels. Delamination, debonding, front and rear cracking of the aluminium sheets, and fibre failure play a significantly role in the reduction of CAI strength. The application of the compression load during CAI tests for specimens subject to high preload levels (ie. 6000 με and 8000 με) caused the aluminium layers of the FML specimen to undergo strain-hardening. The aluminium layers therefore have an increased yield strength, and a greater load is needed to produce additional plastic deformation. This is particularly important for low velocity impacts that generate BVID such that damage tolerance of the FML can reduce significantly even though visible damage is shown to decrease.

A decrease in CAI strength was also measured for FML specimens subject to combined compressive preload and impact. Under compressive preload, rear aluminum cracking and fibre failure initiated at a lower impact energy and preload level compared to the tension preload and unloaded cases. FML specimens under compressive preload experienced fibre failure and aluminium cracking orientated in the 90° direction (perpendicular to CAI loading direction). Upon application of the CAI load, the fibre failure and aluminium cracking produced a ‘weak-point’ from which damage propagation could originate, leading to a reduced CAI strength as compared to FML specimens with fibre failure and aluminium cracking orientated in the 0° direction. At high impact energies (12.8 J and 19.5 J) impact-induced near-perforation of the FML specimen

with significant fibre breakage and aluminium cracking led to low stress CAI failure.

The experimental study into the damage tolerance of FMLs subject to low velocity impact in this project highlighted several critical damage modes that influence the CAI strength of the FML, not previously studied before.

7.2 FUTURE WORK

As a consequence of the scope of this thesis, key areas for further research have been identified. This section briefly describes two research topics which are worthy of further investigation to advance the understanding of FMLs subject to impact damage.

7.2.1 FURTHER ASSESSMENT OF DAMAGE TOLERANCE OF FMLs SUBJECT TO LOW VELOCITY IMPACT

Using the validated FE modelling methodology presented in Chapters 3 to 5, an extension of the work presented should be done to predict the sequence of the progression and damage evolution up to the CAI failure. The ply-based FE model will provide further understanding of the interaction between damage mechanisms underpinning the damage tolerance properties of FMLs, not possible through experimental investigations. A systematic approach combining experimental testing and numerical analysis will be required for the aircraft certification process in the future. The FE modelling methodology can be further extended to consider several geometric parameters for an optimised FML configuration in order to expedite the design process and evaluation of damage tolerance.

7.2.2 DEVELOPMENT OF A STANDARD FOR CAI TESTING FOR FMLs

As mentioned in Chapter 6, no standard for CAI testing of FMLs currently exists. Previous studies have used a wide range of modified test standards such as a modified version of ASTM D7137 for CAI testing of monolithic composite plates over the standard edge compression test for undamaged sandwich panels (ASDM C364). This is because the ASTM C364 standard does not include support for the unloaded edges of the panel, making the specimen vulnerable to failure via global buckling. The ASTM D7137 test standard however applies to specimens thicker than 3 mm, which can be higher than many FML configurations. Due to the layered nature of FMLs, it is

necessary in CAI testing to avoid global buckling so that failure is allowed to propagate via local buckling of the sub-laminates. Without a CAI testing standard, the results of tests are specific to individual studies due to different boundary conditions placed on the FML specimen. A CAI testing standard for FMLs would allow for repeatability of tests and direct comparisons to be made between FML configurations to find an optimised design for damage tolerance.

REFERENCES

1. Kaufman, J.G., *Fracture Toughness of 7075-T6 and -T651 Sheet, Plate, and Multilayered Adhesive-Bonded Panels.* Journal of Basic Engineering, 1967. **89**(3): p. 503-507.
2. Schijve, J., H.T.M. Van Lipzig, G.F.J.A. Van Gestel, and A.H.W. Hoeymakers, *Fatigue properties of adhesive-bonded laminated sheet material of aluminum alloys.* Engineering Fracture Mechanics, 1979. **12**(4): p. 561-579. http://dx.doi.org/10.1016/0013-7944(79)90098-5
3. Straznicky, P.V., J.F. Laliberté, C. Poon, and A. Fahr, *Applications of fiber-metal laminates.* Polymer Composites, 2000. **21**(4): p. 558-567.
4. R.Marissen , J.S., L. B. Vogelesang, *Laminate of aluminum sheet material and aramid fibers*. 1991, Technische Hogeschool Delft.
5. Moussavi-Torshizi, S.E., S. Dariushi, M. Sadighi, and P. Safarpour, *A study on tensile properties of a novel fiber/metal laminates.* Materials Science and Engineering: A, 2010. **527**(18–19): p. 4920-4925. http://dx.doi.org/10.1016/j.msea.2010.04.028
6. Asundi, A. and A.Y.N. Choi, *Fiber metal laminates: An advanced material for future aircraft.* Journal of Materials Processing Technology, 1997. **63**(1–3): p. 384-394. http://dx.doi.org/10.1016/S0924-0136(96)02652-0
7. Fink, A., P.P. Camanho, J.M. Andrés, E. Pfeiffer, and A. Obst, *Hybrid CFRP/titanium bolted joints: Performance assessment and application to a spacecraft payload adaptor.* Composites Science and Technology, 2010. **70**(2): p. 305-317. http://dx.doi.org/10.1016/j.compscitech.2009.11.002
8. Kolesnikov, B., L. Herbeck, and A. Fink, *CFRP/titanium hybrid material for improving composite bolted joints.* Composite Structures, 2008. **83**(4): p. 368-380. http://dx.doi.org/10.1016/j.compstruct.2007.05.010
9. Song, S.H., Y.S. Byun, T.W. Ku, W.J. Song, J. Kim, and B.S. Kang, *Experimental and numerical investigation on impact performance of carbon reinforced aluminum laminates.* Journal of Materials Science & Technology, 2010. **26**(4): p. 327-332. http://dx.doi.org/10.1016/S1005-0302(10)60053-9
10. Sinmazçelik, T., E. Avcu, M.Ö. Bora, and O. Çoban, *A review: Fibre metal laminates, background, bonding types and applied test methods.* Materials & Design, 2011. **32**(7): p. 3671-3685. http://dx.doi.org/10.1016/j.matdes.2011.03.011
11. Cortes, P. and W.J. Cantwell, *Fracture properties of a fiber-metal laminates based on magnesium alloy.* Journal of Materials Science, 2004. **39**(3): p. 1081-1083.
12. Cortes, P. and W.J. Cantwell, *The prediction of tensile failure in titanium-based thermoplastic fibre–metal laminates.* Composites Science and Technology, 2006. **66**(13): p. 2306-2316.
13. Vries, T.J.D., *Blunt and sharp notch behaviour of Glare laminates*. 2001, Delft University of Technology: The Netherlands.
14. Alderliesten, R. and R. Benedictus, *Fiber/metal composite technology for future primary aircraft structures.* Journal of Aircraft, 2008. **45**(4): p. 1182-1189.
15. Vogelesang, L.B. and A. Vlot, *Development of fibre metal laminates for advanced aerospace structures.* Journal of Materials Processing Technology, 2000. **103**(1): p. 1-5. http://dx.doi.org/10.1016/S0924-0136(00)00411-8

16. Botelho, E.C., R.A. Silva, L.C. Pardini, and M.C. Rezende, *A review on the development and properties of continuous fiber/epoxy/aluminum hybrid composites for aircraft structures.* Materials Research, 2006. **9**: p. 247-256.

17. Alderliesten, R.C. and J.J. Homan, *Fatigue and damage tolerance issues of Glare in aircraft structures.* International Journal of Fatigue, 2006. **28**(10): p. 1116-1123. https://doi.org/10.1016/j.ijfatigue.2006.02.015

18. Vlot, A. and J.W. Gunnink, *Fibre Metal Laminates: An Introduction*. 2001: Springer.

19. Aerostructures, F. *GLARE®*. [cited 2013 17 January]; Available from: http://www.fokker.com/Innovations-Glare.

20. FlyAwaySimulation. *Bird strikes on the rise?* 2010 [cited 2013 1 July]; Available from: http://flyawaysimulation.com/news/3945/bird-strikes-on-rise/.

21. Dolbeer RA, W.S., Weller J, Begier MJ., *Wildlife strikes to civil aircraft in the United States 1990-2008*, in *FAA National Wildlife Strike Database*. 2009.

22. Cleary, E.C.D., Richard A.; and Wright, Sandra E., *Wildlife Strikes to Civil Aircraft in the United States 1990-2005*, in *Other Bird Strike and Aviation Materials*. 2006.

23. Administration, F.A. *Aviation Rulemaking Advisory Committee*. Federal Register 1993 [cited 2013 17 January]; 58:[Available from: http://www.faa.gov/regulations_policies/.

24. Meguid, S.A., R.H. Mao, and T.Y. Ng, *FE analysis of geometry effects of an artificial bird striking an aeroengine fan blade.* International Journal of Impact Engineering, 2008. **35**(6): p. 487-498. http://dx.doi.org/10.1016/j.ijimpeng.2007.04.008

25. Heimbs, S., *Energy Absorption in Aircraft Structures*, in *IWHEM2012*. 2012: Huludao, China.

26. Hayduk, R.J., *Hail damage to typical aircraft surfaces.* Journal of Aircraft, 1973. **10**(1): p. 52-55.

27. Baker, A., *Composite Materials for Aircraft Structures*. 2004: American Institute of Aeronautics and Astronautics.

28. Mikkor, K.M., R.S. Thomson, I. Herszberg, T. Weller, and A.P. Mouritz, *Finite element modelling of impact on preloaded composite panels.* Composite Structures, 2006. **75**(1–4): p. 501-513. http://dx.doi.org/10.1016/j.compstruct.2006.04.056

29. Butcher, B.R., *The impact resistance of unidirectional CFRP under tensile stress.* Fibre Science and Technology, 1979. **12**(4): p. 295-326.

30. Vlot, A., *Impact properties of Fibre Metal Laminates.* Composites Engineering, 1993. **3**(10): p. 911-927. http://dx.doi.org/10.1016/0961-9526(93)90001-Z

31. Krishnakumar, S., *Fiber Metal Laminates — The Synthesis of Metals and Composites.* Materials and Manufacturing Processes, 1994. **9**(2): p. 295-354.

32. Esfandiar, H., S. Daneshmand, and M. Mondali, *Analysis of elastic-plastic behavior of fiber metal laminates subjected to in-plane tensile loading*. 2012. Vol. 5. 2012.

33. Abrate, S., *Impact on Laminated Composite Materials.* Applied Mechanics Reviews, 1991. **44**(4): p. 155-190.

34. Malekzadeh, K., M.R. Khalili, and R.K. Mittal, *Response of in-plane linearly prestressed composite sandwich panels with transversely flexible core to low-velocity impact.* Journal of Sandwich Structures and Materials, 2006. **8**(2): p. 157-181.

35. Vlot, A., *Impact loading on fibre metal laminates.* International Journal of Impact Engineering, 1996. **18**(3): p. 291-307. http://dx.doi.org/10.1016/0734-743X(96)89050-6

36. Johnson, W.S., *Impact and Residual Fatigue Behaviour of ARALL and AS6/5245*, in *NASA-TM-89013, NAS 1.15:89013*. 1986, NASA Langley Research Center: Hampton, VA, United States.

37. Liaw, B.M., Y.X. Liu, and E.A. Villars, *Impact damage mechanisms in fiber-metal laminates.* Proceedings of SEM Annual Conference on Experimental and Applied Mechanics, 2001: p. 536-539.

38. Liu, Y. and B. Liaw, *Effects of constituents and lay-up configuration on drop-weight tests of fiber-metal laminates.* Applied Composite Materials, 2010. **17**(1): p. 43-62.

39. Vlot, A., *Impact tests on aluminium 2024 T3, aramid and glass reinforced aluminium laminates and thermoplastic composites*. 1987: Delft University of Technology, Faculty of Aerospace Engineering.

40. Fredell, R., A. Vlot, and M. Verbruggen, *Fatigue and residual strength characteristics of fiber metal laminates subjected to incidental damage.* NASA STI/Recon Technical Report N, 1992. **94**: p. 13803.

41. Vlot, A., *Low-velocity impact loading: on fibre reinforced aluminium laminates (ARALL and GLARE) and other aircraft sheet materials*, in *Delft University of Technology, Faculty of Aerospace Engineering, Report LR-718*. 1993, Delft University of Technology.

42. Vlot, A., E. Kroon, and G. La Rocca, *Impact response of fiber metal laminates.* Key Engineering Materials, 1997. **141**: p. 235-276.

43. Sun, C.T., A. Dicken, and H.F. Wu, *Characterization of impact damage in ARALL laminates.* Composites Science and Technology, 1993. **49**(2): p. 139-144.

44. Lawcock, G.D., L. Ye, Y.W. Mai, and C.T. Sun, *Effects of fibre/matrix adhesion on carbon-fibre-reinforced metal laminates—I.: Residual strength.* Composites Science and Technology, 1998. **57**(12): p. 1609-1619.

45. Vogelesang, L.B. and J.W. Gunnink, *ARALL: A materials challenge for the next generation of aircraft.* Materials & Design, 1986. **7**(6): p. 287-300.

46. Gunnink, J.W., *Damage tolerance and supportability aspects of ARALL laminate aircraft structures.* Composite Structures, 1988. **10**(1): p. 83-104.

47. Cortes, P. and W.J. Cantwell, *The fracture properties of a fibre–metal laminate based on magnesium alloy.* Composites Part B: Engineering, 2006. **37**(2): p. 163-170.

48. Sadighi, M., T. Pärnänen, R.C. Alderliesten, M. Sayeaftabi, and R. Benedictus, *Experimental and numerical investigation of metal type and thickness effects on the impact resistance of fiber metal laminates.* Applied Composite Materials, 2012. **19**(3-4): p. 545-559.

49. Pärnänen, T., R. Alderliesten, C. Rans, T. Brander, and O. Saarela, *Applicability of AZ31B-H24 magnesium in Fibre Metal Laminates–An experimental impact research.* Composites Part A: Applied Science and Manufacturing, 2012. **43**(9): p. 1578-1586.

50. Alderliesten, R., C. Rans, and R. Benedictus, *The applicability of magnesium based Fibre Metal Laminates in aerospace structures.* Composites Science and Technology, 2008. **68**(14): p. 2983-2993.

51. Cortes, P. and W.J. Cantwell, *The impact properties of high-temperature fiber-metal laminates.* Journal of Composite Materials, 2007. **41**(5): p. 613-632.

52. Tarpani, J.R., O. Maluf, and M.C.A. Gatti, *Charpy impact toughness of conventional and advanced composite laminates for aircraft construction.* Materials Research, 2009. **12**(4): p. 395-403.

53. Nakatani, H., T. Kosaka, K. Osaka, and Y. Sawada, *Damage characterization of titanium/GFRP hybrid laminates subjected to low-velocity impact.* Composites Part A: Applied Science and Manufacturing, 2011. **42**(7): p. 772-781.

54. Bernhardt, S., M. Ramulu, and A.S. Kobayashi, *Low-velocity impact response characterization of a hybrid titanium composite laminate.* Journal of Engineering Materials and Technology, 2007. **129**(2): p. 220-226.

55. Fatt, M.S.H., C. Lin, D.M. Revilock Jr, and D.A. Hopkins, *Ballistic impact of GLARE fiber–metal laminates.* Composite Structures, 2003. **61**(1-2): p. 73-88.

56. Morinière, F.D., R.C. Alderliesten, and R. Benedictus, *Energy distribution in GLARE and 2024–T3 aluminium during low-velocity impact.* Proceedings of 28th International Congress of the Aeronautical Sciences, 2012.

57. Vlot, A. and M. Krull, *Impact damage resistance of various fibre metal laminates.* Le Journal de Physique IV, 1997. **7**(C3): p. C3-1045.

58. Hagenbeek, M., *Impact properties*, in *Fibre Metal Laminates: An Introduction*, A. Vlot and J. Gunnink, Editors. 2001, Springer Netherlands. p. 409-426.

59. Laliberté, J., C. Poon, and P.V. Straznicky, *Low-velocity impact damage in GLARE fibre-metal laminates.* Proceedings of International Conference of Composite Materials (ICCM12), 1999. **1001**: p. 12.

60. Caprino, G., G. Spataro, and S. Del Luongo, *Low-velocity impact behaviour of fibreglass-aluminium laminates.* Composites Part A: Applied Science and Manufacturing, 2004. **35**(5): p. 605-616.

61. Aminanda, Y., *Impact study on aircraft type laminate composite plate; experimental, failure criteria and element model review.* In Damage and Fracture of Composite Materials and Structures, 2012: p. 157-188.

62. Gualberto, A.R.M. and J.R. Tarpani, *Residual mechanical properties of hybrid fiber-metal laminates subjected to single and multiple impacts.* Proceedings of 19th Brazilian Congress of Mechanical Engineering (COBEM 19). **1**.

63. Liu, Y.X. and B.M. Liaw. *Drop-weight impact on fiber-metal laminates using various indenters*. in *SEM X International Congress & Exposition on Experimental and Applied Mechanics*. 2004. Costa Mesa, CA.

64. Hufenbach, W., F.M. Ibraim, A. Langkamp, R. Böhm, and A. Hornig, *Charpy impact tests on composite structures–an experimental and numerical investigation.* Composites Science and Technology, 2008. **68**(12): p. 2391-2400.

65. Farsani, R.E., S.M.R. Khalili, and V. Daghigh, *Charpy impact response of basalt fiber reinforced epoxy and basalt fiber metal laminate composites: Experimental study.* International Journal of Damage Mechanics, 2013: p.

66. Khalili, S.M.R., R.K. Mittal, and S.G. Kalibar, *A study of the mechanical properties of steel/aluminium/GRP laminates.* Materials Science and Engineering: A, 2005. **412**(1): p. 137-140.

67. *ASTM D7136 / D7136M-15*, in *Standard Test Method for Measuring the Damage Resistance of a Fiber-Reinforced Polymer Matrix Composite to a Drop-Weight Impact Event*. 2015: West Conshohocken, PA, 2015.

68. Abdullah, M.R. and W.J. Cantwell, *The impact resistance of polypropylene-based fibre–metal laminates.* Composites Science and Technology, 2006. **66**(11-12): p. 1682-1693.

69. Starikov, R., *Assessment of impact response of fiber metal laminates.* International Journal of Impact Engineering, 2013. **59**: p. 38-45.

70. Tsartsaris, N., M. Meo, F. Dolce, U. Polimeno, M. Guida, and F. Marulo, *Low-velocity impact behavior of fiber metal laminates.* Journal of Composite Materials, 2011. **45**(7): p. 803-814.

71. Wu, G., J.-M. Yang, and H.T. Hahn, *The impact properties and damage tolerance and of bi-directionally reinforced fiber metal laminates.* Journal of Materials Science, 2007. **42**(3): p. 948-957.

72. Zhu, S. and G.B. Chai, *Low-velocity impact response of fibre-metal laminates–experimental and finite element analysis.* Composites Science and Technology, 2012. **72**(15): p. 1793-1802.

73. Iaccarino, P., A. Langella, and G. Caprino, *A simplified model to predict the tensile and shear stress–strain behaviour of fibreglass/aluminium laminates.* Composites Science and Technology, 2007. **67**(9): p. 1784-1793.

74. Reddy, J.N., *Mechanics of laminated composite plates and shells: theory and analysis*. Second ed. 2004: CRC Press.

75. Morinière, F.D., R.C. Alderliesten, and R. Benedictus, *Modelling of impact damage and dynamics in fibre-metal laminates–a review.* International Journal of Impact Engineering, 2014. **67**: p. 27-38. https://doi.org/10.1016/j.ijimpeng.2014.01.004

76. Orifici, A., *Degradation models for the collapse analysis of composite aerospace structures*. 2007, Doctoral dissertation, RMIT University.

77. Bagnoli, F., M. Bernabei, D. Figueroa-Gordon, and P.E. Irving, *The response of aluminium/GLARE hybrid materials to impact and to in-plane fatigue.* Materials Science and Engineering: A, 2009. **523**(1–2): p. 118-124. http://dx.doi.org/10.1016/j.msea.2009.05.055

78. Seyed Yaghoubi, A., Y. Liu, and B. Liaw, *Low-velocity impact on Glare 5 fiber-metal laminates: Influences of specimen thickness and impactor mass.* Journal of Aerospace Engineering, 2011. **25**(3): p. 409-420.

79. Lawcock, G.D., L. Ye, Y.W. Mai, and C.T. Sun, *Effects of fibre/matrix adhesion on carbon-fibre-reinforced metal laminates—II. impact behaviour.* Composites Science and Technology, 1998. **57**(12): p. 1621-1628. https://doi.org/10.1016/S0266-3538(97)00094-8

80. Aminanda, Y., *Impact study on aircraft type laminate composite plate; Experimental, failure criteria and element model review*, in *Damage and Fracture of Composite Materials and Structures*, M.N. Tamin, Editor. 2012, Springer Berlin Heidelberg. p. 157-188.

81. Preusch, K., P. Linde, J. Pleitner, H. de Boer, and C. Carmone, *Modelling of fibre metal laminate shells applied to the inter rivet buckling phenomenon.* In European Congress on Computational Methods in Applied Sciences and Engineering (ECCOMAS), 2004.

82. Sridharan, S., *Delamination Behaviour of Composites*. 2008, Woodhead Publishing: Cambridge, United Kingdom.

83. Afaghi-Khatibi, A., G. Lawcock, L. Ye, and Y.-W. Mai, *On the fracture mechanical behaviour of fibre reinforced metal laminates (FRMLs).* Computer Methods in Applied Mechanics and Engineering, 2000. **185**(2-4): p. 173-190.

84. Meola, C., G.M. Carlomagno, F. Ricci, V. Lopresto, and G. Caprino, *Investigation of Impact damage in composites with infrared thermography.* 6th NDT in Progress Proceedings, Prague (Czech Republic) P. Mazal ed, 2011: p. 175-182.

85. Marouf, B.T., R. Bagheri, and R. Mahmudi, *Role of interfacial fracture energy and laminate architecture on impact performance of aluminum laminates.* Composites Part A: Applied Science and Manufacturing, 2008. **39**(11): p. 1685-1693.

86. Hoo Fatt, M.S., C. Lin, D.M. Revilock Jr, and D.A. Hopkins, *Ballistic impact of GLARE™ fiber–metal laminates.* Composite structures, 2003. **61**(1): p. 73-88.

87. Morinière, F.D., R.C. Alderliesten, M.Y. Tooski, and R. Benedictus, *Damage evolution in GLARE fibre-metal laminate under repeated low-velocity impact tests.* Central European Journal of Engineering, 2012. **2**(4): p. 603-611.

88. Phadnis, V.A., K.S. Pandya, N.K. Naik, A. Roy, and V.V. Silberschmidt, *Ballistic impact behaviour of woven fabric composite: finite element analysis and experiments.* Journal of Physics: Conference Series, 2013. **451**(1).

89. Compston, P., W.J. Cantwell, C. Jones, and N. Jones, *Impact perforation resistance and fracture mechanisms of a thermoplastic based fiber-metal laminate.* Journal of Materials Science Letters, 2001. **20**(7): p. 597-599.

90. Langdon, G.S., W.J. Cantwell, and G.N. Nurick, *The blast response of novel thermoplastic-based fibre-metal laminates – Some preliminary results and observations.* Composites Science and Technology, 2005. **65**(6): p. 861-872. http://dx.doi.org/10.1016/j.compscitech.2004.09.025

91. Sadighi, M., R.C. Alderliesten, and R. Benedictus, *Impact resistance of fiber-metal laminates: A review.* International Journal of Impact Engineering, 2012. **49**(0): p. 77-90. http://dx.doi.org/10.1016/j.ijimpeng.2012.05.006

92. Laliberté, J., P.V. Straznicky, and C. Poon, *Impact damage in fiber metal laminates Part 1: Experiment.* AIAA journal, 2005. **43**(11): p. 2445-2453.

93. Fan, J., W.J. Cantwell, and Z.W. Guan, *The low-velocity impact response of fiber-metal laminates.* Journal of Reinforced Plastics and Composites, 2011. **30**(1): p. 26-35.

94. Reyes V, G. and W.J. Cantwell, *The mechanical properties of fibre-metal laminates based on glass fibre reinforced polypropylene.* Composites Science and Technology, 2000. **60**(7): p. 1085-1094. http://dx.doi.org/10.1016/S0266-3538(00)00002-6

95. McKown, S., W.J. Cantwell, and N. Jones, *Investigation of scaling effects in fiber—metal laminates.* Journal of Composite Materials, 2008. **42**(9): p. 865-888.

96. Carrillo, J.G. and W.J. Cantwell, *Scaling effects in the low velocity impact response of fiber-metal laminates.* Journal of Reinforced Plastics and Composites, 2008. **27**(9): p. 893-907.

97. Chai, G.B. and P. Manikandan, *Low velocity impact response of fibre-metal laminates – A review.* Composite Structures, 2014. **107**(0): p. 363-381. http://dx.doi.org/10.1016/j.compstruct.2013.08.003

98. Yaghoubi, A.S., Y. Liu, and B. Liaw, *Stacking Sequence and Geometrical Effects on Low-Velocity Impact Behaviors of GLARE 5 (3/2) Fiber–Metal Laminates.* Journal of Thermoplastic Composite Materials, 2012. **25**(2): p. 223-247.

99. Taheri-Behrooz, F., M.M. Shokrieh, and I. Yahyapour, *Effect of stacking sequence on failure mode of fiber metal laminates under low-velocity impact.* Iranian Polymer Journal, 2014. **23**(2): p. 147-152.

100. Periasamy, M., B. Manickam, and K. Hariharasubramanian, *Impact properties of aluminium-glass fiber reinforced plastics sandwich panels.* Materials Research, 2012. **15**(3): p. 347-354.

101. Atas, C., *An experimental investigation on the impact response of fiberglass/aluminum composites.* Journal of Reinforced Plastics and Composites, 2007. **26**(14): p. 1479-1491.

102. Lawcock, G.D., L. Ye, Y.W. Mai, and C.T. Sun, *Effects of fibre/matrix adhesion on carbon-fibre-reinforced metal laminates--II. Impact behaviour.* Composites science and technology, 1998. **57**(12): p. 1621-1628.

103. Vlot, A., *High strain rate tests on fibre metal laminates*. 1998: Delft University Press.

104. Burstow, C.G., M.C. Corell, and A.C. Rogers, *Mechanisms of Dislocation Motion in 7075-T73 Aluminum Alloy at Strain Rates of 105 s-1.* Materials at High Rates of Strain, Institute of Physics, Bristol, CT, 1989.

105. Kawata, K., S. Hashimoto, S. Sekino, and N. Takeda, *Macro-and Micro-mechanics of High-velocity Brittleness and High-velocity Ductility of Solids*, in *Macro-and Micro-Mechanics of High Velocity Deformation and Fracture*. 1987, Springer. p. 1-25.

106. Davies, R.G. and C.L. Magee, *The Effect of Strain-Rate upon the Tensile Deformation of Materials.* Journal of Engineering Materials and Technology, 1975. **97**(2): p. 151-155.

107. Gilat, A., R.K. Goldberg, and G.D. Roberts, *Strain rate sensitivity of epoxy resin in tensile and shear loading.* Journal of Aerospace Engineering, 2007. **20**(2): p. 75-89.

108. Haque, A. and M.K. Hossain, *Effects of moisture and temperature on high strain rate behavior of S2-Glass–Vinyl ester woven composites.* Journal of Composite Materials, 2003. **37**(7): p. 627-647.

109. Harding, J., ed. *The effect of high strain rate on material properties*. In Materials at High Strain Rates, ed. T.Z. Blazynski. 1987, Elsevier Applied Science London. 133-186.

110. Reyes V, G., *Processing and characterisation of the mechanical properties of novel fibre-metal laminates*. 2002, University of Liverpool.

111. Soltani, P., M. Keikhosravy, R. Oskouei, and C. Soutis, *Studying the tensile behaviour of GLARE laminates: a finite element modelling approach.* Applied Composite Materials, 2011. **18**(4): p. 271-282.

112. Zhou, Y., Y. Wang, and P.K. Mallick, *An experimental study on the tensile behavior of Kevlar fiber reinforced aluminum laminates at high strain rates.* Materials Science and Engineering: A, 2004. **381**(1): p. 355-362.

113. Xia, Y., Y. Wang, Y. Zhou, and S. Jeelani, *Effect of strain rate on tensile behavior of carbon fiber reinforced aluminum laminates.* Materials Letters, 2007. **61**(1): p. 213-215.

114. Wu, H.F., *Effect of temperature and strain rate on tensile mechanical properties of ARALL-1 laminates.* Journal of Materials Science, 1991. **26**(14): p. 3721-3729.

115. McCarthy, M., J. Xiao, N. Petrinic, A. Kamoulakos, and V. Melito, *Modelling of bird strike on an aircraft wing leading edge made from fibre metal laminates–part 1: material modelling.* Applied Composite Materials, 2004. **11**(5): p. 295-315.

116. Cantwell, W.J. and J. Morton, *The impact resistance of composite materials — a review.* Composites, 1991. **22**(5): p. 347-362. http://dx.doi.org/10.1016/0010-4361(91)90549-V

117. Richardson, M.O.W. and M.J. Wisheart, *Review of low-velocity impact properties of composite materials.* Composites Part A: Applied Science and Manufacturing, 1996. **27**(12): p. 1123-1131. http://dx.doi.org/10.1016/1359-835X(96)00074-7

118. Shivakumar, K., W. Elber, and W. Illg, *Prediction of low-velocity impact damage in thin circular laminates.* AIAA journal, 1985. **23**(3): p. 442-449.

119. Vlot, A., *Impact tests on fibre metal laminates under a tensile load*, in *Delft University of Technology, Faculty of Aerospace Engineering*. 1993, Delft University of Technology: The Netherlands.

120. Seyed Yaghoubi, A., Y. Liu, and B. Liaw, *Stacking sequence and geometrical effects on low-velocity impact behaviors of GLARE 5 (3/2) fiber–metal laminates.* Journal of Thermoplastic Composite Materials, 2012. **25**(2): p. 223-247.

121. Iannucci, L., *Progressive failure modelling of woven carbon composite under impact.* International Journal of Impact Engineering, 2006. **32**(6): p. 1013-1043.

122. Linde P, P.J., de Boer H, Carmone C. *Modelling and Simulation of Fibre Metal Laminates*. in *ABAQUS Users Conference*. 2004. Boston, Massachusetts.

123. Hashagen, F., *Numerical analysis of failure mechanisms in fibre metal laminates*. 1998, Doctoral dissertation, Delft University of Technology: The Netherlands.

124. Bienias, J., P. Jakubczak, and K. Dadej, *Low-velocity impact resistance of aluminium glass laminates–Experimental and numerical investigation.* Composite Structures, 2016. **152**: p. 339-348. https://doi.org/10.1016/j.compstruct.2016.05.056

125. Seo, H., J. Hundley, H. Hahn, and J.-M. Yang, *Numerical simulation of glass-fiber-reinforced aluminum laminates with diverse impact damage.* AIAA journal, 2010. **48**(3): p. 676-687.

126. Tita, V., J. de Carvalho, and D. Vandepitte, *Failure analysis of low velocity impact on thin composite laminates: Experimental and numerical approaches.* Composite Structures, 2008. **83**(4): p. 413-428. https://doi.org/10.1016/j.compstruct.2007.06.003

127. Asaee, Z. and F. Taheri, *Experimental and numerical investigation into the influence of stacking sequence on the low-velocity impact response of new 3D FMLs.* Composite Structures, 2016. **140**: p. 136-146.

128. Laliberté, J., C. Poon, and P.V. Straznicky, *Numerical modelling of low-velocity impact damage in fibre-metal-laminates.* In International Congress of Aeronatical Sciences (ICAS), 2002.

129. Lopes, C., P. Camanho, Z. Gürdal, P. Maimí, and E. González, *Low-velocity impact damage on dispersed stacking sequence laminates. Part II: Numerical simulations.* Composites Science and Technology, 2009. **69**(7): p. 937-947.

130. Manikandan, P. and G.B. Chai, *A layer-wise behavioral study of metal based interply hybrid composites under low velocity impact load.* Composite Structures, 2014. **117**: p. 17-31.

131. Yan, H., C. Oskay, A. Krishnan, and L.R. Xu, *Compression-after-impact response of woven fiber-reinforced composites.* Composites Science and Technology, 2010. **70**(14): p. 2128-2136.

132. Setoodeh, A., P. Malekzadeh, and K. Nikbin, *Low velocity impact analysis of laminated composite plates using a 3D elasticity based layerwise FEM.* Materials & Design, 2009. **30**(9): p. 3795-3801.

133. Nguyen, A.T. and A.C. Orifici, *Structural assessment of microvascular self-healing laminates using progressive damage finite element analysis.* Composites Part A: Applied Science and Manufacturing, 2012. **43**(11): p. 1886-1894.

134. Khalili, S.M.R., M. Soroush, A. Davar, and O. Rahmani, *Finite element modeling of low-velocity impact on laminated composite plates and cylindrical shells.* Composite Structures, 2011. **93**(5): p. 1363-1375. http://dx.doi.org/10.1016/j.compstruct.2010.10.003

135. Rathnasabapathy, M., A.P. Mouritz, and A.C. Orifici, *Numerical investigation of fibre-metal laminates subject to impact damage.* Proceedings of 18th International Conference on Composite Materials, 2011.

136. Guan, Z.W., W.J. Cantwell, and R. Abdullah, *Numerical modeling of the impact response of fiber–metal laminates.* Polymer Composites, 2009. **30**(5): p. 603-611.

137. Fan, J., Z. Guan, and W. Cantwell, *Numerical modelling of perforation failure in fibre metal laminates subjected to low velocity impact loading.* Composite Structures, 2011. **93**(9): p. 2430-2436.

138. Mohotti, D., M. Ali, T. Ngo, J. Lu, P. Mendis, and D. Ruan, *Out-of-plane impact resistance of aluminium plates subjected to low velocity impacts.* Materials & Design, 2013. **50**(0): p. 413-426. http://dx.doi.org/10.1016/j.matdes.2013.03.023

139. Lopes, C.S., S. Sádaba, C. González, J. Llorca, and P.P. Camanho, *Physically-sound simulation of low-velocity impact on fiber reinforced laminates.* International Journal of Impact Engineering, 2016. **92**: p. 3-17.

140. Zhou, J., Z. Guan, and W. Cantwell, *Numerical modelling of perforation impact damage of fibre metal laminates.* ICCM2014, Cambridge, England, 2014.

141. Pickett, A.K., M.R.C. Fouinneteau, and P. Middendorf, *Test and Modelling of Impact on Pre-Loaded Composite Panels.* Applied Composite Materials, 2009. **16**(4): p. 225-244. 10.1007/s10443-009-9089-3

142. Kim, M.K., *Impact resistance of composite scarf joints under load*. 2010, MEng Thesis, RMIT University.

143. Ghelli, D. and G. Minak, *Numerical analysis of the effect of membrane preloads on the low-speed impact response of composite laminates.* Mechanics of Composite Materials, 2010. **46**(3): p. 299-316.

144. Choi, I.-H., I.-G. Kim, S.-M. Ahn, and C.-H. Yeom, *Analytical and experimental studies on the low-velocity impact response and damage of composite laminates under in-plane loads with structural damping effects.* Composites Science and Technology, 2010. **70**(10): p. 1513-1522.

145. Choi, I.-H., *Low-velocity impact analysis of composite laminates under initial in-plane load.* Composite Structures, 2008. **86**(1): p. 251-257.

146. Zhang, X., G.A.O. Davies, and D. Hitchings, *Impact damage with compressive preload and post-impact compression of carbon composite plates.* International Journal of Impact Engineering, 1999. **22**(5): p. 485-509.

147. Wiedenman, N. and C.K.H. Dharan, *Ballistic penetration of compressively loaded composite plates.* Journal of Composite Materials, 2006. **40**(12): p. 1041-1061.

148. McGowan, D.M. and D.R. Ambur, *Damage-tolerance characteristics of composite fuselage sandwich structures with thick facesheets.* NASA Langley Technical Report Server, 1997.

149. Herszberg, I. and T. Weller, *Impact damage resistance of buckled carbon/epoxy panels.* Composite Structures, 2006. **73**(2): p. 130-137.

150. Heimbs, S., S. Heller, P. Middendorf, F. Hähnel, and J. Weiße, *Low velocity impact on CFRP plates with compressive preload: Test and modelling.* International Journal of Impact Engineering, 2009. **36**(10–11): p. 1182-1193. http://dx.doi.org/10.1016/j.ijimpeng.2009.04.006

151. Chai, H., *The growth of impact damage in compressively loaded laminates*. 1982, Doctoral dissertation, California Institute of Technology.

152. Kelkar, A.D., J. Sankar, K. Rajeev, R. Aschenbrenner, and G. Schoeppner, *Analysis of tensile preloaded composites subjected to low-velocity impact loads.* AIAA Journal, 1998. **98**(1944): p. 1978-1987.

153. Whittingham, B., I.H. Marshall, T. Mitrevski, and R. Jones, *The response of composite structures with pre-stress subject to low velocity impact damage.* Composite Structures, 2004. **66**(1): p. 685-698.

154. Robb, M.D., W.S. Arnold, and I.H. Marshall, *The damage tolerance of GRP laminates under biaxial prestress.* Composite Structures, 1995. **32**(1): p. 141-149.

155. Sankar, B.V. and C.T. Sun, *Low-velocity impact damage in graphite-epoxy laminates subjected to tensile initial stresses.* AIAA journal, 1986. **24**(3): p. 470-471.

156. Mitrevski, T., I.H. Marshall, R.S. Thomson, and R. Jones, *Low-velocity impacts on preloaded GFRP specimens with various impactor shapes.* Composite Structures, 2006. **76**(3): p. 209-217.

157. Chiu, S.-T., Y.-Y. Liou, Y.-C. Chang, and C.-l. Ong, *Low velocity impact behavior of prestressed composite laminates.* Materials Chemistry and Physics, 1997. **47**(2): p. 268-272.

158. Nettles A, D.V., Branscomb C. *The effects of tensile preloads on the impact response of carbon/epoxy laminates*. in *40th International SAMPE Symposium*. 1995. Anaheim, CA.

159. Sun, C.T. and J.K. Chen, *On the impact of initially stressed composite laminates.* Journal of Composite Materials, 1985. **19**(6): p. 490-504.

160. Cromer, K., *Impact and post-impact response of a composite material to multiple non-coincident impacts*. 2010, Doctoral dissertation, University of Delaware.

161. Abrate, S., *Localized impact on sandwich structures with laminated facings.* Applied Mechanics Reviews, 1997. **50**: p. 69-82.

162. Aminanda, Y., B. Castanié, J.J. Barrau, and P. Thevenet, *Experimental and numerical study of compression after impact of sandwich structures with metallic skins.* Composites Science and Technology, 2009. **69**(1): p. 50-59.

163. Guild, F.J., P.J. Hogg, and J.C. Prichard, *A model for the reduction in compression strength of continuous fibre composites after impact damage.* Composites, 1993. **24**(4): p. 333-339.

164. Cartie, D.D.R. and P.E. Irving, *Effect of resin and fibre properties on impact and compression after impact performance of CFRP.* Composites Part A: Applied Science and Manufacturing, 2002. **33**(4): p. 483-493.

165. Reis, L. and M. De Freitas, *Damage growth analysis of low velocity impacted composite panels.* Composite Structures, 1997. **38**(1-4): p. 509-515.

166. Ishikawa, T., S. Sugimoto, M. Matsushima, and Y. Hayashi, *Some experimental findings in compression-after-impact (CAI) tests of CF/PEEK (APC-2) and conventional CF/epoxy flat plates.* Composites Science and Technology, 1995. **55**(4): p. 349-363.

167. Aymerich, F. and P. Priolo, *Characterization of fracture modes in stitched and unstitched cross-ply laminates subjected to low-velocity impact and compression after impact loading.* International Journal of Impact Engineering, 2008. **35**(7): p. 591-608.

168. *ASTM D7137*, in *Standard Test Method for Compressive Residual Strength Properties of Damaged Polymer Matrix Composite Plates*. 2012: West Conshohocken, PA.

169. Hoogsteden, W.P., *Compression-After-Impact Behavior of ARALL-1 Laminates*. 1992: Wright Lab Wright-Patterson AFB OH.

170. Jakubczak, P., J. Bieniaś, K. Dadej, and W. Zawiejski, *The issue of residual strength tests on thin fibre metal laminates.* Composites Theory and Practice, 2014. **14**(3): p. 134-138.

171. Sánchez-Sáez, S., E. Barbero, R. Zaera, and C. Navarro, *Compression after impact of thin composite laminates.* Composites Science and Technology, 2005. **65**(13): p. 1911-1919.

172. Pavier, M.J. and M.P. Clarke, *Experimental techniques for the investigation of the effects of impact damage on carbon-fibre composites.* Composites Science and Technology, 1995. **55**(2): p. 157-169.

173. Cantwell, W.J. and J. Morton, *Comparison of the low and high velocity impact response of cfrp.* Composites, 1989. **20**(6): p. 545-551. http://dx.doi.org/10.1016/0010-4361(89)90913-0

174. Lopes, C.S., O. Seresta, Y. Coquet, Z. Gürdal, P.P. Camanho, and B. Thuis, *Low-velocity impact damage on dispersed stacking sequence laminates. Part I: Experiments.* Composites Science and Technology, 2009. **69**(7): p. 926-936.

175. Zhang, X., L. Hounslow, and M. Grassi, *Improvement of low-velocity impact and compression-after-impact performance by z-fibre pinning.* Composites Science and Technology, 2006. **66**(15): p. 2785-2794.

176. Petit, S., C. Bouvet, A. Bergerot, and J.-J. Barrau, *Impact and compression after impact experimental study of a composite laminate with a cork thermal shield.* Composites Science and Technology, 2007. **67**(15): p. 3286-3299.

177. Wiggenraad, J.F.M., X. Zhang, and G.A.O. Davies, *Impact damage prediction and failure analysis of heavily loaded, blade-stiffened composite wing panels.* Composite Structures, 1999. **45**(2): p. 81-103.

178. Habib, F.A., *A new method for evaluating the residual compression strength of composites after impact.* Composite structures, 2001. **53**(3): p. 309-316.

179. De Freitas, M. and L. Reis, *Failure mechanisms on composite specimens subjected to compression after impact.* Composite Structures, 1998. **42**(4): p. 365-373.

180. Sela, N. and O. Ishai, *Interlaminar fracture toughness and toughening of laminated composite materials: a review.* Composites, 1989. **20**(5): p. 423-435.

181. Homan, J.J., *Compression after impact.* Report B2v-98-11, Delft University of Technology, Delft, 1998.

182. Dhaliwal, G.S. and G.M. Newaz, *Compression after impact characteristics of carbon fiber reinforced aluminum laminates.* Composite Structures, 2017. **160**: p. 1212-1224. https://doi.org/10.1016/j.compstruct.2016.11.015

183. Bull, D.J., S.M. Spearing, and I. Sinclair, *Observations of damage development from compression-after-impact experiments using ex situ micro-focus computed tomography.* Composites Science and Technology, 2014. **97**: p. 106-114.

184. Rivallant, S., C. Bouvet, E.A. Abdallah, B. Broll, and J.-J. Barrau, *Experimental analysis of CFRP laminates subjected to compression after impact: The role of impact-induced cracks in failure.* Composite Structures, 2014. **111**: p. 147-157.

185. Kilic, Y., *Impact and energy absorption of laminated and sandwich composites*. 2008, Doctoral dissertation, Massachusetts Institute of Technology.

186. Takatoya, T., Y. Sato, I. Susuki, and N. Tsuda, *Compression After Impact Properties of Hybrid Composite Materials.* Proceedings of 16th International Conference on Composite Materials., 2007.

187. Sinke, J., *Manufacturing of GLARE parts and structures.* Applied Composite Materials, 2003. **10**(4-5): p. 293-305.

188. Papanicolaou, G.C., D.J. Bakos, and T.V. Kosmidou, *Effect of the interface stiffness and skin–core adhesion efficiency on the interfacial stress distribution of sandwich structures.* Composites Part A: Applied Science and Manufacturing, 2007. **38**(4): p. 1099-1106. http://dx.doi.org/10.1016/j.compositesa.2006.06.006

189. Cagle, C.V., K. Neville, and H. Lee, *Handbook of Adhesive Bonding*. 1982: T C Press.

190. Park, S.Y., W.J. Choi, H.S. Choi, and H. Kwon, *Effects of surface pre-treatment and void content on GLARE laminate process characteristics.* Journal of Materials Processing Technology, 2010. **210**(8): p. 1008-1016. http://dx.doi.org/10.1016/j.jmatprotec.2010.01.017

191. Rider, A.N., and Parslow, D. , *Progress report on activities in support of composite repair engineering development program tasks AF, AH and AI*, in *Human Protection and Performance Division* 2006, Defence Science and Technology Organisation: Fishermans Bend, Victoria.

192. Díaz-Benito, B., F. Velasco, and M. Pantoja, *Mechanical properties of polyester films painted after silanization of 6063 aluminium alloy with different pretreatment conditions.* Progress in Organic Coatings, 2011. **70**(4): p. 287-292. http://dx.doi.org/10.1016/j.porgcoat.2010.11.008

193. Park, S.Y., W.J. Choi, and H.S. Choi, *The effects of void contents on the long-term hygrothermal behaviors of glass/epoxy and GLARE laminates.* Composite Structures, 2010. **92**(1): p. 18-24. http://dx.doi.org/10.1016/j.compstruct.2009.06.006

194. *ASTM F22 (2002)* in *Standard Test Method for Hydrophobic Surface Films by the Water-Break Test*. 2007: West Conshohocken, PA.

195. Park, S., W. Choi, and H. Choi, *A comparative study on the properties of GLARE laminates cured by autoclave and autoclave consolidation followed by oven postcuring.* The International Journal of Advanced Manufacturing Technology, 2010. **49**(5-8): p. 605-613.

196. Plueddemann, E.P., *Silane Coupling Agents*. Language of Science. 1991: Springer.

197. Jovanović, Ž., J.B. Bajat, R.M. Jančić-Heinemann, M. Dimitrijević, and V.B. Mišković-Stanković, *Methacryloxypropyltrimethoxysilane films on aluminium: Electrochemical characteristics, adhesion and morphology.* Progress in Organic Coatings, 2009. **66**(4): p. 393-399. http://dx.doi.org/10.1016/j.porgcoat.2009.09.002

198. Dragan, K., Ł. Kornas, M. Kosmatka, A. Leski, M. Sałaciński, P. Synaszko, and J. Bieniaś, *Damage detection and size quantification of FML with the use of NDE.* In Fatigue of Aircraft Structures, 2012. **2012**(4): p. 5.

199. *Abaqus 6.11: Analysis User's Manual*. Providence, RI: Dassault Systèmes Simulia Corp. 2013.

200. Crisfield, A., *Non-linear finite element analysis of solids and structures*. 1991: John Wiley & Sons.

201. iMechanica. *Lecture 8: Impact and Postbuckling Analyses*. ABAQUS/Explicit: Advanced Topics 2005 [cited 2013; Available from: http://imechanica.org/files/l8-impact-postbuckling.pdf.

202. Moriniere, F., R. Alderliesten, and R. Benedictus, *Development of fibre-metal laminates for improved impact performance.* The European Physical Journal Special Topics, 2012. **206**(1): p. 79-88.

203. Johnson, G.R. and W.H. Cook. *A constitutive model and data for metals subjected to large strains, high strain rates and high temperatures*. in *Proceedings of the 7th International Symposium on Ballistics*. 1983. The Hague, Netherlands: International Ballistics Committee.

204. Buyuk, M., S. Kan, and M.J. Loikkanen, *Explicit finite-element analysis of 2024-T3/T351 aluminum material under impact loading for airplane engine containment and fragment shielding.* Journal of Aerospace Engineering, 2009. **22**(3): p. 287-295.

205. Hashin, Z. and A. Rotem, *Fatigue failure criterion for fibre reinforced materials.* Journal of Composite Materials, 1973. **7**: p. 448-464.

206. Hashin, Z., *Fatigue Failure Criteria for Unidirectional Fiber Composites*. 1980, DTIC Document.

207. Barbero, E.J., F.A. Cosso, R. Roman, and T.L. Weadon, *Determination of material parameters for Abaqus progressive damage analysis of E-glass epoxy laminates.* Composites Part B: Engineering, 2013. **46**(0): p. 211-220. http://dx.doi.org/10.1016/j.compositesb.2012.09.069

208. Camanho, P.P. and C.G. Dávila, *Mixed-mode decohesion finite elements for the simulation of delamination in composite materials.* NASA-Technical Paper, 2002. **211737**(1): p. 33.

209. Carlomagno, G.M. and C.A. Brebbia, *Computational methods and experimental measurements XV*. Vol. 51. 2011: WIT Press.

210. *ASTM D3039/D3039M*, in *Standard Test Method for Tensile Properties of Polymer Matrix Composite Materials*. 2008: West Conshohocken, PA.

211. Kowalkowski, K.J., N.F. Grace, and S.E. Hodges, *Three-dimensional material properties of composites with S2-glass fibers or ductile hybrid fabric*, in *Lawrence Technological University Report for fulfillment of contract: W56HZV-08-C-0236*. 2013.

212. Canal Casado, L.P., *Experimental and computational micromechanical study of fiber-reinforced polymers*. 2011, Doctoral dissertation, Universidad Polite “cnica de Madrid.

213. Mao, Y., *Micromechanical Modelling of Fibre Reinforced Composite Materials.* 2011.

214. Skyttä, V., O. Saarela, and M. Wallin. *Progressive Failure of Composite Laminates; Analysis vs Experiments*. in *ECF16, Alexandroupolis 2006*. 2013.

215. Zhang, Z., K. Shankar, T. Ray, and M. Tahtali, *Delamination Monitoring of Composite Plates using Vibration-based Surrogate Assisted Optimisation.* Proceedings of 15th Australian International Aerospace Congress (AIAC15), 2013.

216. Turon, A., C.G. Davila, P.P. Camanho, and J. Costa, *An engineering solution for mesh size effects in the simulation of delamination using cohesive zone models.* Engineering Fracture Mechanics, 2007. **74**(10): p. 1665-1682.

217. Orifici, A.C., I. Herszberg, and R.S. Thomson, *Review of methodologies for composite material modelling incorporating failure.* Composite Structures, 2008. **86**(1–3): p. 194-210. http://dx.doi.org/10.1016/j.compstruct.2008.03.007

218. Lapczyk, I. and J.A. Hurtado, *Progressive damage modeling in fiber-reinforced materials.* Composites Part A: Applied Science and Manufacturing, 2007. **38**(11): p. 2333-2341.

219. Song, K., C.G. Dávila, and C.A. Rose. *Guidelines and parameter selection for the simulation of progressive delamination*. in *abaqus User's Conference, Newport, Rhode Island (Hibbit Karlsson and Sorensen, USA, 2008)*. 2008.

220. Vo, T., Z. Guan, W. Cantwell, and G. Schleyer, *Low-impulse blast behaviour of fibre-metal laminates.* Composite Structures, 2012. **94**(3): p. 954-965.

221. Camanho, P.P., C. Davila, and M. De Moura, *Numerical simulation of mixed-mode progressive delamination in composite materials.* Journal of Composite Materials, 2003. **37**(16): p. 1415-1438.

222. Faggiani, A. and B.G. Falzon, *Predicting low-velocity impact damage on a stiffened composite panel.* Composites Part A: Applied Science and Manufacturing, 2010. **41**(6): p. 737-749. http://dx.doi.org/10.1016/j.compositesa.2010.02.005

223. Phadnis, V.A., K.S. Pandya, N.K. Naik, A. Roy, and V.V. Silberschmidt, *Ballistic impact behaviour of woven fabric composite: Finite element analysis and experiments.* ournal of Physics: Conference Series, 2013. **451**(1).

224. González, E., P. Maimí, P. Camanho, A. Turon, and J. Mayugo, *Simulation of drop-weight impact and compression after impact tests on composite laminates.* Composite Structures, 2012. **94**(11): p. 3364-3378.

225. Nguyen, M.Q., D.J. Elder, J. Bayandor, R.S. Thomson, and M.L. Scott, *A review of explicit finite element software for composite impact analysis.* Journal of Composite Materials, 2005. **39**(4): p. 375-386.

226. Abràmoff, M.D., P.J. Magelhaes, and S.J. Ram, *Image processing with J.* Biophotonics International, 2004. **11**(7): p. 36-42.

227. Léonard, F., Y. Shi, C. Soutis, P.J. Withers, and C. Pinna, *Impact damage characterisation of fibre metal laminates by X-ray computed tomography*, in *iCT conference 2014*. 2014: Wels, Austria.

228. Choi, H.Y., R.J. Downs, and F.-K. Chang, *A new approach toward understanding damage mechanisms and mechanics of laminated composites due to low-velocity impact: Part I—Experiments.* Journal of Composite Materials, 1991. **25**(8): p. 992-1011.

229. Liu, D., *Impact-induced delamination—A view of bending stiffness mismatching.* Journal of Composite Materials, 1988. **22**(7): p. 674-692.

230. Joshi, S.P. and C.T. Sun, *Impact induced fracture in a laminated composite.* Journal of Composite Materials, 1985. **19**(1): p. 51-66.

231. Liu, D. and L.E. Malvern, *Matrix cracking in impacted glass/epoxy plates.* Journal of Composite Materials, 1987. **21**(7): p. 594-609.

232. Choi, H.Y., H.-Y.T. Wu, and F.-K. Chang, *A new approach toward understanding damage mechanisms and mechanics of laminated composites due to low-velocity impact: Part II—Analysis.* Journal of Composite Materials, 1991. **25**(8): p. 1012-1038.

233. Caprino, G., V. Lopresto, A. Langella, and M. Durante, *Irreversibly absorbed energy and damage in GFRP laminates impacted at low velocity.* Composite Structures, 2011. **93**(11): p. 2853-2860. http://dx.doi.org/10.1016/j.compstruct.2011.05.019

234. Morinière, F.D., R.C. Alderliesten, and R. Benedictus. *Energy distribution in glare and 2024–T3 aluminium during low-velocity impact*. in *28th International Congress of the Aeronautical Sciences*. 2012. Brisbane, Australia.

235. Whittingham, B., I.H. Marshall, T. Mitrevski, and R. Jones, *The response of composite structures with pre-stress subject to low velocity impact damage.* Composite Structures, 2004. **66**(1–4): p. 685-698. http://dx.doi.org/10.1016/j.compstruct.2004.06.015

236. Subramanian, A., *Damage detection and characterization of fiber-reinforced composites using ultrasonics*. 2013, Doctoral dissertation, Iowa State University.

237. Abrate, S., B. Castanié, and Y.D.S. Rajapakse, *Dynamic Failure of Composite and Sandwich Structures*. Vol. 192. 2012: Springer Science & Business Media.

238. Sun, C.T. and S. Chattopadhyay, *Dynamic response of anisotropic laminated plates under initial stress to impact of a mass.* Journal of Applied Mechanics, 1975. **42**(3): p. 693-698.

239. Silberschmidt, V., *Dynamic Deformation, Damage and Fracture in Composite Materials and Structures*. 2016: Woodhead Publishing.

240. Choi, H.Y., R.J. Downs, and F.-K. Chang, *New approach toward understanding damage mechanisms and mechanics of laminated composites due to low-velocity impact. Part I. Experiments.* Journal of Composite Materials, 1991. **25**(8): p. 992-1011.

241. Schueler, D., N. Toso-Pentecôte, and H. Voggenreiter, *Effects of static preloads on the high velocity impact response of composite plates.* Composite Structures, 2016. **153**: p. 549-556. http://dx.doi.org/10.1016/j.compstruct.2016.06.062

242. Nettles, A.T., *The effects of compressive preloads on the compression-after-impact strength of carbon/epoxy*, in *SAMPE Technical Conference*. 1994, NASA Marshall Space Flight Center: Atlanta, GA; United States.

243. Starnes, J.H., M.D. Rhodes, and J.G. Williams, *Effect of impact damage and holes on the compressive strength of a graphite/epoxy laminate*, in *Nondestructive Evaluation and Flaw Criticality for Composite Materials*. 1979, ASTM International.

244. Heimbs, S. and T. Bergmann, *High-velocity impact behaviour of prestressed composite plates under bird strike loading.* International Journal of Aerospace Engineering, 2012.

245. Heimbs, S., T. Bergmann, D. Schueler, and N. Toso-Pentecôte, *High velocity impact on preloaded composite plates.* Composite Structures, 2014. **111**: p. 158-168.

246. Robb, M.D., W.S. Arnold, and I.H. Marshall, *The damage tolerance of GRP laminates under biaxial prestress.* Composite Structures, 1995. **32**(1-4): p. 141-149.

247. Sun, C.T. and S. Chatopadhyay, *Dynamic Response of Anisotropic Laminated Plates under Initial Stress to Impact of a Mass*. 1976, DTIC Document.

248. Morlo, H. and J. Kunz, *Impact behaviour of loaded composites*, in *Developments in the Science and Technology of Composite Materials*. 1990, Springer. p. 987-991.

249. Ehrich, F., *Low velocity impact on pre-loaded composite structures*. 2013, Doctoral dissertation, Imperial College London.

250. Johnson, A.F., N. Toso-Pentecôte, and D. Schueler, *Damage tolerance of pre-stressed composite panels under impact loads.* Applied Composite Materials, 2014. **21**(1): p. 123-147.

251. Remmers, J.J.C. and R. de Borst, *Numerical modelling: delamination buckling*, in *Fibre Metal Laminates: An Introduction*, A. Vlot and J.W. Gunnink, Editors. 2001, Springer Netherlands: Dordrecht. p. 281-297.

252. Remmers, J.J.C., *Discontinuities in materials and structures: a unifying computational approach*. 2006, Doctoral dissertation, Delft University of Technology: Delft, The Netherlands

253. Soutis, C., *Fibre reinforced composites in aircraft construction.* Progress in Aerospace Sciences, 2005. **41**(2): p. 143-151.

254. Williams, K.V., R. Vaziri, and A. Poursartip, *A physically based continuum damage mechanics model for thin laminated composite structures.* International Journal of Solids and Structures, 2003. **40**(9): p. 2267-2300.

255. Zheng, D. and W.K. Binienda, *Analysis of impact response of composite laminates under prestress.* Journal of Aerospace Engineering, 2008. **21**(4): p. 197-205.

256. Rossikhin, Y.A. and M.V. Shitikova, *Dynamic stability of a circular pre-stressed elastic orthotropic plate subjected to shock excitation.* Shock and Vibration, 2006. **13**(3): p. 197-214.

257. Loktev, A.A., *Dynamic contact of a spherical indenter and a prestressed orthotropic Uflyand–Mindlin plate.* Acta Mechanica, 2011. **222**(1-2): p. 17.

258. Park, R. and J. Jang, *Effect of stacking sequence on the compressive performance of impacted aramid fiber/glass fiber hybrid composite.* Polymer Composites, 2000. **21**(2): p. 231-237. 10.1002/pc.10180

259. Kumar S, T.M., Asokan R, *Compressive strength of the GLARE composite laminates after impact load.* International Journal of Innovative Science, Engineering & Technology, 2015. **2**(3): p. 313-318.

260. Lopes, C.S., P.P. Camanho, Z. Gürdal, P. Maimí, and E.V. González, *Low-velocity impact damage on dispersed stacking sequence laminates. Part II: Numerical simulations.* Composites Science and Technology, 2009. **69**(7): p. 937-947.

261. Abdulhamid, H., C. Bouvet, L. Michel, J. Aboissière, and C. Minot, *Experimental study of compression after impact of asymmetrically tapered composite laminate.* Composite Structures, 2016. **149**: p. 292-303.

262. Malhotra, A. and F.J. Guild, *Impact damage to composite laminates: effect of impact location.* Applied Composite Materials, 2014. **21**(1): p. 165-177.

263. Berketis, K., D. Tzetzis, and P.J. Hogg, *The influence of long term water immersion ageing on impact damage behaviour and residual compression strength of glass fibre reinforced polymer (GFRP).* Materials & Design, 2008. **29**(7): p. 1300-1310.

264. Ghelli, D. and G. Minak, *Low velocity impact and compression after impact tests on thin carbon/epoxy laminates.* Composites Part B: Engineering, 2011. **42**(7): p. 2067-2079.

265. Sjoblom, P. and B. Hwang. *Compression-after-impact- The $5000 data point!* in *International SAMPE Symposium and Exhibition*. 1989.

266. Nettles, A.T. and A.J. Hodge, *Compression-after-impact testing of thin composite materials*, in *International SAMPE Technical Conference*. 1991: Kiamesha Lake, NY; United States. p. 177-183.

267. James, C.T., *Numerical modelling of the compression-after-impact behaviour of composite sandwich panels*. 2015, Doctoral dissertation, Loughborough University.